Katholieke Universiteit Leuven
Arenberg Doctoral School
Faculty of Science
Department of Earth and Environmental Sciences

Development of a pore network model to perform permeability computations on X-ray computed tomography images

Berekening van de permeabiliteit op basis van X-stralen computer tomografie beelden en met behulp van een poriënnetwerkmodel

(met een samenvatting in het Nederlands)

Proefschrift voorgedragen tot het bekomen van de graad van Doctor in de Wetenschappen.
In het openbaar te verdedigen op 13 oktober 2008

door

Philippe Van Marcke

Geboren op 04 Januari 1977 te Vilvoorde (België)

Supervisor: Prof. Dr. R. Swennen
Department of Earth and Environmental Sciences, K.U.Leuven

This research was carried out by:

Philippe Van Marcke
Department of Earth and Environmental Sciences
K.U.Leuven
Celestijnenlaan 200E
3001 Leuven
Belgium

http://ees.K.U.Leuven.be/

The research was financially supported by the Institute for the Promotion of Innovation through Science and Technology in Flanders (IWT-Vlaanderen).

Table of contents

List of figures

List of tables

List of symbols

The symbols are grouped into the different chapters were they appear because some symbols have a different meaning in different chapters. The meaning of the symbols in the equations is also clarified in the text itself. Boldface letters are vectors and italic letters are scalars.

- **Chapter 2**

I	X-ray beam intensity [number of photons]
L_{ray}	length of X-ray path [m]
μ	linear attenuation coefficient [1/m]
$\mathbf{s}$	position along X-ray path [m]
E	energy of X-ray [keV]
d_{detel}	size of detector element [m]
$\%C$	contrast [%]
p_c	critical pressure [Pa]
σ	surface tension [N/m]
θ	contact angle between a fluid and a solid material
r_c	critical radius [m]

- **Chapter 3**

I	X-ray beam intensity [number of photons]
μ	linear attenuation coefficient [1/m]
d	travel distance through object part [m]
P	number of object parts
M_{view}	number of views
$N_{detector}$	number of detector elements
l	travel distance through pixel [m]
J	number of pixels
E	energy of X-ray [keV]
K	number of energy spectrum samples
S	number of source samples
D	number of detector element samples
m	the molecular mass [u]
r	the index in the molecular formula of element
ρ	density [kg/m3]
$w\%_i$	weight percentage [%]
$v\%$	volume percentage [%]
$N_{chemical}$	number of elements in chemical formula
N_{filter}	number of filters
t	thickness of filter [m]
f_R	number of integration frames
k_{noise}	noise factor
s	standard deviation of series
N	number of points in series
n	degree of interpolation
f_s	scatter fraction
d_{app}	apparent detector element size [m]
h	distance between the source and the detector [m]
r	distance between the source and the object [m]
fov	field of view [m]

α	fanangle
w	focal spot size [m]
M	magnification
P_M	primary magnification
S_M	secondary magnification

- **Chapter 5**

$\mathbf{q}$	fluid flux [m³/s]
k	(intrinsic) permeability [m²]
μ	dynamic viscosity [kg/m·s]
S_{sample}	cross-sectional area of the sample [m²]
L_{sample}	length of the sample [m]
p	pressure [Pa]
K	hydraulic conductivity [m³]
α	merge parameter [%]
β	inverse of the merge parameter [%]
N_{voxel}	number of voxels
ρ	density [kg/m³]
$\mathbf{u}$	velocity [m/s]
t	time [s]
$\mathbf{\Pi}$	stress tensor [Pa]
$\mathbf{f}$	external body force [N/kg]
E	total energy per unit mass [J/kg]
A_{TC}	thermal conductivity [W/m·K]
T	temperature [K]
$\mathbf{n}$	outward pointing unit vector
$r_{cylinder}$	radius of cylinder [m]
$L_{cylinder}$	length of cylinder [m]
l_{plate}	aperture between the two plates [m]
L_{plate}	length of plates [m]
a_{plate}	width of two plates [m]
Re	Reynolds number
$L_{characteristic}$	characteristic length [m]
N_{cells}	number of fluid cells
$L_{cross\text{-}sections}$	number of cross-sections
p_c	critical pressure [Pa]
σ	surface tension [N/m]
θ	contact angle between a fluid and a solid material
r_c	critical radius [m]
$S_{bottleneck}$	surface of the bottleneck [m²]

- **Chapter 6**

K	hydraulic conductivity [m³]
p	pressure [Pa]
μ	dynamic viscosity [kg/m·s]
$\mathbf{q}$	fluid flux [m³/s]
k	(intrinsic) permeability [m²]
α	merge parameter [%]
V_{pore}	volume of pore [m³]
$r_{cylinder}$	radius of cylinder [m]
$L_{cylinder}$	length of cylinder [m]

List of abbreviations

CT	Computed Tomography
REV	Representative elementary volume
ERF	Edge Response Function
LSF	Line Spread Function
FWHM	Full Width at Half Maximum
SNR	Signal to Noise Ratio
MTF	Modulation Transfer Function
R(x,y)	Raw radiograph
F(x,y)	Flatfield
ROI	Region Of Interest
Ap	Aperture

Summary

The aim of this work is to use X-ray computed tomography to compute the permeability of a porous sample. By X-ray computed tomography (CT) a 3D image of the sample is acquired. The sample is scanned using an AEA Tomohawk μCT scanner. Subsequently an image of the pore space is extracted from the CT image and the fluid flow through the pore space is modelled.

It is obvious that the quality of the CT images is of crucial importance to get accurate permeability calculations. This quality depends on a lot of factors that are strongly interrelated. By trial-and-error it is possible to look for parameters resulting in an image of a satisfying quality. But such an approach demands a lot of time and is often not possible. Therefore a simulator for the used CT scanners was developed.

The simulator is based on the 2D simulator developed by De Man at UZ Gasthuisberg in 2001 (*De Man, 2001*). Also a 3D simulator was developed. Filtration of the spectrum, noise, scatter and the EEGE effect are included in the simulations. The noise is implemented by using a pragmatic model. The model takes into account the most important features affecting the noise such as the number of integration frames and the use of filters. Scatter is also implemented using a very simple model. More accurate scatter models can be implemented, but they require a lot of computation time.

The simulator is adjusted to the Skyscan 1072 Desktop μCT scanner and the AEA Tomohawk μCT scanner of the Department of Metallurgy and Materials Engineering (MTM) of the K.U.Leuven.

The simulator has the advantage that every parameter or phenomenon in the scanning process can be changed. A lot of simulations can be done in a relatively short time. This makes the simulator a suitable tool to perform a trial-and-error procedure. Moreover, the simulator does not require real objects and the objects simulated are perfectly known. This can be convenient in calibration procedures and to compare the reconstructed to the original image. The use of the simulator in image optimization is demonstrated by a small case. But maybe more important than image optimization is the applicability of the simulator in assessing the impact of several parameters and phenomena on the image quality. The simulator allows the user to examine the limitations of the imaging technique and the processes affecting the image quality and eventually to look for solutions. This is demonstrated by measuring the gold content in rock samples using X-ray computed tomography.

After having scanned the sample, an image of the pore space is obtained by thresholding. A global threshold value is defined and all pixels with a grey value below this threshold value are considered to be pore pixels. The threshold value is selected by matching the porosity of the thresholded images to porosities measured in the laboratory. Using a global threshold value gives rise to errors due to noise in the images, the limited resolution of the images, beam hardening and the EEGE effect. The impact of these factors was assessed by the 3D simulator. The advantage of the simulator is that the objects used are perfectly known which facilitates a comparison between the reconstructed and the original image. The induced errors appeared to be small and thus the chosen threshold approach was maintained.

Once images of the pore structure are obtained, the permeability of the sample is computed. It is assumed that the sample is completely saturated by the fluid for which the permeability is computed. This implies that only one-phase flow is considered and that no relative permeabilities are determined.

Direct numerical simulations solving the Navier-Stokes equations can be applied to compute the permeability. These simulations however require a lot of computational power which becomes immense for large datasets. The datasets used in this work, i.e. the images obtained by computed

tomography, generally contain 1000x1000x1000 voxels[1]. To be able to handle these datasets, a pore network approach is used. A pore network is a simplified representation of the pore space in which the individual pores are replaced by nodes that are connected by hydraulic links.

The partition of the pore space into individual pores brings up the question how a pore can be defined. Different approaches using different definitions for a pore were developed. Delerue first performed a skeletonization algorithm on the pore space and rebuilt the pore space from the skeleton (*Delerue, 2001*). The skeletonization algorithm is beside computationally very expensive, not very robust. A small adaptation to the pore space sometimes gives rise to a completely different partition. A new approach is therefore developed. It is based on the rather intuitive definition that pores are separated from each other at the bottlenecks in the pore space. This turned out to be a fast and robust algorithm dividing the pore space into individual pores. The pores are then replaced by nodes and the nodes of neighbouring pores are connected by links.

The local conductivities of the links are then computed. Again, a new approach is used. Most authors determine these local conductivities by simplifying the links to standard geometrical shapes (*Kovscek et al, 1993; Blunt, 1997a; Blunt, 1998; Fenwick and Blunt, 1998; Dillard and Blunt, 2000; Hui and Blunt, 2000*). This however is a very strong assumption. The local conductivities in this work are computed by a direct numerical simulation solving the Stokes equations. The Stokes equation can be used for non-compressible, Newtonian fluids and for a steady state, laminar flow. Direct numerical simulations offer an accurate method to model the fluid flow. But instead of applying a direct simulation on the sample as a whole the sample is divided into a large number of smaller samples by the network model. In that way, the accuracy of a direct numerical simulation is combined with the advantage of the network model towards computational power.

Once the local conductivities in the network are determined, a mass conservation equation is constructed for every node. From the obtained system of equations the local pressures in and subsequently the flux through the network are computed. In addition a simple cementation and erosion model is implemented. In that way the impact of cementation and erosion on the permeability can be assessed. Also a mercury intrusion experiment can be simulated by the network model. During the partitioning of the pore space the aperture of the bottlenecks in the pore space is computed. In that way the pressure to intrude mercury from one pore into another pore can be determined and thus the intrusion of mercury can be simulated.

The model is validated by several experiments and the errors made in the methodology are demonstrated and further evaluated. A comparison between the permeability of relatively small samples obtained by a direct numerical simulation and the pore network approach however revealed that the results from the both approaches were in the same order of magnitude.

The model developed is more or less generally applicable. A lot of pore network models use standard geometrical shapes to compute the conductivity of the links in the network. Often the used standard shape is chosen in function of the shape of the pores. By using a direct numerical simulations to determine these local conductivities no assumption on the shape of the pores is necessary.

The complete methodology to go from a CT image to a value for the permeability of the sample was considered. As stated already, the quality of the CT images and the thresholding procedure are crucial for accurate permeability computations. By using a simulator for the CT scanning process, the quality of the CT images and the subsequent thresholding was evaluated. It was also demonstrated how the impact of the threshold algorithm and the spatial resolution can be examined. By doing so the user can not only perform permeability computations, but he also gets an idea of the quality of these computations.

[1] A voxel is a volume element representing a value on a 3D regular grid. This is analogous to a pixel, which represents 2D image data. Pore voxels are voxels that are part of the pore space of the sample.

Nederlandse samenvatting

Het doel van dit doctoraatsonderzoek is het bepalen van de permeabiliteit van poreuze stalen op basis van X-stralen computer tomografie, kortweg CT. Het begrijpen van de vloeistofstroming door poreuze media is van belang in tal van onderzoeksdomeinen en industriële toepassingen. Zo speelt de stroming doorheen gesteentes een cruciale rol bij de exploitatie van olie, gas, water en geothermische reservoirs. Ook bij het zoeken naar en evalueren van geschikte geologische formaties voor de berging van afval is inzicht in de permeabiliteit van die formatie en die van de omringende gesteenten van essentieel belang. Andere onderzoeksdomeinen waarin een goed begrip van de vloeistofstroming cruciaal is, zijn hydrologie, bouwfysica, bodemkunde en bodemsaneringen.

Eigenschappen die de vloeistofstroming bepalen, zoals de permeabiliteit en capillaire druk, zijn moeilijk te meten. Dat kan gebeuren met labotests en geofysische loggings, maar deze geven slechts meetresultaten bij één bepaalde set van omstandigheden. Daarenboven geven ze slechts de permeabiliteit weer op bepaalde plaatsen uit bijvoorbeeld een reservoir of aquifer. Om de ruimtelijke variatie in permeabiliteit te bepalen, zijn een groot aantal metingen nodig. Hieruit volgt de behoefte aan een modellering van de vloeistofstroming.

De permeabiliteit van materialen wordt voornamelijk bepaald door de geometrie van de poriënruimte en meer bepaald door de poriëngrootteverdeling en de connectiviteit van de poriën. Met computer tomografie is het mogelijk om een beeld van het inwendige van een staal, en dus ook van de geometrie van de poriënruimte, te bekomen. De techniek bestaat erin dat een bundel X-stralen doorheen het gescande object gestuurd worden. In het object worden de X-stralen geattenueerd. De mate waarin de stralen geattenueerd worden, is afhankelijk van de densiteit en het atoomnummer van de materialen in het object. De verhouding tussen de in- en uitgaande intensiteit wordt weergegeven door de Wet van Beer:

$$\frac{I}{I_0} = \exp(-\int \mu(x) \cdot dx)$$

Hierin is I_0 de oorspronkelijke intensiteit van de X-stralen bundel en I de intensiteit na doorgang door het object. μ is de lineaire attenuatiecoefficient van het materiaal en de integraal beschrijft het pad dat de bundel doorheen het object gevolgd heeft. De intensiteit I bevat dus informatie over de attenuatie langs het gevolgde traject doorheen het staal. Deze intensiteit wordt gemeten door een groot aantal detectorelementen. Door het object onder een groot aantal hoeken te scannen, bekomt men informatie over de attenuatie langs vele trajecten door het object. Uit al die gemeten intensiteiten kan met behulp van een reconstructie-algoritme de attenuatiecoëfficiënt μ in elk punt van het object bepaald worden en op die manier wordt een beeld van het inwendige van het object bekomen.

Een cruciale parameter bij CT scanning is de grootte van de bron aangezien deze in grote mate de resolutie van de beelden bepaalt. Bij klassieke CT scanners ligt de grootte van de bron in een orde van 100 µm. Zogenaamde µCT scanners werken met bronnen in een grootte-orde van enkele tientallen micrometer. Daardoor kan een veel hogere resolutie bereikt worden. Dit gaat evenwel ten koste van de grootte van de objecten die kunnen gescand worden.

In dit onderzoek worden twee µCT scanners gebruikt van het Departement Metaalkunde en Toegepaste Materiaalkunde (MTM) van de K.U.Leuven: een Skyscan 1072 Desktop µCT scanner en aan AEA Tomohawk µCT scanner. De grootte van de stalen die in de Skyscan gebruikt kunnen worden, is beperkt tot 54 mm. Bij de Tomohawk is dat 110 mm.

De kwaliteit van de CT beelden is uiteraard cruciaal voor een verdere berekening van de permeabiliteit op basis van die beelden. De beeldkwaliteit wordt bepaald door vele factoren: het contrast en de

resolutie van de beelden, de hoeveelheid ruis en scatter en het al dan niet voorkomen van artifacten. Al deze factoren zijn nauw verbonden. Zo zal het gebruik van een filter om *beam hardening*[2] te minimaliseren, de hoeveelheid ruis vermeerderen. Het meest optimale beeld hangt af van het doel van de meting en van het gescande staal. Definiëren welke acquisitieparameters resulteren in beelden van een goede kwaliteit kan daardoor niet ondubbelzinnig gebeuren. Het uitvoeren van een *trial-and-error* procedure is vaak niet mogelijk aangezien deze zeer veel tijd vergen. Een simulator voor de CT scanner kan hierbij helpen.

Een simulator biedt de mogelijkheid om relatief snel een groot aantal experimenten uit te voeren waarbij alle scanningsparameters kunnen aangepast worden. Hierdoor kan de invloed van de verschillende parameters die de meting bepalen, onderzocht worden en kan nagegaan worden welke instelparameters bij een specifieke meting een optimaal beeld opleveren. Daarnaast zijn bij een simulatie geen echte objecten nodig en zijn de artificiële stalen in de simulator volledig gekend. Dat vergemakkelijkt een vergelijking tussen het gescande object en het uiteindelijke CT beeld.

Een 3D simulator voor de Skyscan 1072 Desktop µCT scanner en de AEA Tomohawk µCT scanner werd daarom ontwikkeld. De simulator is gebaseerd op een 2D medische CT simulator die in 2001 ontwikkeld werd aan het Universitair Ziekenhuis Gasthuisberg door De Man (*2001*). De simulator leent zich niet enkel tot het uitvoeren van beeldoptimalisatie, maar laat de gebruiker ook toe om de impact van de verschillende instelparameters na te gaan. Dat stelt de gebruiker in staat om in te schatten welke fouten ontstaan bij het scannen en hoe groot deze fouten zijn.

Het bekomen CT beeld van een staal bevat grijswaarden die de attenuatiecoefficient voorstellen. De poriën in het staal hebben een andere attenuatie dan de matrix en hebben dus ook een andere grijswaarde. Door middel van een segmentatie-algoritme kan een beeld van de poriënruimte uit het CT beeld geëxtraheerd worden. Dit gebeurt door een drempelwaarde te definiëren en te stellen dat alle pixels met een grijswaarde lager dan de drempelwaarde poriënruimte vertegenwoordigen. Deze krijgen de waarde “1”. De pixels met een grijswaarde boven de drempelwaarde zijn matrix-pixels en krijgen de waarde “0”. Op die manier ontstaat een binair beeld van de poriënruimte.

Het bepalen van de drempelwaarde is essentieel aangezien een fout beeld van de poriënruimte foute resultaten zal opleveren bij de verdere berekening van de permeabiliteit. Het zoeken naar een juiste drempelwaarde wordt bemoeilijkt door verschillende factoren. De eindige resolutie van CT beelden zorgt ervoor dat de overgang tussen de poriën en de matrix uitgesmeerd wordt. En door *beam hardening* hangt de gereconstrueerde attenuatiecoefficient van eenzelfde materiaal af van zijn positie in het staal. Beide factoren bemoeilijken het gebruik van één drempelwaarde voor het gehele staal. De impact van deze factoren op de segmentatie werd nagegaan aan de hand van de CT simulator.

Na het segmenteren van het CT beeld in een beeld van de poriënruimte wordt de permeabiliteit berekend. Die kan berekend worden door directe numerieke simulaties op basis van de Navier-Stokes vergelijkingen. Dit zijn partiële differentiaalvergelijkingen die de stroming van fluïda beschrijven. Omdat deze vergelijkingen niet analytisch op te lossen zijn, maakt men in de praktijk gebruik van numerieke simulaties en lost men de vergelijking iteratief op. Het nadeel van deze methode is dat ze bijzonder rekenintensief zijn. Grote stalen vergen daardoor veel geheugen en rekentijd. De in dit onderzoek gebruikte beelden zijn ongeveer 1000x1000x1000 pixels groot. Zelfs met parallelle computers is dit te groot om de vloeistofstroming doorheen het staal op die manier te modelleren.

[2] *Beam hardening* is het gevolg van de polychromaciteit van de X-stralen en de energie-afhankelijkheid van de lineaire attenuatiecoëfficiënt. Laag energetische fotonen worden preferentieel geattenueerd waardoor de bundel X-stralen proportioneel rijker wordt aan hoog energetische fotonen. Men zegt dat de bundel harder wordt. Hoe harder de bundel, hoe moeilijker hij geattenueerd wordt. Alle stralen die door een bepaald punt gaan, hebben een ander pad afgelegd. Daardoor zijn ze niet allemaal even “hard” en ondergaan dus niet dezelfde attenuatie in het beschouwde punt. Dit resulteert in afwijkingen die aangeduid worden als *beam hardening* artifacten.

Daarom wordt eerst een netwerkmodel van de poriënruimte geconstrueerd. Hierin worden de poriën vervangen door knopen. De knopen worden verbonden met *links* die de hydraulische connectiviteit tussen de poriën modelleren. Een dergelijk netwerk biedt het voordeel dat de poriënruimte sterk vereenvoudigd is. In plaats van de permeabiliteit van de gehele poriënruimte te bepalen, kan de permeabiliteit van het netwerk berekend worden door eerst de lokale conductiviteiten van de *links* te berekenen. Hiervoor wordt teruggegrepen naar de directe numerieke simulatie. Aangezien de *links* relatief klein zijn, vergen deze berekeningen relatief weinig geheugenruimte en tijd. Op die manier worden de voordelen van beide methodes gecombineerd.

Na het berekenen van de lokale conductiviteiten tussen de knopen in het netwerk, wordt voor elke knoop een vergelijking van behoud van massa opgesteld. Dit leidt tot een matrix-vergelijking waaruit de druk in elke knoop kan berekend worden voor een aangelegd drukverschil over het staal. Nu de druk in elke knoop en de conductiviteit tussen de knopen gekend is, kan de vloeistofstroming doorheen het staal gemodelleerd worden en kan ook de permeabiliteit berekend worden. Bij de modellering wordt uitgegaan van een *steady state*, laminaire stroming en niet samendrukbare, Newtoniaanse vloeistoffen. Daardoor vereenvoudigen de Navier-Stokes vergelijkingen tot de Stokes-vergelijkingen.

Het ontwikkelde model werd gevalideerd door de bekomen permeabiliteit van verschillende stalen te vergelijken met labometingen. De permeabiliteit van kleine stalen werd eveneens berekend door directe numerieke simulatie. Dit toonde aan dat de stroming in het netwerk in sommige gevallen afwijkt van de werkelijke stroming doordat de stroming in het netwerk van knoop naar knoop gaat. Ook de berekening van de lokale conductiviteit van de *links* wijkt in sommige gevallen af van de werkelijke conductiviteit doordat de randvoorwaarden die opgelegd worden bij de directe simulatie niet altijd een realistische simulatie van de werkelijke stroming in de *link* opleveren. Ondanks deze tekortkomingen lag de permeabiliteit bepaald door het model in dezelfde grootte-orde als permeabiliteiten gemeten door een labo-opstelling en berekend met directe numerieke simulatie.

Hieruit kan geconcludeerd worden dat de ontwikkelde methode kan toegepast worden om een idee te verkrijgen van de permeabiliteit van een staal op basis van CT beelden. Het is evenwel belangrijk om daarbij de beperkingen van de methode te onderkennen. Wanneer de resolutie van de CT beelden groter is dan de dimensies van de poriën in het staal, kan de poriënruimte niet accuraat gemodelleerd worden en kan bijgevolg geen nauwkeurige permeabiliteitsberekening uitgevoerd worden.

1. Introduction

Understanding the fluid flow through porous media is of great relevance in many research fields and engineering applications. Examples are the exploration of gas and oil from a petroleum reservoir, hydrology and hydrogeology, building physics, environmental studies, etc. Fluid flow is often subdivided into single-phase and multi-phase flow. In single-phase flow the flow consists of one phase or one component like for instance water flow in the saturated zone of an aquifer. Multi-phase flow refers to the flow of fluids involving more phases or components. Examples are the oil-water interaction in oil reservoirs, the mixture of water and vapour in cavitating pumps, sediment transport, etc. In this thesis only single-phase flow is considered and the computed permeability is the saturated permeability. Saturated permeability means that the sample is completely saturated by the fluid for which the permeability is computed. Although most applications deal with multi-phase flow, the determination of single-phase flow is often a starting point for studies of the more complex multi-phase flow.

The permeability of a sample can be measured in the laboratory and geophysical loggings can be used to assess the permeability in a reservoir or aquifer. These experiments however only reveal fluid flow parameters for one set of conditions. Moreover, they are unlikely to describe the variation on the large scale over which the fluid flow often needs to be determined. This proves the need for a model to predict or simulate the fluid flow under different conditions. Such a model makes it possible to compute the permeability for different fluids, in different directions and to assess the impact of processes changing the pore space geometry such as cementation or the development of secondary porosity due to corrosion. It is the aim of this work to develop a model that determines the permeability of a porous sample.

The permeability of a sample is mainly governed by the pore space geometry, i.e. the pore size distribution and the connectivity of the pores. The model therefore uses an image of the pore space to determine the permeability. This image of the pore space is obtained by first acquiring an image of the internal structure of the sample by X-ray computed tomography. The acquired CT image is a grey-scale image where the grey values represent the linear attenuation coefficient of the material. Pixels having high grey values correspond to an area where the X-rays are highly attenuated. As pores are often filled by air or a fluid which has a relatively low attenuation coefficient, the pore space can be distinguished from the matrix material in the CT image. Subsequently a segmentation method is applied on the CT image to convert it into a binary image of the pore space.

After the image of the pore space is obtained, the permeability of this pore space is computed. Thereto a pore network approach is used. Such a pore network is a simplified representation of the pore structure. By applying such an approach the computation time and memory required for the permeability is significantly reduced. This is necessary as the images acquired by the X-ray CT scanner are too large for a direct numerical simulation of the fluid flow through the sample.

In this research a complete methodology going from the acquisition of a CT image of the sample until the computation of the permeability is developed. The methodology is explained in detail in this thesis. In the sections below the research is situated in the existing research on X-ray computed tomography, image segmentation and pore network modelling. In the last section the scope of the work is outlined and the structure of the thesis is explained.

1.1 X-ray computed tomography

By X-ray computed tomography (CT) the internal structure of objects can be visualized in a non-destructive way. Developed in the 1970's, it was initially used in medical applications. With the construction of μCT scanners in the 1980's, higher resolutions, in the order of tens of micrometers,

were achieved. Over the last decade technical advances exported the technique of X-ray computed tomography to other research areas such as material sciences (*Hallai and Kulcar, 1992; Wevers et al., 2001*), biomedicine (*Bjorndal, 1999; Stoppie et al., 2005; Stoppie et al.,* 2007), building physics (*Franke et al., 1995; Roels et al., 2004*), soil and rock characterization (*Anderson and Hopmans, 1994*) and geology (*Van Geet, 2000; Ketcham and Carlson, 2001; Van Geet et al., 2001; Carlson et al., 2003; Mees et al., 2003*).

The possibility to acquire 3D images of the internal structure of objects evidently opened numerous applications where the characterization or quantification of the internal architecture of materials is of importance. Jansen *et al.* (*2007a, 2007b*) observed the anatomics of wood using CT while Parnas *et al.* (*2003*) and Desplentere *et al.* (*2005*) used the technique to study the architecture of textiles. Kerckhofs *et al.* (*2008*) validated X-ray CT as an imaging technique for porous structures.

Another strength of X-ray CT is its entirely non-destructive nature, at least at the scale of the sample. This makes it highly suitable to monitor active processes, such as water flow (*Ruiz de Argandoña et al., 2003 ; Carmeliet et al., 2003*) or moisture uptake (*Roels et al., 2003; Roels et al., 2004; Roels and Carmeliet, 2006*) in building materials. Also the research on the degradation of building materials benefits from this non-destructive nature as alterations in the structure of these materials can be monitored (*Degryse et al., 2001; Cnudde and Jacobs, 2004; De Graef et al., 2005; Jacobs and Cnudde, 2005*).

In soil and rock mechanics CT is applied to observe fracture patterns and their development. This can for instance by done by scanning a sample that is mechanically loaded in a load cell (*Sellars et al., 2003; Ganne et al., 2007).* Vandersteen *et al.*(*2003a, 2003b*) quantified fracture apertures which is useful in soil research and reservoir studies.

Computed tomography was also successfully applied for numerous geological applications. Rogers (*1999*) and Rowe *et al.* (*2001*) determined the morphology of fossils and Gnos *et al.* (*2002*) applied CT to study meteorites. The detection of economic trace phases by X-ray CT was done by Tivey (*1998*), Taylor *et al.* (*2000*) and Spiess *et al.* (*2001*). Van Geet (*2000*) performed a visualization and quantification of coal macerals. This can provide important information in coalbed-methane research.

Over the last years CT has made its way towards applications in petroleum geology (*Van Geet et al., 2000; Akin and Kovscek, 2003*). In contrast to more classical petrographic techniques like the analysis of thin sections or polished sections using respectively transmitted and incident light microscopy, CT can provide real 3D data in a non-destructive way. This led to the quantification of pore size distributions (*Lindquist et al., 1999; Lindquist et al., 2000; Farber et al., 2003*), the connectivity of pores and cement phases (*Ikeda et al., 2000*), fracture characteristics, such as length, orientation, cementation and aperture (*Van Geet and Swennen, 2001; Weerakone and Wong, 2006*) and the morphology of mineral phases (*Ohtani et al., 2001; Ketcham, 2005*). Information on the pore structure, fractures and the connectivity of pores and cement phases of a reservoir rock is essential when assessing the potential of the reservoir rock for the exploration of oil or gas. Information on the shape of the pores and the rock fabric is important in diagenetic research.

By computing the permeability from CT data many new opportunities arise in reservoir research (*Rangel-German et al., 2005; Le Guen and Kovscek, 2006*). Permeable lithologies can be recognized very fast and simulations can be performed to examine the effect of erosion or cementation or to assess the effect of permeability enhancements techniques, as applied in improved oil recovery (*Gharbi, 2004*).

This research follows this promising path for X-ray CT by developing a methodology to determine the permeability of a sample based on a CT image of the sample. The methodology covers the complete procedure from the acquisition of X-ray CT images, to the subsequent image segmentation that is applied and the final permeability computation. Obviously the quality of the acquired CT images affects the quality of the resulting permeability. It is thus of crucial importance to acquire images of a

sufficiently high quality. The quality of CT images depends on a lot of factors. By changing the acquisition parameters, the user can affect the image quality. The effect of some acquisition parameters is however not always straightforward. Another difficulty is that the factors determining the image quality are strongly interrelated. Choosing the parameters resulting in an optimal image is therefore very complex and depends on the purpose of the measurement and on the object that is scanned. Looking for optimal acquisition parameters by trial-and-error is often not possible as this would in most cases require too much time.

Therefore a simulator of the CT scanner is developed. This enables examining the effect of the acquisition parameters by trial-and-error. Also the need for real objects disappears and the object simulated is perfectly known. This facilitates a comparison with the reconstructed CT image. A 2D simulator was built by De Man to examine metal artifacts in medical scans (*De Man, 1999*). A new simulator based on the work De Man (2*001*) is built, but some aspects were adjusted and the 2D simulator was extended to a 3D simulator.

Beside the advantage of being able to relatively quickly search for optimal acquisition parameters, the simulator can be used to examine the impact of several parameters and phenomena occurring during the scanning process. This can be useful when new applications are examined. Drawbacks and limitations of the technique can very quickly be identified and possible solutions can be tested in advance. This is demonstrated in appendix D where the simulator is used to investigate the applicability of computed tomography in measuring the gold content of rock samples.

1.2 Image segmentation

After having acquired a CT image of the sample, the pore space of the sample has to be extracted from the CT image. This is done by a segmentation method that converts the grey-scale CT image into a binary image where the pore voxels[3] have the value "1" and the matrix voxels are assigned the value "0". A wide variety of segmentation methods exists.

The most straightforward technique to segment a grey-scale CT image into a binary image is to define a threshold value. Voxels with a grey value higher or lower than that threshold value are considered to be foreground voxels while the other voxels are considered to be background material. But as simple as this idea might be, as complicated the choice of the threshold value can be. This value depends on many parameters: the considered material, the heterogeneity of the material, the size of the sample and pores, the amount of noise and scatter, the presence of beam hardening, etc.

An often used procedure to select a threshold value is by calibration (*Ding et al., 1999*). The amount of foreground material can be determined prior to thresholding. When this foreground material is the pore space, the porosity of the concerning sample is determined in advance. The threshold value is then the value giving the best fit between the threshold results and the measurements experimentally obtained. Remeysen (*2007*) used a calibration procedure to select a threshold value to estimate the porosity of limestone and dolomite reservoir rocks of the Khuff Formation in Oman. The porosity of some samples was measured and a threshold value was defined matching the porosity of the thresholded image to the measured porosity. Evidently, this approach is only applicable when the calibration samples are representative for the other samples. Van Geet (*2001*) and Vandersteen *et al.* (*2003*) used phantom objects for which the fracture aperture is known to establish a calibration procedure between the real aperture and the aperture measured on CT images. Such a calibration then allowed determining the fracture aperture on other CT images.

[3] A voxel is a volume element representing a value on a 3D regular grid. This is analogous to a pixel, which represents 2D image data. Pore voxels are voxels that are part of the pore space of the sample.

Another approach to determine the threshold value uses the grey value histogram of the image. The histogram of objects consisting of two materials contains two peaks. This kind of histogram is called bimodal. Figure 1.1 shows the histogram of the CT image of a homogeneous, but porous material. The grey values are clearly grouped into two distinguishable peaks. The grey value in the valley can be used to separate the pores from the matrix. Various methods are developed to select this "valley threshold" (*Nakagawa and Rosenfeld, 1979; Otsu, 1979; Rosenfeld and Kak, 1982; Kittler and Illingwood, 1986; Cho et al., 1989; Pal and Pal, 1991; Pal and Bhandari, 1992; Glasbey, 1993; Gupta and Sortrakul, 1998*).

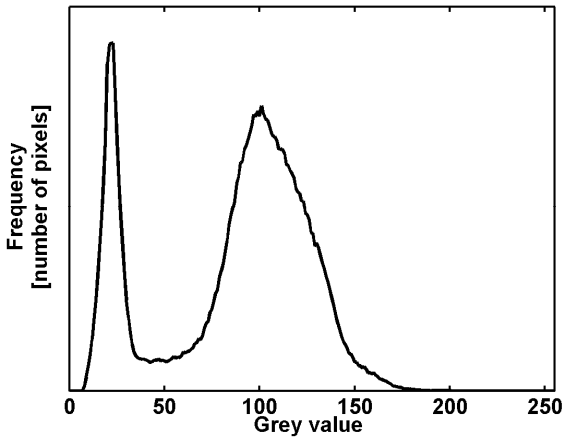

Figure 1.1: Bimodal histogram of a CT image of a homogeneous, but porous sample. The peak on the left corresponds to the pore voxels, the peak on the right to voxels belonging to the rock matrix. The grey value in the valley between these peaks can be used as threshold value segmenting the image in pore voxels and matrix voxels.

The selection of the threshold value has to be performed for each different application as it depends on the material, the size of the object and the acquisition settings of the CT image. Moreover noise can seriously affect the segmentation and the grey values of the foreground material have to differ clearly from the grey values of the background materials.

An alternative approach is not to directly detect whether or not a voxel belongs to the background or foreground material, but to detect the edges between both materials. Edge detection algorithms are mostly based on the abrupt changes in grey levels at an edge. As edges are local features, these algorithms use local information and spatial details are taking into account. Edge detection algorithms are mostly combined with region growing algorithms (*Kelly, 1971; Chien and Fu, 1974; Davis, 1975; Zhou et al., 1989; Cox et al., 1993; Gambotto, 1993*). The procedure consists in first using a severe threshold value for the foreground and the background material. The selected voxels are then supposed to belong certainly to the foreground or background material. These voxels, called seeds, are subsequently propagated. The propagation is based on the gradient in grey value. This gradient is high near the edges between the foreground and background material. Depending on the value of the gradient it is decided whether or not the binary value of a voxel is propagated to its neighbouring voxel.

The previous methods all contain operations involving crisp decisions (i.e. yes or no) about regions, features, properties, etc. Yet, regions in images are not always crisply defined and some of these decisions cannot be made without a given uncertainty. Fuzzy methods[4] avoid this kind of decisions

[4] Fuzzy methods use a probabilistic approach instead of a deterministic one. These methods use fuzzy sets whose elements have degrees of membership. In classical set theory, the membership of elements in a set is assessed in binary terms according to a bivalent condition: an element either belongs or does not belong to the

and use a probabilistic approach (*Trivedi and Bezdek, 1986; Keller and Carpenter, 1990*). The definition of a threshold value based on the histogram can for example be either crisp or fuzzy. When the fuzzy approach is used, threshold values are often determined by minimising a measure of fuzziness[5] (*Keller et al., 1986; Murthy and Pal, 1990*).

The techniques discussed so far are not well applicable for images containing a lot of noise. Iterative methods can then be used, but these are often computationally expensive. Examples of iterative segmentation algorithms are the Markov Random Field model or the Gibbs Random Field model (*Asker and Derin, 1981; Derin et al., 1984; Geman and Geman, 1984; Derin and Elliott, 1987*). Both models assume that the values of the voxels are inter-dependent. Their mutual influence is characterized by a conditional distribution. This distribution is then used to iteratively segment the image.

A very good review on segmentation methods can be found in (*Pal and Pal, 1993*). It is not the purpose of this work to develop a technique to segment a CT image into a binary image of the pore space. Therefore an existing technique is selected and evaluated for its purpose in the scope of this work.

1.3 Pore network model

Once the pore structure is known, a direct numerical simulation solving the Navier-Stokes equation can compute the fluid flow in the pore space. These methods are relatively accurate, but computationally very expensive. This limits their applicability to relatively small samples. The samples acquired in μCT often have dimensions of 1000x1000x1000 voxels. Such large datasets require an immense amount of memory and computation time when using direct numerical simulations.

To be able to handle such large samples, a pore network approach is followed. Such a pore network is a simplification of the geometry of the pore space. The pores are replaced by nodes which are connected by links. Instead of directly computing or modelling the fluid flow in the whole pore space, the flow is first computated in the links of the network. As these links are relatively small, they do not require a lot of computational power. Once these local permeabilities of the links are known, the global permeability of the complete network can easily and rapidly be determined.

The use of a network model was introduced by Fatt (*1956a, b & c*). The author used a regular 2D lattice of pores and throats to compute relative permeability curves for drainage. This author also calculated the permeability of the lattice by constructing an equivalent network of electrical resistors as flow equations could not be numerically solved those days (1956).

Yet, a major shortcoming of Fatt's model is the use of a 2D regular network to describe a 3D pore space with a very irregular and complex geometry. Chatzis and Dullien (*1977*) showed that these 2D networks were not reliable to predict the behaviour in 3D. They also described the impact of the coordination number[6] on the predicted flow properties. Jerauld *et al.* (*1984a and b*) experimented with random networks by starting from networks with a coordination number of 15 and then removing the longest links until an average coordination number of 6 was reached. This was supposed to better describe the real morphology of the pore space, but their results differed little compared to regular networks (*Jerauld and Salter, 1990*).

set. By contrast, fuzzy set theory permits the gradual assessment of the membership of elements in a set. This is described with the aid of a membership function valued in the real unit interval [0,1].

[5] A measure of fuzziness indicates a degree of uncertainty.

[6] The coordination number is the number of links connected to the nodes in the network.

Several attempts were made to predict flow properties by the use of regular networks (*Blunt and King, 1991; Dixit et al., 1998*). But representing the pore space by a regular network failed to grasp the statistics of the pore structures. It was Bryant *et al.* (*1992, 1993a and b*) who first used a network derived from a real pore. The authors tried to simulate the invasion of a non-wetting fluid into Fontainebleau sandstones containing a wetting fluid. These sandstones were modelled by a random close packing of equal spheres. This is a simple, but more or less realistic model of an unconsolidated well-sorted sandstone. Still, their approach appeared not to be applicable for more complex sandstones as the simplification was in those cases too strong.

This led to the conclusion that the pore space itself has to be analysed to capture the real complexity of the pore structure. Thovert *et al.* (*2001*) determined statistical properties of the pore structure to reconstruct the porous medium using spheres. Vogel (*2000*) and Vogel and Roth (*2001*) quantified the complex pore geometry in terms of the pore size distribution and pore connectivity. Both characteristics were obtained from serial 2D sections through an impregnated sample (*Vogel, 1997*). The regular network was adjusted to be consistent with the measured pore size distribution and connectivity. The obtained network was then used to determine the relative permeability of the sample. Carmeliet *et al.* (1999) used the pore radius distribution of a porous space at different scales to derive an isotropic 2D non-planar cross-squared network. The combined water vapour and liquid water transfer in porous materials was studied by these networks. Valvatne and Blunt (*2004*) tried to generate geologically realistic networks by adjusting the pore size distribution of their network to match experimentally obtained capillary pressures. Their purpose was also the prediction of relative permeabilities. Bentz (*1997*) and Garboczi and Bentz (*1996*) used a 3D computer model to simulate the hydration of concrete. They first measured the particle size distribution of the sample of interest and obtained 2D images of the sample by electron microscopy. These images were used to determine the volume and surface area fractions of the different phases of the material. Subsequently they placed spherical particles at random locations in a 3D computational volume following the measured particle size distribution. The particles are then moved, merged, enlarged or scaled down to match the volume and surface fractions.

When X-ray computed tomography became more popular in other than medical applications, researchers started to use this technique to acquire a 3D image of the pore space of samples. This evidently offered new possibilities to generate realistic pore networks. Lindquist and Venkatarangan (*1999*) investigated the 3D geometry of porous samples from CT images. To handle the complexity and irregularity of the pore geometry, a skeleton of the pore space was built (*Lindquist et al., 1996*). This provides a lower dimensional representation of the pore space which is easier to analyse. The skeletonization was performed by a thinning algorithm in which the pore space is eroded until only the centre-lines remain (*Lee et al., 1994*).

Delerue used CT images of the sample to derive the pore space of the sample. A skeleton of the pore space was then generated by using a Voronoi approach (*Delerue, 2001; Delerue et al., 2003*). Subsequently non-overlapping spheres were placed on the skeleton which were inflated to fill the whole pore space. Replacing these spheres by nodes and connecting neighbouring nodes by links resulted in a network representation of the pore space. The pore network was used to simulate mercury intrusion experiments and to compute the permeability of the sample.

However no skeletonization approach is used here as developing a robust skeletonization algorithm is complex and difficult. Watershed methods (*Beucher, 1991; Beucher and Meyer, 1992*) exist which perform an image partitioning without the construction of a skeleton. These methods consider the image data as topographical information. The grey values in a CT image can for example be interpreted as values indicating an altitude. Subsequently this imaginary landscape is flooded starting from the minima. The water coming from different sources is prevented to merge. In that way the image becomes partitioned into catchment basins and watershed lines. In a marker based watershed method (*Moga and Gabbouj, 1998*) the flooding starts from specified markers that are defined in advance by the user or by morphological operators. Such a more interactive approach can enhance the quality of the partition.

In this work a similar partition approach is developed. The pore space is partitioned into individual pores by separating pores at bottlenecks in the pores space. This is mathematically translated by the apertures of the pore voxels. The aperture of a pore voxel is its distance to the border with the matrix. These apertures provide the topographical information for the watershed algorithm. The developed partition algorithm appeared to be more robust and computationally less demanding than the skeletonization approach used by Delerue.

After the pore space is partitioned into individual pores, a network can be replacing the pores by nodes and connecting neighbouring nodes by links. Subsequently the conductivity of these links is computed. Many authors compute the permeability of the links in the network by representing them by standard geometrical shapes. A wide variety of shapes was used such as squares (*Blunt, 1997a & 1998; Fenwick and Blunt, 1998; Dillard and Blunt, 2000*), triangles (*Hui and Blunt, 2000*), cylinders (*Delerue, 2001*) or even a network consisting of stars shaped links (*Kovscek et al., 1993*). Vandersteen *et al.* (*2003*) used a network model of parallel plates to derive the hydraulic properties of a fractured limestone sample. Carmeliet *et al.* (*2003*) described the flow characteristics of 3D cracks in concrete by a network model consisting of parallel plates.

It is however a very strong assumption that the irregular shape of the pore space can be simplified to channels with regular and standard geometrical shapes. Therefore it is chosen to compute the conductivity of the links by a direct numerical simulation solving the Stokes equations. So instead of applying a direct numerical simulation on the sample as a whole which is computationally very expensive, the sample is divided into a large number of small samples by the network model. In that way, the advantage and power of a direct numerical simulation are combined with the advantage of the network model. After having determined the local conductivities, the permeability of the network is computed. This is done by writing down a mass conservation equation for every node in the network. A matrix equation is thus obtained from which the local pressures in the network can be determined for a given pressure difference over the complete sample. Subsequently the flux through the complete sample and the permeability of the complete sample are computed.

1.4 Scope and structure of this work

As explained above, the aim of this work is to developed a methodology to determine the permeability of a sample from a CT image of that sample. This modelling approach has some advantages compared to laboratory measurements and geophysical loggings. CT is more and more used in several research fields. In the characterization of reservoirs CT can be used to get 3D information on the porosity and mineralogy of samples (*Remeysen, 2007*). Once the pore space of these samples is obtained, the permeability of the sample can, relatively quickly, be assessed in addition by the pore network model. For samples where the pore space is cemented, the cementation material can be removed from the CT image by thresholding and the permeability can be computed in the assumption that the pore space was not cemented. Also the impact of erosion and cementation of the pore space on the permeability can be examined.

The methodology thus aims to determine the permeability of a sample that can be scanned by X-ray computed tomography and to assess the impact of processes like erosion or cementation on the permeability of the sample. As explained, this can be useful information in the characterization of, for instance, a reservoir rock. However, it has to be emphasized that a complete characterization of the reservoir permeability requires a multi-scale approach and the determination of a representative elementary volume (REV). An REV is the minimum sample volume that is required to be representative for the sample. When given properties are measured on an REV, these measurements become independent of the size of the sample. In that way the REV concept allows a porous medium, which is essentially a discontinuous, multi-phase system, to be treated as a continuum (*Cressie, 1993; VandenBygaart and Protz, 1999; Brown et al., 2000; Vogel et al., 2002; Wildenschild et al., 2002; Vogel and Brown, 2003; Arns et al., 2005*).

It is beyond the scope of this work to develop such a multi-scale approach. The approach developed here is only occupied by the question how the permeability of a sample can be derived from a CT image of that sample. The advantage of such an approach compared to classical measurement tools, like laboratory measurements and geophysical loggings, is discussed above. The added value of this work compared to already existing research consists in the development of a complete and a more generally applicable approach.

With complete approach it is meant that the methodology treats every aspect going from the acquisition of the CT image to the final permeability computation. As stated already, the quality of the CT images and the thresholding procedure are crucial for accurate permeability computations. By using a simulator for the CT scanning process, the quality of the CT images and the subsequent thresholding can be evaluated.

The pore network model is more or less generally applicable in contrast to a lot of existing pore network models. A lot of pore network models use standard geometrical shapes to compute the permeability of the links in the network. Often the used standard shape is chosen in function of the shape of the pores. By using direct numerical simulations to determine these local conductivities no assumption on the shape of the pores is necessary. However, the partition procedure can still be optimized, in particular for channel-shaped pores. This is further discussed in the last chapter where conclusions are summarized and recommendations for further research are formulated.

In the different steps of the methodology assumptions are made and errors are induced. Only single-phase flow is considered and the computed permeability is the saturated permeability. The permeability is computed by solving the Stokes equations. As the Stokes equations are only valid for steady-state laminar flow of an non-compressible fluid, the methodology is also only applicable under these conditions.

The errors that are made throughout the application of the methodology are indicated in the chapters describing the different steps of the methodology. Their impact on the computed permeability is assessed in the validation. Finally they are summarized in the conclusions and recommendations for improvement are given.

The thesis is structured as follows:

- Chapter 2 discusses the technique of X-ray computed tomography.
- Chapter 3 presents the developed CT simulator and demonstrates its use.
- Chapter 4 deals with the selection and evaluation of the segmentation method converting the grey-scale CT image into a binary image.
- Chapter 5 explains the pore network model.
- Chapter 6 describes the validation of the developed methodology.
- Chapter 7 summarizes the main conclusions, recommendations and perspectives.

2. X-ray computed tomography

X-ray computed tomography (CT) is a non-destructive technique that makes it possible to visualize the internal structure of objects. The technique was developed in the 1970's and was initially intended for medical purposes. Technical advances in the 1980's enabled the construction of so-called micro-CT instruments (μCT). “Micro” refers to the size of the X-ray source which is in the case of μCT scanners in the order of micrometers. This is substantially smaller than the source in medical CT scanners, usually in the order of hundreds of micrometers. The size of the X-ray source is a crucial parameter as it determines the resolution that can be achieved.

Figure 2.1 illustrates the working principle of X-ray computed tomography.

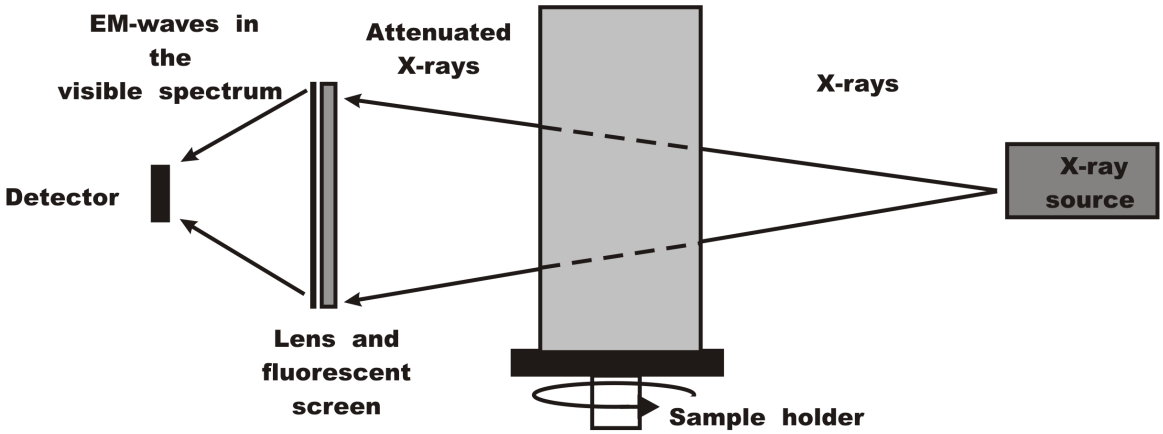

Figure 2.1: Schematic overview of the working of a CT scanner. The X-rays are generated in an X-ray source. Subsequently they travel through the scanned object where they are attenuated, i.e. their intensity diminishes. The amount of attenuation depends on the material of the object and in that way the attenuated rays contain information on the composition of the object. Finally the intensity of the attenuated X-rays is measured by the detector.

X-rays are generated in an X-ray source after which they pass through the scanned object. During this passage the X-rays are attenuated and their intensity decreases. The amount of attenuation mainly depends on the density and the atomic number of the object and on the energy of the X-ray. At the end the intensities of the attenuated X-rays are measured by a detector consisting of a large number of detector elements.

Since the measured intensities depend on the materials lying on the path of the ray, they contain information on the inside of the object. By rotating the source and the detector around the object, different views containing information on different paths through the object are obtained. The measurements of all views in all detector elements are collected in the so-called sinogram $p(d,\theta)$ where d refers to a detector element and θ to a view. Based on this sinogram, a mathematical algorithm can reconstruct the internal structure of the object.

This briefly described process is explained into more detail in the following sections. Section 1 deals with the acquisition of the data (the scanning process itself) and the differences between CT and μCT. Section 2 describes the algorithms that reconstruct the interior of the scanned object from the acquired scans. The quality and processes deteriorating the quality of the CT images are discussed in section 3. A short overview of the different types of CT scanners is given in section 4 and in section 5 the

samples considered in this work are presented. For a more detailed description on X-ray computed tomography, the reader is referred to the large amount of literature available (*Ter-Pogossian et al., 1977; Herman, 1980; Kak and Slaney, 1988; Cho et al., 1993; Suetens, 2002*).

2.1 Data acquisition

The acquisition of the CT images comprises three processes:

- the generation of X-rays in the X-ray source (*Johns and Cunningham, 1971; Randmer et al., 1981*)
- the attenuation of the X-rays in the scanned object (*Johns and Cunningham, 1971; Pullan et al., 1981; Curry et al., 1990*)
- the detection of the X-rays in the detector (*Freundlich and Zaklad, 1981; Haque, 1981; Haque and Stanley, 1981; Peschmann, 1981; Jenkins, 1989; Photometrics, 1990*)

These processes are shortly described below. Again, for a more elaborate description of these processes, one is referred to the references given.

2.1.1 X-ray source

X-rays are electromagnetic waves with a wavelength in the range of 0,01 to 10 nanometers. X-ray radiation is often referred to as Röntgen radiation after one of its first investigators, Wilhelm Conrad Röntgen.

The X-rays are generated in a vacuum tube with a cathode and an anode (figure 2.2). A current flows through the cathode (the cathode current) where electrons are released by thermal excitation. The tube voltage between the cathode and anode accelerates the released electrons towards the anode. This flux of electrons between the cathode and anode is called the tube current. When the electrons hit the anode, they lose their energy by heat and by radiating X-rays.

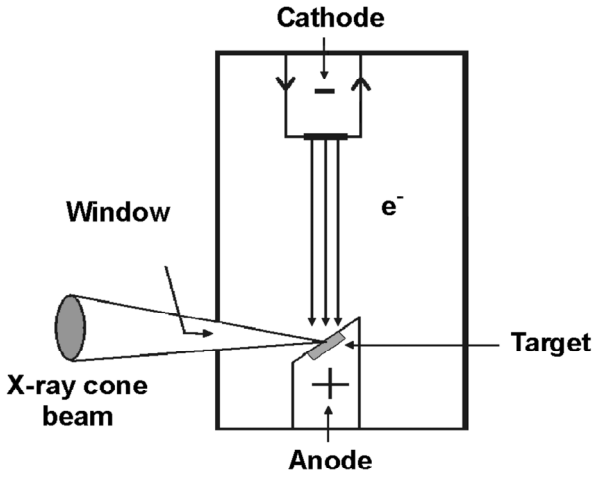

Figure 2.2: Schematic representation of an X-ray tube. Electrons are released from a current in the cathode by thermal excitation. These released electrons accelerate from the cathode towards the anode where the kinetic energy of the electrons is partially converted into X-ray radiation.

The photons in the X-ray beam cover a whole spectrum of energies in the order of tens of keV. The number of generated photons (the intensity) is determined by the number of electrons striking the target (the tube current) and by the tube voltage. Changing the cathode current has a proportional effect on the emitted number of photons without affecting the spectral distribution (*Randmer et al., 1981*). Changing the tube voltage will also affect the spectral distribution of the emitted photons.

Because of the heat generation that occurs at the anode, the target anode must be highly heat resistant. An often used material is tungsten. The spectrum of a tungsten source at a tube voltage of 130 kV is shown in figure 2.3 (*Hammersberg, 1998*).

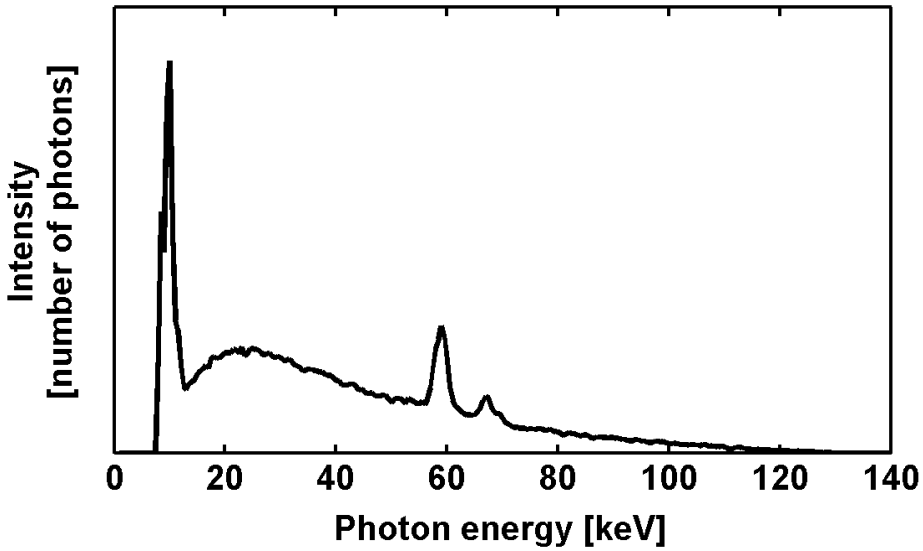

Figure 2.3: The X-ray spectrum of a tungsten source at a nominal tube voltage of 130 kV (*Hammersberg, 1998*). The spectral distribution is determined by the tube voltage. Changing the cathode current changes the intensity of the beam, but does not affect the X-ray spectrum.

An important characteristic of the X-ray source is the size of the target anode, the so-called focal spot size. The main difference between CT and µCT is the focal spot size. Focal spot sizes in CT scanners are in the order of 100 µm while the focal spot in a µCT scanner has dimensions in the order of 10 µm. The focal spot size determines the resolution that can be achieved (*Blumenfeld and Glover, 1981; Simons et al., 1997; Van Geet et al., 2000*), as is illustrated in figure 2.4.

All the X-rays detected between (a) and (b) have travelled through the object and are attenuated. To the right of (c) the highest X-ray intensities will be measured since the X-rays detected here are not attenuated. Between (b) and (c) only a part of the X-rays are attenuated. This zone, which is the transition from maximum attenuation to no attenuation, is called the penumbra interval and creates a blurring of the object edge on the image. Reducing the spot size reduces the penumbra interval and the associated image blurring. As smaller source sizes are used in µCT scanners compared to CT scanners, higher resolutions can be achieved in µCT scanners.

The small spot size in µCT scanners is achieved by focussing the electron beam on the anode by magnetic lenses.

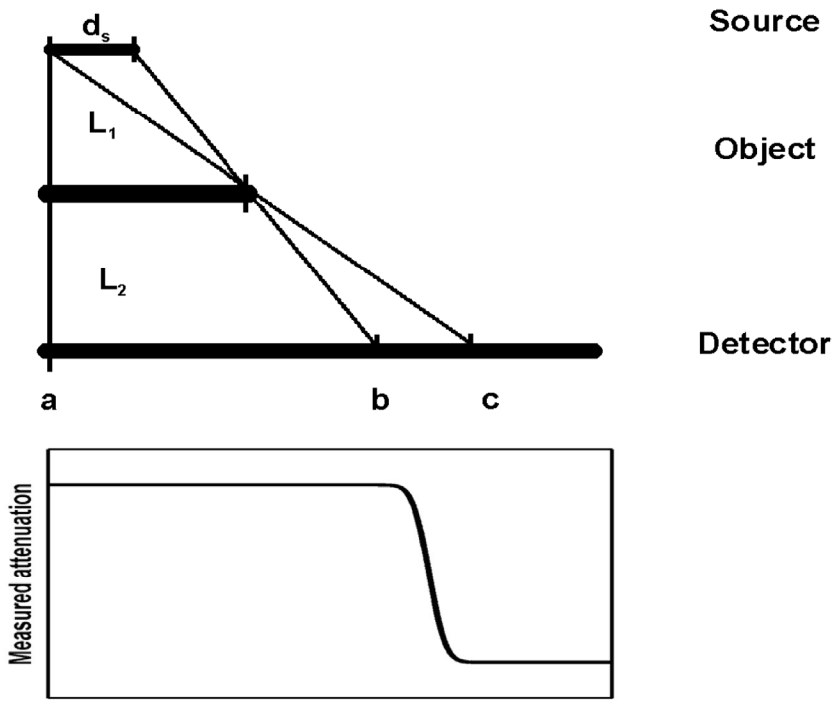

Figure 2.4: Impact of the focal spot size d_s on the spatial resolution. The finite size of the source creates a gradual transition from maximum attenuation to no attenuation at the object edge. This results in a blurring of the object edge and in a decreased resolution.

2.1.2 X-ray attenuation

When the X-rays emitted by the source, pass through the object, they are attenuated. The amount of attenuation is given by Beer's Law:

$$I(E) = I_0(E) \cdot \exp\left(- \int_0^{Lray} \mu(s, E) \cdot ds \right) \tag{2.1}$$

$I_0(E)$ is the ingoing intensity, s the position in the sample along the path the ray travels through the object and L_{ray} is the length of that path. $\mu(E)$ is called the linear attenuation coefficient and is a measure for the attenuation per unit length. The linear attenuation coefficient depends on the energy of the X-ray photons and on the density and atomic number of the material (*Alvarez and Macovski, 1976; Pullan et al., 1981*).

The attenuation of X-rays in a material is caused by several processes (*Curry et al., 1990*):

- **photo-electric effect**
  An incident photon is completely absorbed by an atom. The atom loses its extra energy by ejecting an orbital electron. This only occurs at discrete energy levels. For low energy X-rays, the photo-electric effect is the dominant process.

- **coherent and incoherent scatter**
  Scatter occurs when the direction of an incident photon is changed. In coherent scatter the photon is only deflected and no energy is lost. Photons that undergo

incoherent scatter lose a part of their energy by ejecting an orbital photon. Coherent scatter only occurs noticeably at low energy. Incoherent scatter, also called Compton scattering, becomes relatively more important at higher energies.

- **pair production and annihilation**
  When a high energetic photon comes close to a nucleus, its energy can be partly or totally transferred into mass by converting into an electron and a positron.

In X-ray computed tomography only the photo-electric effect and scatter are important. A part of the scattered photons will be measured by the detector. Obviously, these photons do not contain relevant information since they are deviated from their original path. Scattered photons therefore have a negative impact on the image quality.

The acquisition of the X-rays in the scanned object depends on the composition of the object. In that way the attenuated rays contain information on the inside of the object. It is possible to reconstruct the interior of that object from rays that have travelled along different paths through the scanned object. Most CT scanners are used for medical applications where one wants to look inside a patient. The different views, resulting in information about different paths, are acquired by turning the X-ray source and detector around the patient. In most µCT scanners it is the object that is turned around between a fixed X-ray source and detector. This procedure is less prone to vibrations and thus enhances the resolution.

The objects in CT scanners have generally dimensions in the order of decimetres while the objects in µCT scanners are in the order of 30 mm.

2.1.3 X-ray detector

Finally the intensity of the attenuated X-rays is measured. This is done by the detector which consists of a large number of detector elements. Obviously, the smaller these detector elements are, the higher is the resolution that can be achieved. The detector captures the X-rays and converts them into an electrical signal. The relation between this electrical output signal and the number of detected photons is a characteristic for every detector type. Ideally the output signal is proportional to the number of detected photons.

The efficiency of most detectors is low in the spectral area of X-rays, but is relatively high in the spectral area of visible light (figure 2.17). Therefore fluorescent screens are placed between the object and the detector to convert X-rays into light photons. Because detectors are very small (≈ 1 cm² in µCT scanners), a scaling down is necessary. This is performed by placing an optical lens or tapered fibres after the fluorescent screen to focus the photons on the detector. Both the fluorescent screen and the optical lens have a negative impact on the resolution.

In CT scanners the detector is one-dimensional and the entire volume is imaged by scanning consecutive slices in the third dimension. In µCT scanners the entire volume is directly scanned using a 2D detector (figure 2.5).

An elaborate description of detectors and the different detector types can be found in *Jenkins* (*1989)* and *Photometrics (1990*).

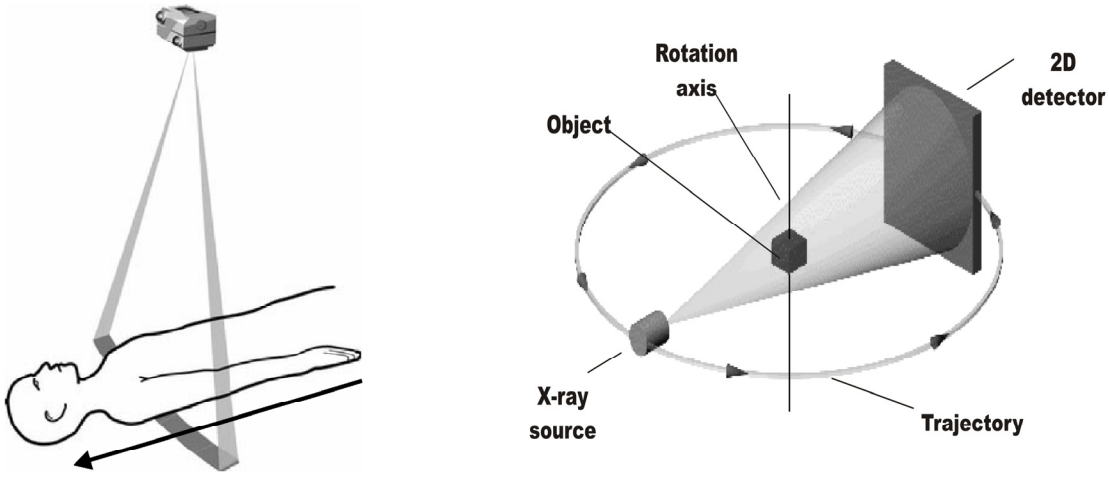

(a) (b)

Figure 2.5: Different scanning setups are used in CT and µCT. (a) In CT scanners the object volume is scanned by taking consecutive 1D slices in the third dimension. (b) A 2D detector is used in most µCT scanners enabling directly scanning the entire volume.

2.2 Image reconstruction

The intensities measured in all the detector elements and for all views are collected in the sinogram. The question is then how the interior of the object can be reconstructed from this huge amount of intensity measurements. Or, more mathematically expressed, how an attenuation distribution *f(x,y)* can be computed from the sinogram *p(d,θ)*. *d* stands for the detector elements, *θ* for the scanning angle.

Solving this question is looking for a transformation from *p(r,θ)* to *f(x,y)*. The opposite transformation, going from a function *f(x,y)* to its parallel beam projection form (figure 2.6), is well known and is called the Radon transform:

$$p(r,\theta) = \Re[f(x,y)] \tag{2.2}$$

Thus, the reconstruction of *f(x,y)* from the sinogram *p(r,θ)* can be performed by the inverse Radon transform.

$$f(x,y) = \Re^{-1}[p(r,\theta)] \tag{2.3}$$

This inverse Radon transform is determined by the so-called projection theorem. This theorem states that the two-dimensional Fourier transform $F(k_x,k_y)$ of the function *f(x,y)* is equal to the one-dimensional Fourier transform *P(k,θ)* of the sinogram *p(d,θ)* (*Herman, 1980; Macovski and Herman, 1981; Kak and Slaney, 1988*):

$$P(k,\theta) = F(k_x,k_y) \tag{2.4}$$

where

$$F(k_k,k_y) = \int_{-\infty}^{+\infty}\int_{-\infty}^{+\infty} f(x,y)e^{2\pi i(k_x x + k_y y)}dxdy \tag{2.5}$$

$$P(k,\theta) = \int_{-\infty}^{\infty} p(r,\theta)e^{2\pi i(k\cdot r)}dr \tag{2.6}$$

According to this theorem, it is possible to calculate *f(x,y)* for each point *(x,y)* by applying Fourier and inverse Fourier transformations. This procedure is called direct backprojection and would perfectly work for projections $p(r,\theta)$ where θ varies continuously between 0 and π. But as only projections at a finite number of angles θ are available, a discrete dataset is acquired. This requires an interpolation to transform $p(r,\theta)$ into $P(k,\theta)$ and $F(k_x,k_y)$ into $f(x,y)$ which seriously limits the performance of the direct backprojection.

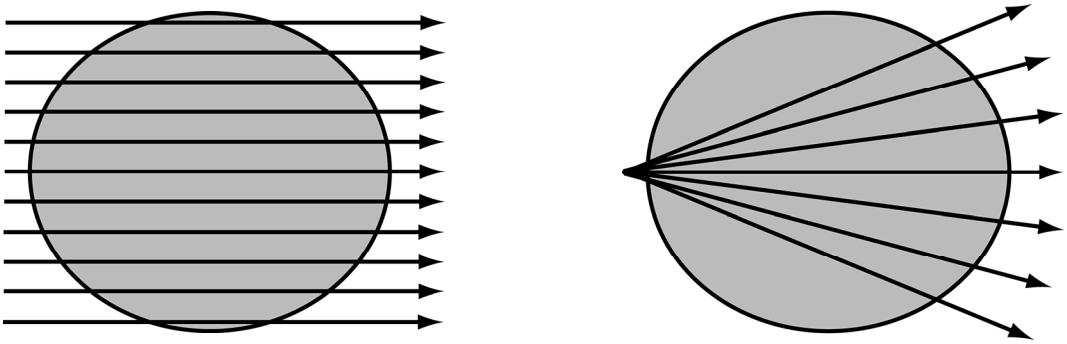

Figure 2.6: Illustration of a parallel beam (a) and fan beam geometry (b). In CT scanners the X-rays make up a fan beam geometry. In µCT scanners, where a 2D detector is used, the X-rays form a cone beam.

The interpolations can be avoided by applying a filtered backprojection where the polar version of the 2D inverse Fourrier transformation is used:

$$\begin{aligned} f(x,y) &= \int_0^{\pi}\int_{-\infty}^{\infty} P(k,\theta)|k|e^{i2\pi kr}\,dk\,d\theta \\ &= \int_0^{\pi}\int_{-\infty}^{\infty} P^*(k,\theta)e^{i2\pi kr}\,dk\,d\theta \\ &= \int_0^{\pi} p(r,\theta)\,d\theta \end{aligned} \tag{2.7}$$

where:

$$p(r,\theta) = \int_{-\infty}^{\infty} P^*(k,\theta)e^{i2\pi kr}\,dk \tag{2.8}$$

In these equations is $|k|$ the absolute value of the Jacobian of the polar transformation and $P^*(k,\theta)$ is the product of $P(k,\theta)$ with $|k|$. This can be considered as a filtering operation on $P(k,\theta)$ where $|k|$ is the applied filter. In practice a ramp filter is often used for $|k|$. When d_{detel} is the size of the detector elements, frequencies above $1/2\ d_{detel}$ do not contain relevant information. Therefore the ramp filter is cut off at frequencies above $1/2\ d_{detel}$. The resulting kind of filter is called the Ram-Lak filter and is shown in figure 2.7. Most reconstruction algorithms also use an additional smoothing filter, i.e. a Hamming filter, to reduce noise artifacts (*Herman, 1980; Kak and Slaney, 1988*).

As already mentioned, the projection theorem gives a mathematical expression for the reconstruction for a parallel beam geometry. In CT scanners the X-rays however make up a fan beam geometry and in µCT a cone beam geometry (figure 2.6). These different geometries require a different reconstruction algorithm and therefore algorithms for a fan beam and a cone beam geometry have also been developed. More detailed information on these backprojection algorithms can be found in *Shepp and Logan (1974)*, *Brooks and DiChiro (1976a)*, *Herman et al. (1976)*, *Herman (1980)*, *Cormack (1981)*, *Lewitt (1983)* and *Kak and Slaney (1988*).

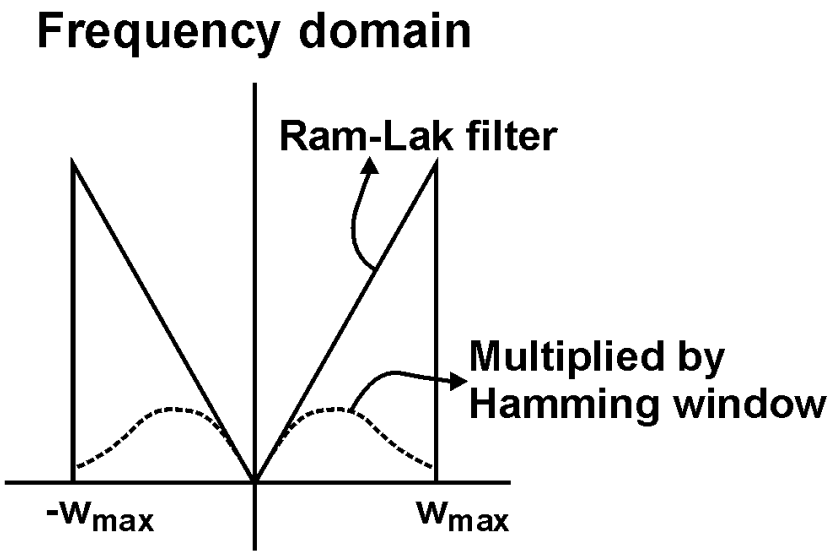

Figure 2.7: In filtered backprojection the Fourrier transform of the sinogram is multiplied with a Ram-Lak filter (solid line). This is a ramp filter cutting off the frequencies above half the detector element size as these frequencies do not contain relevant information. To reduce noise artifacts, an additional smoothing filter (Hamming) is often used. The dashed line shows the product of the Ram-Lak filter with the Hamming filter.

Beside backprojection other reconstruction algorithms are developed like iterative reconstruction algorithms. An iterative reconstruction starts with a homogeneous image and calculates the projections of this image at all views θ. These are then compared with the measured projections after which the image is adapted based on the difference between both. This process is repeated until the projections at all views converge to a minimum difference with the measured projections. Iterative reconstruction algorithms can be very convenient in optimising the image quality and suppressing some artifacts (*De Man, 2001*). For more information on these reconstruction algorithms, one can be referred to (*Herman and Lent, 1976; Oppenheim, 1977; Robertson and Huang, 1986; Kak and Slaney, 1988; Wang et al., 1996; De Man, 2001*).

2.3 Quality of CT images

The quality of CT images is defined by the spatial and contrast resolution that can be achieved and the presence or absence of artifacts as noise, scatter, beam hardening, etc. The factors affecting the image quality are discussed in this section. A further illustration and explanation is given in section 3.3 where the use of a CT simulator is demonstrated.

2.3.1 Spatial resolution

The spatial resolution is the ability to distinguish two objects which are located a small distance apart. An often used measure for the resolution is the Point Spread Function (PSF). The PSF is the two-dimensional response of the system to an infinitesimally small point. The resolution can be represented by the Full Width at Half Maximum (FWHM) of the PSF. Similar to the PSF is the Line Spread Function (LSF). This is the one-dimensional response of the system to an infinitesimally small line (figure 2.8).

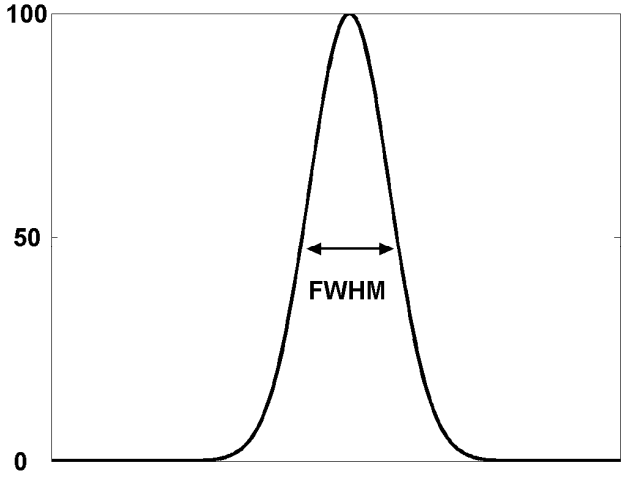

Figure 2.8: The resolution of an imaging system can be measured by considering the Line Spread Function (LSF) of the system. This is the response of the system to an infinitesimally small line. The Full Width at Half Maximum (FWHM) of the LSF can be taken as a measure for the resolution.

Since it is practically not possible to take an image of an infinitesimally small point or line, the response of the system to a straight boundary between adjacent areas is taken. This is called the Edge Response Function (ERF) and is directly related to the LSF since the LSF is the derivative of the ERF in a direction perpendicular to the edge:

$$LSF(x) = \frac{\mathrm{d}ERF(x)}{\mathrm{d}x} \tag{2.9}$$

The resolution of a CT scanner can thus be measured by imaging an edge between a high and a low X-ray transmission area and taking the derivative. In that way the LSF of the system is obtained and the FWHM of this LSF is a measure for its resolution.

The limited spatial resolution gives rise to a blurring of the object edges (figure 2.4) and to the partial volume effect that is discussed in section 2.3.3.5. The factors affecting the spatial resolution in the final CT image can be grouped in geometrical factors (*Villafana, 1975; Yester and Barnes, 1977*), the reconstruction algorithm and display parameters. The display parameters are determined by the monitor and are not further discussed as they have nothing to do with the scanning process itself and as they do not represent a serious limitation to the resolution of the CT image.

The geometrical parameters determine the inherent spatial resolution of a CT scanner. These parameters are the focal spot size, the detector aperture and the distances between the object and source and between the object and detector (figure 2.4). Beside these parameters, the fluorescent screen and the optical lens also influence the resolution of the scanner.

Whether this inherent spatial resolution is achieved, depends on the reconstruction algorithm and how accurately the data are collected. Using not enough detector elements or scanning at too few views gives rise to aliasing artifacts (cf. section 2.3.3.4). When a direct backprojection would be applied on the different projections, a blurry image would be obtained due to the discrete nature of the dataset. This was solved by applying a convolution on the dataset (filtered backprojection; cf. section 2.2). This convolution results in a blurring of the image and hence in a decreased resolution. It is not possible to eliminate this blurring completely and different filters will have different blurring effects on the sharpness and quality of the final image. The impact of the reconstruction algorithm on the spatial resolution will not be further examined as this is beyond the scope of this study.

Noise and scatter do not directly have a negative impact on the spatial resolution sensu stricto. They however decrease the contrast resolution and in that way they deteriorate the ability to distinguish two low contrast objects located close to each other.

2.3.2 Contrast resolution

The contrast resolution is the ability to detect small contrast differences between two adjacent areas. Contrast can be defined as the percentage difference of the reconstructed attenuation coefficient of the object and the background:

$$\%C = 100 \cdot \frac{\mu_{object} - \mu_{background}}{\mu_{background}} \tag{2.10}$$

The contrast resolution can be defined as the minimum contrast of an object with a specified size and shape which can just be discriminated. Measuring the contrast resolution is however much more difficult than measuring the spatial resolution and, as the definition mentions, the contrast resolution depends on the size and shape of the object. Large objects will be detected at a lower contrast than small objects.

Apart from factors related to the scanned object (i.e. its size and attenuation coefficient), the contrast depends mainly on the spectrum of the X-ray beam and on the level of noise and scatter. The X-ray spectrum affects the contrast as the amount of attenuation is higher when the highest intensities are in the energy range of the highest attenuation. By using filters, the X-ray spectrum can be shaped into a more efficient ratio of photons useful for attenuation to photons that hardly interact with the object.

The major disadvantage of filtration is a reduction in the total intensity of the X-ray beam which has a negative impact on the contrast and on the signal-to-noise ratio (SNR) (cf. section 2.3.3.1). Finding the optimal filter setup is generally a process of trial-and-error. In section 3.3.3.6 a case where the simulator is used to search for an optimal filter set-up, is discussed.

Noise and scatter also have a negative impact on the contrast.

2.3.3 Artifacts

The quality of the CT images is distorted by noise, scatter and artifacts. Artifacts are discrepancies between the reconstructed image and the object and arise during the reconstruction process. The reconstruction algorithm uses all X-ray measurements and assumes that all these measurements are consistent. Often this is not the case and artifacts are generated. More information on artifacts can be found in *Joseph (1981*).

2.3.3.1 Noise

The three primary sources of noise are dark current, preamplifier noise and photon noise. Dark current is a leakage of charge in the detector. Dark current is relatively low and can be minimized by cooling. Preamplifier noise is generated by the output amplifier and is proportional to the readout speed of the detector. Photon noise arises because the total number of photons emitted by the source is not constant. This number varies according to a Poisson distribution (*Guan and Gorden, 1981; Hsieh, 1988*). Likewise, the number of detected photons exhibits the same Poisson distribution. The photon noise is proportional to the square root of the number of detected photons (i.e. the intensity).

$$photonnoise \approx \sqrt{I} \tag{2.11}$$

The effect of the noise on the image quality can be expressed by the signal-to-noise ratio (SNR). When the number of photons (i.e. the intensity) is assumed to be high enough, the noise caused by dark current and the preamplifier noise can be neglected. The SNR is then expressed by the following equation:

$$SNR = \frac{I}{photonnois\ e} \approx \sqrt{I} \tag{2.12}$$

Thus the higher the intensity is the higher is the SNR. The SNR can be improved by taking the average over N measurements. This is called frame averaging and results in a reduction of the noise by a factor $\sqrt{N}$. When more integration frames are used, the acquisition time increases proportionally. The noise level can also be decreased by applying a smoothing filter during the filtered backprojection. However, this in turn is at the cost of spatial resolution.

More information on noise in CT images can be found in *Duerinckx and Macovski (1979)*, *Guan and Gorden (1981), Hsieh (1988)* and *Photometrics (1990*).

2.3.3.2 Scatter

Scatter occurs when photons are deflected from their original path. This goes along with (Compton scattering) or without (coherent scattering) loss of energy. Coherent scatter only occurs noticeably at low energy while Compton scattering becomes relatively more dominant at higher photon energies. Obviously, these photons are useless for the reconstruction and contaminate the measurements. In a parallel beam geometry scatter can be prevented by using a detector that is perfectly collimated. In that way, X-rays that are not travelling in a straight line between the source and detector, i.e. scattered photons, are not measured. A perfectly collimated detector is however very difficult to build. Some scattered photons thus pass through the collimator and the detector measures both scattered as non-scattered photons.

The main effect of scatter is a decrease in contrast (cf. section 3.3.3.2). Beside this effect, scatter induces non-linear errors in the reconstruction of the attenuation values. As the scatter profile is approximated by a constant profile added to the measurements (*Glover, 1982*), this leads to an underestimation of the attenuation, which is more pronounced in high attenuation regions. Also streak and cupping artifacts are induced (*Joseph, 1981*) similar to beam hardening artifacts (cf. section 2.3.3.3). This is because both effects cause a non-linear reduction in the measured attenuation.

2.3.3.3 Beam hardening artifacts

The linear attenuation coefficient generally decreases with increasing energy. This means that low energies are more easily absorbed. Thus, when a polychromatic X-ray beam passes through an object, the lower energies are preferentially absorbed and the mean energy of the beam increases. As the mean energy increases, the beam will be less easily attenuated. The beam is said to become "harder" and the total attenuation is no longer a linear function of the absorber thickness. This phenomenon is called beam hardening and causes several artifacts such as cupping and streaks.

Figure 2.9 illustrates the intensity of a monochromatic and polychromatic beam during their passage through an object.

In monochromatic measurements X-rays are attenuated linearly with the distance travelled. Due to beam hardening this is not the case for polychromatic X-rays. The longer the path or the higher the attenuation, the bigger is the difference between the monochromatic and polychromatic measurements and the more pronounced is the impact of this non-linearity.

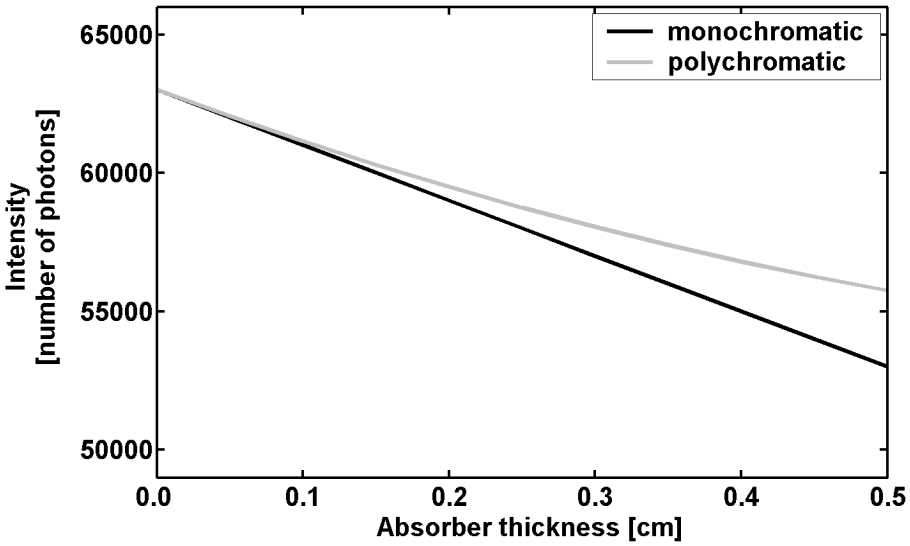

Figure 2.9: Intensity evolution in a monochromatic and polychromatic X-ray beam during passage through an absorber. The lower energies in the polychromatic beam are more easily absorbed than the higher energies. Therefore the mean effective energy of the beam increases. This in turn implies that the beam is less easily attenuated. The mean effective energy and thus the attenuation of the monochromatic beam remain constant.

Polychromatic X-rays that have gone through the central part of a cylindrical object, have travelled a longer path and are therefore proportionally less attenuated than X-rays having travelled near the outer edges. As a result, the attenuation in the central part of the object is underestimated and cupping can be seen on the reconstructed image (figure 2.10). A distinct, but related phenomenon is the generation of streak artifacts. After having passed through a dense inclusion, the X-ray beam has become harder. The attenuation in the subsequent trajectory will therefore be less. When the object contains several dense inclusions, bright streaks connecting these inclusions are visible in the reconstructed image as the attenuation in these regions is underestimated (*Brooks and DiChiro, 1976; Zatz and Alvarez, 1977; Duerinckx and Macovski, 1978; Moström and Ytterbergh, 1986; Berland, 1987; De Man et al., 1999*). Cupping and streak artifacts are shown in figure 2.10.

The use of hardware filters can reduce the beam hardening artifacts as the low energies already have partly been absorbed by the filter material. Completely eliminating beam hardening by filters is however not possible as filtration makes the spectrum also more homogeneous. Moreover, filtration results in an increase of the SNR and a decrease in contrast (*Pang and Genna, 1976; Jennings, 1988*).

Another way to correct CT measurements for beam hardening is the application of a linearization procedure (*Herman, 1979; Hammersberg and Mångård, 1997*). This procedure consists of a correction of the intensity of the polychromatic beam. The intensity of a monochromatic beam in a homogeneous material decreases linearly. Since the polychromatic beam becomes harder during its passage through the material, the intensity deviates from this linear trend (figure 2.9). In the linearization procedure the intensities of the polychromatic beam is measured for different material thicknesses. By then correcting every point lying on this polychromatic curve towards the linear trend line, the beam hardening artifact is eliminated. The disadvantage of this technique is that it is only valid for a specific incident X-ray spectrum and a homogeneous material. When several materials are present within the object, for instance a polymineralic rock, the procedure is no longer correct.

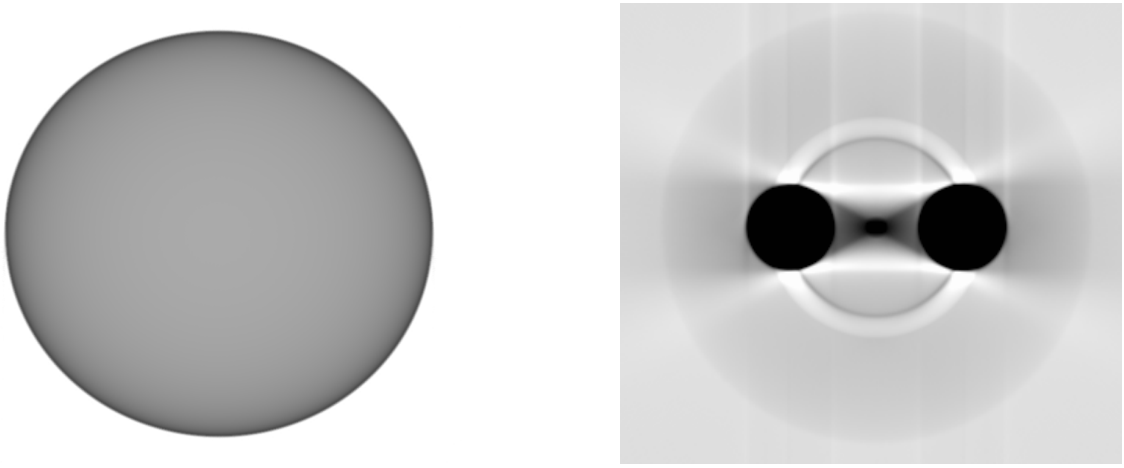

(a) (b)

Figure 2.10: Beam hardening typically results in two kinds of artifacts. (a) Rays that have travelled through the central part of a cylindrical object are, compared to rays having travelled near the outer edges, proportionally less attenuated. This can be seen as cupping: the central part is brighter as its attenuation is underestimated due to beam hardening. (b) Dense inclusions result in bright streaks connecting these inclusions in the reconstructed image.

A last correction method for beam hardening is dual energy scanning (*Remeysen and Swennen, 2006*). In dual energy scanning the sample is scanned at two different energy levels. Based on these two scans, it is possible to reconstruct an energy independent image which is free from beam hardening artifacts. This is a mathematically correct and elegant way to remove beam hardening artifacts, but it is computationally very intensive and requires a calibration procedure. This calibration depends on the type of scanner and on the material that is scanned. More information on this method can be found in *Alvarez and Macovski (1976)*, *Duerinckx and Macovski (1979)*, *Stonestrom et al. (1981)*, *Johns and Yaffe (1985)*, *Cardinal and Fenster (1990)*, *Goh et al. (1997)*, *Van Geet (2001)* and *Remeysen (2007)*.

2.3.3.4 Aliasing artifacts

The reconstruction algorithm is able to exactly calculate the attenuation coefficient in each point of the object. It therefore needs an infinite number of rays and views. This is of course not possible and puts a limit on the achievable spatial resolution, as explained above. Moreover it causes aliasing artifacts. Aliasing artifacts are the result of an undersampling in the number of X-rays, i.e. the number of detector elements, or an undersampling in the number of views.

Aliasing is a general known phenomenon that occurs when a continuous signal is sampled. To make sure that all frequencies of the signal are represented in the sampled signal, the sampling frequency must be at least twice the highest frequency in the continuous signal. This is known as the Nyquist criterion. Frequencies higher than twice the sampling frequency will be recognized as a lower frequency and cause an error in the sampled frequency. This effect is called aliasing. Figure 2.11 illustrates this effect.

It is not straightforward to determine the minimum number of detector elements and views needed in CT. They depend on several factors such as the scanned object, the beam width, the geometry of the scanner and the reconstruction algorithm (*Herman, 1980; Berland, 1987*). In practice, aliasing artifacts are always present, at least at a very low level. Several approaches to reduce aliasing artifacts exist.

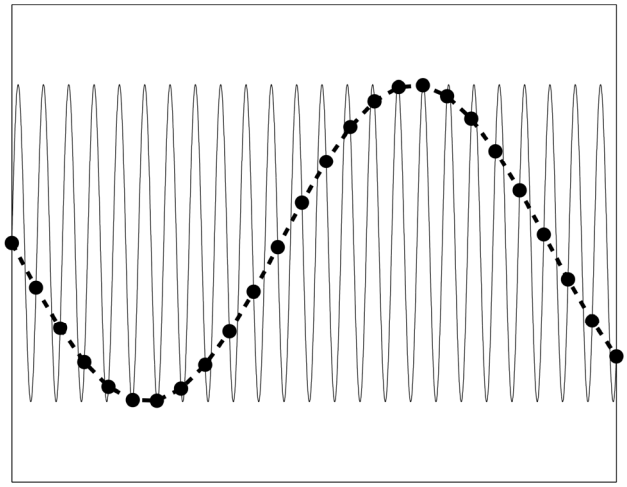

Figure 2.11: Aliasing occurs when a continuous signal is undersampled. The signal shown as a full grey line is sampled at a given frequency (black dots). As the signal frequency is higher than twice the sampling frequency, a signal with a lower frequency is recognized (dashed black line). This effect is called aliasing.

Aliasing due to detector undersampling can be reduced by using more detector elements, but this number is of course limited. An elegant solution to increase the number of available detector elements is obtained by the principle of quarter detector offset. This consists of shifting the focal spot laterally over a small distance, so that the line connecting the focal spot and the center of rotation intersects the detector row at one quarter of a detector element from the middle. The opposite projection lines (obtained after 180° rotation) intersect the detector row at one quarter of a detector element from the middle in the opposite direction. Thus, in a 360° acquisition the projections on opposite sides are sampled at a distance of half a detector element of each other and the number of detector elements is doubled. This principle is illustrated in figure 2.12

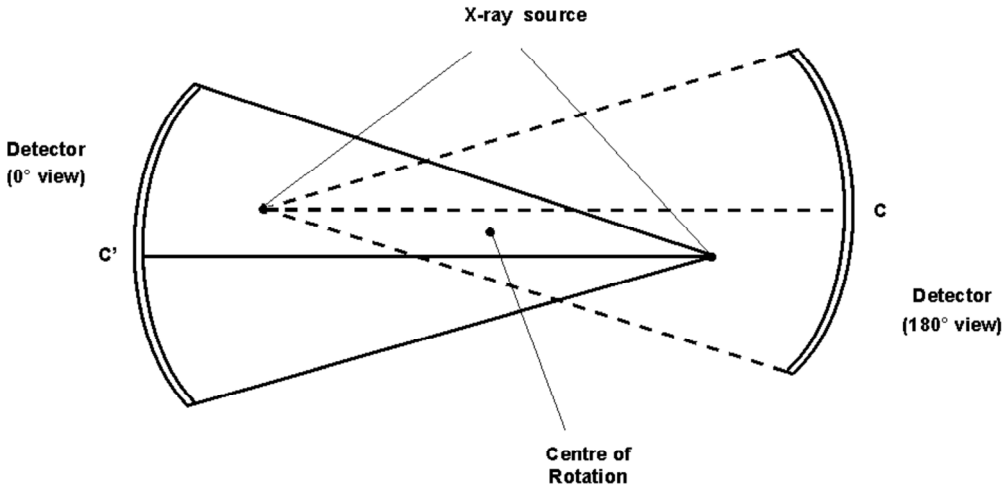

Figure 2.12: Illustration of the quarter detector offset technique to suppress aliasing in rotation detector machines. The focal spot is shifted over a quarter detector element so that opposite projections are sampled half a detector element apart from each other. In that way the number of detector elements is doubled.

Unlike aliasing due to detector undersampling, aliasing due to view undersampling can always be suppressed by using a smoothing filter in the reconstruction. This however also reduces the spatial resolution.

2.3.3.5 Partial volume effect and the exponential edge-gradient effect

The voxels in the reconstructed image have a limited size which is mainly determined by the size of the detector elements. A voxel in the reconstructed image generally does not fully coincide with borders in the scanned object and the reconstructed attenuation of one voxel represents a weighted average of all substances present in that voxel. This artifact is called the partial volume effect (*Robertson and Huang, 1986; Wellington and Vinegar, 1987; Johns et al., 1993; Ketcham and Carlson, 2001*) and causes a blurring of the border as can be seen in figure 2.13.

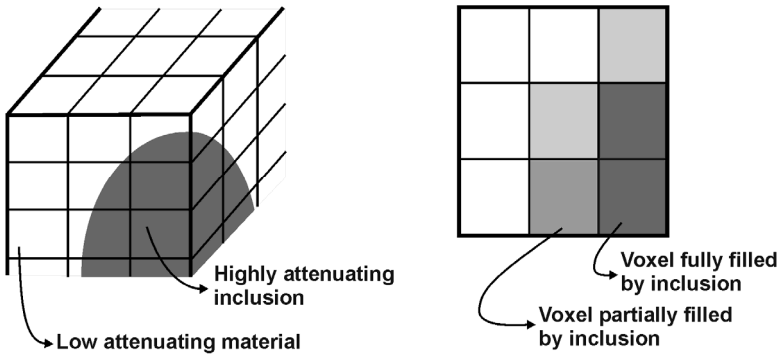

Figure 2.13: Illustration of the partial volume effect. The attenuation of a voxel in the reconstructed image (b) is the weighted average of all substances present in that voxel (a). As these voxels generally not coincide with a border in the object, this results in a blurring of the border.

Related to the partial volume effect is the exponential edge-gradient effect (EEGE) (*Joseph, 1981; Berland, 1987*). This is caused by the finite width of the X-ray beam and by the fact that each measurement represents a spatial average of X-ray intensities while the reconstruction algorithm assumes a spatial average of attenuation coefficients. Both averages are in general not equal resulting in an artifact. This effect arises most strikingly at sharp edges of high contrast. Figure 2.14 illustrates what happens when such a sharp edge of high contrast is encountered and when this edge lies within the beam width corresponding to one detector element.

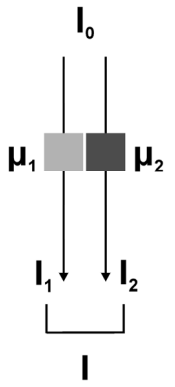

Figure 2.14: Illustration of the exponential edge-gradient effect. Due to the finite size of the detector elements a spatial average of X-ray intensities is measured. The reconstruction algorithm then calculates the attenuation coefficient that corresponds to this average intensity. This is always smaller than or equal to the average of the attenuation coefficients.

The detector measures the intensity I and the reconstruction algorithm calculates the attenuation coefficient by taking the logarithm of the intensity I over the original intensity I_0:

$$\mu = -\ln\frac{I}{I_0} = -\ln\left(\frac{I_1 + I_2}{2 \cdot I_0}\right) \tag{2.13}$$

This calculated average attenuation coefficient is smaller than or equal to the real average attenuation coefficient:

$$\begin{aligned} \mu &= -\ln\left(\frac{I_1 + I_2}{2 \cdot I_0}\right) \\ &\leq^{7} -\ln\sqrt{\frac{I_1}{I_0} \cdot \frac{I_2}{I_0}} \\ &\leq \frac{1}{2}\left[-\ln\frac{I_1}{I_0} - \ln\frac{I_2}{I_0}\right] \\ &\leq \frac{\mu_1 + \mu_2}{2} \end{aligned} \tag{2.14}$$

The attenuation coefficient calculated by the reconstruction algorithm is an underestimation of the average attenuation in the object voxel. Thus, a gradient perpendicular to the direction of an X-ray beam causes a negative error in the corresponding estimated attenuation value. This error is more pronounced where strong spatial gradients of attenuation are present. That is why this effect is called the exponential edge-gradient effect.

2.3.3.6 Ring and line artifacts

When certain detector pixels continuously register wrong measurements, these measurements give rise to ring artifacts in the reconstructed image (figure 2.15). Ring artifacts can be avoided by randomly moving the sample or the detector during the scanning process. After the acquisition of the data, the sinogram is corrected for this random motion. In that way the false measurements of malfunctioning detector elements are smeared out over several places in the sinogram. Corrections can also be performed in the post-processing. A continuous error in one detector element can be seen as a vertical line in the sinogram. These vertical lines in the sinogram can be searched for and corrected (*Bernard and Chirazi, 2006*).

Where a ring artifact is caused by a continuously malfunctioning detector element, a line artifact arises when cosmic rays or high energy X-rays directly hit the detector. This causes an abnormally bright pixel in the sinogram and a perfectly straight, bright line in the reconstructed image (figure 2.15). Here too, these line artifacts can be removed by detecting and correcting these bright pixels in the sinogram (*Berland, 1987; Van Geet, 2001*).

[7] $\frac{a+b}{2} \leq \sqrt{a \cdot b}$

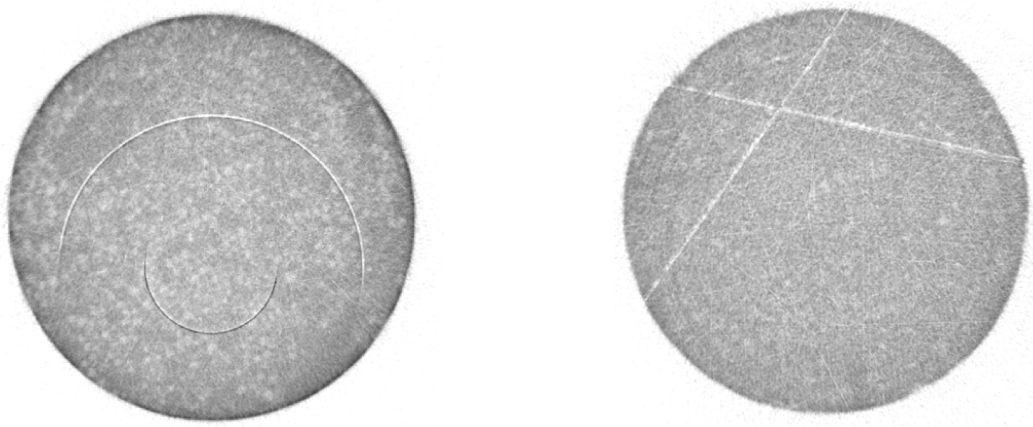

(a) (b)

Figure 2.15: (a) Ring artifacts are the result of a continuous malfunctioning of one or more detector elements. (b) When cosmic rays or high energy X-rays directly hit the detector, an abnormally bright pixel in the sinogram is generated. This can be seen in the reconstructed image as perfectly straight, bright line.

2.4 Computed tomography scanners

The first CT scanners were developed for medical purposes and are therefore often referred to as medical CT scanners. These scanners nowadays have focal spot sizes in the order of 100 µm. This is the most important difference with µCT scanners where the source size is in the order of 10 µm. The spatial resolution is mainly determined by the focal spot size (figure 2.4) and hence a higher resolution can be achieved using µCT images. This higher resolution is at the cost of the sample size that can be scanned. A higher resolution due to a smaller focal spot can of course only be useful when the detector element size is below this resolution. Standard detectors in µCT scanners have 1024 by 1024 detector elements. The limited size of the detector elements therefore also limits the size of the sample that can be scanned. In general, samples with dimensions in the order of decimetres can be scanned in medical scanners. In µCT scanners the samples are mostly in the order of centimetres.

Beside a different source, µCT scanners also have a different detector (figure 2.5). In most medical scanners a 1D detector is used. The entire object is scanned by sliding it through the scanner and by taking consecutive slices in the third dimension. The resolution in the third dimension is often smaller than in the 2D slices. In µCT scanners the object is directly scanned using a 2D detector. Moreover, where in most medical CT scanners the source and detector are rotated around the object, in µCT scanners it is the object that is turned. By doing so it is less prone to vibrations. This again results in a higher resolution.

Nowadays also nano-CT scanners exist. These scanners have focal spot sizes at nanoscale. Again, the price for the higher resolution is a smaller sample size which is in the order of millimetres.

Medical, micro- and nano-CT scanners all generate polychromatic X-ray beams. As explained, this results in beam hardening artifacts. These are avoided in synchrotron scanners where monochromatic rays are used (*Ashbridge et al., 2003; Tsuchiyama et al., 2005*). Also a very high resolution, hundreds of nanometres, can be achieved with these scanners. Synchrotron scanners are however much more expensive and are less available. Another drawback is the limited size of the samples than can be scanned (1 mm or less).

In this research two µCT scanners were used: a Skyscan 1072 Desktop µCT scanner and an AEA Tomohawk µCT scanner. Both scanners are available at the Department of Metallurgy and Materials Engineering (MTM) of the K.U.Leuven.

2.4.1 Skyscan 1072 Desktop µCT scanner

The Skyscan 1072 Desktop µCT (*Skyscan, 1997*) scanner (figure 2.16) uses an X-ray tube with a L6622-01 130 kV microfocus X-ray source from Hamamatsu Photonics K.K. The X-ray source operates between 20 and 130 kV. The maximum current is 300 µA. A focal spot size of 10 µm or 40 µm can be chosen. The target can handle a total energy of 13 W when using the small spot size and 39 W when using the big spot size. The emitted X-ray spectrum is not exactly known and cannot easily be measured (cf. section 3.2.2).

Figure 2.16: Skyscan Desktop µCT scanner

The sample holder can move horizontally between the X-ray source and the detector to change the geometrical magnification. This horizontal position can be defined with a precision of 5 µm. The vertical position can be adjusted with a precision of 2 µm. The object can rotate with a minimum stepsize of 0.225°. The rotation of the object is performed between the sequential projections. This procedure is called “step and shoot”. The field of view is limited to 60 mm. The largest object that can be scanned has dimensions of 54 mm.

The detection system comprises a phosphor screen and a CCD detector. The used phosphor screen is a Mamoray detail S V1 with Mamoray HDR-film of AGFA. The emission spectrum of this screen lies around 550 nm. The afterglow of the screen is 2 µs. The CCD chip is a C4742-95 digital CCD Camera of Hamamatsu Photonics K.K. which is cooled by air and Peltier effect. During acquisition a maximum of 1024x1024 pixels, each 6.7x6.7 µm in size, can be used. The quantum efficiency of the CCD camera as a function of the wavelength is given in figure 2.17. The area with the highest efficiency lies between 340 nm and 600 nm corresponding to the emission spectrum of the phosphor screen.

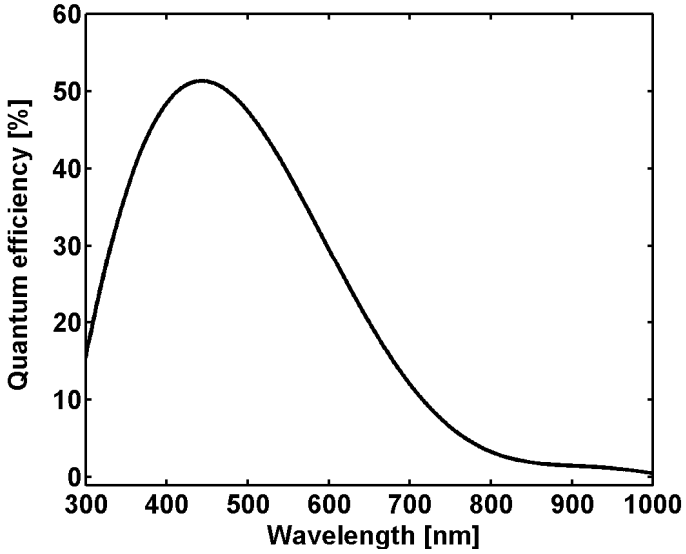

Figure 2.17: Quantum efficiency of the CCD camera used in the Skyscan 1072 Desktop CT scanner. The highest efficiency lies between 340 nm and 600 nm which is way above the wavelengths of X-rays. A phosphor fluorescent screen is used to convert the X-rays into visible light. The emission spectrum of the screen lies around 550 nm which is in the wavelength area where the detector is most efficient.

2.4.2 AEA Tomohawk µCT scanner

The source in the Tomohawk scanner is a Philips microfocus X-ray tube with a maximum tube voltage of 160 kV and a maximum tube current of 3.2 mA. The user can chose between a tungsten, a copper or a molybdenum target. The focal spot size ranges from 5 to 200 µm and the maximum sample size is approximately 150 mm (*Van Geet, 2001*). The field of view is limited to 220 mm and the size of the biggest object that can be scanned is 110 mm. The detector consists of a TH 9428HX image intensifier and a 1024 by 1024 pixel CCD camera (Adimec MX12P).

The object can be moved towards the source or away from the source to respectively increase or decrease the magnification. Also movement in the vertical direction and to the left or right with respect to the central axis of the focal spot and the centre of the camera are possible. The smallest angle increment is 0.5° and radiographs can be taken over 180° plus the fanangle of the X-ray beam (circa 7°) or over 360°.

2.5 Description of the test samples

Four samples are used to validate and test the methodology developed in this research. Two are porous concrete pavestones and two are porous reservoir limestones. All samples are cylindrical. The pavestones are approximately 70 mm long and 35 mm in diameter, the limestones are 60 mm long and 45 mm in diameter. A picture of one of the pavestones and one of the limestones is shown in figure 2.18. The samples will be referred to as pavestone A and B and limestone A and B.

The pavestones are used as pavement on parking places. Such a pavement has to be permeable to drain off water. Pavestone A is a new sample, pavestone B is taken from a test parking place which was affected by a mudflow. The second sample is therefore supposed to be less permeable due to the

infiltration of mud. The samples are provided by the "Opzoekingscentrum voor de Wegenbouw" (OCW)[8].

The limestones are taken from the Altamura Formation, some meters above the Cenomanian-Turonian boundary (younger than 93 million years).

(a) (b)

Figure 2.18: Picture of pavestone sample (a) and limestone sample (b) used in this research. The pavestones are approximately 70 mm long and 35 mm in diameter, the limestones 60 mm long and 45 mm in diameter.

The porosity and permeability of the samples were determined in the laboratory. The limestones were sent to the "Core Lab Petroleum Services" (CoreLab)[9] where also a mercury intrusion experiment was performed. The pavestone samples could not examined by CoreLab due to a mismatch between the dimensions of the samples and the experimental equipment. Their permeability and porosity were measured at the laboratory of Building Materials and Building Technology (Department of Civil Engineering) at the K.U.Leuven.

The limestone samples were first cleaned to remove all unknown fluid content (formation water, drilling mud filtrate, etc.) and then dried. Subsequently the porosity was measured using helium expansion and the application of Boyle's Law to quantify the pore volume. Helium is used because it is chemically inert and it is the smallest naturally occurring molecule. It can therefore very quickly enter the smallest pores. This experiment evidently measures the open porosity. When the term "porosity" is used in this work, it is always the open porosity unless explicitly mentioned.

The air permeability was measured for different pressures to compensate for the Klinkenberg effect (*Klinkenberg, 1941; Takinawa and Shimamoto, 2006*). This effect is due to slip flow of gas at pore walls which enhances gas flow when pore sizes are very small. The Klinkenberg results in a higher permeability for gas than for fluida. The higher the imposed gas pressure, the more pronounced this

[8] Opzoekingscentrum voor de Wegenbouw; http://www.ocw.be
[9] Core Lab Petroleum Services, Aberdeen, Scotland; http://www.corelab.com

effect. Measuring the permeability for different pressures therefore allows compensating for the Klinkenberg effect.

The porosity of the pavestones was measured by first weighting the completely water saturated sample. Then the sample is dried and weighted again. The loss in water gives the pore space volume. The volume of the rock is determined by comparing the weight of the rock immersed in water and the weight in air by using Archimedes' principle. The permeability of the pavestones was determined by imposing a pressure difference of respectively 1, 3, 5 and 7 bar over the sample and measuring the water flux through the sample.

Table 2.1 gives the measured porosity and permeability of the samples.

	open porosity [%]	**permeability [10^{-15} m²]**
pavestone A	24,9	31478
pavestone B	19,5	0
limestone A	15,5	10
limestone B	13,3	23047

Table 2.1: The open porosity and permeability of the pavestone and limestone samples as determined in the laboratory.

In a mercury intrusion experiment mercury is forced to intrude the sample. The pressure needed to intrude the mercury depends on the sizes of the pores in the sample. For smaller pores a higher pressure is required to inject the mercury. In that way the mercury intrusion experiment gives information on the pore size distribution of the sample. Figure 2.19 shows the results from the mercury intrusion experiment on the limestone samples.

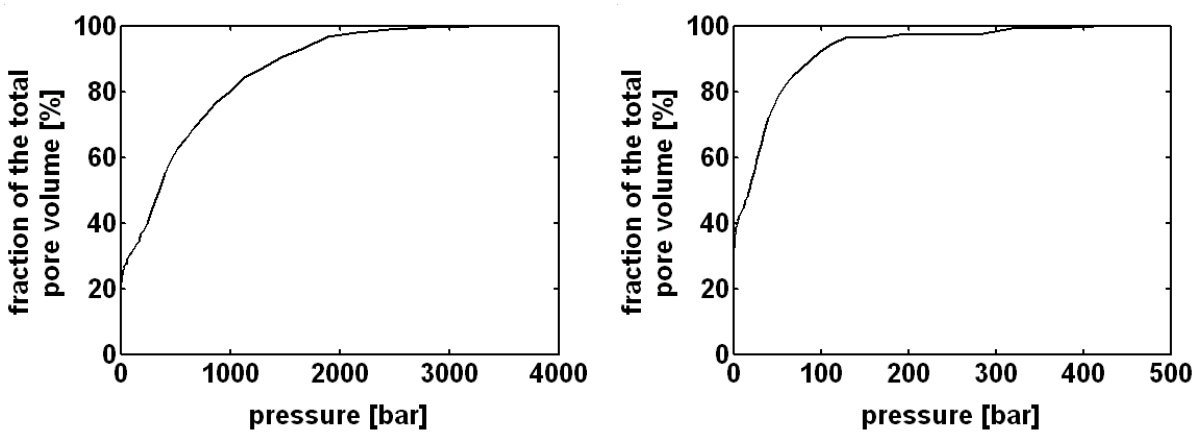

(a) (b)

Figure 2.19: Mercury intrusion measurements on the limestone sample A (a) and limestone sample B (b).

The pressures used for limestone A are higher than for limestone B and thus the pore sizes in limestone A sample are smaller than in the limestone B sample. The critical pressure p_c required to force a non-wetting fluid into a cylindrical pore with radius r_c is given by:

$$p_c = -\frac{2\sigma\cos\theta}{r_c} \tag{2.15}$$

In this equation σ is the surface tension of the fluid and θ is the contact angle between fluid and solid material. At room temperature the surface tension σ between mercury and air amounts 485 mN/m. The contact angle θ between mercury and the air-filled sample depends on the sample material, but in most cases 140° is a good assumption. Figure 2.20 shows the estimated pore sizes resulting from the mercury intrusion experiment.

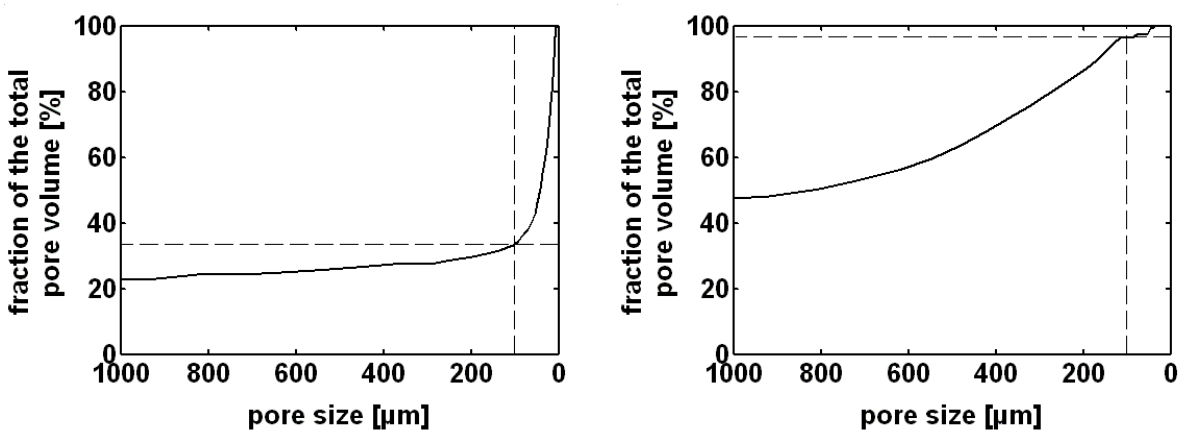

Figure 2.20: Cumulative pore size distribution of the limestone sample A (a) and limestone sample B (b) as derived from the mercury intrusion experiment. The dashed lines indicate the cumulative volume at a pore size of 95 µm (the pixel size in the CT image).

At a pressure of 156 bar, corresponding to the voxel size of 95 µm, only 34,5% of the total volume of the limestone A sample is filled with mercury. When interpreting these data it is important to take into account that smaller pores can prevent the intrusion of larger pores which results in an underestimation of the intruded volume (cf. section 5.4.2). Therefore one cannot conclude that 65,5% of the pore volume has dimensions below 95 µm. But it is an indication that a large fraction of the pore volume might fall below the image resolution. For the limestone B sample, shown in figure 2.20b, 96,5% of the pore volume is intruded by mercury at a pressure of 156 bar. This implies that at least 96,5% of the pore volume is above the resolution and can be detected from the CT images.

Here, a first error is introduced as pores smaller than the voxel size in the CT image fall below the resolution of the imaging system and are not detected in the resulting CT image (**error 1: resolution error**). The loss of these smaller pores in the CT image can result in a loss of connectivity of the pore space and hence it will affect the permeability computation. This error can expected to be larger for the limestone A sample than for the limestone B sample as a larger fraction of the pore space falls below the resolution.

The samples are scanned with the Tomohawk µCT scanner at a tube voltage of 90 kV and using a copper filter of 0,01 mm. The voxel size in the images is 95 µm. The acquisition parameters are chosen by the aid of a CT simulator (cf. section 3.4). The development and use of the simulator are demonstrated in the next chapter.

2D slices from the CT images of pavestone sample A and limestone sample A are shown in figure 2.21. A 3D visualization of both samples is given in figure 2.22. It appears from these images that the pavestone contains larger pores than the limestone.

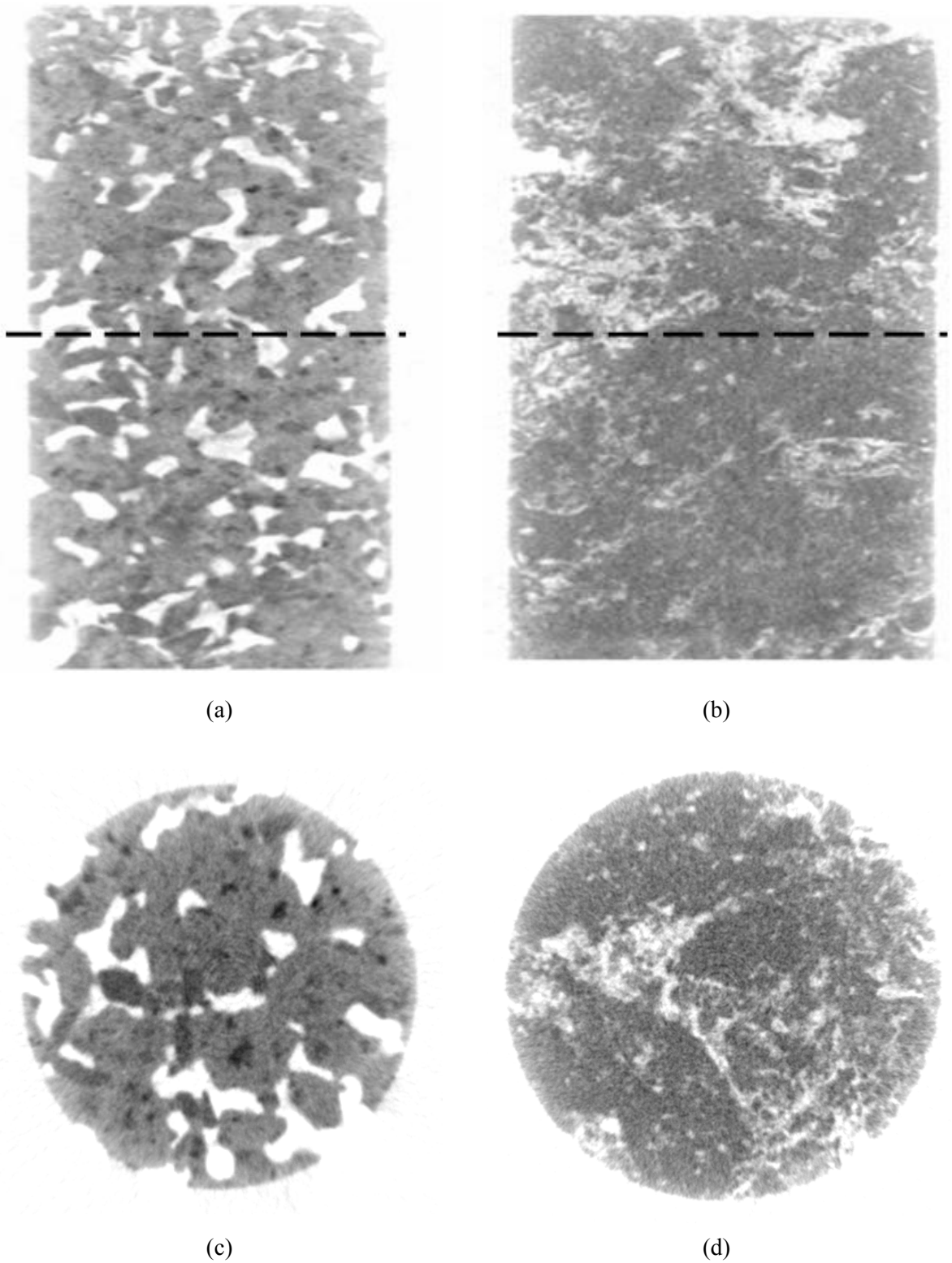

(a) (b)

(c) (d)

Figure 2.21: Horizontal and vertical 2D slice from the CT image of the pavestone A ((a) and (c)) and limestone A sample ((b) and (d)). The dashed lines on the vertical slices indicate where the horizontal slice is taken. The grey pixels represent solid material. The size of the pores in the pavestone is clearly bigger than in the limestone.

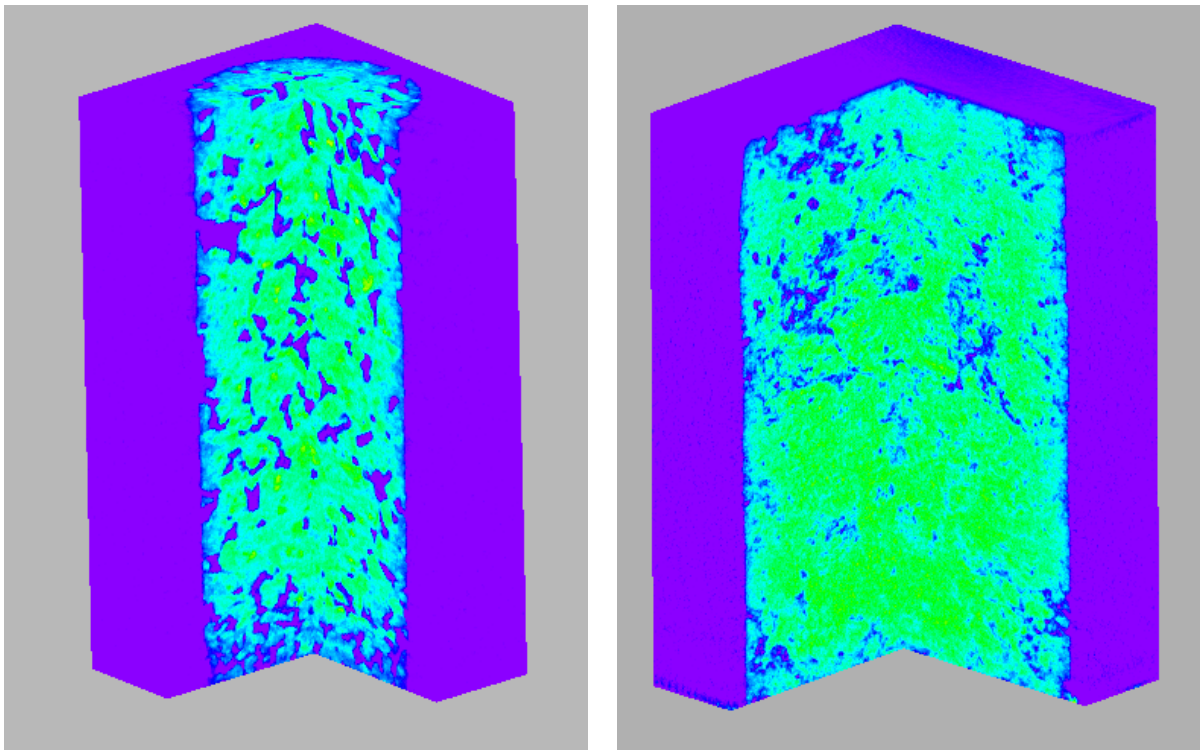

(a) (b)

Figure 2.22: 3D visualization of the pavestone A (a) and limestone A sample (b). In the visualization one quadrant of the samples is removed to make the insight of the samples visible. The high attenuation areas are drawn in blue-green, the low attenuating areas in purple.

3. The CT simulator

As explained in chapter 2, the quality of CT images depends on a lot of factors. By choosing the acquisition parameters and the scanning setup (for instance the use of filters) the user can influence the image quality. The effect of some acquisition parameters is however not always straightforward. Another difficulty is that the factors determining the image quality are strongly interrelated. Choosing the parameters resulting in an optimal image is therefore very complex and also depends on the purpose of the measurement and on the object that is scanned. For some applications or materials the contrast resolution can for instance be the critical factor. This is the case when trying to separate dolomite, anhydrite and calcite in CT images as the attenuation coefficients of these materials lie close to each other (*Remeysen, 2007*). In applications where an accurate determination of the pore sizes of a sample is the goal, the spatial resolution is the main concern.

Looking for optimal acquisition parameters by trial-and-error is often not possible as this would in most cases require too much time. A simulator of the CT scanner might therefore be useful as this allows examining the effect of the acquisition parameters by trial-and-error. There is also no need for real objects to be scanned and the object simulated is perfectly known. This facilitates a comparison with the reconstructed CT image of the known object.

Beside the advantage of being able to relatively quickly look after optimal acquisition parameters, the simulator can also be used to examine the impact of several parameters and phenomena occurring during the scanning process. Scatter for example generates similar artifacts as beam hardening. Both phenomena can be investigated separately using the simulator as they can be turned on or off. This can be useful when new applications are examined. Drawbacks and limitations of the technique can very quickly be identified and possible solutions can be tested before scanning the real objects. In that way, time can be saved and it can lead to the conclusion whether or not X-ray computed tomography is suitable for the given application. This is demonstrated in appendix D, where the simulator is used to investigate the applicability of computed tomography in measuring the gold content of rock samples.

A 2D simulator was built by De Man to examine metal artifacts in medical scans (*De Man, 1999*). A new simulator based on the work De Man (2*001*) is developed. Some aspects of his simulator are adjusted and the 2D simulator is extended to a 3D simulator. The new simulator is presented in this chapter. First it is explained how the simulator works. Then the simulator is adjusted to the Skyscan 1072 Desktop µCT scanner and the Tomohawk µCT scanner. Finally the use of the simulator is demonstrated and the main conclusions are summarized.

3.1 Development of the CT simulator

The simulator is written in IDL[10] and only deals with the acquisition process. No reconstruction algorithms are implemented. Reconstructions are performed by existing software.

The principle behind the simulator is very simple: calculate the attenuation of the rays going from the source to the detector elements and do this for all views. This is first performed for monochromatic X-rays and an infinitesimally small source and infinitesimally small detector elements. Subsequently this basic and theoretical case is extended to polychromatic X-rays and to a source and detector element setting with finite sizes.

[10] Interactive Data Language, Research Systems Inc., Boulder, Colorado

3.1.1. Monochromatic X-rays and a point source and point detector elements

Before it can be explained how the simulator calculates the intensity of a monochromatic X-ray that has passed through an object, it must be explained how objects are defined in the simulator. Objects are defined as the superposition of a number of object parts, each with their own size, position, composition and resolution. This is illustrated in figure 3.1.

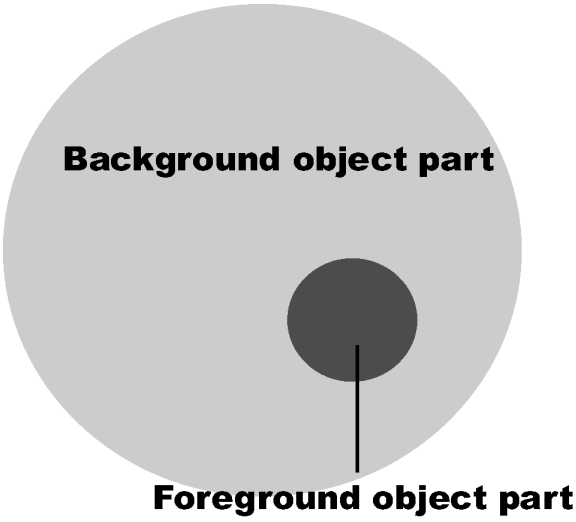

Figure 3.1: The objects in the simulator are defined as a superposition of object parts. Each object part has its own size, position, composition and resolution. Every object part is defined by a foreground and a background substance. The actual attenuation of an object part is the foreground attenuation minus the background attenuation.

Every object part is defined by a foreground and a background substance. The actual attenuation of an object part is calculated by subtracting the background attenuation from the foreground attenuation. This enables defining object parts contained within other, larger object parts. The superposition approach has the advantage that, for instance, different object part can be defined at a different resolution. This makes it possible to accurately simulate a smaller part by using a lot of pixels while relatively few pixels are used for the larger parts. By doing so computation time is saved.

Every object part is enclosed in a square of pixels for 2D simulations and in a cube of voxels for 3D simulations. The object part gets its shape by assigning the value $\rho=1$ to those pixels which belong to the object part and assigning the value $\rho=0$ to those pixels which do not (figure 3.2).

The intensity of a monochromatic beam that has passed through an object consisting of P object parts can then be calculated by Beer's law:

$$I_i = I_0 \cdot \exp\left(-\sum_{p=1}^{P} \left[\mu_p \cdot d_p \right] \right) \tag{3.1}$$

μ_p is the linear attenuation coefficient of the foreground object minus the background object at the energy level of the monochromatic X-ray beam. The index i ranges from 1 to $M_{view} \cdot N_{detector}$ with M_{view} being the number of views and $N_{detector}$ the number of detector elements. d_p is the distance travelled through each object part and is calculated by the projector. Figure 3.2 illustrates how the projector works.

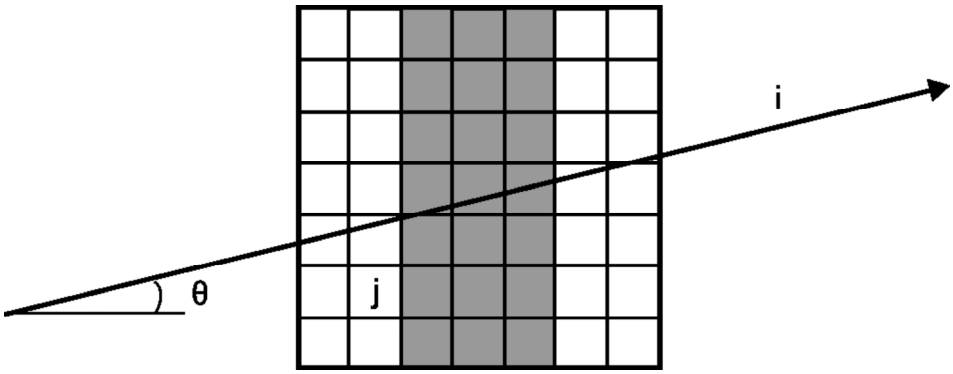

Figure 3.2: Illustration of the working of the projector. Every object part is enclosed in a square of pixels for 2D simulations and in a cube of voxels for 3D simulations. The shape of the objects is constructed by assigning the value $\rho=1$ to those pixels which belong to the object part and assigning the value $\rho=0$ to those pixels which do not. The projector calculates the distance travelled through each pixel or voxel and sums the distances of those having a value $\rho=1$.

The calculation performed by the projector is described by the following equation:

$$d_i = \sum_{j=1}^{J} l_{ij} \rho_j \tag{3.2}$$

l_{ij} is the distance that ray i travels through pixel j, ρ_j is the value of the pixel j (0 when the pixel is not a part of the object and 1 when the pixel does make part of the object) and J_p is the total number of pixels in object p. The formula (3.1) describing the intensity of the beam then becomes:

$$I_i = I_0 \cdot \exp\left(-\sum_{p=1}^{P} \left[\mu_p \cdot \sum_{j=1}^{J_p} l_{pij} \rho_{pj} \right] \right) \tag{3.3}$$

The simulator repeats this calculation a large number of times. First monochromatic calculations are grouped into polychromatic ones. Then the finite sizes of the source and detector elements are modelled by sampling both parts and by summing the photon flux over the source width and detector element width.

3.1.2. Simulating the polychromatic X-ray spectrum

The spectrum of the X-ray tube is modelled by summing a number of monochromatic simulations. The spectrum is therefore divided into a number of regions R_k with equal area as shown on figure 3.3. For each region a monochromatic simulation is performed using an attenuation coefficient μ_k. μ_k is the weighted average of the linear attenuation coefficient $\mu(E)$ over the corresponding part of the spectrum:

$$\mu_k = \frac{\int_{R_k} \mu(E) \cdot I(E) \cdot dE}{\int_{R_k} I(E) \cdot dE} \tag{3.4}$$

$I(E)$ represents the simulated spectrum.

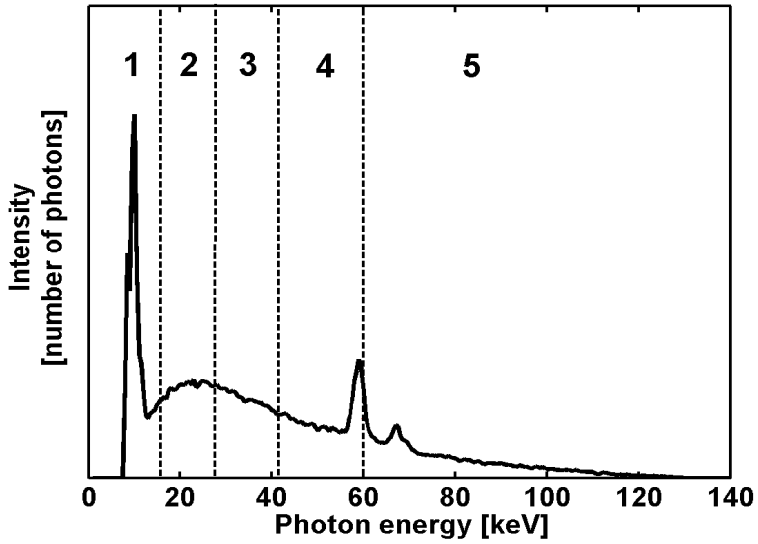

Figure 3.3: The spectrum is divided into a number of regions with an equal spectra area. For each region a monochromatic simulation is performed. These monochromatic simulations are then summed to simulate the polychromatic character of the spectrum. The attenuation coefficient used for each region is the weighted average of the linear attenuation coefficient over that part of the spectrum.

The formula describing the intensity of a polychromatic beam that has passed through an object consisting of P object parts is then:

$$I_i = \frac{1}{K}\sum_{k=1}^{K} I_0 \cdot \exp\left(-\sum_{p=1}^{P}\left[\mu_{kp} \cdot \sum_{j=1}^{J_p} l_{pij}\rho_{pj} \right] \right) \tag{3.5}$$

Equation (3.5) shows another advantage of the superposition approach used to define objects. This approach allow increasing the number of simulated energies with only marginal increase in computation time. In case the object would have been defined as one object consisting of pixels having different attenuation coefficients, the projections would have to be calculated for each monochromatic simulation. By defining the objects as a superposition of object parts, the index k can be brought outside the projection in equation (3.5). This reduces the number of projections by a factor K. A factor P is introduced, but P is usually much smaller than K.

The simulator still offers the possibility to perform monochromatic simulations at a specific energy level.

3.1.3. Simulating the finite sizes of the source and detector elements

Finally the finite sizes of the X-ray source and the detector elements are taken into account. This is done by sampling both parts at high resolution and summing the photon flux over the source and the detector element width. In the 2D simulator the source is modelled as a uniformly radiating line while a uniformly radiating square is used in the 3D simulator. This is schematically shown in figure 3.4.

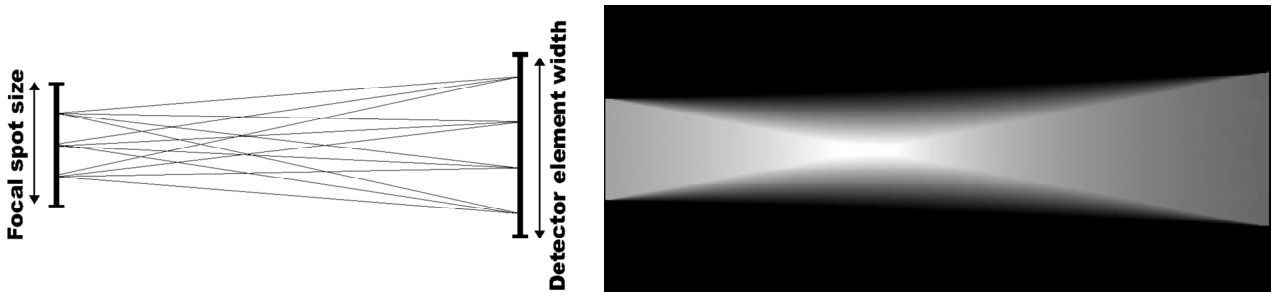

(a) (b)

Figure 3.4: (a) The finite sizes of the focal spot and the detector elements are modelled by sampling both parts and summing the photon flux over the source and detector element width. (b) The intensity distribution that is obtained by sampling the source and detector elements and summing the photon flux.

This results in the following formula:

$$I_i = \frac{1}{S}\frac{1}{D}\frac{1}{K}\sum_{s=1}^{S}\sum_{d=1}^{D}\sum_{k=1}^{K} I_0 \cdot \exp\left(-\sum_{p=1}^{P}\left[\mu_{kp}\cdot\sum_{j=1}^{J_p} l_{sdpij}\rho_{pj}\right]\right) \tag{3.6}$$

S and *D* are respectively the number of source and detector samples. Detector cross-talk can be taken into account by including detector samples from neighboring elements or by applying a convolution function on the sinogram (cf. section 3.1.8). Cross talk between detector elements occurs when photons hitting one detector element are measured by a neighbouring detector element. Cross-talk is mostly due to the alignment, or the lack thereof, of the detector elements.

Equation (3.6) describes how the simulator works. In the next sections it is described how the attenuation spectra of materials are defined and how some additional "features" as filtration of the spectrum, noise, scatter, etc. are implemented.

3.1.4. Attenuation spectra of materials

The simulator includes the calculation of the attenuation spectrum of every material with a known chemical composition. The simulator contains the mass attenuation coefficients[11] of all chemical elements. This allow calculating the mass attenuation coefficient of a homogeneous material[12]:

$$mac(E) = \frac{\sum_{i=1}^{N_{chemical}} r_i \cdot m_i \cdot mac_i(E)}{\sum_{i=1}^{N_{chemical}} r_i \cdot m_i} \tag{3.7}$$

m_i and r_i are respectively the molecular mass and the index in the molecular formula of element *i* and $N_{chemical}$ is the number of elements in the chemical formula of the material. The mass attenuation

[11] The mass attenuation coefficient is the linear attenuation coefficient μ over the density ρ: $\mu=\rho \cdot mac$.

[12] By a homogeneous material, a material that can be described by one molecular formula is meant. Non-porous minerals for example can be interpreted as a homogeneous material.

coefficient of materials composed of several homogeneous materials is calculated from the mass (*m%*) or volume (*v%*) percentages and the mass attenuation coefficients of their components:

$$\begin{aligned} mac(E) &= \sum_{i=1}^{N_{chemical}} m\%_i \cdot mac_i(E) \\ &= \frac{\sum_{i=1}^{N_{chemical}} \rho_i \cdot v\%_i \cdot mac_i(E)}{\sum_{i=1}^{N_{chemical}} \rho_i \cdot v\%_i} \end{aligned} \tag{3.8}$$

ρ_i is the density of material i and $m\%_i$ and $v\%_i$ the mass and volume percentages of the material i. By using the calculated mass attenuation coefficients and the density of the material, the linear attenuation spectra are determined. Eventual microporosity[13] can be taken into account by adjusting the density.

3.1.5. Simulating the use of hardware filters

The use of hardware filters in the scanning process is simulated by adjusting the intensity and spectrum emitted by the X-ray source. The altered spectrum is calculated using Beer's Law:

$$I(E) = I_0(E) \cdot \exp\left(- \sum_{i=1}^{N_{filter}} \mu_i(E) \cdot t_i \right) \tag{3.9}$$

where N_{filter} is the number of filters and t_i and μ_i are respectively the thickness and the linear attenuation coefficient of filter i.

3.1.6. Intensity and attenuation averaging

Two simulation modes are available: intensity averaging and attenuation averaging. The standard simulation uses intensity averaging and performs a summation of the beam samples after exponentiation (i.e. a summation of the intensities of the beam samples). This is the most realistic simulation mode. Alternatively, the summation of the beam samples can be performed before exponentiation. That will be referred to as attenuation averaging. The following simulation formula is then used:

$$I_i = \frac{1}{K} \sum_{k=1}^{K} I_0 \cdot \exp\left(- \frac{1}{S} \frac{1}{D} \sum_{s=1}^{S} \sum_{d=1}^{D} \sum_{p=1}^{P} \left[\mu_{kp} \cdot \sum_{j=1}^{J_p} l_{sdpij} \rho_{pj} \right] \right) \tag{3.10}$$

This simulation mode is implemented to investigate the exponential edge-gradient effect (EEGE) (cf. section 2.3.3.5). This effect results from averaging the intensity over the beam width. The standard simulation mode, the intensity averaging, includes this effect. Attenuation averaging eliminates this effect. By comparing simulations performed in both modes, the impact of the EEGE effect can be investigated.

[13] Microporosity is that part of the pore space that has a characteristic dimension less than 1 micron. In µCT the resolution is in the order of micrometers and therefore microporosity cannot be seen in these images.

3.1.7. Non-linearity of the detector

The detector is assumed to be linear. This means that the output of the detector, an electrical signal, is proportional to the amount of incoming photons. Some detectors however show a non-linear behaviour. An eventual non-linearity of the detector can be taken into account by applying a polynomial to the calculated sinogram.

3.1.8. Impact of the fluorescent screen and optical lens

As already explained in section 2.1.3, a fluorescent screen is used to increase the efficiency of the detector. The fluorescent screen converts X-ray radiation into light photons which are more efficiently detected. This screen is a few square centimeters large while the detector is around one square centimeter. To bridge both parts a scaling down is necessary. This is done by an optical lens.

The fluorescent screen and the optical lens result in an unsharpness in the acquired image and hence in a decreased resolution. This is simulated by applying a convolution function on the sinogram. The effect of detector cross-talk can also be simulated by a convolution function.

3.1.9. Noise

The three primary sources of noise are dark current, preamplifier noise and photon noise (cf. section 2.3.3.1). Once the intensity is high enough, it can be assumed that the noise caused by dark current and the preamplifier noise are negligibly small. The photon noise is proportional to the square root of the number of detected photons (i.e. the intensity) (*Guan and Gorden, 1981; Hsieh, 1988*). The intensities obtained by X-ray measurements are however not the intensities directly measured by the detector. The measured intensities are corrected for geometrical variations in the detector responsivity by a flat field. This flat field is an image taken in the absence of an object. The applied correction is described by the following formula:

$$I_{final}(x,y) = I_0(x,y) \cdot \frac{R(x,y)}{F(x,y)} \tag{3.11}$$

$I_0(x,y)$ is the original intensity, $F(x,y)$ is the flat field and $R(x,y)$ the raw radiograph. Since $R(x,y)$ and $F(x,y)$ are not constant in the image, the level of noise also varies in the image. The level of photon noise in the final image is:

$$noise(x,y) = \frac{I_0(x,y)}{F(x,y)} \cdot \sqrt{\frac{R(x,y)}{f_R}} \tag{3.12}$$

f_R is the number of integration frames and $I_{final}(x,y)$ is the intensity determined by the simulator without including any noise. A flat field $F(x,y)$ acquired with the scanner can be included in the simulator. $R(x,y)$ can then be calculated by equation (3.11) and consequently the level of photon noise $noise(x,y)$ can be determined using equation (3.12). This noise is then added to the intensity $I_{final}(x,y)$ already computed by the simulator.

This is a rather rough assessment of the noise level. To be able to more or less adjust the level of noise, it is possible to multiply the noise in the simulations by a constant factor k_{noise}. The model to simulate the noise can thus be described as follows:

$$noise(x,y) = k_{noise} \cdot \frac{I_0(x,y)}{F(x,y)} \cdot \sqrt{\frac{R(x,y)}{f_R}} \tag{3.13}$$

This proposed noise model is validated in the section 3.2.3.

Although Poisson noise is not autocorrelated, the noise in CT images sometimes exhibits a degree of autocorrelation. This affects the level of noise in the first derivative. Since the first derivative of images is used in procedures to determine the spatial resolution (cf. section 2.3.1), it is important that the simulated noise exposes the same behaviour.

When random noise, Gaussian distributed, is derived, the level of noise increases by a factor √2 (cf. table 3.1 – degree of interpolation 1; cf. appendix A). When the noise is autocorrelated, the level of noise in the first derivate can decrease. This behaviour is simulated by the following very simple and easily implemented method. Consider a series with z points and a standard deviation s_0. This series is extended to $n \cdot z$ points by adding new points between the existing points. The value of these new points is determined by interpolating between the values of the old points. The standard deviation of the new series is then:

$$s_n = \sqrt{\frac{n^2 + 2 \cdot \sum_{i=1}^{N} (i-1)^2}{n^3}} \cdot s_0 \tag{3.14}$$

The standard deviation of the first derivative of this new series is:

$$s'_n = \sqrt{\frac{2 \cdot n}{n^2 + 2 \cdot \sum_{i=1}^{n} (i-1)^2}} \cdot s_n \tag{3.15}$$

The mathematical derivations for both formulas are given in appendix A. Table 3.1 contains values for the factors of equations (3.14) and (3.15) for a given n. By choosing an appropriate value for n, the level of noise in the derivative of the simulated images can be more or less matched to the level of noise in the derivative of the scanned images. As n also decreases the level of noise (table 3.1), the latter is also corrected. In that way the degree of interpolation n does not change the noise level and only affects the noise level in the first derivative.

degree of interpolation n	$\frac{s_n}{s_0} = \sqrt{\frac{n^2 + 2 \cdot \sum_{i=1}^{N} (i-1)^2}{n^3}}$	$\frac{s'_n}{s_n} = \sqrt{\frac{2 \cdot n}{n^2 + 2 \cdot \sum_{i=1}^{n} (i-1)^2}}$
1	1,00	1,41
2	0,87	0,82
3	0,84	0,56
4	0,83	0,43
5	0,83	0,34

Table 3.1: Impact of the extension of a series to its standard deviation and to the standard deviation of its derivative. The original series is extended by adding n new points between the existing points. The value of these new points is the interpolation between the values of the old points. This changes the standard deviation of the new series and the ratio of standard deviation of the derivative over the standard deviation of the series.

A theoretically sound approach might be preferable over the presented, empirical approach. The latter however offers a convenient method to more or less simulate the presence of noise in CT images. Correctly simulating noise is a cumbersome and complicated task as different sources of noise are present. Assessing the weight of each source in the final amount of noise cannot be done in a straightforward way either. Therefore the more pragmatic approach presented above is maintained.

3.1.10. Scatter

Due to the nearly isotropic angular distribution of the Compton scattering process, the scatter intensity contains very little high spatial frequencies. Therefore the scatter is simulated by a constant scatter profile which is expected to be a reasonably good approximation (*Glover, 1982*). This scatter profile is a fraction f_s of the intensity I_0 emitted by the source and is added to the simulations.

$$I(x,y) = I_{simulated}(x,y) + f_s \cdot I_0 \tag{3.16}$$

Slightly more complicated scatter models are proposed in *Hangartner (1987)* and *Ohnesorge et al. (1999*) and scatter models using Monte Carlo simulations are described in *Chan and Doi (1985)*, *Cheng et al. (1995)* and *Leliveld (1996*). These latter are probably more reliable, but demand a very high computation time. Because of the fast increase in computation time when using more complicated scatter models, the very simple model of using a constant scatter profile was preferred over the other models.

3.2 Adjusting the simulator to the Skyscan µCT scanner

After the development and the implementation of the simulator, this simulator needs some fine-tuning to the scanner for which it is applied for. The scanners used in this research are the Skyscan 1072 Desktop µCT scanner and the AEA Tomohawk µCT scanner. The raw radiographs obtained in the AEA Tomohawk (rad-files) need post-processing and are difficult to read. Therefore not all properties of the AEA Tomohawk could be determined and a complete fine-tuning is only performed and described for the Skyscan 1072. The properties determined for the AEA Tomohawk are given in appendix B. The values for these properties are obtained by applying the same procedure that is performed for the Skyscan and that is explained in this section.

The following properties of the Skyscan 1072 µCT scanner are examined:

- an eventual non-linearity of the detector
- the X-ray spectrum
- the level and eventual autocorrelation of the noise
- the impact of the fluorescent screen
- the geometrical parameters of the scanner

The amount of scatter is not determined, as it cannot directly be derived from CT images. Scatter can be measured using a well collimated detector and mounting this detector slightly out of the imaging plane. Doing this is however not possible with the used scanners.

3.2.1 Linearity of the detector

The linearity of the detector can be checked by changing the emitted intensity and comparing it to the measured intensity. Altering the emitted intensity can be done by changing the cathode current which

affects the number of photons proportionally without changing the spectral distribution (cf. section 2.1.1). Another approach is changing the exposure time which proportionally changes the emitted intensity. The results of both methods are given in figure 3.5. The measurements were performed using a high number of integration frames (16) to reduce the noise in the images.

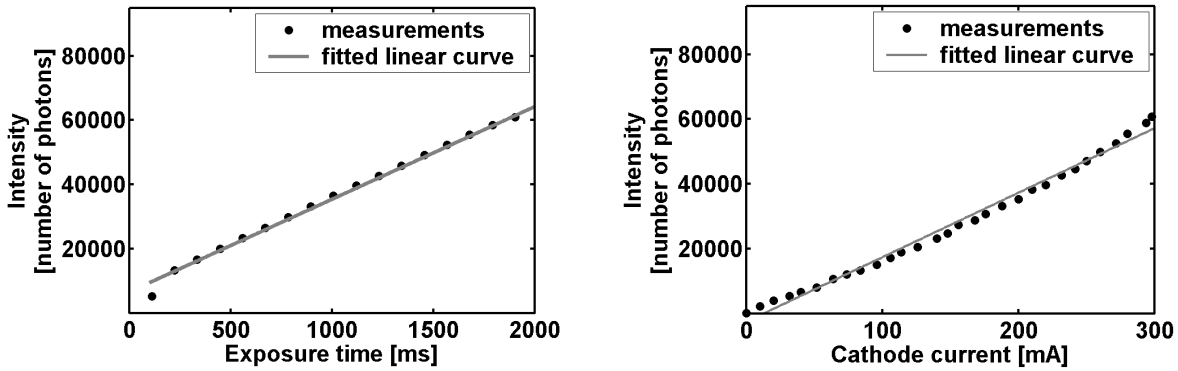

(a) (b)

Figure 3.5: Changing the exposure time or the cathode current proportionally affects the emitted intensity. In (a) the mean detected intensity is plotted over the exposure time. In (b) the mean detected intensity is plotted over the cathode current. Both curves show a linear trend indicating a linear response of the detector.

A linear trend is clearly visible in both figures. Fitting a linear polynomial on these curves results in a goodness of fit, i.e. the coefficient of determination R^2, of 0.9994 and 0.9863 respectively. A deviation from the linear trend can be seen for the lower exposure times when the intensity is plotted over the exposure time (figure 3.5a). This deviation might result from dark current. In that case however, a similar deviation can be expected when the intensity is plotted over the applied cathode current (figure 3.5b). But there is not such a deviation in this curve. Nevertheless, as the deviation is relatively small and only occurs in the first plot, the detector is assumed to be linear.

3.2.2 The X-ray spectrum

The emitted spectrum of the X-ray source is not exactly known and is difficult to measure. Moreover the emitted intensity is not constant in time. In figure 3.6 the evolution of the intensity in time is shown. The intensity was measured by scanning in the absence of an object, called a blank scan, over a wide span of time.

A trend can be seen which increases relatively fast in the first 2 hours reaching a maximum between the 2nd and the 4th hour when the intensity stays fairly constant. After 4 hours the trend gradually decreases. Superposed on this trend, the intensity exhibits some fluctuations: sudden, abrupt increases followed by a gradual decrease.

This could of course have influenced the measurements in section 3.2.1. Therefore these measurements were taken after 2 hours of scanning when the emitted intensity is more or less constant. Moreover these measurements were rescaled using the trend shown in figure 3.6 to eliminate the effect of the intensity changing over time.

The tube voltage affects the resulting CT image because a different tube voltage results in a different X-ray spectrum (cf. section 2.1.1). This impact is simulated by using that X-ray spectrum in the simulation that corresponds to the simulated tube voltage.

The X-ray spectra were measured by a detector which is, together with dedicated software, able to perform a spectral reconstruction of the radiation produced by X-ray tubes (*Aiello et al., 2004; Stumbo et al., 2004*). The apparatus could only measure tube voltages up to 60 kV. The spectra for higher tube voltages are computed by fitting Hammersberg spectra (*Hammersberg, 1998*) to the measured spectra at lower tube voltages. This should not seriously limit the representativity of these computed spectra as the lower energies are most important and as these are directly measured by the apparatus. The resulting spectra are given in appendix C.

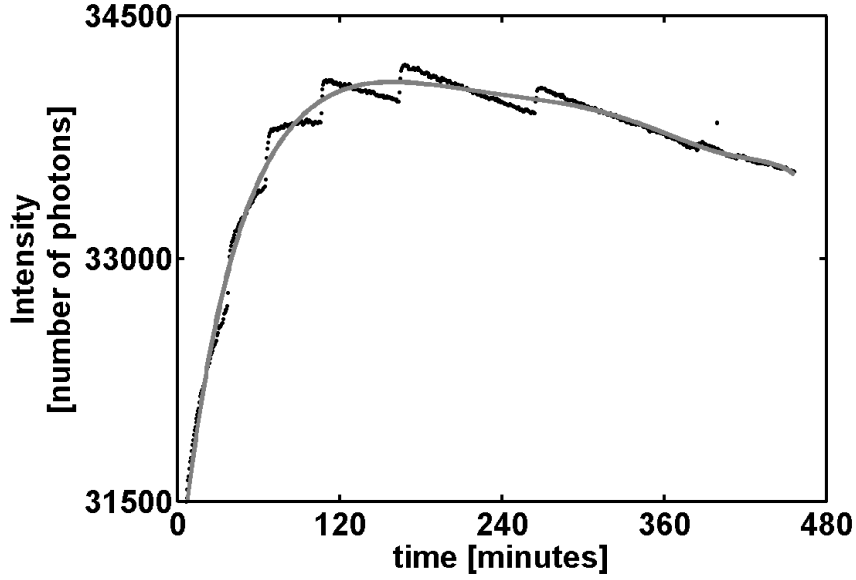

Figure 3.6: Evolution of the mean measured intensity over time. The X-ray source does not emit a constant intensity in time. A clear trend of a steep increase in intensity in the first two hours followed by a gradual decrease is visible. Abrupt changes are superposed on this trend.

3.2.3 Noise

As previously described, the level of noise depends on the number of integration frames, the intensity in the raw radiograph and the intensity in the flat image. The effect of these parameters on the level of noise is described by formula (3.12):

$$noise(x,y) = \frac{I_0(x,y)}{F(x,y)} \cdot \sqrt{\frac{R(x,y)}{f_R}}$$

To assess the level of noise blank scans were taken using a different number of integration frames. The standard deviation of the intensity is taken as a measure of the level of the noise. Table 3.2 summarizes the level of noise in these measurements and the level of noise in simulations using identical acquisition parameters. All the simulations are performed using a noise factor k_{noise} of 1 (equation (3.13)). By comparing the noise in these simulations and in the real measurements, the noise factor is determined.

The noise decreases with increasing number of integration frames. The noise in the scanned and the simulated images follows the same trend. The noise in the simulated images is a factor 2,4 to 3,4 smaller and the ratio of the noise in the scanned images over the noise in the simulated images increases with increasing number of integration frames.

Number of integration frames	Noise in scanned images	Noise in simulated images	Ratio of scanned over simulated images
1	536	226	2,4
2	399	160	2,5
4	293	113	2,6
8	226	80	2,8
20	171	50	3,4

Table 3.2: Comparison between the noise in scanned and simulated images when changing the number of integration frames. Using more integration frames lowers the noise level. The noise in the simulated CT images is approximately a factor 2,4 to 3,4 lower than the noise in the scanned images.

A second experiment consists of altering the intensity in the raw radiographs and in the flat field. In all these measurements only 1 integration frame is used. These measurements are summarized in table 3.3. Again, a noise factor k_{noise} of 1 is used. The measurements were taken at a maximum of 80% of the exposure time that was used for the acquisition of the flat field. Using a higher exposure time makes the detector occasionally go into saturation and results in a flattening of the noise. This is due to the fact that the scanner can only register 2 byte numbers. When the detector goes into saturation, the higher intensities cannot be recorded and they are topped off. Hence intensity fluctuations because of noise will also be topped off and the level of noise will be underestimated.

Ratio[14]	exposure time 2800 ms			exposure time 2240 ms			exposure time 1680 ms		
	Noise scans	Noise simula-tions	ratio	Noise scans	Noise simula-tions	ratio	Noise scans	Noise simula-tions	ratio
80%	538	225	2,4	594	245	2,4	655	281	2,3
60%	460	195	2,4	502	213	2,4	560	243	2,3
40%	352	159	2,2	414	176	2,4	482	198	2,4
20%	242	113	2,1	301	129	2,3	359	141	2,6

Table 3.3: Comparison between the noise in scanned and simulated images when changing the intensity in the raw radiograph and in the flat field. Only 1 integration frame is used. The noise level decreases with an increasing intensity in the flat field and with a decreasing intensity in the raw radiograph. The ratio between the noise level in scanned and simulated images fluctuates around 2,4.

From equation (3.12) it is learnt that the noise level decreases with an increasing intensity in the flat field and with a decreasing intensity in the raw radiograph. This is confirmed by the measurements summarized in table 3.3. The ratio between the noise level in scanned and simulated images fluctuates around 2,4. This is most probably due to simplifications such as the assumption that the preamplifier noise can be neglected. However, the noise in the simulated images shows the same trend as the noise in the scanned images and their ratio is more or less a constant. Therefore, the proposed model is maintained using a constant noise factor k_{noise} of 2,4.

An eventual autocorrelation present in the noise can be checked by taking a semivariogram of a blank scan, as shown in figure 3.7. A semivariogram describes the degree of spatial dependence in data. As geometrical variations in the detector response are corrected by the use of a flat field, the differences in intensities in a blank scan are due to noise. When the noise would contain no autocorrelation, the

[14] This is the ratio of the exposure time used in the scans over the exposure time used to acquire the flat field.

semivariogram would be a constant equal to the level of the noise. The semivariogram however shows that the average difference between points close to each other is smaller than the average difference between points lying further away from each other. This reveals a spatial dependence and thus the noise shows a degree of autocorrelation.

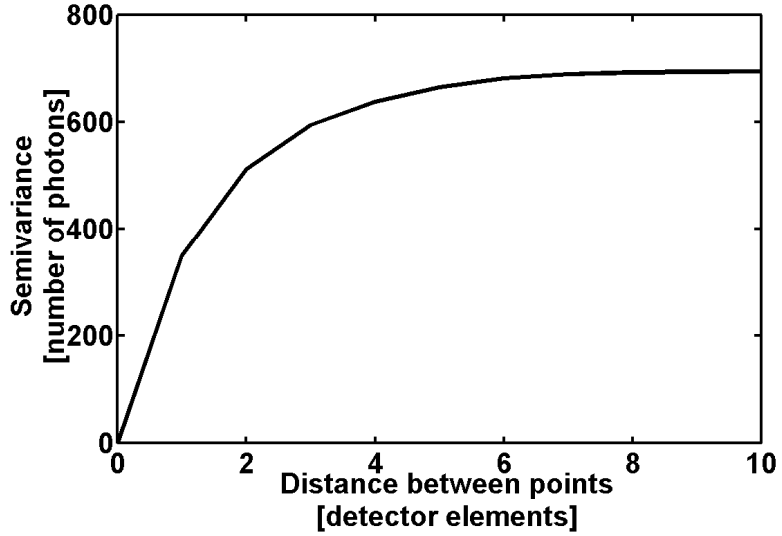

Figure 3.7: Semivariogram of the intensity in a blank scan. The semivariogram reveals a spatial dependence in measured intensity as the average difference between points close to each other is smaller than the average difference between points lying further away from each other.

The degree of autocorrelation in the noise influences the level of noise in the first derivative which is often used to determine the resolution of the image. Therefore it is important that not only the noise levels in the scanned and simulated images are more or less equal, but also the noise levels in their first derivatives. A basic method was developed to generate noise with a degree of autocorrelation. This method consists of generating a series of z random points and extending this series to $n \cdot z$ points by adding interpolated points (cf. section 3.1.9). The parameter n is called the degree of interpolation and affects the noise level in the first derivative. Table 3.4 shows how much the noise level in the first derivative is reduced compared to the noise level in the image as a function of the number of integration frames.

The degree of autocorrelation increases with increasing number of integration frames. When 1 to 8 integration frames are used, a degree of interpolation of 2, resulting in a reduction of 0,82, can be used. To simulate the noise autocorrelation in the images where 20 integration frames are used, it is better to use a degree of interpolation of 3 (cf. table 3.1).

number of integration frames	noise reduction
1	0,83
2	0,81
4	0,78
8	0,74
20	0,64

Table 3.4: The reduction in noise level in the first derivative in function of the number of integration frames.

3.2.4 Impact of the fluorescent screen

The fluorescent screen creates an additional unsharpness to the geometrical unsharpness inherent to the finite sizes of the source and the detector elements. This is simulated by applying a convolution function on the sinogram. This convolution function can be derived from the Modulation Transfer Function (MTF) of the fluorescent screen. This MTF describes the spatial frequency response of the fluorescent screen. The used screen in the Skyscan 1072 Desktop is a phosphor screen, a Mamoray detail S V1 with Mamoray HDR-film of AGFA. The MTF of this screen is shown in figure 3.8 (*Bastiaens, 2000*):

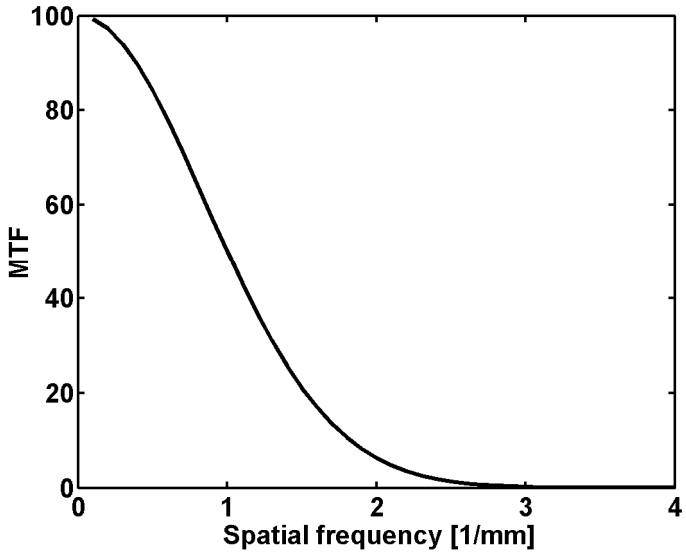

Figure 3.8: The Modulation Transfer Function of the fluorescent screen. The MTF describes the spatial frequency response of an imaging system or component.

From this MTF, the LSF is derived. According to Nickeloff and Riley (*1985*), the LSF can usually be described by a Gaussian function:

$$LSF(x) = A \cdot \exp\left(-(\alpha \cdot x)^2\right) \tag{3.17}$$

in which A en α are constants. The MTF is the Fourier transform of this Gaussian curve:

$$MTF(k_x) = \left|\Im\left(LSF(x)\right)\right| = \frac{A \cdot \sqrt{\pi} \cdot \exp\left(-\left(\frac{\pi \cdot k_x}{\alpha}\right)^2\right)}{\alpha} \tag{3.18}$$

By fitting this equation on the MTF curve of figure 3.8, A and α can be determined. This results in the LSF of the fluorescent screen:

$$LSF\ (x) = 804\ \cdot \exp\left(-(14{,}26 \cdot x)^2\right) \tag{3.19}$$

The parameter x is a measure for the length, expressed in mm, in the fluorescent screen. The convolution function is applied on the detector elements of the sinogram. Therefore equation (3.19) has to be written as a function of apparent detector elements in the fluorescent screen instead of millimeters. The luminated area on the screen is 67,2 by 67,2 mm (cf. section 3.2.5) and the detector

consists of 1024 by 1024 detector elements. The apparent detector element size d_{app} is therefore 65,6 by 65,5 µm. Equation (3.19) then becomes:

$$LSF\ (d_{app}) = 804\ \cdot \exp\left(-\left(0{,}96 \cdot d_{app}\right)^2\right) \tag{3.20}$$

Applying this convolution function, shown in figure 3.9, on the sinogram simulates the impact of the fluorescent screen.

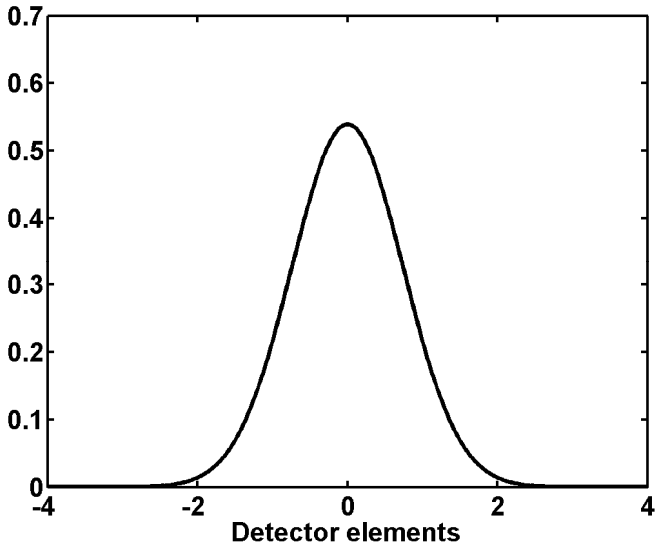

Figure 3.9: The convolution function simulating the effect of the fluorescent screen. The convolution is expressed in apparent detector elements.

3.2.5 Determining the geometrical parameters

The simulator needs to know the geometry of the scanning process. This geometry is defined by the distance *h* between the source and the detector, the distance *r* between the source and the object, the field of view *fov*, the fanangle *α* and the focal spot size *w*. These parameters are illustrated in figure 3.10.

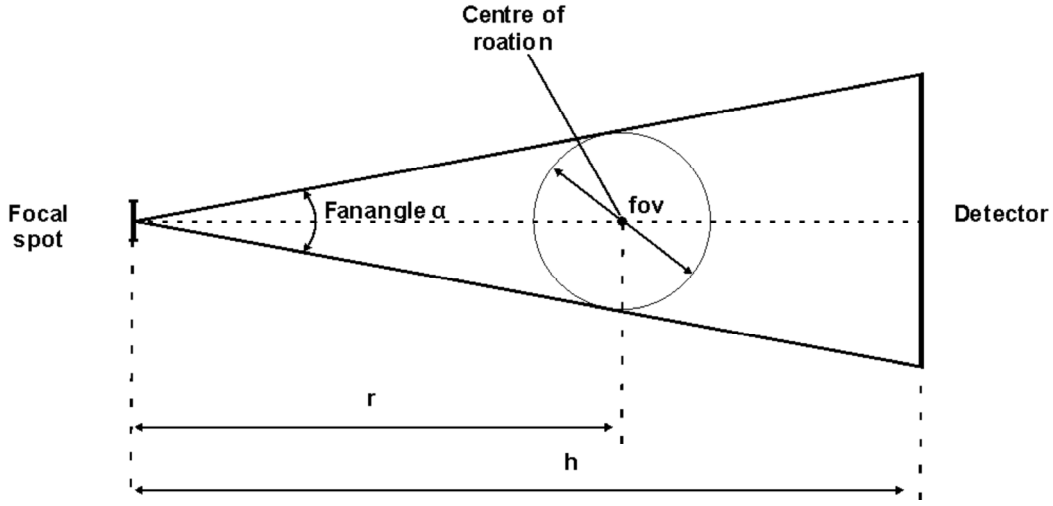

Figure 3.10: Illustration of the geometrical parameters involved in the scanning process.

The distances r and h cannot be measured directly because the X-ray source and detector are encapsulated. They can however be derived from the achieved magnification which depends on the ratio of both distances, as can be seen in figure 3.10. Yet, it is not possible to directly derive the ratio h/r from the magnification since this magnification consists of a primary and a secondary magnification. The primary is the geometrical magnification P_M defined by the distances h and r. The secondary is an artificial, electronic magnification S_M. The final magnification M is achieved by multiplying the primary and the secondary magnification:

$$M = P_M \cdot S_M \tag{3.21}$$

By measuring the distance a between a fixed point in the scanner and the position of the object for different magnifications, the geometrical and secondary magnification can be determined. The fixed point was placed 238 mm from the detector (i.e. the fluorescent screen). This is illustrated in figure 3.11. Table 3.5 contains the results of the different measurements.

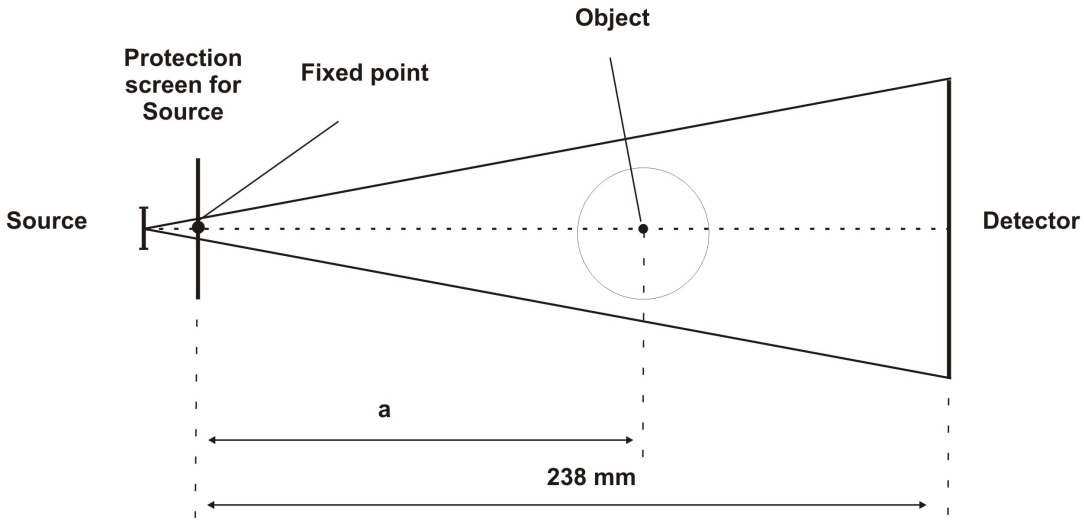

Figure 3.11: The distance to the source cannot be measured as it is protected by a screen. Therefore the distance a to a fixed point (located on the protecting screen) is measured and a projection image is taken of a known object. By doing this for several magnifications the distance between the source and the fixed point can be determined. Hence the distance between the source and detector is also known.

These measurements are consistent when the distance between the fixed point and the source is 32 mm. The distance h between source and detector is thus 270 mm. S_M can then be calculated from the measurements in table 3.5 resulting in a value of 4,2.

Now that the distances r and h are known for specific magnifications, the fanangle α can be calculated from the pixel size for that magnification by using the following formula:

$$\alpha = 2 \cdot \arctan\left(\frac{pixelsize \cdot 1024}{2 \cdot r}\right) \tag{3.22}$$

The pixel sizes for different magnifications and the resulting values for α are summarized in table 3.6.

scanner magnification	distance *a* to the fixed point [mm]	scanner magnification	distance *a* to the fixed point [mm]
5,23	185	13	55
6	157	14	49
7	130	15	44
8	110	16	39
9	94	17	35
10	82	18	31
11	71	19	28
12	63	20	25

Table 3.5: Distance of the center of rotation to the fixed point in function of the magnification.

scanner magnification	r [mm]	pixel size [µm]	fanangle α [degrees]
5,23	217	52,28	14,19
6	189	45,57	14,19
7	162	39,06	14,19
8	142	34,18	14,19
9	126	30,38	14,19
10	113	27,34	14,19
11	103	24,86	14,19
12	94	22,79	14,19
13	87	21,03	14,19
14	81	19,53	14,19
15	76	18,23	14,19
16	71	17,09	14,19
17	67	16,08	14,19
18	63	15,19	14,19
19	60	14,39	14,19
20	57	13,67	14,19

Table 3.6: Pixel size in function of the magnification. From the knowledge of the pixel size the fanangle can be determined.

The width of the illuminated area at the fluorescent screen is then:

$$width\ \_of\ \_area\ = 2 \cdot h \cdot \tan\left(\frac{\alpha}{2}\right) = 67,2\,mm \tag{3.23}$$

The sole geometrical parameter that remains to be determined is the focal spot size. This is an important parameter as it affects the resolution that can be achieved (cf. section 2.1). The greater the spot size is, the greater is the penumbra interval and the more blurring occurs at the edges of an object. This is illustrated in figure 2.4.

A focal spot size of 10 µm or 40 µm can be chosen in the Skyscan 1072 Desktop µCT scanner. There is however often a certain amount of off focal radiation. Off focal radiation, also called extra focal radiation, is X-ray radiation produced at locations other than that of the focal spot. Off focal radiation is usually generated when electrons hit the target at points outside the focal spot and produce X-rays at their point of impact. This can occur when beam electrons, called primary electrons, are not focused on the focal spot. But off focal radiation is mostly produced by so-called secondary electrons. These

electrons are emitted when primary electrons hit the target area and generate other electrons instead of X-rays. These electrons mostly return to the target at points outside the focal spot area and cause off focal radiation.

Due to off focal radiation the focal spot size appears to be bigger than the real spot size. This apparent focal spot size can be determined by comparing the resolution in simulations using different values for the focal spot size with the resolution in real µCT images. As described in the previous section, the resolution can be measured by taking the FWHM of the LSF. The LSF is the derivative of the ERF which can be obtained by taking the image of an edge. The exact procedure to apply this method is described in *ASTM (1981)*. Caution is however necessary when applying this method as it is not very robust and sensitive for small changes.

Figure 3.12 contains the results of the resolution measurements for different magnifications. The scanned measurements and simulations were performed using 4 integration frames and the noise was simulated using a degree of interpolation of 2.

Evidently, the FWHM, expressed in apparent detector elements, increases with increasing magnification and increasing focal spot size. Using a focal spot size of 40 µm clearly results in an underestimation of the resolution. The simulations using a focal spot size of 60 µm match best with the scanned measurements.

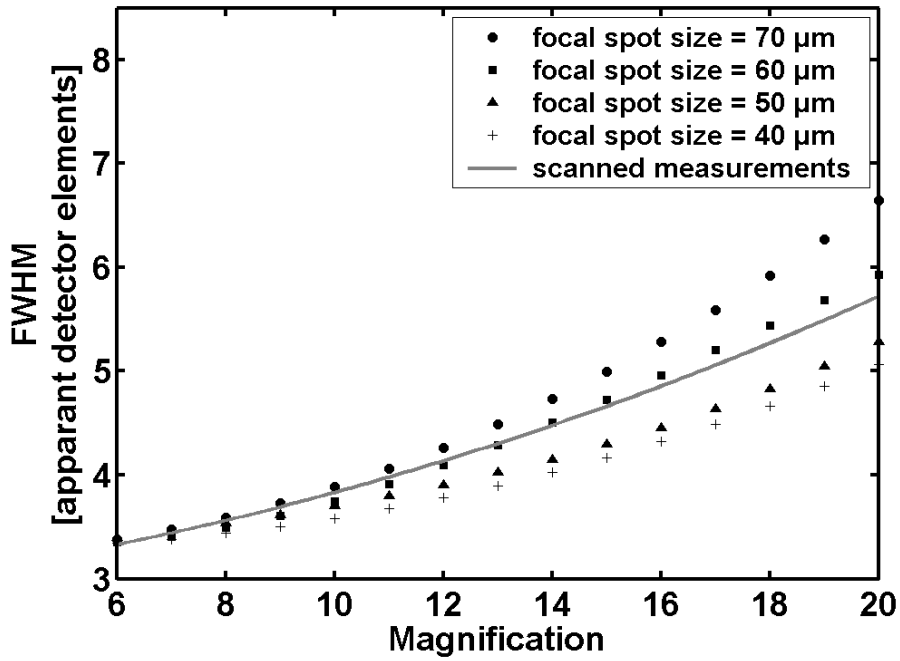

Figure 3.12: Resolution (measured as FWHM of the LSF) in scanned images and in simulations using different values for the focal spot size and different magnifications.

As conclusion the determined geometrical parameters are summarized:

- distance between source and detector: 270 mm
- secondary magnification: 4,2
- fanangle: 14,2°
- focal spot size: 60 µm
- apparent detector element: 65,6 x 65,6 µm²

3.3 Demonstration of the simulator

The quality of CT images is defined by the spatial and contrast resolution that can be achieved, the level of noise, the amount of scatter and the presence or absence of artifacts. These factors are strongly interrelated and defining what the most optimal image is, cannot unambiguously be done. Depending on the purpose of the measurement, the spatial resolution, the contrast resolution or artifacts can for instance be the critical factor. Another factor is the acquisition time. This has no direct impact on the image quality, but can put a limit on how profound an optimization of the image quality can be performed. Using a lot of integration frames for example reduces the noise, but the acquisition time increases proportionally.

The simulator can be used to assess the impact of these factors on the image quality. In that way it is a useful tool to check whether or not a good quality can be achieved for given acquisition parameters and eventually to perform an image optimization. This is demonstrated in this section. Only 2D simulations are presented as all phenomena can perfectly be explained in 2D and as these phenomena are more easily demonstrated using 2D images.

3.3.1 Spatial resolution

The impact of the geometrical parameters on the spatial resolution is examined by performing simulations using different geometrical parameters. Figure 3.12 shows how the focal spot size and the magnification affect the spatial resolution. Figure 3.13 shows the effect of the fluorescent screen on the spatial resolution using different magnifications. A focal spot of 60 µm was used in these simulations. The fluorescent screen results in a higher FWHM value and thus in a lower resolution.

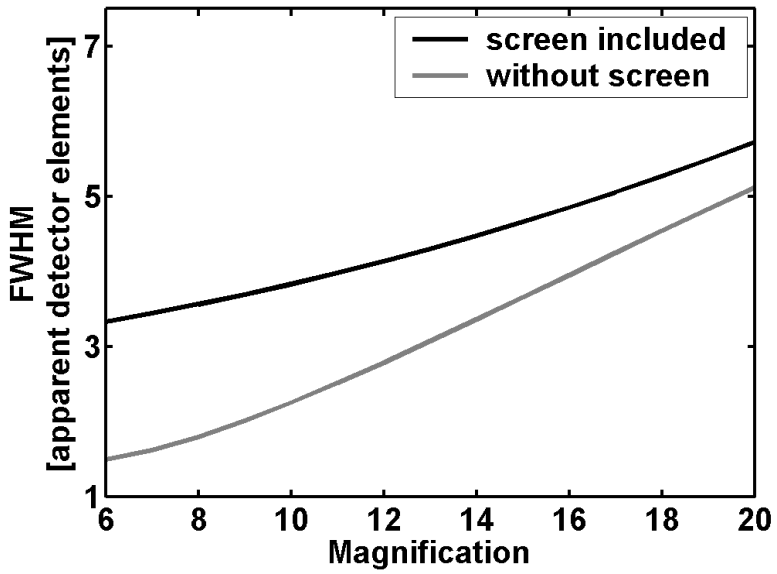

Figure 3.13: Impact of the fluorescent screen on the spatial resolution for different magnifications. A focal spot size of 60 µm was used. The fluorescent screen increases the measured FWHM and thus decreases the resolution. This effect is more pronounced for smaller magnifications.

The acquisition parameters determining the resolution, i.e. the focal spot size and the detector element size, are fixed for a specific scanner and a given magnification. Therefore the resolution can often not be optimized. Still, it is interesting to alter the achieved resolution with the simulator and check the

effect of the improved resolution. A higher number of detector elements can for instance be used to increase the resolution. In that way an idea of the sensitiveness of the calculations based on the CT images to the resolution can be acquired. This is demonstrated in section 4.2.5 where the impact of the limited resolution on the thresholded image is examined.

3.3.2 Contrast resolution

In contrast to the spatial resolution which can hardly be affected by user chosen parameters as it is more or less inherent to the used scanner, the contrast can more easily be optimized. The contrast can be influenced by the choice of target material, tube voltage and filters. These affect the X-ray spectrum and in that way can shape it into a more efficient spectrum. A more efficient spectrum has a higher ratio of photons that are strongly attenuated over photons that hardly interact with the object. Figure 3.14 shows the effect of different tube voltages on the contrast between a dolomite sample and a calcite inclusion. The simulated sample is purely an artificial object used here to demonstrate the effect of the tube voltage. Polychromatic simulations are performed and no scatter or noise is included.

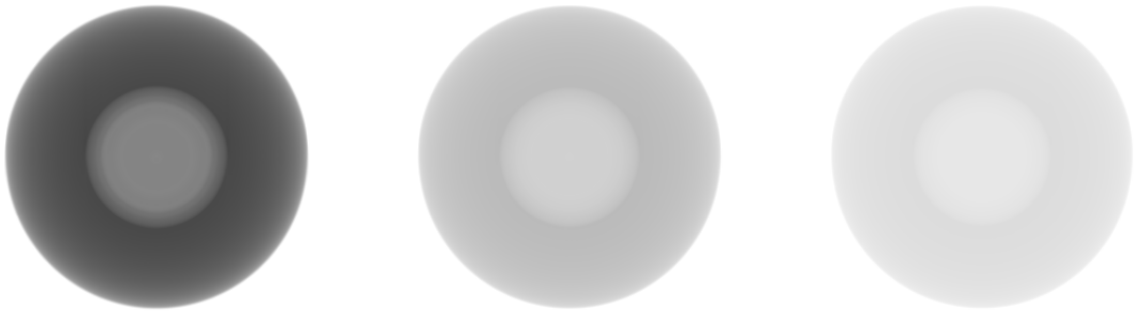

(a) (b) (c)

Figure 3.14: Impact of the used tube voltage on the contrast between dolomite and a calcite inclusion. Polychromatic simulations at 40 kV (a), 80 kV (b) and 120 kV (c) are performed and no scatter or noise is included. Increasing the tube voltage will increase the fraction of high energy photons in the spectrum. These photons hardly interact with dolomite and calcite and are therefore useless to make a distinction between both materials. The contrast therefore diminishes when the tube voltage is increased.

The contrast is mainly determined by the ratio of photons distincting both material from each other over photons that are almost evenly attenuated by both materials. When a higher tube voltage is used, the spectrum contains more high energy photons. The high energy photons are hardly attenuated by the dolomite and calcite and result in a higher reconstructed attenuation coefficient and a relatively lower density difference between the dolomite and calcite. This is clearly visible on figure 3.14 where the reconstructed images become brighter for higher tube voltages and the contrast between both materials has decreased.

Filtration can also be used to acquire a better ratio of photons that are differently attenuated by both materials over photons almost evenly attenuated. Filtering the spectrum however also reduces the signal-to-noise ratio and this might in turn deteriorate the contrast. Finding a filter that increases the contrast is therefore often a matter of trial-and-error and a simulator can be useful to look for a good filter setup. An example of such an image optimization using the simulator is given in section 3.3.3.6.

Noise and scatter also have a negative effect on the contrast. This is discussed in the following sections.

3.3.3 Artifacts

3.3.3.1 Noise

The noise in the simulation is generated using a simple and pragmatic model. As mentioned before, this model does not enable computing or simulating the exact level of noise under given scanning conditions, but it allows comparing the noise under different scanning conditions. The effect of using more integration frames and of filtration on the noise level can be simulated. This is shown in section 3.3.3.6 where an image optimization case is performed.

3.3.3.2 Scatter

In the same way high energy photons are useless to distinct materials from each other, scatter does not contain relevant information and decreases the relative density differences in the sample. Scatter is simulated by adding a constant intensity to all detector elements. The resulting higher intensity leads to an underestimation of the attenuation, which is of course more pronounced in high attenuation regions (*Joseph, 1981*). This gives rise to a decreased contrast and similar artifacts as beam hardening artifacts, namely cupping and streak artifacts.

In figure 3.15 the effect of scatter can be observed. These are simulations of a dolomite matrix with dense (pyrite) inclusions and including a constant scatter profile equal to respectively 0.005 and 0.05 times the emitted intensity I_0. The simulations are monochromatic to eliminate beam hardening as this causes similar artifacts.

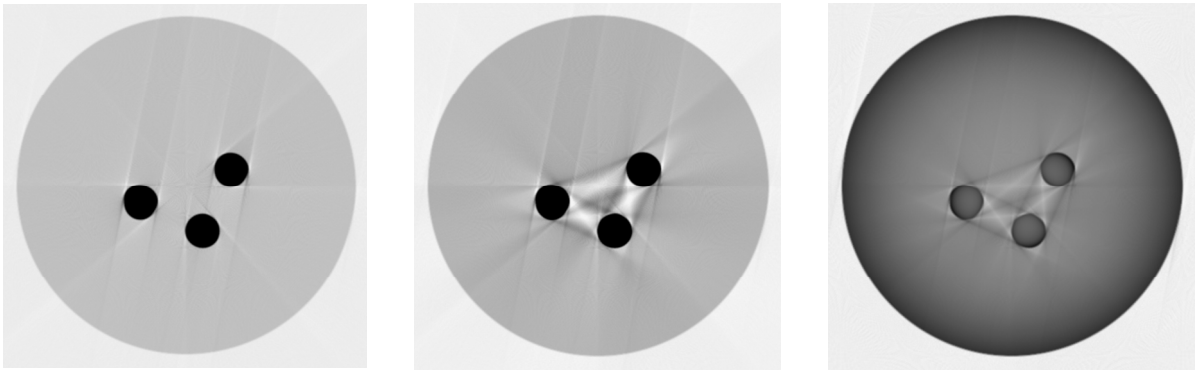

(a) (b) (c)

Figure 3.15: Monochromatic simulation of a dolomite sample with pyrite inclusions: (a) no scatter is included; (b) 0,005 of the original intensity is included resulting in streak artifacts; (c) 0,05 of the original intensity is included leading to a decrease in contrast and streak and cupping artifacts.

Streaks connecting the dense inclusions can already be seen using a scatter intensity of 0,005 of the blank scan intensity. A scatter intensity of 0,05 of the blank scan intensity results in a decrease in contrast and streak and cupping artifacts.

3.3.3.3 Beam hardening artifacts

The effect of beam hardening is investigated by comparing polychromatic and monochromatic simulations (figure 3.16). The mean effective energy in the polychromatic simulation was taken as the energy for the monochromatic simulations. No scatter was included as this causes similar artifacts as beam hardening. Noise was also not taken into account in the simulations.

The monochromatic simulation is free of beam hardening. In the polychromatic simulation cupping and streak artifacts are visible. This can be seen more clearly when the difference between the artifact-free, monochromatic simulation and the polychromatic simulation is taken.

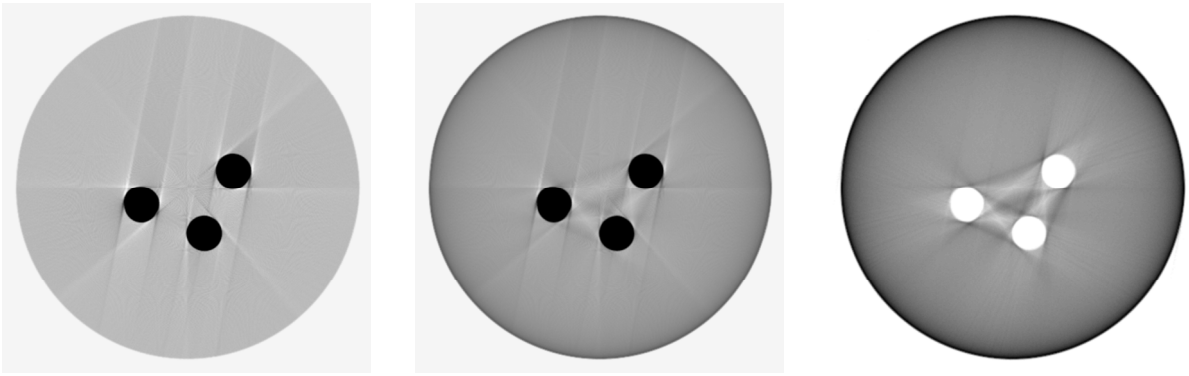

(a) (b) (c)

Figure 3.16: Comparison between a monochromatic (a) and polychromatic (b) simulation of a dolomite sample with pyrite inclusions to demonstrate the effect of beam hardening. (c) shows the difference between both images revealing streak and cupping artifacts.

Using hardware filters can reduce artifacts due to beam hardening as the low energies are partly absorbed by the filter material (*Herman, 1979; Hammersberg and Mångård, 1997*). This increases the effective energy and reduces the beam hardening artifacts. Eliminating beam hardening by filtration is however not possible and as filtration also lowers the emitted intensity, it results in an increase of the SNR and a decrease in contrast (cf. sections 2.3.2 and 3.3.3.6) (*Pang and Genna, 1976; Jennings, 1988*). Choosing the optimal filter is often a matter of trial-and-error. Figure 3.17 illustrates the effect of a copper filter with a thickness of 0.2 mm on the X-ray spectrum and on the reconstructed image. The cupping and streak artifacts are not visible anymore.

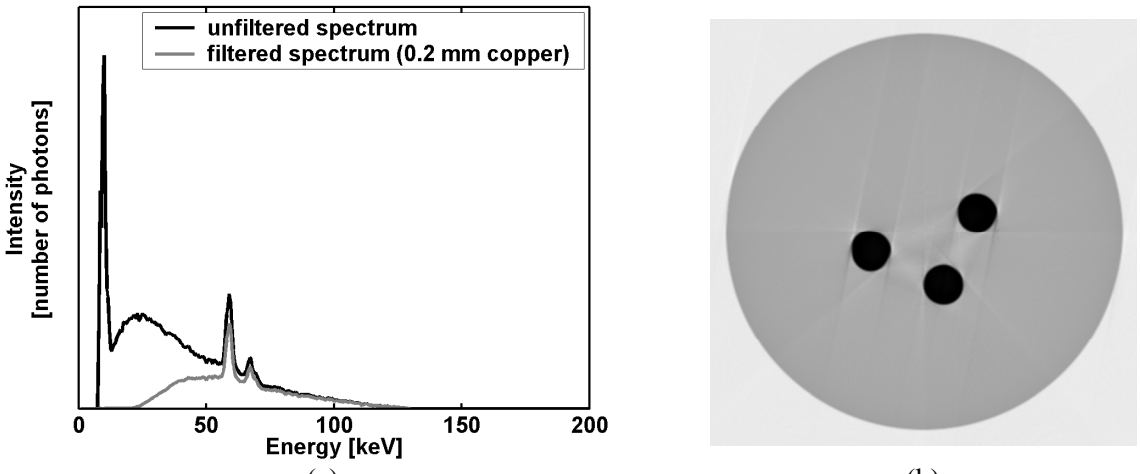

(a) (b)

Figure 3.17: Beam hardening artifact can be minimized using a filter. The effect of a 0,2 mm copper filter on the X-ray spectrum is shown in (a). The effective energy of the spectrum has increased and this reduces the beam hardening artifacts in the reconstructed image (b).

For homogeneous samples beam hardening can be eliminated by a linearization procedure (cf. section 2.3.3.3). This requires a calibration procedure in which the intensities of the polychromatic beam for different material thicknesses are measured. The simulator can be used to rapidly perform

this calibration without the need for calibration samples (i.e. samples of different thicknesses). Also dual energy scanning can be used to eliminate beam hardening in polymineralic samples (*Remeysen and Swennen, 2006*). This also requires a calibration procedure. Again, the simulator offers the possibility to relatively quickly and easily perform this calibration.

3.3.3.4 Aliasing artifacts

In figure 3.18 simulations using different number of views are shown.

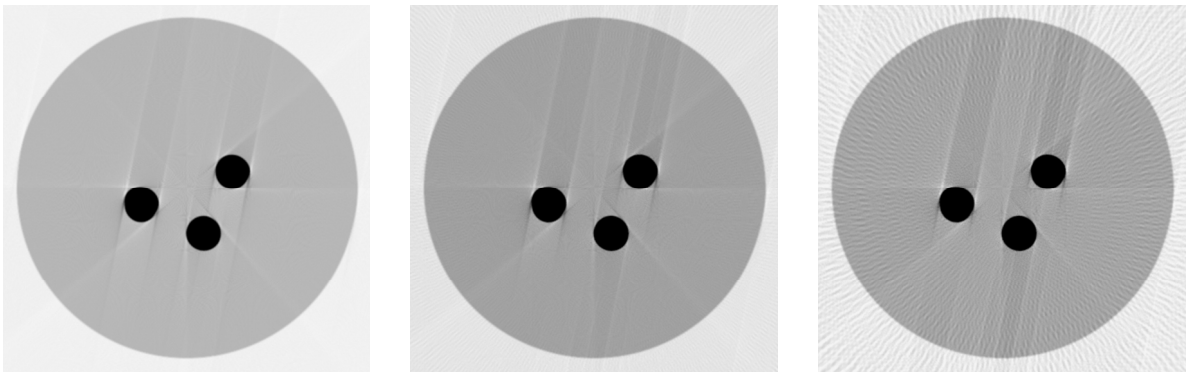

(a) (b) (c)

Figure 3.18: Impact of the number of scanning views on the image quality. Using 200 (a) or 100 (b) views, corresponding to an angle increments of 0,9° and 1,8° between the views, is enough to avoid aliasing artifacts to distort the image. When 50 (c) views are used, aliasing artifacts become clearly visible. This corresponds to an angle increment of 3,6°.

When using only 50 views aliasing artifacts arise. But although aliasing artifacts are always present due to the finite amount of detector elements and views, they are hardly visible and rarely pose serious limitations to the image quality.

3.3.3.5 Partial volume effect and the exponential edge-gradient effect

The limited size of the detector elements gives rise to the partial volume effect. The size of the detector elements is fixed for a given scanner and detector and can therefore not be optimized. With the simulator the detector element size can be decreased. This offers the possibility to assess the impact of the partial volume effect.

The exponential edge-gradient effect cannot be minimized either, as it is due to finite width of the beam. Again, its effect can be examined using the simulator. As explained in section 3.1.6, two simulation modes are available: intensity averaging and attenuation averaging. The standard simulation mode, intensity averaging, is realistic and includes the EEGE effect. Using attenuation averaging eliminates this effect. Figure 3.19 shows the simulation of the dolomite sample with pyrite inclusions in both modes. As no difference is visibly, a subtraction of both reconstructed images is also given. The simulations are monochromatic and no scatter and noise are included.

The EEGE effect arises most strikingly at edges of high contrasting objects. This can be seen in the subtracted image where the contours of the edges are visible. Although these edges are clearly visible, these errors are relatively small: circa 3% of the contrast between the pyrite and the dolomite. Furthermore the edge-gradient effect creates noise due to the errors that are induced at the edges.

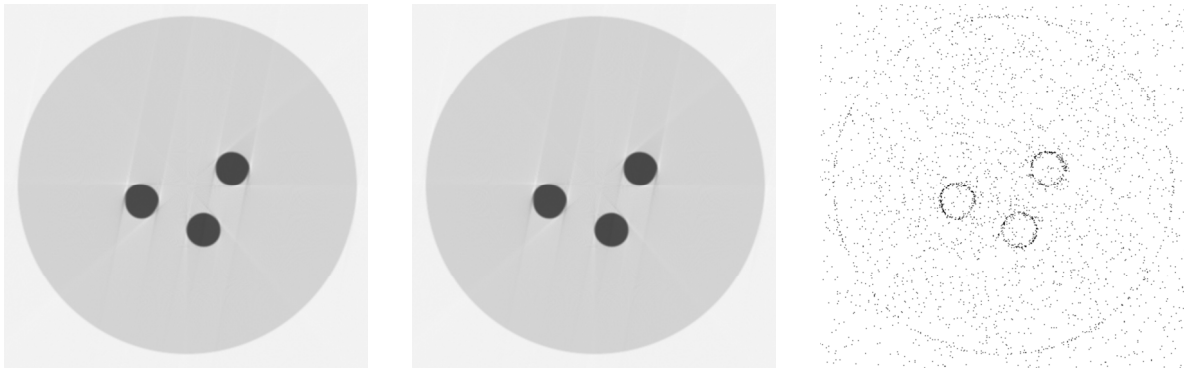

(a) (b) (c)

Figure 3.19: Monochromatic, scatter-free simulations of a dolomite sample with pyrite inclusions using intensity averaging (a) and attenuation averaging (b). In the first simulation the edge-gradient effect is included while this effect is eliminated in the second simulation. As the effect on the image is not visible, a subtraction of both simulations is given in (c). The contours of the edges are clearly visible in the subtracted image.

3.3.3.6 Optimization case

A rather basic, yet very representative case of image optimization using the simulator is demonstrated in this section. To that purpose a dolomite sample with calcite veins is considered. A picture of this sample is shown in figure 3.20a. The grey values have no physical meaning. The picture only illustrates the shape of both mineral phases. Distinguishing calcite from dolomite in CT images is often difficult as their attenuation coefficients are very similar (*Remeysen, 2007*). In this small case study acquisition parameters resulting in a satisfying contrast between the dolomite and calcite are determined with the aid of the simulator.

A first, polychromatic simulation is performed using 1 integration frame and no filters (figure 3.20b). The calcite veins have almost completely disappeared in the noise of the image. Therefore another simulation was performed using 16 integration frames reducing the noise by a factor 4. As can be seen in figure 3.20c, the noise level has decreased significantly and the contrast has increased.

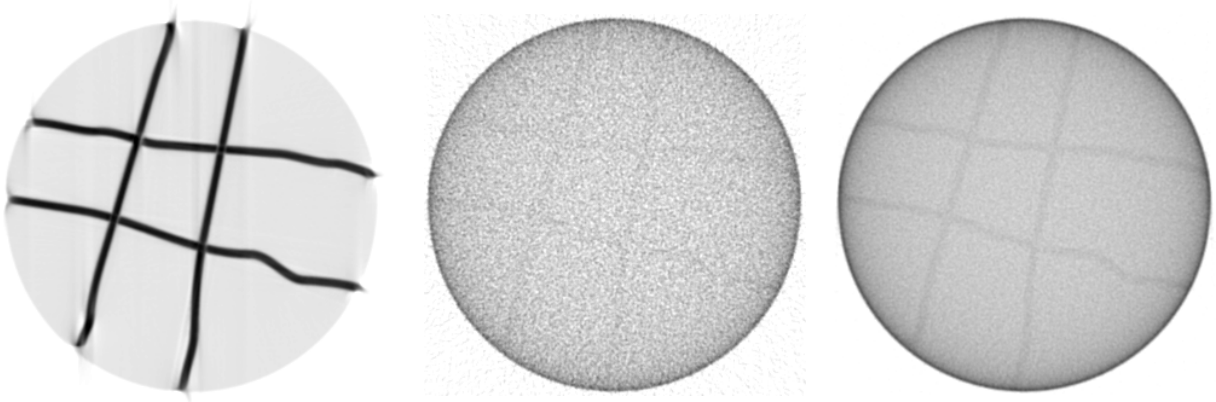

(a) (b) (c)

Figure 3.20: Polychromatic simulations performed on a dolomite sample including calcite veins. (a) Picture of the sample: the matrix material is dolomite and the veins are calcite. (b) Simulation using 1 integration frame. Because of the high level of noise the veins are hardly visible. (c) Using 16 integration frames reduces the level of noise by a factor 4. The reduction in noise results in a better contrast between the dolomite and calcite.

Another factor affecting the contrast is beam hardening. Beam hardening causes cupping which is clearly visible on the simulations (figure 3.20). By performing a monochromatic simulation beam hardening is eliminated. A monochromatic simulation is shown in figure 3.21a. It is performed at the mean effective energy of the polychromatic simulations and using 16 integration frames to reduce the noise level. No cupping artifacts can be seen and the contrast has increased. In synchrotron scanners it is possible to generate monochromatic X-rays and perform monochromatic measurements. This is not possible in standard CT scanners. Although beam hardening cannot be avoided, it can be minimized. One approach is using hardware filters. Low energies are partly absorbed by the filter material and hence beam hardening is reduced (cf. section 2.3.3.3 and 3.3.3.3). Figure 3.21b shows a polychromatic simulation where a 0,01 mm thick copper filter is used. The beam hardening is reduced and the veins become more visible. Filters however have the disadvantage of reducing the intensity of the beam and thus reducing the signal-to-noise ratio. When a copper filter of 0,1 mm is used (figure 3.21c), the noise level has increased and the contrast is reduced so radically that the calcite almost completely disappears in the noise.

Using a hardware filter reduces beam hardening and increases the noise level. Both have an opposite effect on the contrast. The simulator offers a useful tool to determine the optimal thickness as demonstrated by the above example. The acquisition parameters and scanning conditions can easily be changed with the simulator. Moreover the simulator enables generating a lot of measurements in a short period of time. This makes it possible to test a wide variety of scanning conditions.

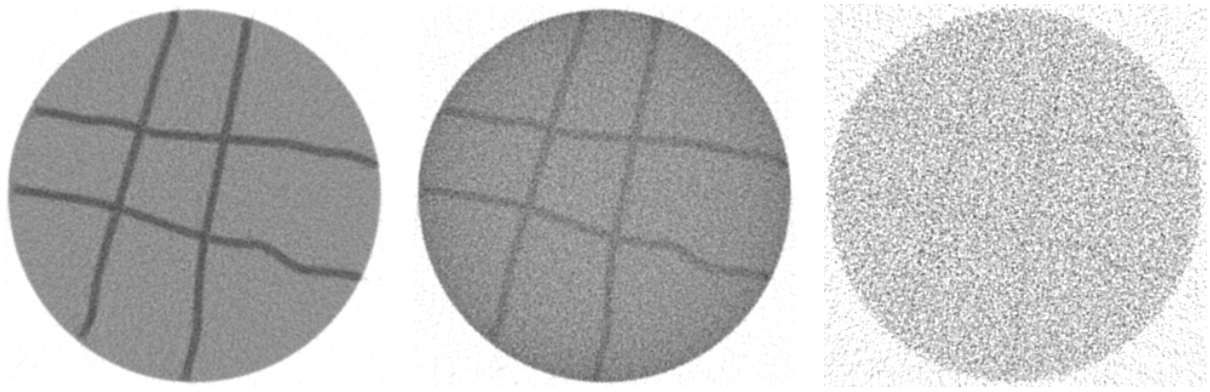

(a) (b) (c)

Figure 3.21: These illustrations of the simulations, all using 16 integration frames, demonstrate the effect of beam hardening on the contrast between the dolomite and calcite. (a) Monochromatic simulation where beam hardening is absent. Comparing to a similar, but polychromatic simulation (figure 3.20c) clearly shows the negative effect of beam hardening on the contrast. (b) Polychromatic simulation using a 0,01 mm copper filter. The filter reduces the beam hardening and hence increases the contrast. (c) Polychromatic simulation using a 0,1 mm copper filter. The filter reduces beam hardening, but also the signal-to-noise ratio. Using this filter increases the noise so drastically that calcite veins are hardly visible.

3.4 Optimization of CT image quality of the test samples

The purpose of the CT images of the samples is to be able to extract an image of the pore space of these samples. The next chapter deals with the extraction of the pore space from the CT image. Obviously, the quality of the CT images affects the accuracy of the pore space images. In this section the simulator is used to optimize the quality of the CT images of the test samples. Completely eliminating these limitations is not possible. In the next chapter the magnitude of the limitations that are inevitably induced are examined and quantified.

The simulations are performed in 2D as the phenomena that are examined can as well be treated in 2D as in 3D. The spatial resolution that can be achieved is a characteristic of the scanning system (focal spot size, detector element size, fluorescent screen) and cannot be optimized. The simulator can however still be used to assess the error made due to the limited spatial resolution. This is demonstrated in section 4.2.5.

Basically, the acquisition parameters have to be chosen in such a way that the contrast is maximized and beam hardening is minimized. For a given sample composition and structure, the contrast and the presence of beam hardening artifacts are determined by the tube voltage and the eventual use of filters. First a filter set-up is selected to minimize beam hardening. Hereto, two spherical 2D samples of 40 mm in diameter are constructed. The first sample is composed of concrete[15] while the second is composed of limestone. Simulations at a tube voltage of 90 kV are performed on these samples using respectively no filter and a 0,01 mm thick copper filter. Noise is not considered to be a limiting factor as it can be decreased by increasing the number of integration frames. Twenty-five integration frames are used in the scans and simulations. The simulations are given in figures 3.22 and 3.23.

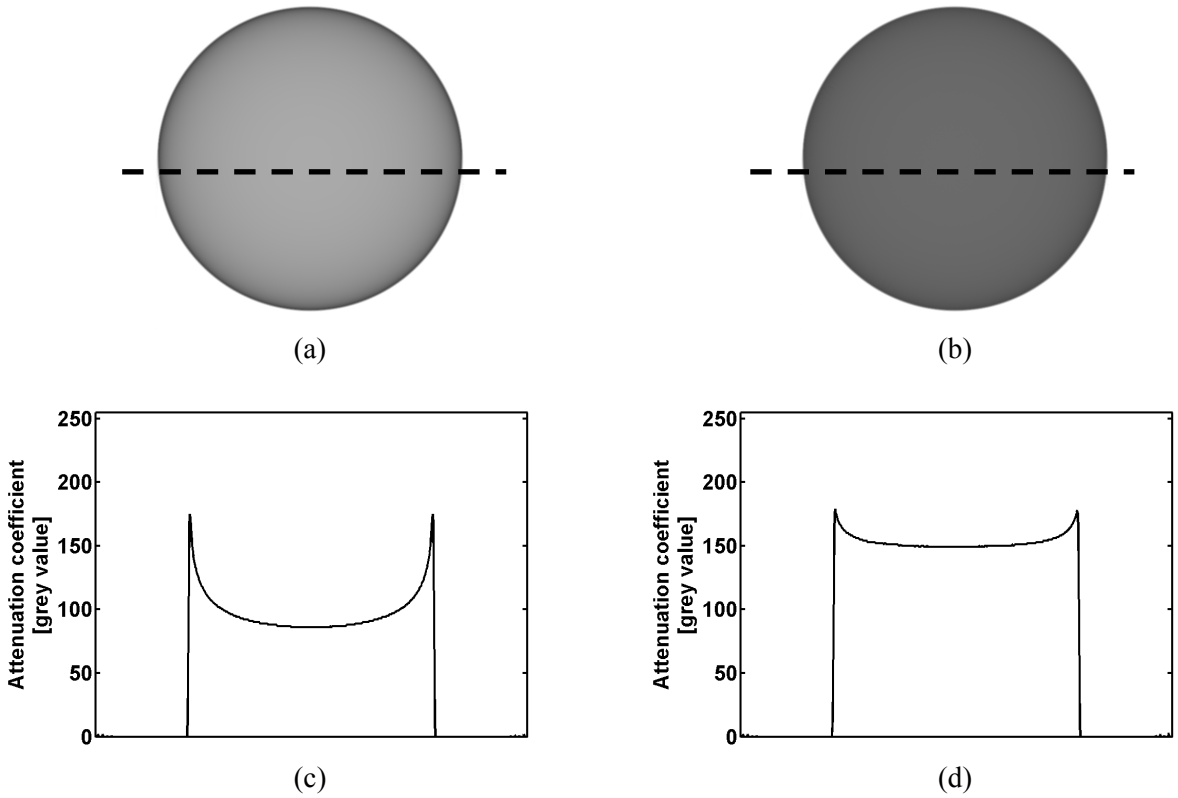

Figure 3.22: (a) Simulated 2D section of a circular pavestone sample (40 mm in diameter) at 90 kV without using a filter. Cupping artifacts due to beam hardening are visible. This cupping effect is more obvious on a profile through the centre of the sample (dashed line) (c). (b) Simulated 2D section using a 0,01 mm copper filter and profile through the centre of the sample (dashed line) (d). The cupping effect is minimized by the filter.

[15] As the exact composition of the pavestone sample is unknown, a common type of cement is used to describe the material composition. The composition used consists of 56% C_3S, 20% C_2S, 10% $3CaO.Al_2O_3$, 7% $4CaO.Al_2O_3.Fe_2O_3$, 3% MgO, 3% SO_3 and 1% CaO. No quartz granulates are taken into account. The attenuation of this material is computed by equations (3.7) and (3.8). The attenuation spectra for the different chemical elements are obtained from http://physics.nist.gov/PhysRefData/XrayMassCoef/tab3.html

Beam hardening has significantly been reduced by using a 0,01 mm thick copper filter. It is therefore chosen to use such a filter when scanning the samples.

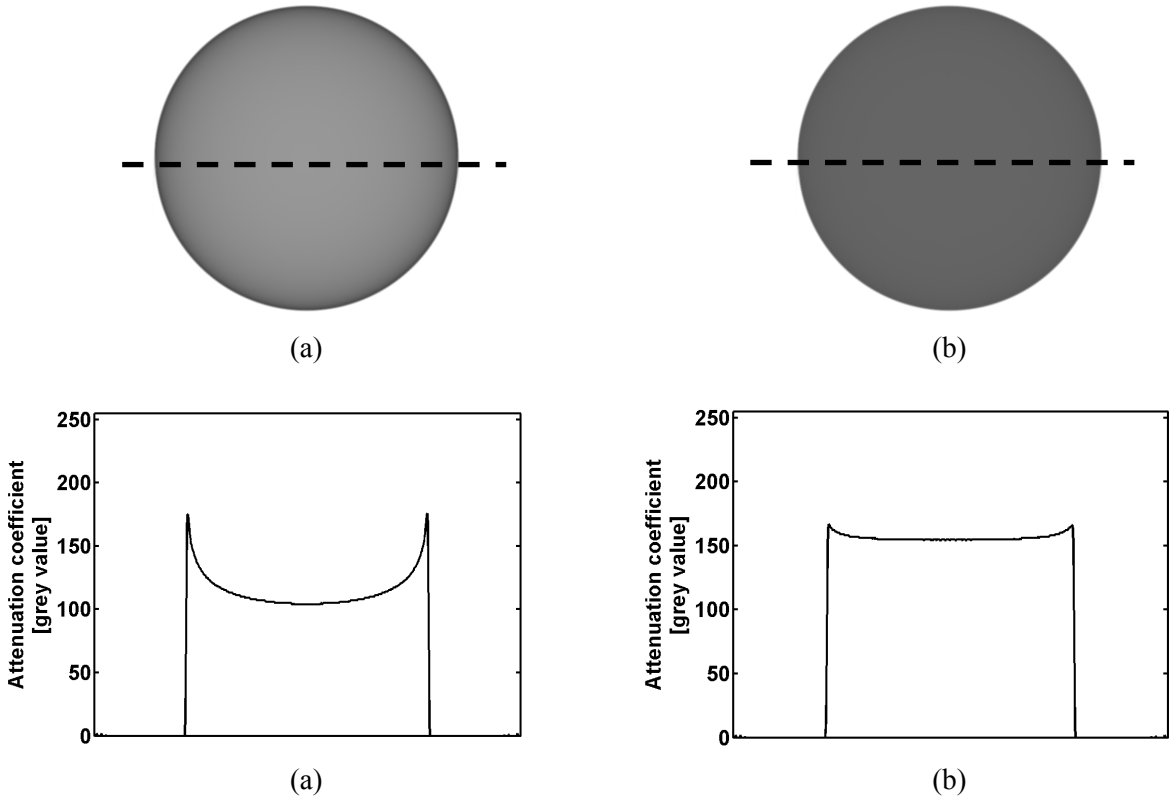

Figure 3.23: (a) Simulated 2D section of a circular limestone sample (40 mm in diameter) at 90 kV without using a filter. Cupping artifacts due to beam hardening are visible. This cupping effect is more obvious on a profile through the centre of the sample (dashed line) (c). (b) Simulated 2D section using a 0,01 mm copper filter and profile through the centre of the sample (dashed line) (d). The cupping effect is minimized by the filter.

The impact of the tube voltage on the contrast is investigated by performing simulations at different tube voltages on two samples including circular air-filled pores of different sizes. A 0,01 mm copper filter is included in these simulations. The simulations for both samples at tube voltages of 60 kV, 90 kV and 120 kV are shown in figures 3.24 and 3.25.

The X-ray spectrum at 60 kV is attenuated too much by the copper filter and by the sample. The X-rays are completely attenuated and therefore contain no information on the internal composition of the sample. The spectra at 90 kV and 120 kV provide CT images on which pores are visible. The contrast between the pores and the sample material is higher for a 90 kV spectrum. The 120 kV spectrum contains a larger fraction in high energy photons. This fraction however hardly interacts with the material and does therefore not contribute to the distinction between the pores and the matrix material. Table 3.7 and 3.8 contain the resulting contrasts of the pores of different sizes for both samples. The contrast is defined by formula (2.10). As the pores are not visible on the CT images taken at 60 kV, no contrast can be computed for these images.

Based on these simulations, it is decided to perform the X-ray scans at a tube voltage of 90 kV and to use a 0,01 mm copper filter to reduce beam hardening.

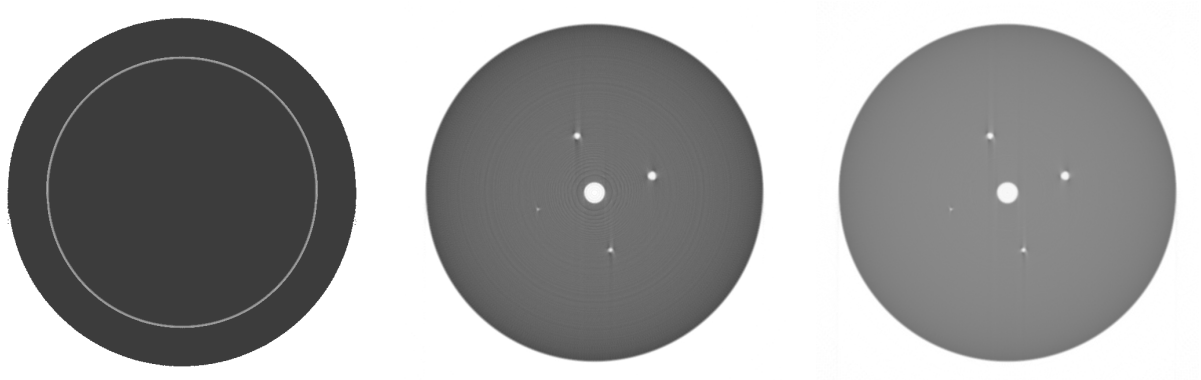

(a) (b) (c)

Figure 3.24: Simulations of a circular pavestone sample (40 mm in diameter) at different tube voltages: (a) 60 kV; (b) 90 kV; (c) 120 kV. A 0,01 mm copper filter is included to minimize beam hardening. The sample contains 5 circular pores of different sizes (50 µm (west), 100 µm (south), 150 µm (north), 200 µm (east) and 500 µm (centre)).

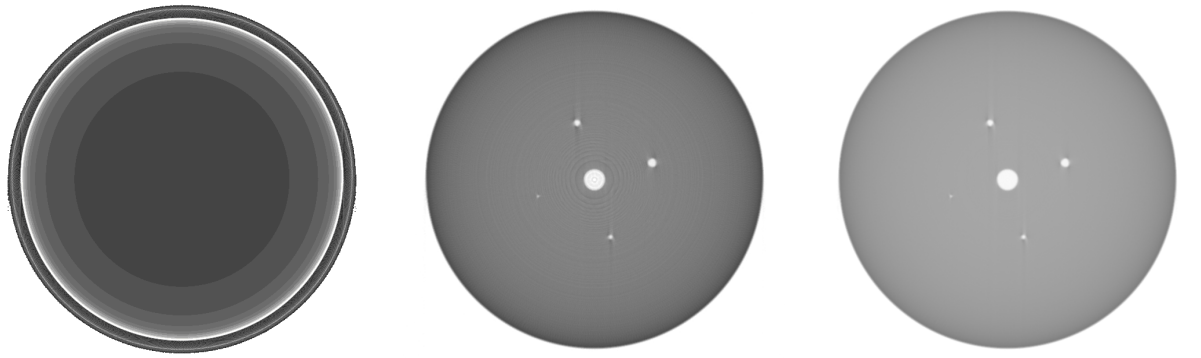

(a) (b) (c)

Figure 3.25: Simulations of a circular limestone sample (40 mm in diameter) at different tube voltages: (a) 60 kV; (b) 90 kV; (c) 120 kV. A 0,01 mm copper filter is included to minimize beam hardening. The sample contains 5 circular pores of different sizes (50 µm (west), 100 µm (south), 150 µm (north), 200 µm (east) and 500 µm (centre)).

diameter pore [µm]	**contrast pavestone [%]**						
	60 kV	**70 kV**	**80 kV**	**90 kV**	**100 kV**	**110 kV**	**120 kV**
50	-	15.5	46.7	45.8	44.8	43.2	42.0
100	-	20.1	85.8	85.2	84.8	84.5	84.1
150	-	31.2	95.5	94.4	93.8	92.8	92.3
200	-	37.0	97.4	96.6	94.7	93.8	92.5
500	-	45.6	100.0	100.0	99.2	97.2	95.7

Table 3.7: Contrast of circular pores of different sizes in a pavestone sample as a function of the tube voltage. The contrast is calculated by using formula (2.10).

diameter pore [μm]	contrast limestone [%]						
	60 kV	70 kV	80 kV	90 kV	100 kV	110 kV	120 kV
50	-	12.5	45.0	44.3	43.0	41.2	40.6
100	-	18.4	83.0	81.8	81.0	80.0	79.5
150	-	28.2	91.0	90.5	89.6	88.0	87.6
200	-	35.0	92.3	91.2	90.8	89.8	89.3
500	-	43.0	100.0	100.0	97.8	95.1	93.3

Table 3.8: Contrast of circular pores of different sizes in a limestone sample as a function of the tube voltage. The contrast is calculated by using formula (2.10).

3.5 Conclusions

A CT simulator is developed and presented. The simulator allows changing nearly every parameter or phenomenon involved in the scanning process separately and in that way it offers a tool to examine their effect on the final CT images. Not only can every parameter be changed, a lot of simulations can be performed in a relatively short time. The 2D simulations shown in this chapter generally took only a few minutes. This makes it possible to perform trial-and-error experiments which are useful to look for acquisition parameters or a scanning setup that result in images with an optimal quality. Moreover the impact of certain parameters or phenomena can be assessed.

The simulator is based on the work of De Man who developed a 2D simulator to examine metal artifacts in medical scans (*De Man, 1999 and 2001*). Beside some adaptations and extensions to his simulator, also a 3D simulator was built. The principle behind the simulator is very simple. The intensities of all rays going from the source to the detector elements are computed. This was first performed for monochromatic X-rays and an infinitesimally small source and infinitesimally small detector elements. Subsequently this basic and theoretical case is extended to polychromatic rays and to a source and detector elements with finite sizes. This extension is done by sampling the X-ray spectrum and the source and detector elements.

Important is the way objects are constructed in the simulator. They are defined as the superposition of a number of object parts, each with its own size, position, composition and resolution. This superposition approach has the advantage that, for instance, a smaller part can be simulated very accurately by using a lot of pixels while relatively few pixels are used for the bigger parts. In that way computation time is saved. Moreover, this approach makes it possible to increase the number of simulated energies with only marginal increase in computation time.

Subsequently, additional features are implemented. The effect of hardware filters is simulated by adjusting the intensity and spectrum emitted by the X-ray source. Also the exponential edge-gradient effect can be switched on or off by using two different simulation modes. An eventual non-linearity of the detector and the impact of the fluorescent screen are included by respectively applying a polynomial and a convolution on the sinogram. Simulating noise is complicated as noise has different sources. Simulating these processes and assigning a weight to each process is very complicated. Therefore a pragmatic noise model is implemented. Eventual autocorrelation in the noise was roughly simulated by importing an extra parameter n (degree of interpolation) to the model. Scatter is simulated by adding a constant scatter profile to the sinogram. Also here more accurate models or approaches could be opted for, but they demand much computation power.

After the development and the implementation of the simulator, it is adjusted to a Skyscan 1072 Desktop μCT scanner. For that purpose the linearity of the detector, the X-ray spectrum, level and eventual autocorrelation of the noise, the impact of the fluorescent screen and the geometrical

parameters of the μCT scanner were measured or determined. The amount of scatter is not measured as this cannot directly be done. The implemented noise model appeared to underestimate the noise by a factor of approximately 2,4 to 3,4. This is most probably due to simplifications such as the assumption that the preamplifier noise can be neglected. Beside this underestimation, the noise model was able to simulate the behaviour of the noise in real CT images. Therefore, the proposed model is maintained and the noise generated in simulations is multiplied by a factor lying between 2,4 to 3,4.

The use of the simulator is demonstrated by performing several experiments. The impact of the fluorescent screen on the spatial resolution and the effect of the tube voltage on the contrast are illustrated. Also scatter and beam hardening artifacts were simulated. As both phenomena result in similar artifacts, the impact of scatter is assessed using monochromatic simulations. Beam hardening artifacts are shown in polychromatic simulations without scatter. The simulator thus makes it possible to examine both effects separately and in that way their individual impact can be investigated. Furthermore also other artifacts as aliasing and the exponential edge-gradient effect were illustrated. In a small case of image optimization it is shown how filtration gives rise to two effects: a minimization of beam hardening and a decrease in signal-to-noise ratio. Both effects have an opposite impact on the contrast. By trial-and-error using different filter thicknesses, a good filter setup can be determined.

Finally the simulator is used to optimize the acquisition parameters for the scanning of the test samples. A 0,01 mm copper filter was selected to minimize beam hardening and a tube voltage of 90 kV appeared to be resulting in the highest contrast between the pore space and the solid material. Twenty-five integration frames were used to reduce the level of noise.

Beside in optimization cases, the simulator is also useful to assess whether or not X-ray computed tomography is suitable for a given application. This is done in appendix D where the applicability of X-ray CT in measuring the gold content of rock samples is investigated. Gold is a very attenuating material and can thus easily be detected in CT images. Therefore X-ray computed tomography might be a useful technique to obtain a quick indication of the gold content. Several other techniques exist to measure the gold content in rock samples like fire assaying or geochemical analyses. But these techniques are difficult to perform and CT measurements are often performed faster and more easily. The simulator is used to assess the suitability of X-ray CT for this application. The impact of several phenomena on these measurements can be assessed very well as these phenomena can be examined separately. Moreover, a lot of simulations can be performed in a relatively short time and the input material in the simulator is exactly known. This is not always so when real samples are used and it facilitates a comparison between the measured and the real gold content.

4. Image segmentation

A segmentation is applied to convert the grey-scale CT images into binary images of the pore space. Obviously, this is a crucial step in the assessment of the permeability. When an incorrect image of the pore space is obtained, the modelling of the fluid flow through the sample will also be incorrect.

A segmentation is applied in many applications and the performed segmentation largely determines the quality of the subsequent analysis or computations. Often, a small change of the segmentation parameters considerably affects the outcoming result (*Hara et al., 2002*). This chapter is concerned with the selection of a segmentation method suitable for its purpose in this research. No method with globally relevance and applicability however exists. The recommended segmentation method and its optimal segmentation parameters depend on the material used, the application and the quality of the images (*Otsu, 1979; Ding et al., 1999*).

A segmentation method is first selected and applied and the chosen methodology is then validated. This is done with the assistance of the 3D CT simulator.

4.1 Selection and evaluation of the segmentation method

The CT images are converted into binary images by applying a threshold method using a global threshold value. Pixels with a grey value lower than the threshold value are considered to be pore pixels while the other pixels are considered to be matrix material. The threshold value is determined by matching the porosity of the thresholded image to the porosity measured in the laboratory.

4.1.1 Segmentation method

The CT images of the samples are obtained using 25 frames to reduce the noise level and a 0,01 mm copper filter to minimize beam hardening. A global threshold value is then selected to match the porosity of the thresholded images to the porosity measured in the laboratory (table 2.1). The porosity determined in the laboratory, the selected threshold value and the resulting porosity of the thresholded image are summarized in table 4.1. Only open porosity is considered. The open porosity in the thresholded image is determined by checking whether or not the pores are connected to the inlet and outlet of the sample. The closed porosity in the thresholded image is also determined and given in table 4.1. It appears that the limestones contain a larger fraction in closed porosity than the pavestones where the bulk of the pore space is open.

	porosity measured in laboratory [%]	**threshold value [grey value]**	**open porosity of the thresholded image [%]**	**closed porosity of the thresholded image [%]**
pavestone A	24,9	60	24,8	25,1
pavestone B	19,5	48	19,5	20,1
limestone A	15,5	58	15,4	19,4
limestone B	13,3	62	13,3	19,9

Table 4.1: The porosity of the samples is first measured in the laboratory. Subsequently a global threshold value is defined so that the porosity of the thresholded image matches the measured porosity. The grey values in the CT image ranges from 0 to 255.

4.1.2 Shortcomings of the selected segmentation method

An error is made by when matching the porosity of the thresholded image to the porosity measured in the laboratory. Pores that fall below the resolution of the imaging system are not detected in the CT images. Consequently these do not contribute to the porosity of the thresholded image. But they do contribute to the porosity measured in the laboratory. This implicates that the larger pores in the thresholded image compensate for the smaller pores that are not detected. Thus the obtained image of the pore space differs from the correct image of the pore space: the size of pores larger than the image resolution are overestimated (**error 2: threshold value error**) and the pores smaller than the resolution are absent. The latter error is the "error 1: resolution error" discussed in section 2.5. Both errors will be more important for the limestone A sample than for the limestone B sample (cf. section 2.5; figure 2.20) as a larger fraction of the pore space of the first sample falls below the image resolution.

Thus determining the threshold value by matching the porosity of the thresholded image to the porosity measured in the laboratory, introduces an error. This is an error related to the choice of the one threshold value which is not completely correct. But also the segmentation procedure of using one global threshold value itself has some shortcomings and introduces some errors (**error 3: segmentation error**). These are mainly the result of the limited resolution of the imaging technique. The resolution is in first instance limited by the finite voxel size. In most µCT scanners the voxel size is in the order of tens of micrometers. Objects smaller than the voxel size only partly fill the voxel volume. Their reconstructed attenuation coefficient is the weighted average of the attenuations coefficients of all the substances present in the voxel. This is called the partial volume effect (cf. section 2.3.3.5) (*Robertson and Huang, 1986; Wellington and Vinegar, 1987; Johns et al., 1993; Ketcham and Carlson, 2001*).

Secondly, non-idealities of the CT acquisition process as the finite size of the source and the impact of the fluorescent screen and optical lens result in a blurring of the image. This blurring can mathematically be expressed by a point-spread function (PSF) (cf. section 2.3.1). Because of the blurring of the pore edges different threshold values result in different estimations of the dimensions of the pore, as shown in figure 4.1.

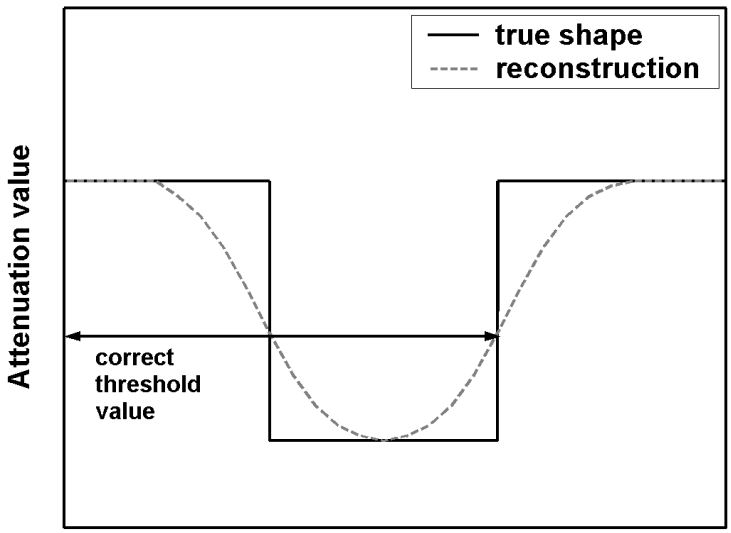

Figure 4.1: Attenuation profile of a pore (solid line). In the reconstructed CT image the edges of the pore are smeared out (dashed line). Different threshold values result in different estimations of the pore size. The threshold value resulting in a correct estimation of the pore size is also shown on the figure.

When the pore is smaller than the PSF, not only the edges are smeared out, but there is also a decrease in attenuation in the pore. A threshold value that correctly determines the dimensions of a pore bigger than the PSF, underestimates the size of a pore smaller than the PSF. This is illustrated in figure 4.2.

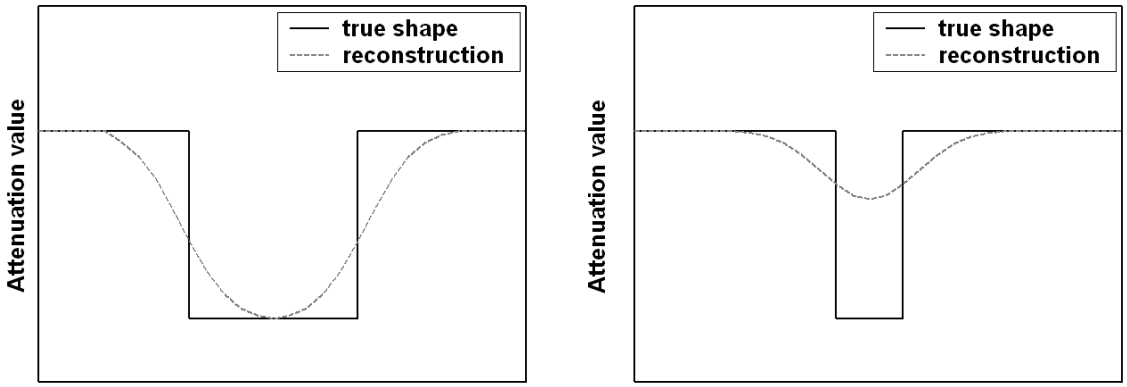

(a) (b)

Figure 4.2: Effect of the PSF on a pore bigger (a) and a pore smaller (b) than the PSF. Pores bigger than the PSF are smeared out, but their bottom value remains the same. Pores smaller than the PSF are not only smeared out, but their bottom valley is also higher. This complicates the use of one global threshold value as different pore sizes require different threshold values.

Thresholding is also affected by beam hardening and the heterogeneity of the sample. Due to beam hardening and an eventual heterogeneity of the sample the reconstructed attenuation value of the matrix material is not constant. Pores at the edge therefore require different threshold values than pores at the centre of the sample (figure 4.3).

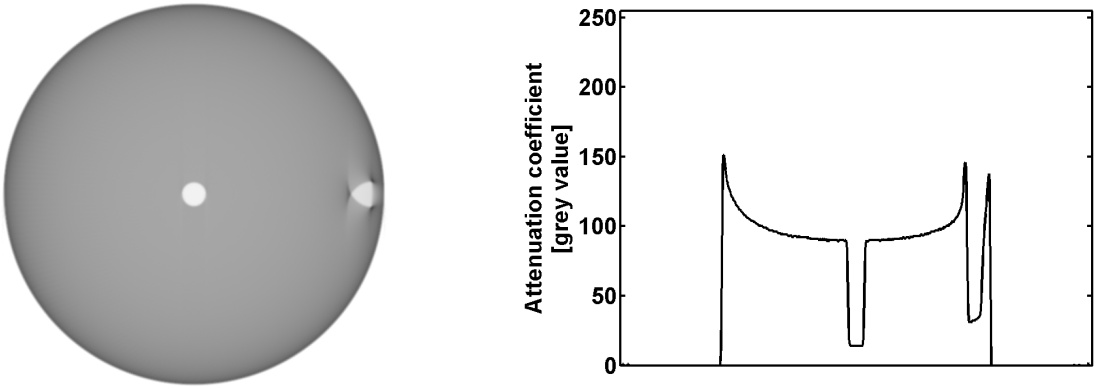

Figure 4.3: Beam hardening results in cupping artifacts. The centre of the object is brighter than the edges. This implies that the threshold value that correctly determines the dimensions of the pores is different in the centre than near the edges of the object.

Noise in the CT image evidently also distorts the thresholded results (*Vandersteen et al., 2003*). Furthermore the exponential edge-gradient effect (EEGE) can hinder the threshold procedure (cf. section 2.3.3.5). The EEGE effect gives rise to errors which are most pronounced at sharp edges of high contrast. As thresholding deals with the recognition of these edges, it might be affected by this artifact.

The impact of noise, beam hardening, the EEGE effect and the limited resolution on the threshold approach is examined more quantitatively in the next section where the threshold procedure is validated.

4.2 Validation of the threshold method

For the validation of the threshold method and the determined threshold values, the 3D simulator is used. The simulator enables manipulating all parameters in the scanning process. Moreover, the object used in the simulations is exactly known. This makes it possible to compare the thresholded image to its original image.

To be able to simulate the scanning of the pavestone and limestone sample, objects similar to those samples have to be constructed. The pixel size of the CT images acquired was 95 µm. It is possible to achieve a higher resolution (i.e. smaller pixels than 95 µm) with the simulator, but this is of course useless if the object that is simulated has a pixel size of 95 µm. In order to obtain an image with a smaller pixel size and which still is representative for the samples used here, a smaller part of the sample (a region of interest (ROI) of 20 mm in diameter and 20 mm long) of both samples is scanned at a resolution of 30 µm. The CT image of this smaller piece of the sample is thresholded using the threshold values of table 4.1. It is this thresholded object that will be used as input in the following simulations (sections 4.2.2 to 4.2.5). In these sections the input sample is simulated and subsequently thresholded. The porosity of the thresholded image is compared to the porosity of the input image. In that way the impact of different parameters and phenomena involved in the scanning process (noise, beam hardening, the EEGE effect and the resolution) on the threshold procedure are assessed. As the input object for these simulations is derived from a smaller piece of the original samples, its porosity is not equal to the porosity of the original sample. Table 4.2 contains the porosities of the samples used as input for the simulator in the subsequent sections.

	porosity [%]
artificial pavestone	24,94
artificial limestone	14,86

Table 4.2: The porosity of the artificial pavestone and limestone samples that will be used as input for the simulations used for evaluating the threshold procedure.

The explained procedure is shown in figure 4.4: a smaller piece of the sample (A) is scanned at a higher resolution and thus a CT image with a smaller pixel size (B) is acquired. This CT image is then thresholded using the threshold values of table 4.1. In that way, an artificial sample (C) similar (but not equal) to the test sample is acquired. The artificial sample has a higher resolution than the scanned and simulated image (95 µm) and an improvement of the resolution in these simulations now makes sense. The subsequently simulated image (D) is again thresholded (E). The finally obtained, thresholded image (E) has to be compared to the simulator input (C) being the thresholded image of the smaller sample.

First the sensitivity of the porosity to the threshold value is evaluated. The sensitivity of the permeability to the threshold value is evaluated in section 6.4.1. Subsequently, the simulator is used to quantify the errors that result from noise, beam hardening, the EEGE effect and the limited resolution. This allows assessing the magnitude of these errors. The validation is demonstrated for the pavestone A and limestone A samples.

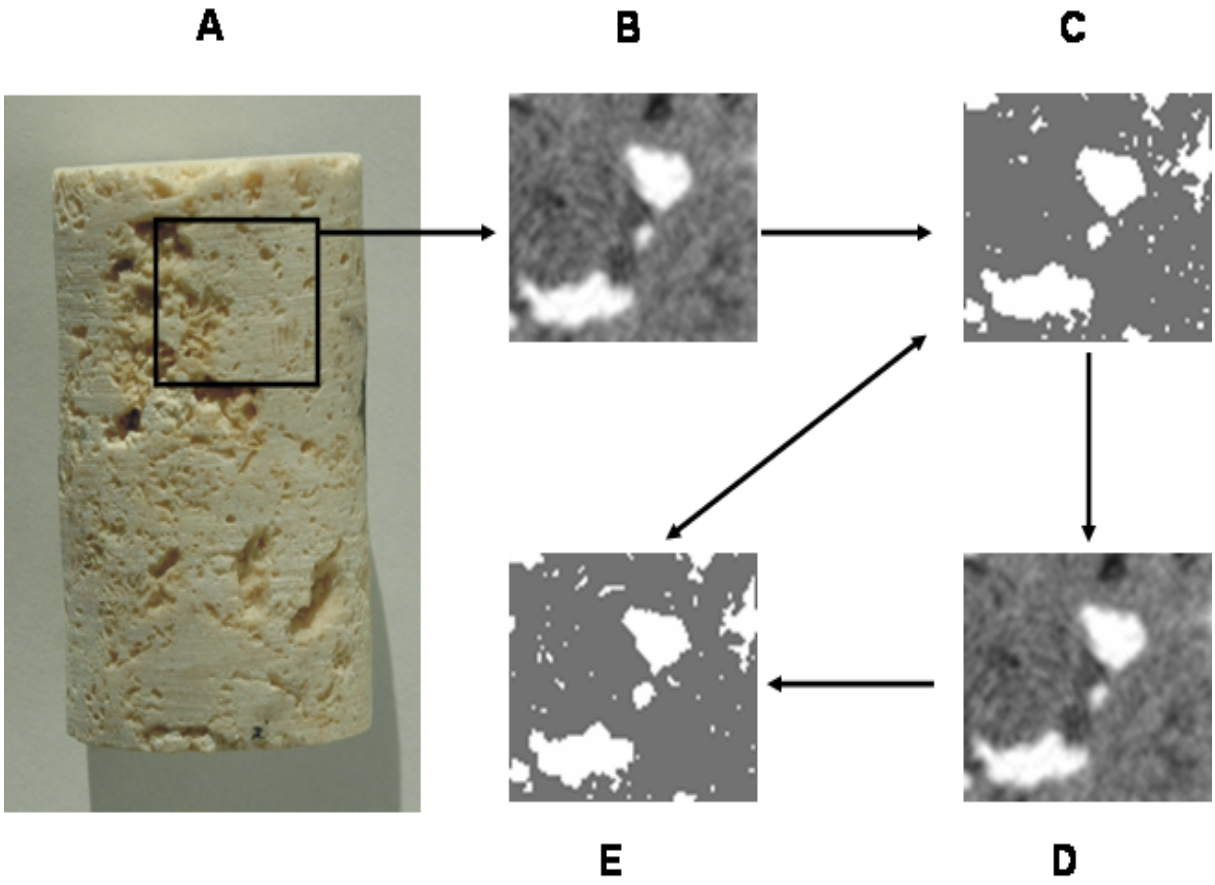

Figure 4.4: A smaller piece (20 mm in diameter and 20 mm long) of the sample (A) is scanned at a resolution of 30 µm. The obtained CT image (B) is thresholded using the threshold value given in table 4.1. A sample similar (but not equal) to the test sample is thus created (C). This artificial sample is used in the simulations. The simulated images (D) are again thresholded (E). This finally obtained image (E) has to be compared to the image that is used as input for the simulator (C).

4.2.1 Sensitivity of the porosity to the threshold value

The porosities of the thresholded pavestone and limestone samples are computed for different threshold values. The results are plotted on figure 4.5 for both samples together with their derivatives. The formerly determined global threshold values of 60 for the pavestone and 58 for the limestone (table 4.1) lie in the region where the change in porosity is relatively small.

Table 4.3 illustrates the impact of the threshold value on the porosity of the thresholded image for the pavestone A and limestone A sample.

A change of 5 units in the threshold value results in an absolute change in porosity of circa 2% for the pavestone and circa 1,5% for the limestone sample.

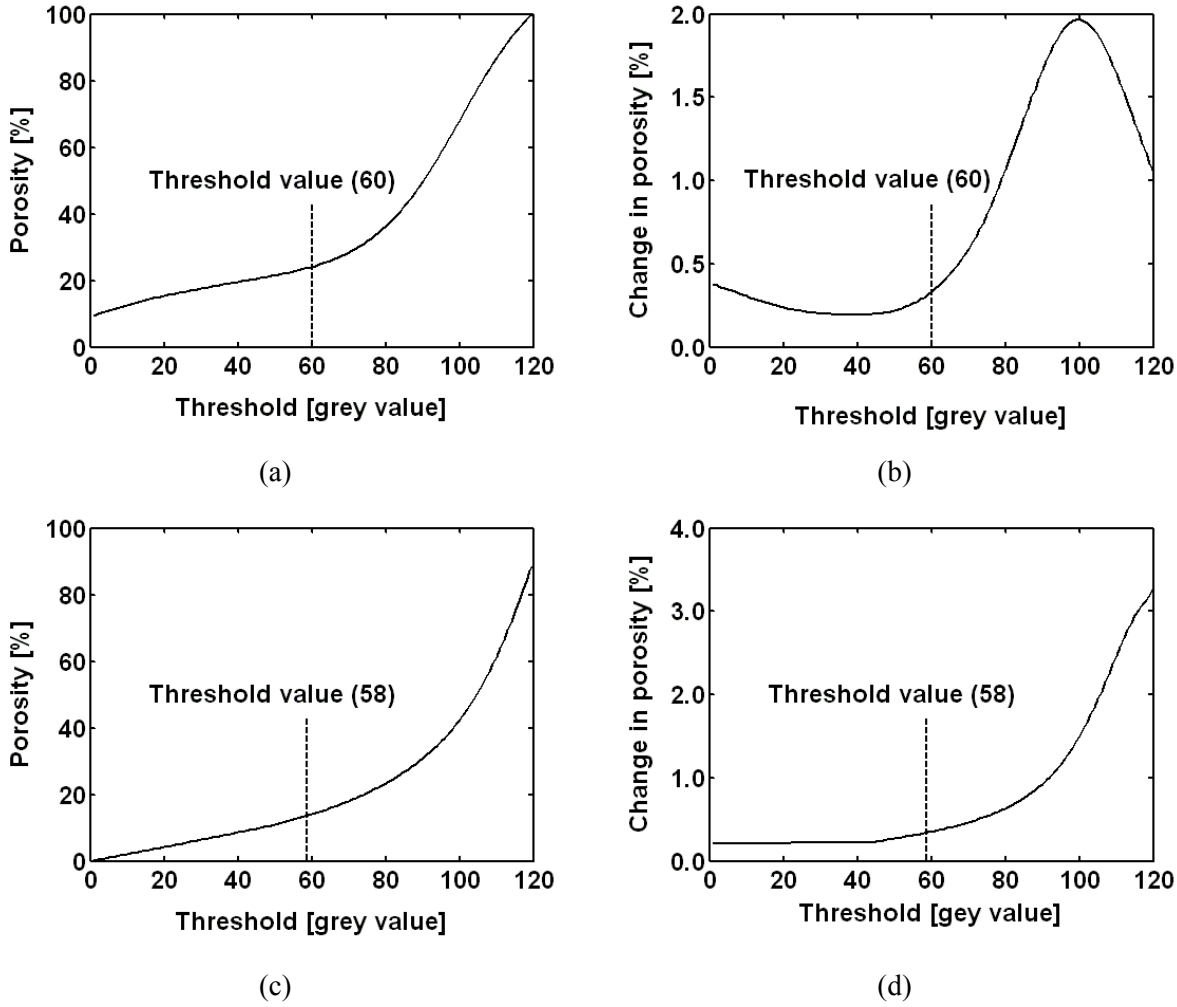

Figure 4.5: Porosity of the thresholded pavestone (a) and limestone (c) sample over the used threshold value. The derivatives of these curves are shown in (b) and (d) respectively. The global threshold values determined in the previous section lies in the region where the porosity change with changing threshold value is relatively small.

pavestone A		limestone A	
threshold value [grey value]	**porosity [%]**	**threshold value [grey value]**	**porosity [%]**
55	23,2	53	13,7
56	23,5	54	14,0
57	23,8	55	14,4
58	24,1	56	14,7
59	24,4	57	15,1
60	24,8	58	15,4
61	25,2	59	15,9
62	25,6	60	16,2
63	26,0	61	16,7
64	26,4	62	17,0
65	26,9	63	17,5

Table 4.3: Sensitivity of the porosity of the pavestone and limestone sample in relation to the threshold value.

4.2.2 Impact of noise

The impact of noise on the thresholded image is examined by comparing noise-free simulations to simulations where noise is included. Both simulations are monochromatic and use a focal spot size of 1 µm and twice as much detector elements (resulting in a pixel size of 47,5 µm) and the fluorescent screen is not included. By doing so the spatial resolution is increased and thus the error that arises from the limited resolution is decreased. To eliminate the error due to the EEGE effect, the simulations are performed using attenuation averaging (cf. section 3.1.6). Table 4.4 contains the porosities for both simulations.

	porosity different from artificial pavestone sample [%]	**porosity different from artificial limestone sample [%]**
noise excluded	0,24	0,81
noise included (25 integration frames)	1,53	9,89

Table 4.4: Impact of noise on the porosity of the thresholded image for the pavestone and the limestone sample.

The porosity increased due to the presence of noise. Yet, the increase is relatively small. The porosity might however not be a good indicator for the error induced by noise. Some pore voxel can be recognized as solid due to noise and some solid voxels can be seen as pore voxels. Both can compensate for each other. Therefore the percentage of voxels that have changed from pore to solid and vice versa is taken as a measure for the error made by the noise. This amounted 0,34% for the pavestone sample and 0,63% for the limestone sample.

4.2.3 Impact of beam hardening

The simulations to assess the impact of beam hardening use attenuation averaging, a focal spot size of 1 µm and twice as much detector elements and the fluorescent screen is not included. The impact of beam hardening is examined by performing a monochromatic simulation, a polychromatic simulation without filtering and a polychromatic simulation using a 0,01 mm copper filter. The porosities of the thresholded simulations are given in table 4.5.

The porosity in the polychromatic simulation is higher than in the monochromatic simulation. By filtering the spectrum, beam hardening and the error it induces, are reduced. Plotting a profile through the samples gives an idea on the severity of beam hardening. This is shown in figure 4.6. A slice from the CT image of the limestone and pavestone is given together with a profile through the slice. The CT image is obtained from the polychromatic simulation using a 0,01 mm copper filter.

The attenuation in the CT images of both samples appears to be more or less constant. This indicates the absence of cupping artifacts caused by beam hardening. It can thus be expected that beam hardening does not seriously affect the thresholding procedure. This is also confirmed by the results in table 4.5.

	porosity different from artificial pavestone sample [%]	porosity different from artificial limestone sample [%]
monochromatic	0,24	0,81
polychromatic	7,55	9,69
polychromatic; 0,01 mm copper filter	0,56	1,28

Table 4.5: Impact of beam hardening on the porosity of the thresholded image for the pavestone and the limestone sample.

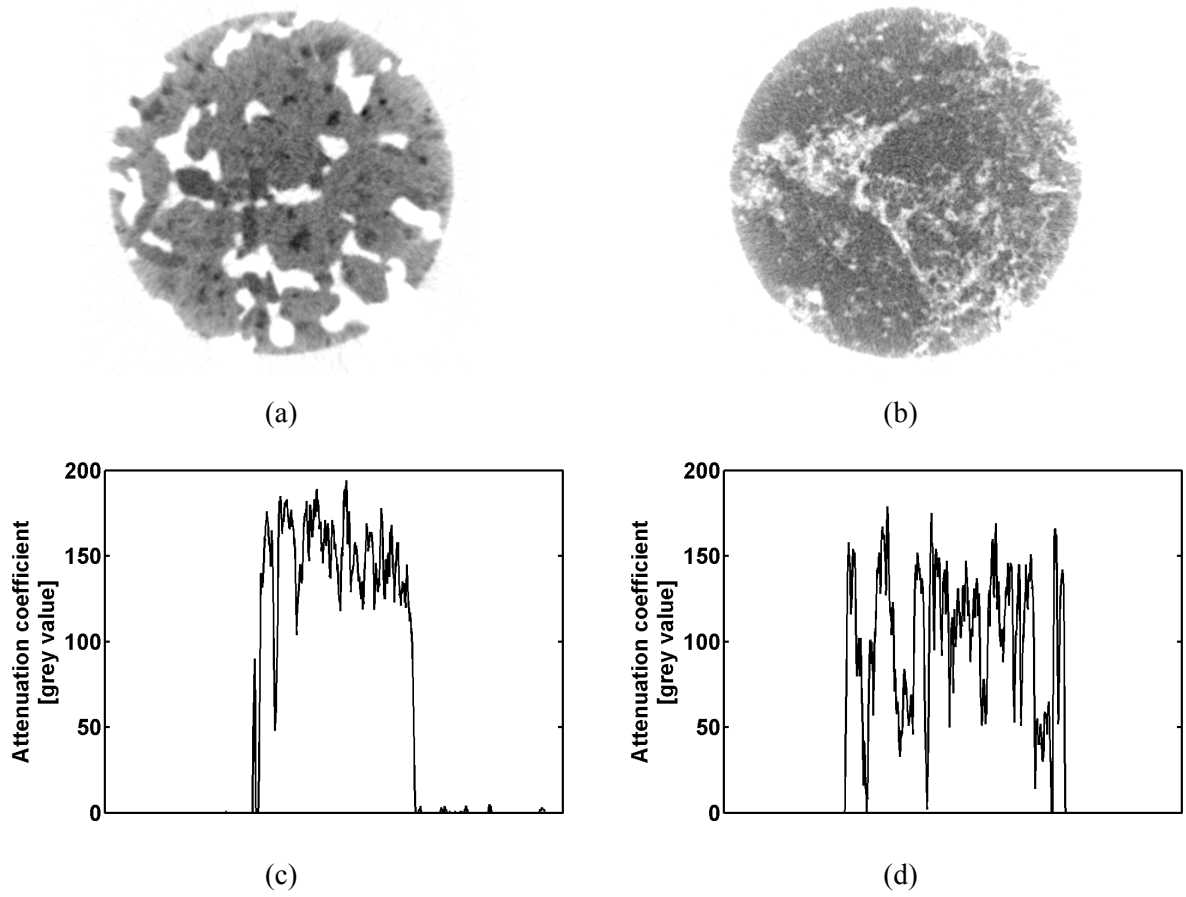

Figure 4.6: Slice from the CT image of the pavestone (a) and limestone (b) sample. The image is obtained from the polychromatic simulation using a 0,01 mm copper filter. The attenuation appears to be more or less constant in these slices. This can also be seen when a profile through the centre of the slices is plotted. No pronounced cupping can be seen.

4.2.4 Impact of the EEGE effect

The error induced by the EEGE effect is examined by comparing simulations using intensity and attenuation averaging. These simulations are monochromatic and again a focal spot size of 1 µm and small detector elements (resulting in a pixel size of 47,5 µm) are used and no fluorescent screen is included. Table 4.6 contains the resulting porosities for both samples and both simulations. The impact of the EEGE effect on the porosity of the thresholded samples is very limited.

	porosity different from artificial pavestone sample [%]	**porosity different from artificial limestone sample [%]**
attenuation averaging	0,24	0,81
intensity averaging	0,16	0,81

Table 4.6: Impact of the EEGE effect on the porosity of the thresholded image for the pavestone and limestone sample.

4.2.5 Impact of the limited resolution

Finally the effect of the spatial resolution is evaluated. Monochromatic simulations using attenuation averaging are performed. The first uses a focal spot size of 1 µm and small detector elements resulting in a pixel size of 47,5 µm. The fluorescent screen is not included in this first simulation. In the second simulation a realistic focal spot size of 60 µm and detector elements twice as big resulting in a pixel size of 95 µm are used. The fluorescent screen is included in the simulator by applying a convolution on the sinogram (cf. section 3.2.4). Table 4.7 contains the resulting porosities of these simulations.

	porosity different from artificial pavestone sample [%]	**porosity different from artificial limestone sample [%]**
focal spot size = 1 µm; pixel size = 47,5 µm; no fluorescent screen	0,24	0,81
focal spot size = 60 µm; pixel size = 95 µm; fluorescent screen	-2,01	-6,12

Table 4.7: Impact of the limited resolution on the porosity of the thresholded image for the pavestone and limestone sample.

The porosity of the pavestone obtained after thresholding is only slightly affected by lowering the resolution. The impact of the resolution is larger for the limestone where the porosity drops with almost 2% when a lower resolution is used. This can be explained by the presence of a larger fraction in small pores in the limestone compared to the pavestone.

Therefore these results should also be treated with caution. As mentioned, the estimated size of the small pores is much more affected by the limited resolution than the estimated size of the larger pores. But the large pores mainly contribute to the porosity. Errors mainly occurring in small pores, like errors due to a limited resolution, might thus be obscured. These small pores can however have a large impact on the connectivity of the pore space and in that way they can significantly affect the permeability. It thus remains important to check the impact of the spatial resolution on the permeability and to assess the sensitivity of the permeability to the threshold value and the spatial resolution. This is done in section 6.4.

Finally a simulation including noise, beam hardening, the EEGE effect and a realistic resolution is performed to get an idea of their cumulative effect. This simulation takes into account noise (25 integration frames), a polychromatic spectrum and a 0,01 mm copper filter. Intensity averaging is applied, the focal spot size is 60 µm and the pixel size is 95 µm. A fluorescent screen is included in the simulation. Table 4.8 compares the resulting porosity to the porosity of a monochromatic simulation using attenuation averaging and a high resolution (focal spot size = 1 µm; pixel size = 47,5 µm and no fluorescent screen).

These simulations give an indication on the impact of the several errors that arise when using a global threshold value. They also allow the user to increase its comprehension on the phenomena affecting the thresholded image.

	porosity different from artificial pavestone sample [%]	**porosity different from artificial limestone sample [%]**
monochromatic; attenuation averaging focal spot size = 1 µm; pixel size = 47,5 µm no fluorescent screen, noise excluded	0,24	0,81
polychromatic; 0,01 mm copper filter; intensity averaging; focal spot size = 60 µm; pixel size = 95 µm; fluorescent screen, noise included (25 integration frames)	0,80	7,13

Table 4.8: Cumulative impact of beam hardening, the EEGE effect and the limited resolution on the porosity of the thresholded image for the pavestone and limestone sample.

4.3 Conclusions

An image of the pore space is extracted from the CT images by thresholding. A global threshold value is defined and pixels with a grey value lower than that threshold value are considered to be pore pixels and assigned the value “1”. The other pixels are considered to be matrix material and are assigned the value “0”. In that way the grey-scale CT image is converted to a binary image of the pore space.

This is applied on pavestone and limestone samples. The threshold value is then chosen in such a way that the porosity of the thresholded image matches the porosity of the sample. By doing so an error is introduced because pores smaller than the image resolution are not detected in the CT images and do not contribute to the porosity of the thresholded image. Thus the larger pores in the thresholded image are overestimated as they have to compensate for the non-detected pores.

Also the use of one global threshold value poses some problems. The limited resolution of the imaging technique causes a blurring of the edges and pores having different sizes require different threshold values. And due to beam hardening the reconstructed attenuation does not only depend on the material contained in a pixel, but also on the position of that pixel in the object. Pores at the edge therefore might by thresholded differently than pores at the centre of the sample. Also the EEGE effect causes errors in the reconstruction of the attenuation coefficient and might hinder a correct thresholding.

The impact of these factors is assessed using the 3D simulator. The simulator makes it possible to examine noise, beam hardening, the EEGE effect and the limited resolution separately. Moreover, the object used in the simulations is exactly known. This facilitates a comparison between the thresholded image and the original image. The thresholding was mainly affected by the limited resolution which has a bigger impact for the limestones. This is explained by the larger fraction in small pores in the limestones. A decrease in resolution mainly affects the detection of the small pores and the estimation of their size.

5. The pore network model

It is important to clearly define the terminology that will be used in this chapter. The permeability k [m²] of a porous medium is generally defined by the Darcy law which relates the fluid flow through a porous medium to the pressure gradient applied on the fluid:

$$q = -\frac{k}{\mu} \cdot S_{sample} \cdot \frac{\Delta p}{L_{sample}} \tag{5.1}$$

where μ is the dynamic viscosity of the fluid and S_{sample} and L_{sample} respectively the cross-sectional area and length of the sample. The permeability is however a homogenized, macroscopic property of the medium that can only be defined on a representative elementary volume (REV). The concept of the REV allows a porous medium, which is essentially a discontinuous system, to be treated as a continuum (*Cressie, 1993; VandenBygaart and Protz, 1999; Brown et al., 2000; Vogel et al., 2002; Wildenschild et al., 2002; Vogel and Brown, 2003; Arns et al., 2005*). For an REV the equations that can be applied on a microscale, such as the Navier-Stokes equations, can be scaled up to the macroscale (*Whitaker, 1969*), i.e. to Darcy's law.

The permeability is often denoted as the intrinsic permeability because it is independent of the fluid that is considered. The conductivity K, expressed in [m³], of a sample incorporates the dimensions of the sample considered:

$$q = -\frac{K}{\mu} \cdot \Delta p \tag{5.2}$$

In this work a model to compute the saturated permeability is developed. Saturated permeability means that the sample is completely saturated by the fluid for which the permeability is computed. Thus only one-phase flow is considered and no relative permeabilities are determined. The saturated permeability for a given fluid is mainly governed by the pore geometry, i.e. the pore size distribution and the connectivity of the pores. Therefore the model developed is based on the image of the pore space of the sample. This image is obtained by X-ray computed tomography.

Once the pore structure is known, direct numerical simulations can be used to compute the fluid flow in the pore space solving the Navier-Stokes equation. Their power is that they are mathematically accurate and do not require a lot of simplifications or assumptions limiting their applicability. They are however computationally very demanding. Computing the permeability of a pore space image of 1000x1000x1000 voxels for instance, requires an immense amount of memory and computation time.

Therefore another approach is followed in this work to assess the permeability of samples. The approach first builds a pore network representation of the pore space. Such a pore network is a simplification of the geometry of the pore space. The pores are replaced by nodes which are connected by links. By computing the conductivity of the links in the network, the global conductivity and permeability of the complete network can easily and rapidly be determined. Instead of directly computing or modelling the fluid flow in the whole pore space, the flow is first computed in the links in the network. By doing so, a reduction in computational power and time can be achieved compared to direct numerical simulations.

The developed model is presented in this chapter. First the construction of the pore network is explained. The subsequent two sections deal with the computation of the local conductivities in the

network and the permeability calculation of the entire network. Finally some other applications using the pore network are discussed.

5.1 Construction of the pore network

A pore network consists of a set of nodes, representing the individual pores, and links between the nodes of neighbouring pores. Physical properties as the volume of the pore or the conductivity between two nodes can subsequently be assigned to these nodes and links. In that way the pore network is a simplified representation of the pore space. Two classes of pore models can be distinguished in literature: intersecting tube models and chamber-and-throat models. In the intersecting tube models (*Fatt, 1956a, b & c; Wise, 1992*) the complete volume of the pore space is concentrated in the links between the nodes. The nodes themselves only connect the different links, but do not have a volume. In the chamber-and-throat models (*Lin, 1982; Koplik, 1982; Koplik and Lasseter, 1985; Constantinides, 1989*) a volume is assigned to both the links and the nodes. In the model developed here the nodes represent the pores and contain the complete volume of the pore they represent. The links are only assigned a conductivity. The developed model can therefore not be considered as an intersecting tube model, neither as a chamber-and-throat model.

To construct the pore network, the pore space has to be partitioned first into a set of individual pores. The question how a "pore" is defined then immediately pops up. Figure 5.1a shows a 2D image of a pore space. Several different partitions can be made as is shown in figures 5.1b and 5.1c. Both partitioned images might seem logical and one cannot define which is the "best" partition.

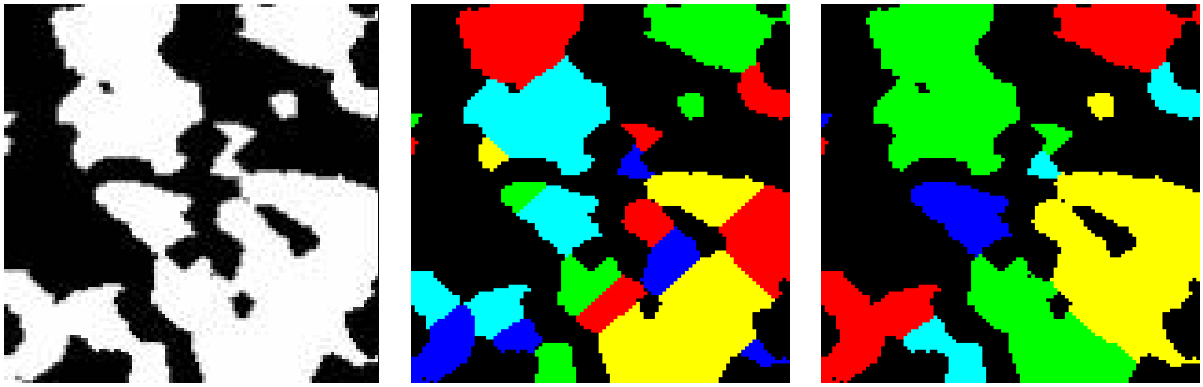

(a) (b) (c)

Figure 5.1: (a) 2D image of a pore space in which white pixels represent the pore space and black pixels the matrix. (b) and (c) show two possible partitions of this pore space into individual pores. This illustrates the ambiguity in the partitioning of the pore space.

Different approaches using different definitions for a pore were developed. These different approaches often result in different partitions. As described in the literature overview above, pore networks based on a real image of the pore space often use a skeletonization approach. Delerue (*2001*) used a Voronoi diagram to extract a skeleton of the pore space. This author then used this skeleton to rebuild the pore space using non-overlapping balls which were inflated to fill the whole pore space. Figures 5.2a, 5.2b and 5.2c illustrate this methodology for a very simple part of a pore space. The drawback of such an approach is that skeletonization algorithms are often computationally expensive, sensitive to noise and not very robust. A minor adaptation to the pore space can give rise to a different skeleton and a different, sometimes not very logical partition. This is demonstrated in figures 5.2d, 5.2e and 5.2f where the methodology is applied on the same sample, but with a minor adaptation.

Therefore a different approach is developed here. The side step of first simplifying the pore space to a skeleton and subsequently rebuilding this pore space is avoided. This will prove to be a much more robust approach and will be computationally less expensive.

The new approach is based on the idea that pores are separated from each other at the bottlenecks in the pore space. This follows the definition by Dullien (*1992*) that states that a pore is defined as a portion of the pore space bounded by solid surfaces and planes erected where the hydraulic radius of the pore space exhibits minima. This can be illustrated by figure 5.1 One might intuitively partition the pore space of figure 5.1a into the pores shown in figure 5.1b. Every pore is separated from the other ones at the bottlenecks between the pores. The new approach therefore divides the pore space at these bottlenecks. Bottlenecks, or throats, can be defined by the use of the aperture of a pore voxel. This is the distance of the pore voxel to the border of the pore space. Throats are located at local minima in the aperture map which contains for each pore voxel its aperture.

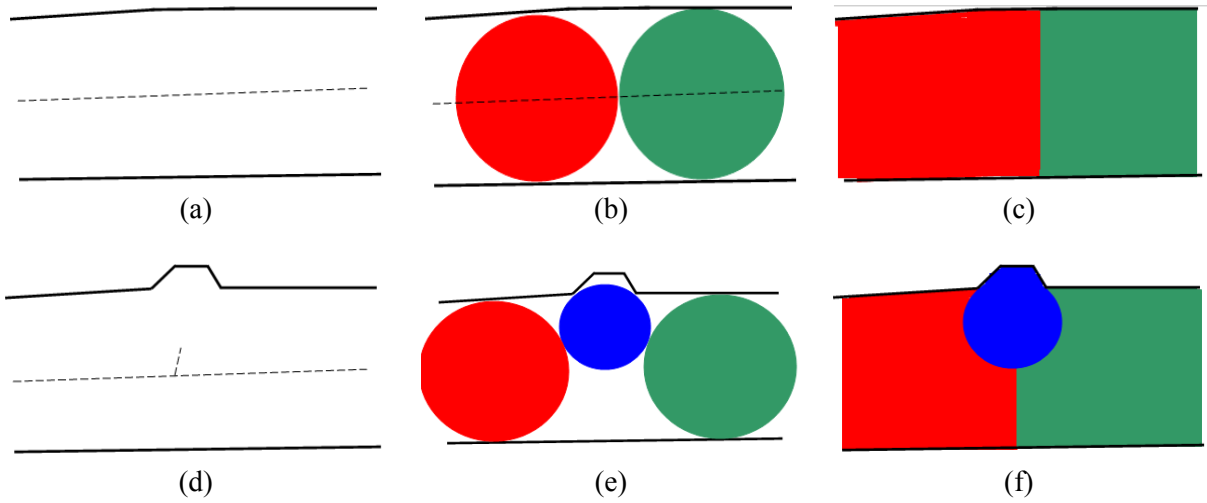

Figure 5.2: (a) 2D image of a part of a pore space (full lines) with skeleton (dashed line). (b) The biggest possible non-overlapping balls are placed on the skeleton. (c) The balls are inflated to fill the whole pore space. (d) The same part of the pore space is considered, but a small deviation is added to the image. This also alters the skeleton which now has a branch. (e) The branch in the skeleton results in an extra ball. (f) A different partition compared to the former situation is achieved.

The new approach follows the same philosophy as applied in watershed methods (*Beucher, 1991; Beucher and Meyer, 1992*). These methods consider the image that is partitioned as a topographical image and simulates the flooding of water in the imaginary landscape. The approach developed here uses the aperture of the pore voxels (i.e. its distance to the border) as topographical information. This approach has the advantage that no simplification or skeletonization is necessary which makes it less sensitive to adaptations in the pore space geometry. The algorithms are developed and applicable in 3D, but they are explained using 2D images. This makes the developed methodology easier to explain and comprehend.

5.1.1 Construction of an aperture map

The first step is the construction of the aperture map. The aperture map contains for each voxel the distance of that voxel to the border. The Manhattan distance is used to compute this distance. The Manhattan distance between two points is the sum of the (absolute) differences of their coordinates. This differs from the Euclidean distance that is more generally used as definition for distance. Both definitions are illustrated in figure 5.3.

Figure 5.4a contains the pore space that was formerly shown. Figure 5.4b shows the aperture map of this pore space. The aperture map allows quantifying what is intuitively described above as bottlenecks. The aperture map can also be illustrated by plotting it as a topological map, shown in figure 5.4c.

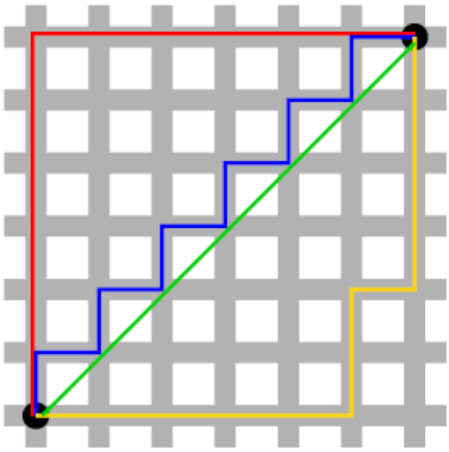

Figure 5.3: Manhattan distance versus Euclidean distance: the green line is the Euclidean distance between the two points and follows the unique shortest path. The blue, red and yellow line illustrate the Manhattan distance between the two points. They all have the same Manhattan length.

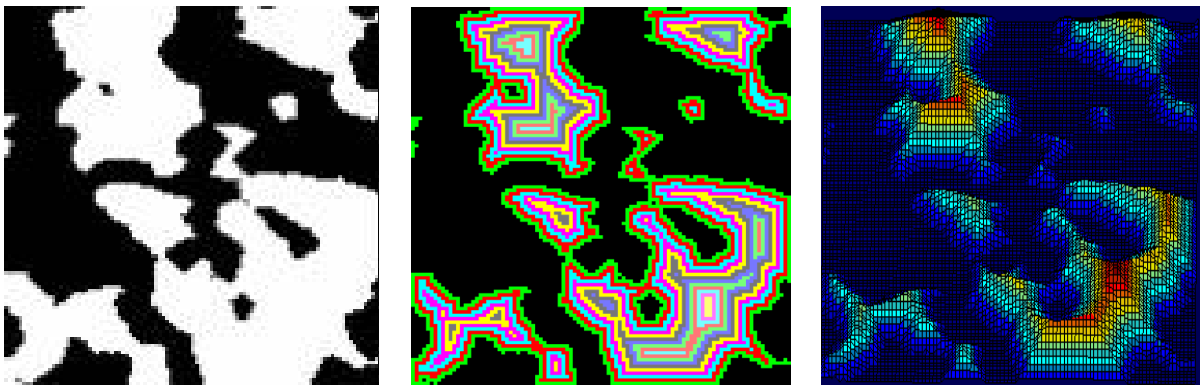

(a) (b) (c)

Figure 5.4: (a) 2D image of a pore space. Again, the white pixels represent the pore space and the black pixels the matrix. (b) The aperture map of this pore space contains for each pore voxel its distance to the border of the pore space. (c) Topological representation of the aperture map.

5.1.2 Selecting and expanding the local maxima

The local maxima of the aperture map (the peaks of the hills in the topological map) are determined and assigned a number. They will make up the pores in the partitioned pore space. The maxima are then expanded contour by contour, starting from the biggest maximum. This can be comprehended by imagining the aperture map as a landscape of hills which is completely flooded. As the water level decreases step by step, these hills become more and more visible and grow isohypse by isohypse. In the same way the local maxima in the aperture map grow contour by contour, as is demonstrated in figure 5.5.

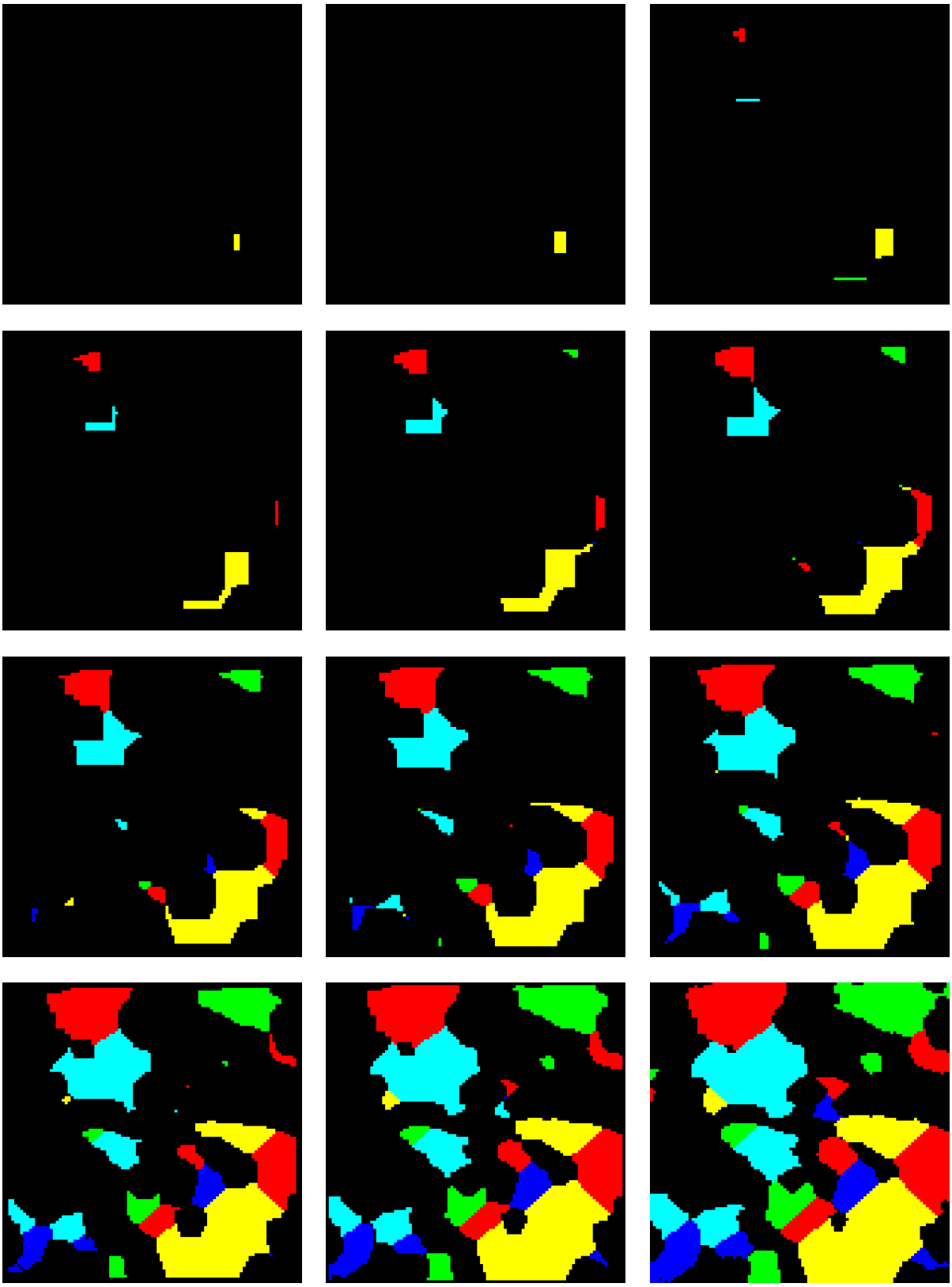

Figure 5.5: The local maxima in the aperture map are determined and assigned a different number, shown on these figures as different colours. The local maxima are then expanded by adding the contours of the aperture map. This expansion is executed starting from the biggest local maxima and gradually adding more and more contours.

5.1.3 Merge criterion for touching maxima

When two expanding maxima touch (figure 5.6a), they are either merged or a boundary between them is constructed. Different criteria can be defined to decide whether two expanding pores are to be merged or not. The following criterion is used:

$$Ap(C) \geq \alpha \cdot \min\left[Ap(M_1), Ap(M_2)\right] \tag{5.3}$$

α is a user defined parameter expressing a percentage, $Ap(M_1)$ and $Ap(M_2)$ are the apertures of the maxima M_1 and M_2 and $Ap(C)$ is the aperture for which there is contact between the two expanding maxima. These parameters are shown in figure 5.6b. If the criterion (5.3) is fulfilled, the expanding maxima are merged. In the other case, the expanding maxima are considered as different pores and a boundary between them is constructed. This boundary follows the highest gradient in the aperture map. Expanding maxima cannot cross this boundary.

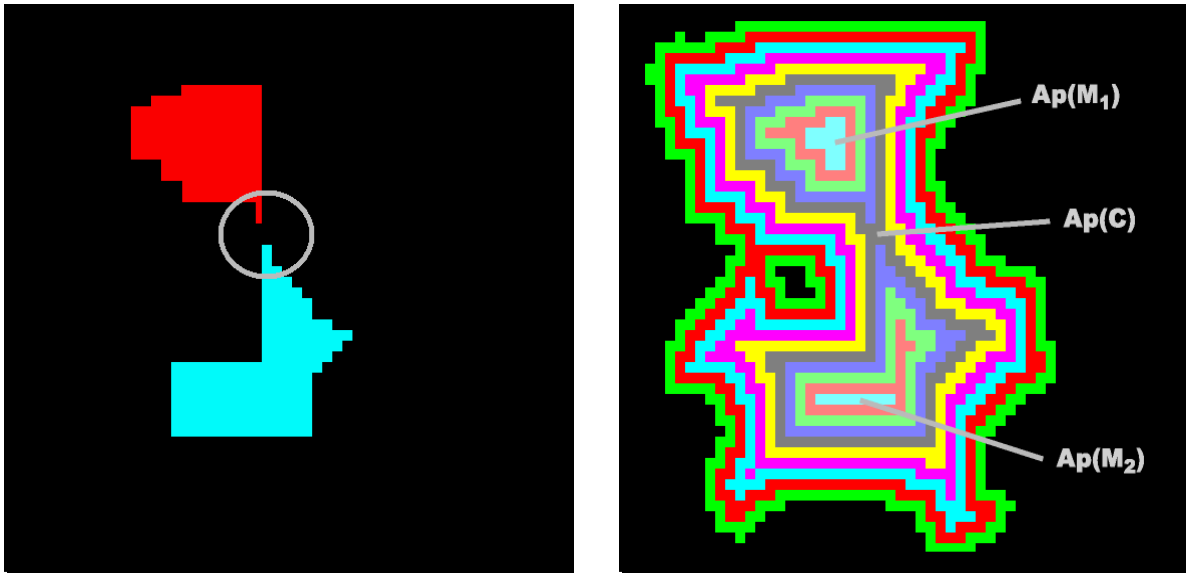

(a) (b)

Figure 5.6: (a) When two expanding maxima touch, they are merged or a boundary between them is constructed. An eventual boundary follows the highest gradient in the aperture map starting from the contact point between the two expanding maxima. (b) The decision whether or not to merge is based on a criterion which uses the apertures of the expanding maxima $Ap(M_1)$ and $Ap(M_2)$ and the aperture $Ap(C)$ for which there is contact between the expanding islands.

The merge criterion defines that when the throat aperture (i.e. the aperture of the contact point) between two pores is sufficiently wide compared to the smallest aperture of the pores, the throat is not regarded as a real throat between two pore. In that case it is more considered to be a narrowing within one pore. This is illustrated in figure 5.7.

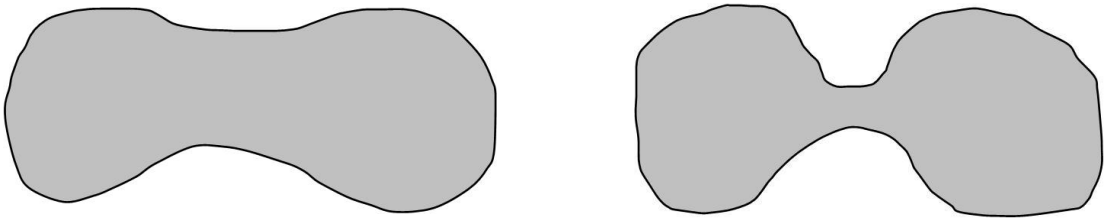

(a) (b)

Figure 5.7: Whether or not a narrowing in the pore space is considered to be a throat between two individual pores depends on the aperture of the narrowing compared to the smallest aperture of the pores. (a) The aperture of the narrowing is too large compared to the smallest aperture of the two pores. The pore space is therefore considered to be one pore. (b) The aperture of the throat is sufficiently small and the pore space is considered to be made up of two separate pores separated by a throat.

The merge criterion tries to capture this intuitive and qualitative idea into a mathematical formula. It is a more or less arbitrary and pragmatic answer to the question how it can be decided when the narrowing between two pores is considered as a throat. Yet, it contains a physical meaning and logic. The relation between the throat aperture and the smallest aperture of the pores can be expressed as a relation between the pressures required to intrude a non-wetting fluid into the throat and into the pore with the smallest aperture. This can be derived as follows (σ is the surface tension between the non-wetting fluid and air, θ is the contact angle between the non-wetting fluid and the air-filled sample which is larger than 90° and smaller than 180°):

$$Ap(C) \geq \alpha \cdot \min\left[Ap(M_1), Ap(M_2)\right] \quad \overset{\text{equation (2.15) and } \cos\theta < 0}{\Rightarrow} \quad -\frac{2\sigma\cos\theta}{Ap(C)} \leq -\frac{2\sigma\cos\theta}{\alpha \cdot \min\left[Ap(M_1), Ap(M_2)\right]}$$

$$\overset{\beta=1/\alpha}{\Rightarrow} \quad p_C \leq \beta \cdot p_{\min[M_1,M_2]} \qquad (5.4)$$

As α is smaller than or equal to 100%, β is larger than or equal to 100%. Thus the merge criterion can also be explained in terms of the pressure required to intrude a non-wetting fluid into the throat between the pores. If the pressure for which the fluid will intrude the throat p_c, is higher than the pressure needed to intrude the pore with the smallest aperture $p_{min[M1,M2]}$ multiplied by a factor $\beta \geq 100\%$, the throat is considered to be small enough. Obviously the throat shown in figure 5.7a is intruded at a lower pressure than the throat shown in figure 5.7b. Therefore, for a given β, the throat in figure 5.7a is considered to be a narrowing in one pore while the throat in figure 5.7b is considered as a throat between two separate pores.

By the use of the merge criterion, the maxima are further expanded until the whole pore space is filled and partitioned into different pores. Different values for α result in different partitions as is shown in figure 5.8. When α is 100% no expanding maxima are merged and the pore space is partitioned into a maximal number of pores having a maximal connectivity[16]. Using an α equal to zero makes every connected pore to be merged into one pore. This leads to a very rough partition in which the connectivity of the pores is zero.

[16] The connectivity of a node is the number of connections to other nodes. The connectivity of a pore network is the average connectivity of the nodes of the network.

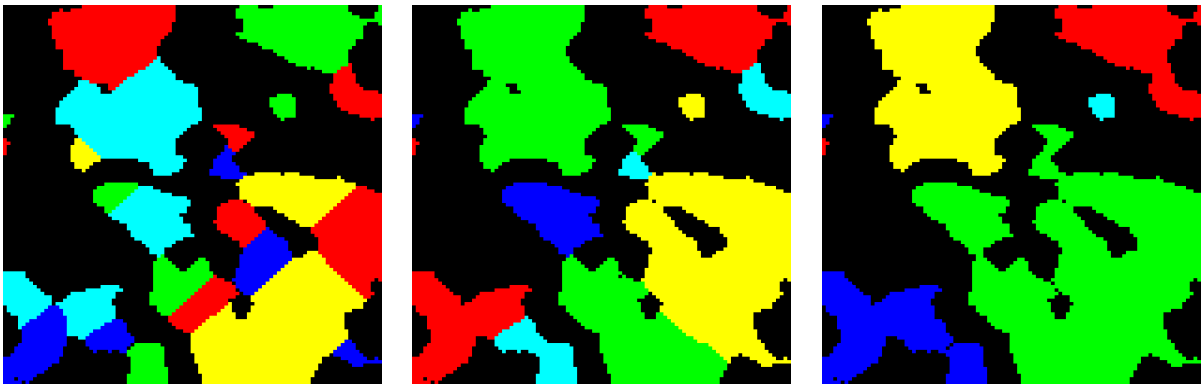

(a) (b) (c)

Figure 5.8: The obtained partitions of the pore space shown in figure 5.1a are given for different values of α: (a) $\alpha = 100\%$; (b) $\alpha = 50\%$; (c) $\alpha = 0\%$.

Figure 5.9 gives the average connectivity of the partitions for the four test samples as a function of α. The connectivity increases with an increasing α and for an α equal to zero, the connectivity also drops to zero. As α increases, the average size of the pores in the partitioned image decreases. This is shown in figure 5.10.

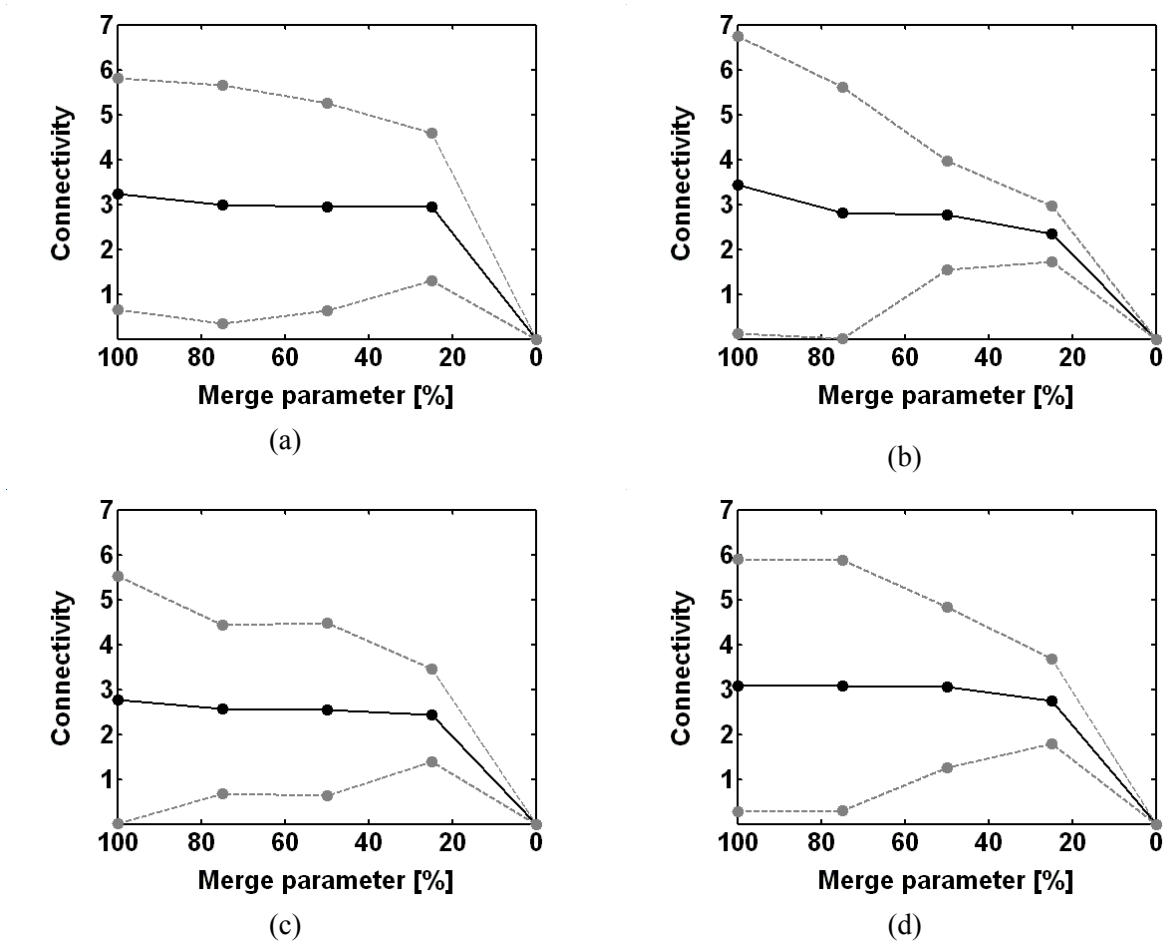

Figure 5.9: The average connectivity of the partitioned images of the test samples in relation to the value of the merge parameter α: (a) pavestone A; (b) pavestone B; (c) limestone A; (d) limestone B. The full (black) line indicates the average connectivity of the nodes in the network. The dashed (grey) line gives the standard deviation on this connectivity. A lower α results in a lower connectivity and ultimately the connectivity is zero for an α of zero.

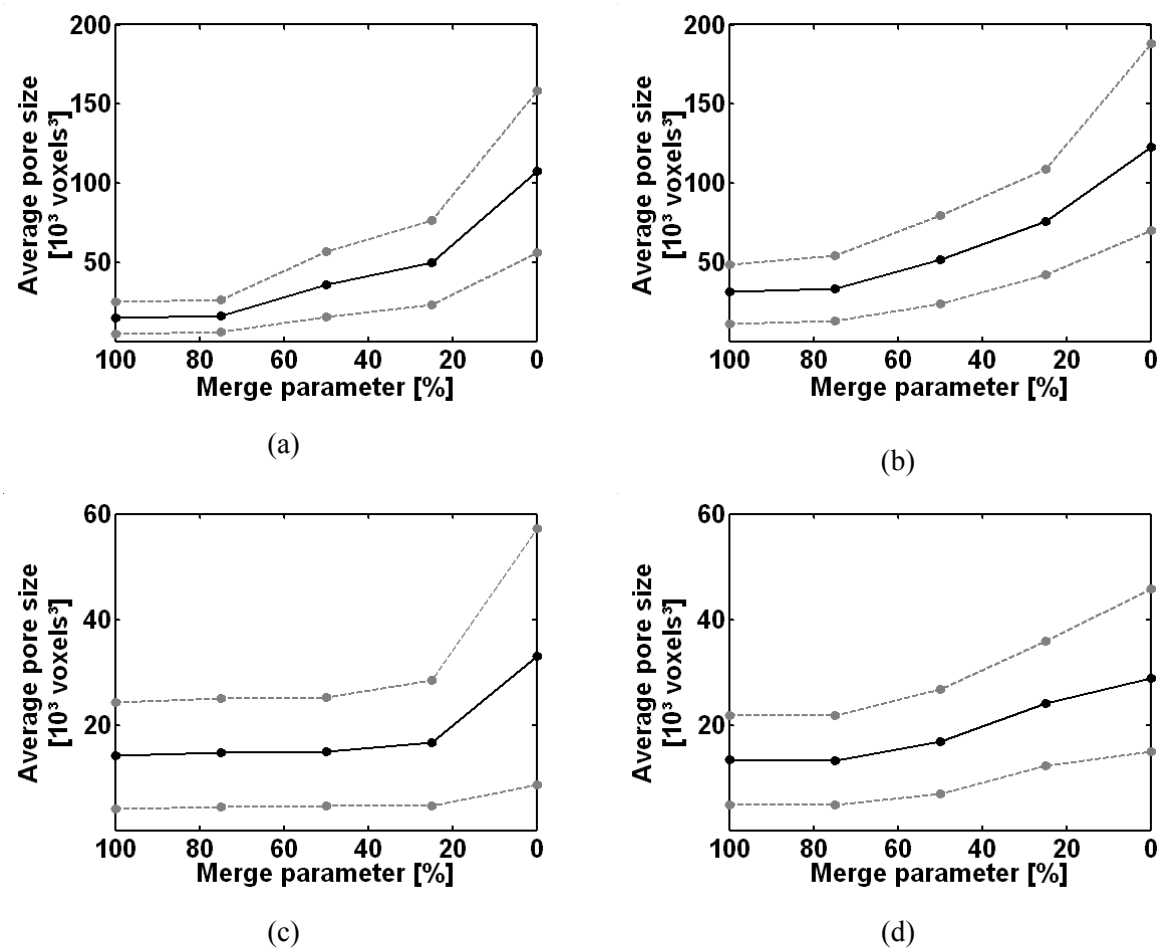

Figure 5.10: The average pore size in the partitioned images of the test samples in relation to the value of the merge parameter α: (a) pavestone A; (b) pavestone B; (c) limestone A; (d) limestone B. The full (black) line indicates the average pore size of the nodes in the network. The dashed (grey) line gives the standard deviation on this pore size. As α decreases more pores are merged and the average pore size of the pores in the partition increases.

5.1.4 Construction of the network from the pore space partition

The partitioned image of the pore space is then converted into a pore network. Every separate part in the partition is considered as a pore and is replaced by a node. The node is placed at the maximum aperture of the pore. In case this maximum aperture contains several voxels, the node is placed in the geometrical centre of these voxels. The geometrical centre (x_C,y_C,z_C) of a number of voxels N_{voxel} is computed as follows:

$$x_C = \text{round}\left(\frac{1}{N_{voxel}}\sum_{i=1}^{N_{voxel}} x_i\right) \tag{5.5}$$

$$y_C = \text{round}\left(\frac{1}{N_{voxel}}\sum_{i=1}^{N_{voxel}} y_i\right) \tag{5.6}$$

$$z_C = \text{round}\left(\frac{1}{N_{voxel}}\sum_{i=1}^{N_{voxel}} z_i\right) \tag{5.7}$$

The function "round" rounds the number off to the nearest integer.

The construction of the network is completed by connecting the neighbouring pores by links between their nodes. The resulting set of nodes and links make up the pore network (figure 5.11b).

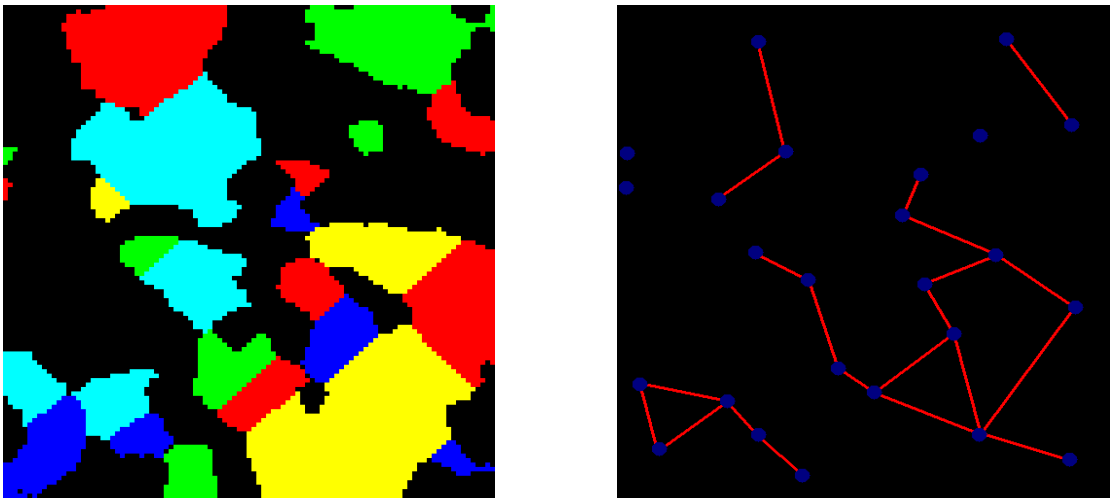

(a) (b)

Figure 5.11: The partitioned image (a) is simplified to a pore network (b) in which each pore is represented by a node. Neighbouring pores are connected by links. These nodes and links make up the pore network.

The nodes of pores that cannot be reached from the inlet and outlet do not contribute to the permeability and are removed from the network. In the methodology developed here, dead-end pores also do not affect the permeability. Therefore they are also removed.

The choice to place the nodes in the network is not always successful as in some cases the position of the nodes induces an error (**error 4: network topography error**). In the next step of the methodology the conductivity of the link between these nodes is computed, as is explained in the next section. Hence, the fluid is forced to flow from node to node in the network. This flow path can in some cases differ from the real flow path. This is illustrated in figure 5.12.

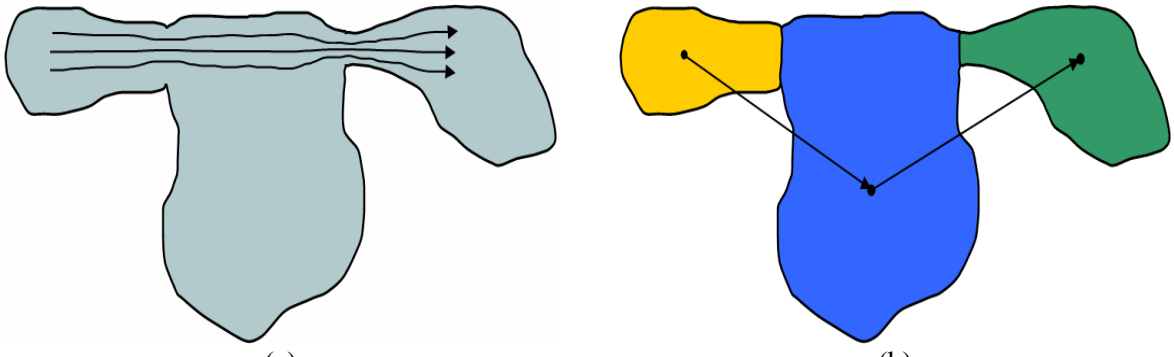

(a) (b)

Figure 5.12: (a) The fluid flow through an extract of a pore space. (b) The partitioning results in three individual pores. These pores are replaced by nodes at the voxels with the maximum aperture of the pore. The node in the central pore does not lie on the flow path. As the flow in the network is forced to flow from node to node, the flow path in the network differs from the real flow path.

In figure 5.12a the flow in a small extract of a pore space is shown. In figure 5.12b the pore space is partitioned into individual pores and the nodes are placed at the maximum aperture of these pores. Subsequently the conductivity of the link between these nodes is computed. Hence the fluid in the pore network is forced to flow from node to node. The links between the nodes however do not coincide well with the flow path and the conductivity between the links is an underestimation of the real conductivity the fluid experiences between the pores. This is further demonstrated and also validated in the next chapter.

5.2 Computation of the local conductivities in the network

After having modelled the pore space as a network, the fluid flow through the links and, more in particular, the conductivity of the links is computed. The motion of fluids is described by the Navier-Stokes equations. These are non-linear differential equations and cannot analytically be solved. Often simplifications (Stokes equations), specific configurations (Poiseuille's law) or volume averaging (Darcy's law) are considered or applied to provide a solution for a specific problem. Direct numerical simulations are also generally used to iteratively solve the Navier-Stokes equations.

First the equations describing fluid flow are explained. Then it is described how the local conductivities in the network can be computed. Many pore network models estimate these conductivities by simplifying the links to standard geometrical shapes. Mostly this standard shape is a cylinder and Poiseuille's law is used to determine the conductivity of these cylinders.

It is however a very strong assumption that the irregular shape of the pore space can be simplified to channels with regular and standard geometrical shapes. Therefore it is chosen to compute the conductivity of the links by a direct numerical simulation solving the Stokes equations. This is explained in section 5.2.3.

5.2.1 Fluid flow equations

5.2.1.1 The Navier-Stokes equations

The Navier-Stokes equations are derived by considering the conservation of mass, energy and momentum for an arbitrary control volume. They are a set of three coupled nonlinear partial differential equations. In their most general form, these equations are:

$$\rho\left(\frac{\partial \mathrm{u}}{\partial t} + \mathrm{u}\cdot\nabla\mathrm{u}\right) = -\nabla p + \nabla\cdot\prod + \mathrm{f} \tag{5.8}$$

$$\rho\left(\frac{\partial E}{\partial t} + \mathrm{u}\cdot\nabla E\right) - \nabla\cdot\left(\alpha_{TC}\nabla T\right) + p\nabla\cdot\mathrm{u} = 0 \tag{5.9}$$

$$\frac{\partial \rho}{\partial t} + \nabla\cdot\left(\rho\mathrm{u}\right) = 0 \tag{5.10}$$

Equation (5.8) describes the conservation of momentum in which **u** represents the flow velocity, ρ the fluid density, p the pressure, **Π** a stress tensor and **f** the body forces acting on the fluid per unit of volume. The left side of equation (5.8) describes the acceleration of the fluid and is composed of the derivative of the velocity over time and a convective term. The latter is the effect of time independent acceleration of a fluid with respect to space. This acceleration happens for example when fluid moves down a diverging duct and decelerates. Though the flow is steady (time independent), it is subjected to an acceleration.

The pressure gradient ∇p arises from the normal stresses in the fluid and makes the fluid to flow from high to low pressure. The stress tensor **Π** describes viscous forces on the fluid. For incompressible fluids, these are shear forces. When the fluid is assumed to be Newtonian, this term can be written as follows:

$$\nabla \cdot \prod = \mu \cdot \nabla^2 \mathrm{u} \tag{5.11}$$

μ denotes the dynamic viscosity of the fluid. For laminar flow the convective term $\mathrm{u} \cdot \nabla \mathrm{u}$ is assumed to be negligibly small compared to the viscous term $\mu \cdot \Delta \mathrm{u}$. As only steady-state flow is examined in this work, also the time derivative can be omitted. Equation (5.8) then takes the following form:

$$-\nabla p + \mu \cdot \nabla^2 \mathrm{u} + \mathrm{f} = 0 \tag{5.12}$$

The conservation of energy is expressed by equation (5.9) where E stands for the total energy per unit mass, α_{TC} for the thermal conductivity and T for the temperature. For isothermal flow the energy conservation equation can be omitted. Conservation of mass is finally reflected by equation (5.10). For incompressible flow the density ρ is constant and the equation becomes:

$$\nabla \cdot \mathrm{u} = 0 \tag{5.13}$$

Equations (5.12) and (5.13) are the Stokes equations and represent the Navier-Stokes equations for steady-state laminar flow of an incompressible, Newtonian fluid. This kind of flow is considered here and thus these equations are used to describe the motion of the fluid in the links of the network.

5.2.1.2 Poiseuille's law

The Stokes equations are linear, but they remain difficult to solve. For specific applications some further simplifications can be applied which enables solving the Stokes equations analytically. Poiseuille solved the Stokes equations for a steady-state laminar flow through a cylinder:

$$\mathrm{u} = -\frac{r_{cylinder}^{\ 2}}{8\mu} \cdot \frac{\Delta p}{L_{cylinder}} \tag{5.14}$$

$L_{cylinder}$ and $r_{cylinder}$ denote respectively the length and radius of the cylinder, Δp is the pressure difference over the cylinder and **u** the mean fluid velocity in the cylinder. The negative sign is needed because fluids flow from high pressure to low pressure. Poiseuille also described steady-state laminar flow through parallel plates ($a_{plate} >> l_{plate.}$):

$$\mathrm{u} = -\frac{l_{plate}^{\ 2}}{12\,\mu L_{plate}} \cdot \Delta p \tag{5.15}$$

The geometrical parameters a_{plate}, l_{plate} and L_{plate} are explained in figure 5.13.

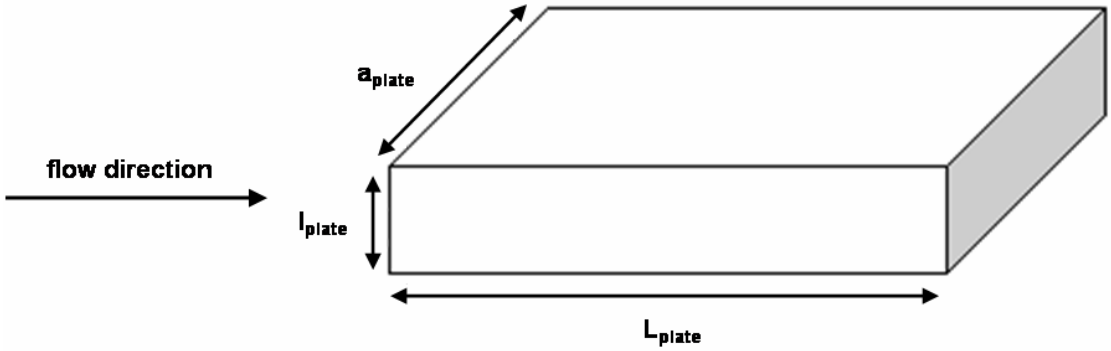

Figure 5.13: Geometry of a parallel plate: L_{plate} is the length and l_{plate} the aperture between the two plates and a_{plate} is the width of the opening.

The conductivity of a cylinder is then expressed as follows:

$$K = -\mu \cdot \frac{\mathrm{q}}{\Delta p} = -\mu \cdot \frac{\mathrm{u} \cdot \pi r_{cylinder}^{\ 2}}{\Delta p} = \frac{\pi r_{cylinder}^{\ 4}}{8 L_{cylinder}} \tag{5.16}$$

The conductivity of parallel plates is:

$$K = \frac{a_{plate} l_{plate}^{\ 3}}{12 L_{plate}} \tag{5.17}$$

5.2.1.3 Darcy's law

The Stokes equations are linear equations and therefore lead to a linear relation between the pressure gradient and the flux. Darcy's law describes the fluid flow through a porous medium:

$$\mathrm{q} = -\frac{k \cdot S_{sample}}{\mu} \cdot \frac{(p_2 - p_1)}{L_{sample}} = -\frac{K}{\mu} \Delta p \tag{5.18}$$

S_{sample} is the cross-sectional area and L_{sample} is the length of the sample over which the pressure drop takes place. The permeability is a homogenized macroscopic property of the medium describing the relation between the average velocity in the medium and the imposed pressure difference. Figure 5.14 illustrates the difference between the effective velocity and average velocity through a (schematic and small) porous medium.

Darcy's law defines the permeability, but does not tell how it can be computed. Although it is applied on the macroscopic scale, the permeability depends on the internal structure of the medium, i.e. the microscale. Darcy's law can be derived by scaling up the Stokes equations to the macroscale or by averaging them over a representative volume on the macroscale (cf. *Du and Ostoja-Starzewski, 2006*).

The computation of the conductivities of the links also uses the Stokes equations. But different ways to solve them can be followed. A common approach is to assume the links to be cylindrical and use Poiseuille's law. This is explained in section 5.2.2. An alternative approach, namely the use of a direct numerical simulation, is presented in section 5.2.3.

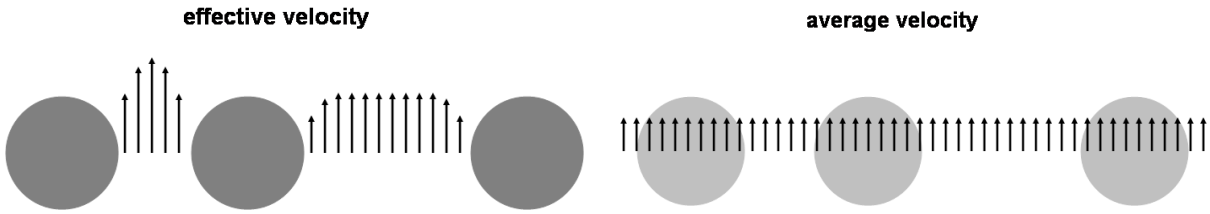

(a) (b)

Figure 5.14: (a) The effective fluid velocity is the actual velocity of the fluid passing through the medium. (b) The average velocity averages the effective velocity over the cross-section of the sample.

5.2.2 Computation of the local conductivities using Poiseuille's law

Delerue (*2001*) considered the links in the network to be cylindrical. The conductivity between two nodes can then be computed as a serial connection of two cylinders. The length of these cylinders is the distance from the centre of the pore to the geometrical centre (cf. equations (5.8) to (5.10)) of the interface between the pores. The radius of the cylinders is the radius of the inflated spheres that make up the network (figure 5.15).

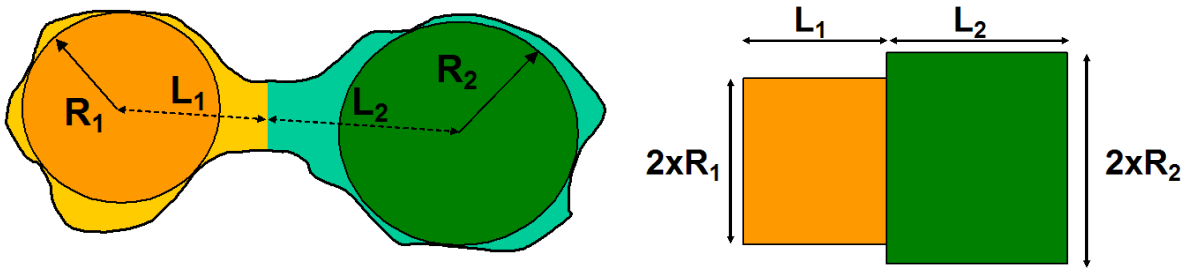

(a) (b)

Figure 5.15: Delerue's network is constructed by placing non-overlapping balls on the skeleton of the pore space. The centres of the balls are the nodes in the pore network (a). The conductivity of the links between the nodes is computed by considering them as a serial connection of cylinders (b). The length of the cylinders is the distance from the centre of the pores to the interface between the pores. The cylinder radius is the radius of the balls.

The conductivity of a cylinder can be determined by Poiseuille's law (equation (5.12)). The conductivity of this serial link is then given by:

$$K_{link} = \frac{1}{\frac{1}{K_1} + \frac{1}{K_2}} \tag{5.19}$$

where K_1 and K_2 are the conductivities of the individual links.

Many authors follow a similar approach using a wide variety of geometrical shapes as squares (*Blunt, 1997a & 1998; Fenwick and Blunt, 1998; Dillard and Blunt, 2000*), triangles (*Hui and Blunt, 2000*) or even a network consisting of stars shaped links (*Kovscek et al., 1993*). Vandersteen *et al.* (*2003*) used a network model of parallel plates to derive the hydraulic properties of a fractured limestone sample.

Carmeliet *et al.* (*2003*) described the flow characteristics of 3D cracks in concrete by a network model consisting of parallel plates.

The simplification of the irregular pore space to uniform channels with regular cross-sectional shapes is however a radical simplification. The power of a pore network model compared to mathematically more accurate methods like direct numerical simulations lies in the fact that it is less demanding towards computational power. This, however, is no argument why these more accurate approaches should not be used to compute the local conductivities. By computing the local conductivities using these methods, their advantages and power are combined with the computational advantage of network models. Direct numerical simulations offer an accurate method to solve the fluid flow. But instead of applying these methods on the sample as a whole which is computationally very expensive, the sample is divided into a large number of small samples by the network model. Applying a direct numerical simulation on these samples is computationally less demanding. It is therefore chosen to compute the conductivity of the links by a direct numerical simulation.

5.2.3 Computation of the local conductivities using a direct numerical simulation

The question that has to be solved, comes to the computation of the fluid flux **q** between two nodes for a given pressure difference. This is illustrated in figure 5.16. When the flux is determined, the conductivity of the link follows from Darcy's law (equation (5.18)). The conductivities of the links can then be used to determine the fluxes in the network for a given pressure difference and compute the overall conductivity of the network.

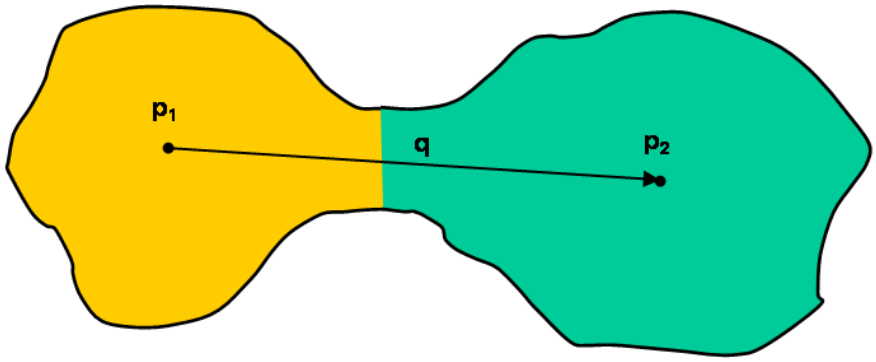

Figure 5.16: Two neighbouring pores are modelled as nodes connected by a link. The conductivity of this link relates the fluid flux to the pressure difference between the nodes.

The fluid flow through the link is computed by a direct numerical simulation. First a grid is constructed, then Stokes equations are discretized and the boundary conditions are formulated. Finally the set of equations is numerically solved.

5.2.3.1 Generation of the grid

Most available CFD (computational fluid dynamics) packages solve the (Navier-)Stokes equations by discretizing them on an irregular grid. It is chosen here to use a regular grid because it allows using the freely available finite difference Navier-Stokes solver NaSt3DGP of the Institute for Numerical

Simulation (INS) in Bonn[17] (*Griebel et al., 1998*). This solver was adapted to a Stokes solver by Verleye *et al.* (2007 & 2008).

The cells in the grid are parallel to the link connecting the two nodes (figure 5.17). The cells containing a voxel belonging to one of the two pores of the link that is considered, are fluid cells. The other cells are solid cells. Also the voxels belonging to pores other than the two pores considered, are solid cells.

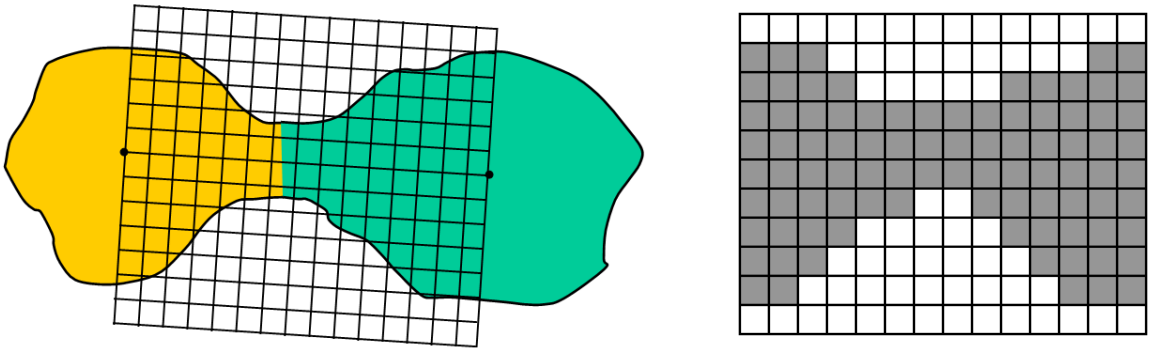

(a) (b)

Figure 5.17: (a) A regular grid is constructed between the two nodes. The cells in the grid are parallel to the link between the nodes. (b) The cells that contain a voxel of one of the two pores of the link are fluid cells (grey). The other cells are solid cells (white).

As the samples are relatively small, the number of cells in the grid does not largely affect the computation time and memory required. Therefore the grid can be constructed at a high resolution. Still a discretization error is made because the cells at the edges of the grid do not always coincide perfectly with the voxels of the pore space image (**error 5: discretization error**).

The grid starts at a line that goes through the node of the first pore and that lies perpendicular on the link between the two pores. The grid end at a similar line through the node of the second pore. Again, the line is drawn perpendicularly to the link between the nodes. This is illustrated in figure 5.18.

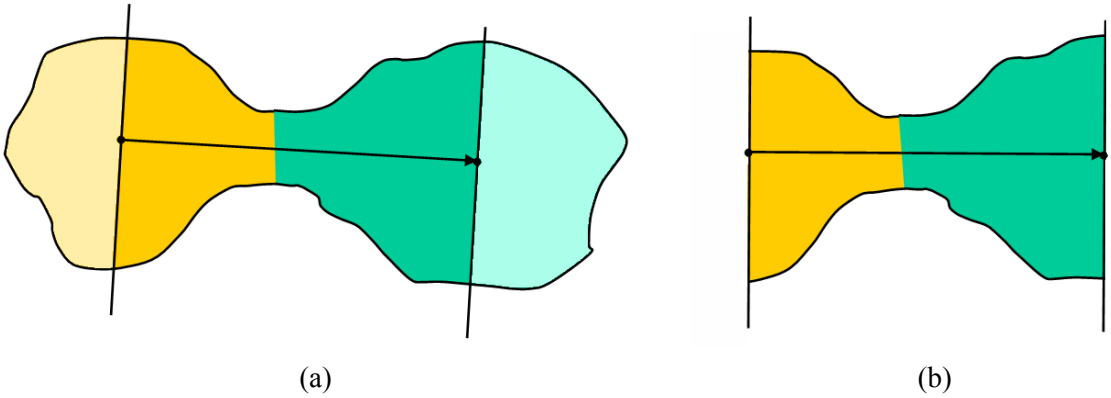

(a) (b)

Figure 5.18: (a) The pores are cut by two lines lying perpendicular to the link between the nodes and going through each node respectively. (b) For the computation of the permeability of the link only the area between these two lines is taken into account.

[17] http://wissrech.ins.uni-bonn.de/research/projects/NaSt3DGP/index.htm.

The choice to construct a grid where the cells lie parallel to the links between the nodes is made because a body force is imposed on the grid. The body force makes the fluid to flow from the inlet to the outlet. The body force imitates the pressure difference between the nodes and has therefore to be parallel to the link. This implies that the cells in the grid are also parallel to the link.

This construction has some shortcomings and gives rise to errors, as illustrated in figure 5.19. Only the two pores that are connected by the link are taken into account (figure 5.19a). This means that the blue pore is neglected and that the boundary between the blue and the yellow pore is considered to be solid. As the body force is imposed parallel to the link, the inflow in the link is also parallel to the link. For the situation shown in figure 5.19a, the links and corresponding applied body forces follow more or less the flow path between the blue and green pore. But in some partitions the blue and yellow pore are merged (figure 5.19b). In the computation of the conductivity of the link between the blue and green pore, the body force, imposed parallel to this link, does not accurately imitate the real flow path (**error 6: boundary condition error**).

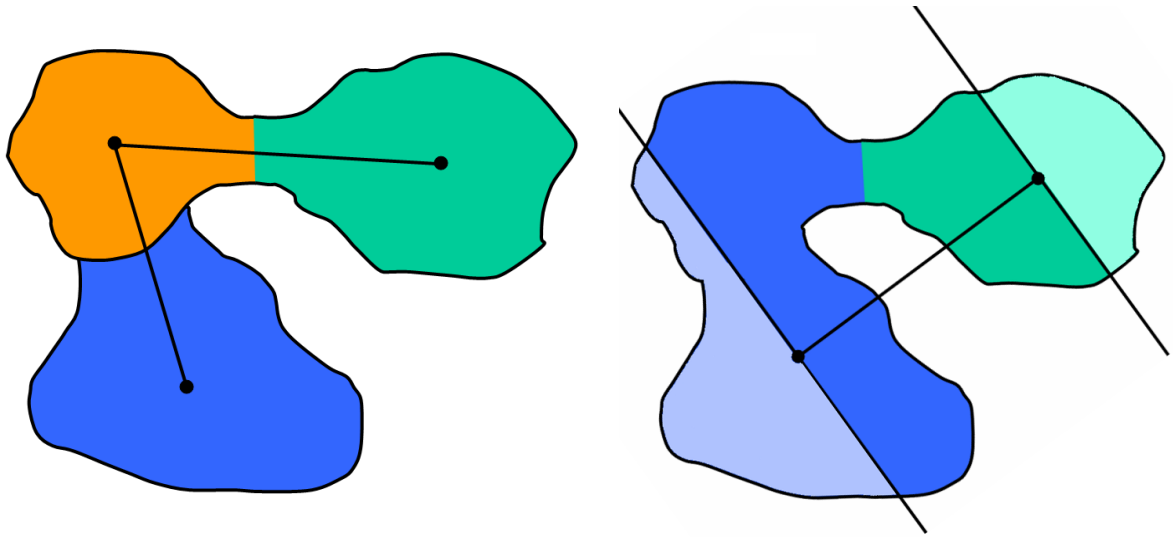

(a) (b)

Figure 5.19: The boundary conditions imposed in the computation of the conductivities of the links do not result in some cases in a realistic simulation of the fluid flow. (a) The links follow more or less the expected flow path between the blue and the green pore. As the body force is imposed parallel to the links, the flow path for the computation of the local conductivities is well simulated. (b) In some partitions (depending on the merge parameter α), the blue pore and the yellow pore are merged. (c) The link now directly connect the node of the blue pore to the node of the green pore and a body force is imposed parallel to this link. The boundary conditions on the computation of the conductivity of this link will not give a realistic simulation of the real path.

Still, the errors induced are assumed to be smaller than the ones that result from the simplification of the links to standard geometrical shapes as explained in section 5.2.2. This assumption is validated in the next chapter.

5.2.3.2 Discretization of the equations

As steady-state, laminar flow of non-compressible, Newtonian fluids is considered, the Stokes equations can be used:

$$\nabla p - \mu \nabla^2 \mathbf{u} = \mathbf{f} \tag{5.20}$$

$$\nabla \cdot \mathbf{u} = 0 \tag{5.21}$$

f represents the body forces acting on the fluid per unit of volume, μ the fluid viscosity and p and **u** respectively the pressures and velocities. These equations are solved numerically by performing a discretization of the equations on a regular grid. Central differentiation is used to represent the single and double differentiations. The pressure and the components of the velocity vector are located at the voxel centre. For the x-component equation (5.12) becomes:

$$\begin{aligned} &\frac{p_{(i+1,j,k)} - p_{(i-1,j,k)}}{2\Delta x} - \mu \frac{\mathrm{u}_{x,(i+1,j,k)} - 2\mathrm{u}_{x,(i,j,k)} + \mathrm{u}_{x,(i-1,j,k)}}{\Delta x^2} \\ &- \mu \frac{\mathrm{u}_{x,(i,j+1,k)} - 2\mathrm{u}_{x,(i,j,k)} + \mathrm{u}_{x,(i,j-1,k)}}{\Delta y^2} - \mu \frac{\mathrm{u}_{x,(i,j,k+1)} - 2\mathrm{u}_{x,(i,j,k)} + \mathrm{u}_{x,(i,j,k-1)}}{\Delta z^2} \\ &= \mathrm{f}_{x,(i,j,k)} \end{aligned} \tag{5.22}$$

The discretized form of equation (5.13) is then:

$$\frac{\mathrm{u}_{x,(i+1,j,k)} - \mathrm{u}_{x,(i-1,j,k)}}{2\Delta x} + \frac{\mathrm{u}_{y,(i,j+1,k)} - \mathrm{u}_{y,(i,j-1,k)}}{2\Delta y} + \frac{\mathrm{u}_{z,(i,j,k+1)} - \mathrm{u}_{z,(i,j,k-1)}}{2\Delta z} = 0 \tag{5.23}$$

5.2.3.3 Boundary conditions

A no-slip boundary condition is imposed at the boundaries between fluid and solid voxels (represented by Γ):

$$\mathrm{u} = 0 \quad \text{on } \Gamma \tag{5.24}$$

The no-slip boundary condition states that the fluid sticks to the boundary and the fluid velocity is zero.

For the boundary condition for the pressure a zero pressure gradient in the normal direction of the boundary is assumed. This is founded by the fact that, whether slip or no-slip boundary conditions for the velocity are imposed, there is no fluid flow in the direction perpendicular to the boundary. Thus no pressure difference is present in that direction (*Verleye, 2008*). Therefore the following boundary condition for the pressure is used:

$$\mathrm{n} \cdot \nabla p \equiv \frac{\partial p}{\partial \mathrm{n}} = 0 \tag{5.25}$$

n is the outward-pointing unit normal vector.

The Stokes equations and the defined boundary conditions allow computing the pressure and velocity in every point of the fluid. When i is a fluid voxel on the boundary between solid and fluid, $\mathbf{u}_{i-1}$ does not exist as $i-1$ is a solid voxel. This problem is handled by the boundary condition which assumes that the fluid sticks to the boundary and the fluid velocity is zero. The components of the velocity vector are located at the centre of a voxel and the boundary between the fluid and solid lies on the border between two voxels. The boundary condition is met by stating $\mathbf{u}_{i-1} = -\mathbf{u}_i$ and assuming a linear

interpolation between the two voxel centres. The velocity on the border is then equal to zero (figure 5.20).

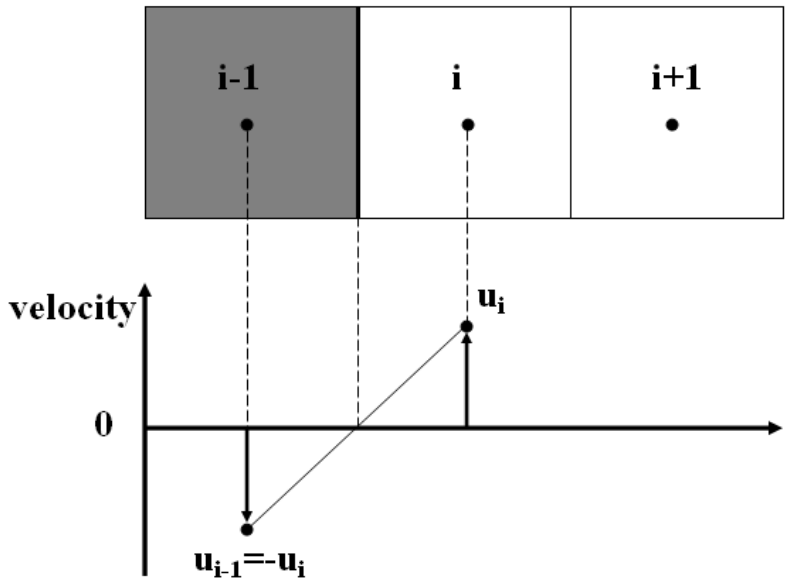

Figure 5.20: When the fluid voxel *i* (fluid voxels are drawn in white; matrix voxels in grey) lies on the fluid-solid border, *i-1* (or *i+1*) is a solid voxel where no fluid velocity can be considered. This is solved by applying the no-slip boundary condition (**u**=0) and assuming a linear interpolation of the velocity between the centres of the voxels. In that case the boundary condition can only be met when $\mathbf{u}_{i-1} = -\mathbf{u}_i$.

In that way $\mathbf{u}_{i-1}$ can be removed from the above equations for which the fluid voxel *i* lies on the boundary between solid and fluid:

$$\frac{u_{x,(i+1,j,k)} - 2u_{x,(i,j,k)} + u_{x,(i-1,j,k)}}{\Delta x^2} \Rightarrow \frac{u_{x,(i+1,j,k)} - 3u_{x,(i,j,k)}}{\Delta x^2} \tag{5.26}$$

$$\frac{u_{y,(i,j+1,k)} - 2u_{y,(i,j,k)} + u_{y,(i,j-1,k)}}{\Delta y^2} \Rightarrow \frac{u_{y,(i,j+1,k)} - 3u_{y,(i,j,k)}}{\Delta y^2} \tag{5.27}$$

$$\frac{u_{z,(i,j,k+1)} - 2u_{z,(i,j,k)} + u_{z,(i,j,k-1)}}{\Delta z^2} \Rightarrow \frac{u_{z,(i,j,k+1)} - 3u_{z,(i,j,k)}}{\Delta z^2} \tag{5.28}$$

A similar problem arises for voxels at the inlet and outlet of the sample. For inlet voxels no voxel *i-1* and for the outlet voxels no voxel *i+1* exists. This is solved by imposing symmetric boundary conditions. The sample is then virtually extended at its both sides by its reflection (figure 5.21b). By doing so the non-existing value $\mathbf{u}_{i-1}$ is replaced by $\mathbf{u}_{i+1}$ at the inlet and the opposite operation occurs at the outlet. This is a mathematical method to be able to solve the equations at the edges of the sample. It is assumed to have only a marginal effect on the resulting conductivity as it only occurs at the inlet and outlet.

Figure 5.21b demonstrates the application of symmetric boundary conditions. Periodic boundary conditions (figure 5.21c) cannot be applied here as for the small samples used here the connectivity can be lost when using periodic boundary conditions. This evidently leads to wrong calculations of the conductivity.

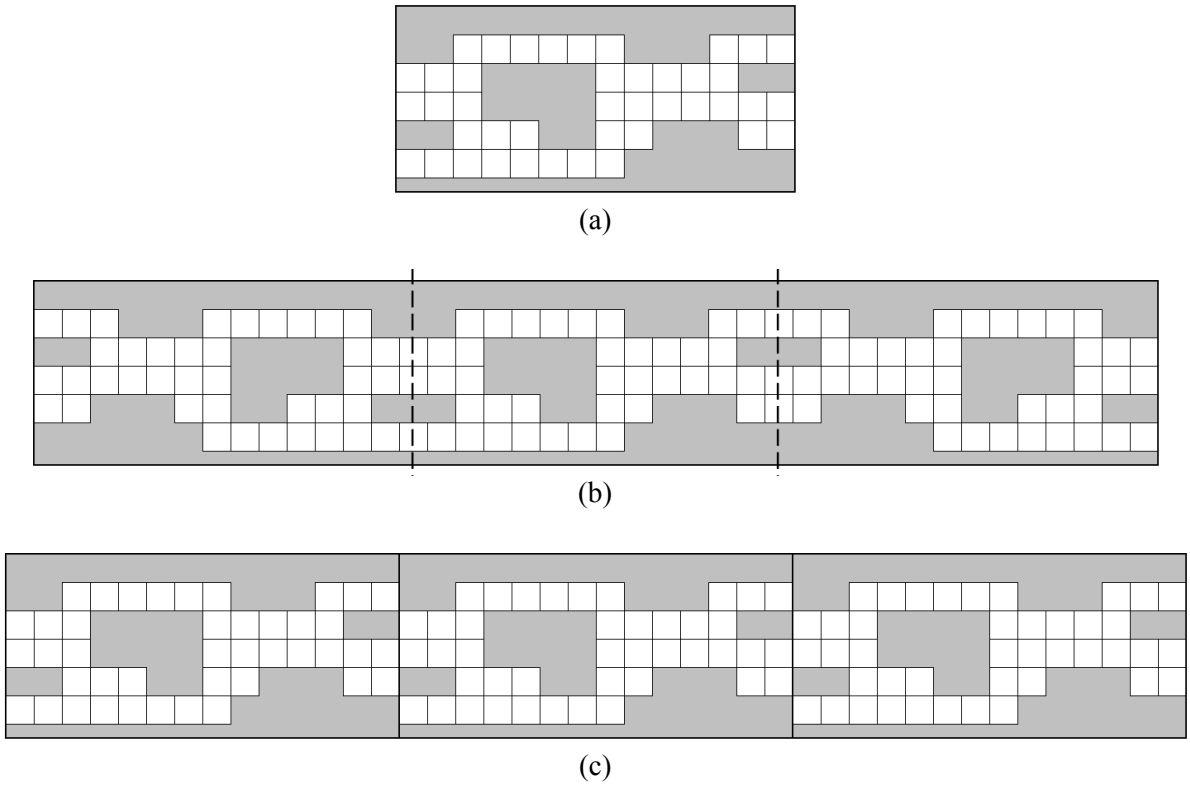

Figure 5.21: (a) When voxels *i* at the inlet or outlet are considered, respectively *i-1* and *i+1* do not exist. Their velocity is however needed when solving the discretized Stokes equations. (b) A value for the velocity in these (non-existing) points can be obtained by reflecting the sample over the inlet and outlet voxels (symmetric boundary conditions). (c) Another possibility is to use periodic boundary conditions. For samples having an irregular pore space, the connectivity can be lost using periodic boundary conditions.

For the inlet voxels the discretized equations can be rewritten without the nodes *i-1* using the following expressions:

$$\frac{u_{x,(i+1,j,k)} - 2u_{x,(i,j,k)} + u_{x,(i-1,j,k)}}{\Delta x^2} \Rightarrow \frac{2u_{x,(i+1,j,k)} - 2u_{x,(i,j,k)}}{\Delta x^2} \tag{5.29}$$

$$\frac{u_{y,(i,j+1,k)} - 2u_{y,(i,j,k)} + u_{y,(i,j-1,k)}}{\Delta y^2} \Rightarrow \frac{2u_{y,(i,j+1,k)} - 2u_{y,(i,j,k)}}{\Delta y^2} \tag{5.30}$$

$$\frac{u_{z,(i,j,k+1)} - 2u_{z,(i,j,k)} + u_{z,(i,j,k-1)}}{\Delta z^2} \Rightarrow \frac{2u_{z,(i,j,k+1)} - 2u_{z,(i,j,k)}}{\Delta z^2} \tag{5.31}$$

5.2.3.4 Numerical solution

A body force **f** is imposed on the sample. The equations are then solved iteratively by the Generalized Minimal Residual (GMRES) solver (*Saad and Schultz, 1986*) which gives the numerical solution of a system of linear equations. An ILu (incomplete lower upper) preconditioner is used to increase the convergence speed. In that way the fluid velocity vector and the pressure in every voxel is obtained.

Once the velocities in the fluid are determined for a given body force **f**, the flux resulting from that force can be computed. The flux q_n is normal to the cross-section and is of course independent from the cross-section of the sample that is considered and is the sum of all velocities normal to the considered cross-section[18]:

$$q_n = \sum_{f=1}^{N} u_{n,f} \tag{5.32}$$

N is the number of fluid cells in the cross-section and u_n is the velocity normal to the cross-section. As stated, this calculation can be performed in every cross-section and this will in theory always give the same result. But for numerical reasons the average of the q_n's calculated for every cross-section is taken:

$$q_{average} = \frac{1}{L_{cross-sections}} \cdot \sum_{f=1}^{N_{cells}} u_{n,f} \tag{5.33}$$

N_{cells} is the total number of fluid cells and $L_{cross\text{-}sections}$ is the number of cross-sections. $L_{cross\text{-}sections}$ is equal to the length of the link, but is dimensionless. The resulting conductivity is then:

$$K = \frac{\mu \cdot q_{average}}{f_n} \tag{5.34}$$

f_n is the component of the body force normal to the cross-section. This direct numerical simulation is applied on every link in the network and in that way the local conductivities, defining the relation between the pressure difference over the nodes and the resulting fluid flux between them, are computed.

5.3 Computing the permeability of the network

When the local conductivities in the network are computed, its global conductivity and permeability can be determined. Figure 5.22 shows a schematic representation of a pore network.

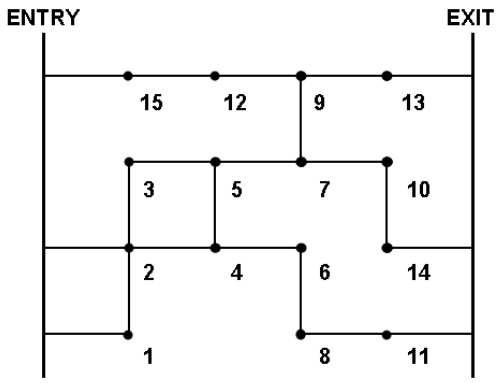

Figure 5.22: Schematic representation of a pore network. The dots represent the numbered nodes while the lines are the connections between these nodes.

[18] The unit cells in the discretization are assumed to have unity dimensions.

The fluid flow through a sample is determined for a given pressure difference over the sample. The sample is assumed to be saturated by the fluid and the flow is supposed to be laminar. As the flux **q** through the sample is computed for the given pressure difference, the global permeability k can be calculated from Darcy's law:

$$k = -\frac{\mu L_{sample}}{S_{sample}} \cdot \frac{\mathrm{q}}{p_{out} - p_{in}} \tag{5.35}$$

S_{sample} and L_{sample} are respectively the surface and length of the sample (figure 5.23) and μ is the dynamic viscosity of the fluid. A pressure p_{in} is imposed at the inlets and p_{out} at the outlets of the network.

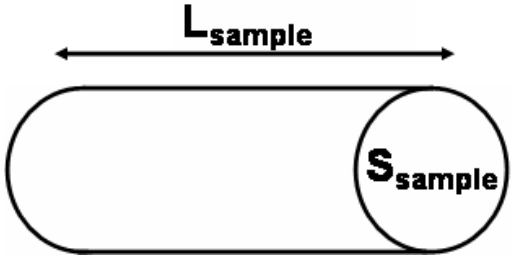

Figure 5.23: Geometrical parameters describing the sample: S_{sample} is the cross-sectional area and L_{sample} is the length of the node.

Then the local pressures in each node are calculated. This can be done by writing a mass conservation equation in each node i, i.e. by stating that the fluxes entering a node are equal to the fluxes leaving this node. The fluxes between the nodes are given by:

$$\sum_j \mathbf{q}_{ij} = \sum_j \frac{K_{ij}}{\mu}(p_i - p_j) = 0 \tag{5.36}$$

$\mathbf{q}_{ij}$ is the fluid flux from pore i to its neighbour pore j, K_{ij} is the local conductivity between both pores and p_i and p_j are the local pressures in pores i and j. In the case of a network with n nodes, a system of n equations with n unknown pressures p_i is obtained. This system of equations can be written down in a matrix equation:

$$\underbrace{\begin{pmatrix} K_{in1}+K_{12} & -K_{12} & 0 & \cdots & 0 \\ -K_{21} & K_{in2}+K_{21}+K_{23}+K_{24} & -K_{23} & \cdots & 0 \\ 0 & -K_{32} & K_{32}+K_{35} & \cdots & 0 \\ \vdots & \vdots & \vdots & \ddots & \vdots \\ 0 & 0 & 0 & -k_{n(n-1)} & K_{nout}+K_{n(n-1)} \end{pmatrix}}_{A} \cdot \underbrace{\begin{pmatrix} p_1 \\ p_2 \\ p_3 \\ \vdots \\ p_n \end{pmatrix}}_{B} = \underbrace{\begin{pmatrix} K_{in1} \cdot p_{in} \\ K_{in2} \cdot p_{in} \\ 0 \\ \vdots \\ K_{nout} \cdot p_{out} \end{pmatrix}}_{P} \tag{5.38}$$

A is a banded, symmetric, positive definite matrix. The nodes in the network are numbered is such a way that the bandwidth of matrix A is minimized. This in turn minimizes the memory required to store the matrix and the computation time needed to solve the matrix equation.

When the local pressures in the network are known, the fluxes entering and leaving the network can be calculated. This is done by summing the fluxes entering the inlet pores or leaving the outlet pores:

$$q = -\sum_{i \in inlet} \frac{K_{in-i}}{\mu}(p_i - p_{in}) = -\sum_{i \in outlet} \frac{K_{i-out}}{\mu}(p_{out} - p_i) \tag{5.38}$$

The global flux through the network is now known for a given pressure difference. Equation (5.35) then allows computing the permeability *k* of the network.

5.4 Other applications of the pore network

In the above sections it is explained how the pore space of a sample is converted into a pore network and how it is used to compute the permeability of the sample. Additionally the effect of a (simplified) erosion and cementation process on the permeability can be simulated, as well as a mercury intrusion experiment applied on the sample (cf. section 6.3.1).

5.4.1 Erosion and cementation

Erosion occurs when the fluid flowing through a sample breaks off or dissolves particles of the matrix and transports these particles out of the sample. In that way the pore space becomes bigger at the expense of the matrix. Cementation can be seen as the opposite process. Minerals dissolved in the fluid are deposited on the matrix. Evidently, both processes occur at the interfaces between the pore space and the matrix.

A simplified model of erosion and cementation is assumed where the decrease of respectively matrix and pore space volume occurs uniformly at the interface between both. This is simulated by altering the voxels at the interfaces from the one form into the other. In the case of erosion matrix voxels become pore space voxels. When cementation is simulated pore space voxels are turned into matrix voxels. This is illustrated in figure 5.24 where this erosion and cementation model is applied on a small pore space.

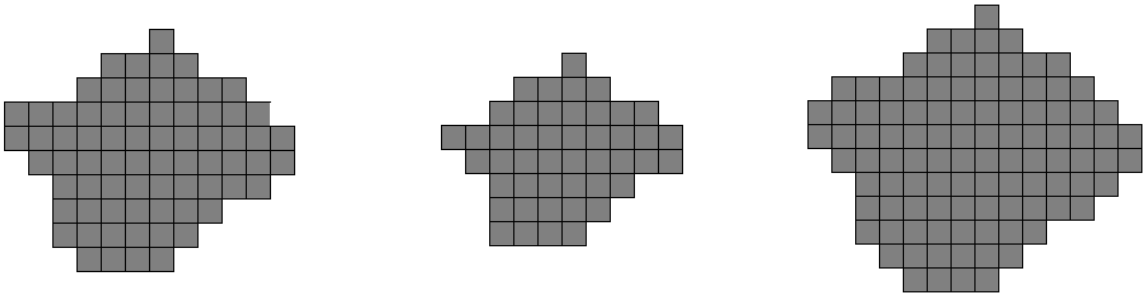

(a) (b) (c)

Figure 5.24: (a) Image of the pore space (grey voxels) on which the erosion and cementation model is applied. (b) Cementation is simulated by altering pore space voxels into matrix voxels at the interface between both. (c) When simulating erosion the opposite operation is performed and matrix voxels are turned into pore space voxels.

In chapter 6 the pore network methodology is applied on some samples to compute their permeability. In addition the impact of erosion and cementation on the permeability is determined using the erosion and cementation model described here. In reality erosion or cementation does not take place uniformly over the interface surface. It is however not the purpose of this research to develop an accurate and

fine erosion or cementation model. When assessing the impact of both processes on the permeability, existing and finer models (*Russ, 2002; The MathWorks, Inc., 2007*) can be used or the processes can first be simulated on real samples in a laboratory. The simple model presented here is only used to get a first and rather rough indication and to demonstrate the applicability of the pore network model approach.

5.4.2 Mercury intrusion experiments

Mercury intrusion is often used in porosimetry experiments. Porosimetry is a technique to assess various geometrical parameters as for instance the pore size distribution of the pore space[19]. The technique is based on the phenomenon that smaller pores require a higher pressure to force a non-wetting fluid to enter these pores. The critical pressure p_c required to force a non-wetting fluid into a cylindrical pore with radius r_c is expressed by:

$$p_c = -\frac{2\sigma \cos\theta}{r_c} \tag{5.39}$$

In this equation σ is the surface tension of the fluid and θ is the contact angle between fluid and solid material. In a porosimetry experiment a non-wetting fluid, mostly mercury, is injected into a porous sample. At room temperature the surface tension σ between mercury and air amounts 485 mN/m. The contact angle θ between mercury and the air-filled sample depends on the sample material, but in most cases 140° is a good assumption. When a higher pressure is applied on the mercury during the injection, the mercury is able to enter smaller and thus more pores and the injected volume increases. However the relation between the intruded volume at a given pressure and the pore sizes can be distorted because small pores can prevent the mercury to intrude larger pores. This phenomenon is illustrated in figure 5.25.

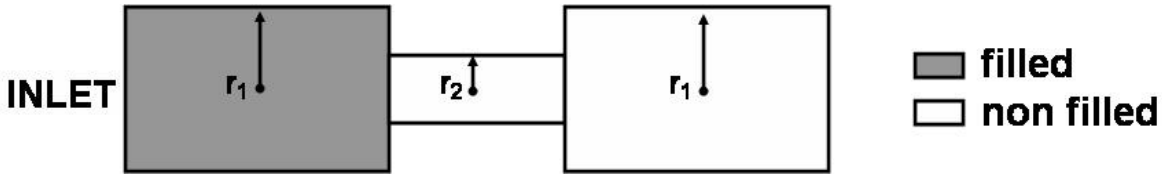

Figure 5.25: A smaller pore can prevent the mercury to enter a pore that is large enough to be intruded by the mercury at the given pressure. As a result the intruded volume does not always correspond to the fraction of the pore sizes corresponding to the applied pressure.

The pore network model lends itself to simulate mercury intrusion into the pore space as the pores are separated from each other at the bottlenecks between them. The surface of these bottlenecks determines the pressure required to intrude the mercury from the one pore into the other. By computing an apparent radius for the bottleneck and assuming the bottleneck to be cylindrical, this pressure can be approximated. The apparent pore entry radius r_c is computed from the surface $S_{bottleneck}$ of the bottleneck by the following equation:

$$r_c = \sqrt{\frac{S_{bottleneck}}{\pi}} \tag{5.40}$$

[19] The pore size distribution is the distribution of the pore volume with respect to the pore size.

For mercury (σ = 485 mN/m; θ = 140°) the relation between the required pressure p_c and the radius r_c of the cylindrical throat becomes:

$$p_c = -\frac{0.743}{r_c} \tag{5.41}$$

A mercury intrusion experiment is then simulated by gradually increasing the imposed pressure on the sample and computing the volume that is intruded by the mercury for these pressures. These computations can easily and rapidly be done as the radii of the pore entries are already known in the network. Thus the required pressures to inject mercury from every pore into its neighbouring pores can directly be determined. The simulation of the mercury intrusion is then performed by a relatively simple algorithm, shown in figure 5.26.

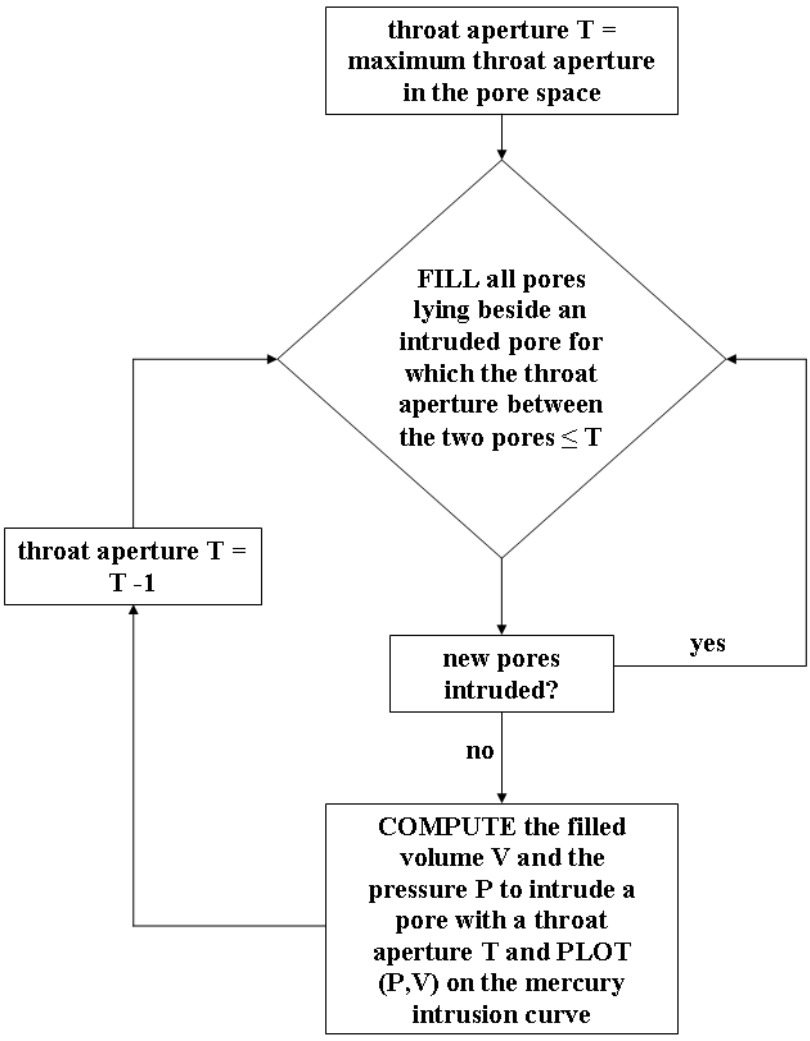

Figure 5.26: Algorithm applied on the pore network to simulate mercury intrusion.

5.5 Conclusions

An approach to compute the permeability of a saturated, porous sample is presented. Several numerical methods solving the Navier-Stokes equations are able to accurately model the fluid flow

through porous samples. For large datasets their computational demand becomes however immense. Therefore an alternative approach is proposed in which the pore space is simplified to a pore network representation. In these networks the pores are replaced by nodes. The nodes of neighbouring pores are hydraulically connected by links.

The pore network is constructed using X-ray computed images. This enables starting from a real image of the pore space of the sample. In many pore network models, the partition of the pore space first simplifies that pore space to a skeleton. Subsequently the pore space is rebuilt from this skeleton by objects having standard shapes, such as a sphere. But developing a robust skeletonization algorithm is complex and difficult. Therefore an alternative approach is used here. The pore space is kept as it is and the partition is performed by separating pores at bottlenecks in the pores space. This appeared to be more robust and computationally less demanding than the skeletonization approach used by Delerue (*2001*).

Subsequently the conductivities of the links in the network are computed. These are determined by using a direct numerical simulation solving the Stokes equations. The Stokes equation can be used for non-compressible, Newtonian fluids and for a steady state, laminar flow. So instead of applying the direct numerical simulation on the sample as a whole which is computationally very expensive, the sample is divided into a large number of small samples by the network model. In that way, the advantage and power of a direct numerical simulation are combined with the advantage of the network model. After having determined the local conductivities, the permeability of the network is computed. This is done by writing down a mass conservation equation for every node in the network. A matrix equation is thus obtained from which the local pressures in the network can be determined for a given pressure difference over the complete sample. Subsequently the flux through the complete sample and the permeability of the complete sample are computed.

The model also allows examining the effect of erosion and cementation on the permeability and to simulate mercury intrusion in the sample.

Both in the construction of the pore network as in the computation of the conductivity of the links errors are made. The placement of the nodes in the voxels with the maximum aperture in the pore leads in some cases to a flow path differing from the real flow path. A discretization error is made by the construction of the grid that is constructed for the computation of the local conductivity of the link. And also the use of a body force parallel to the link induces an errors in the computation of the local conductivities. These errors are further discussed and evaluated in the next chapter.

6. Validation of the pore network model

The developed methodology to compute the permeability of samples based on their X-ray computed tomography images is validated in this chapter. Several experiments are therefore used. First the pore network approach is applied on artificial samples for which the permeability can be computed analytically. A comparison between the analytical solution and the pore network results gives a better insight in the network approach and its shortcomings. The pore network computations are performed using different values for the parameter α in the merge criterion (cf. equation (5.3)) to evaluate its impact.

The methodology is further validated by comparing pore network model results to permeabilities obtained by direct numerical simulations and laboratory experiments. Again, the impact of the parameter α is evaluated. Also mercury intrusion experiments and mercury intrusion simulations are performed to acquire an indication on the quality of the pore partition.

Subsequently the effect of the threshold value and the spatial resolution on the permeability is examined. Also a comparison to Delerue's model (*Delerue, 2001)* is made. In the previous chapter the simplification of the irregular shape of the pore space to cylindrical links was considered to be too radical. Therefore a numerical method using finite differences to solve the Stokes equations was preferred. This demands more computation time, but is expected to be more accurate. This assumption is checked here. Finally, it is demonstrated how the impact of erosion and cementation on the permeability can be assessed using the pore network approach.

6.1 Permeability computation on artificial samples

To test the methodology and to gain a better insight in it, the methodology is first applied on three generic samples and compared to their analytical solutions. The samples are completely artificial and are not acquired from a real pore space or a real situation. Yet, they give insight in the developed methodology and allow to indicate where some errors are made in the methodology.

6.1.1 Case 1

The first sample consists of two parallel, rectangular channels that run from the inlet to the outlet. The sample is 1000 voxels long. The first rectangular contains 200x100 voxels in cross-section, the second 200x50 voxels (figure 6.1).

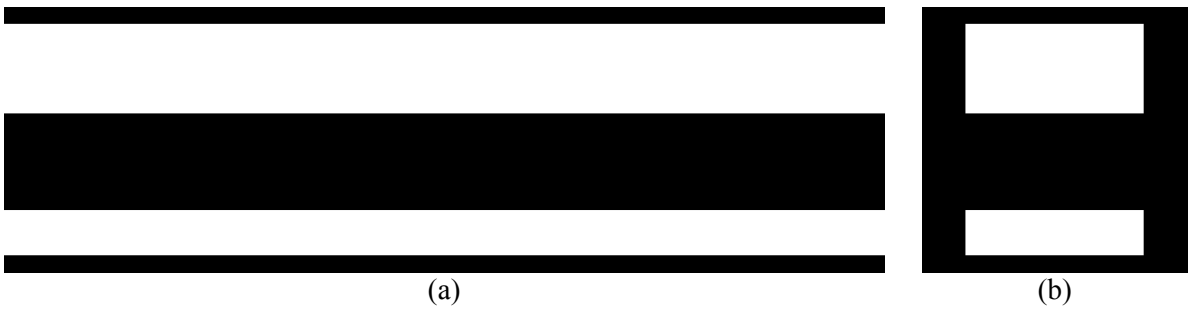

(a) (b)

Figure 6.1: Geometry of the artificial sample: (a) slice in the longitudinal direction taken in the middle of the sample; (b) cross-section of the sample. The sample is 1000 voxels long and it contains two rectangular channels: the upper one has 200x 100 voxels and the lower one 200x50 voxels.

The conductivity of both channels can be computed using Poiseuille's law for parallel plates (equation (5.17)). The conductivity for both channels, expressed in voxel³, is then respectively 16667 and 2083. The conductivity of the whole sample is the sum of both conductivities, being 18750.

Now the conductivity of the sample is computed by the pore network approach. First the pore space is partitioned into individual pores. The resulting partition and network are given in figure 6.2. This partition is obtained for each value of α.

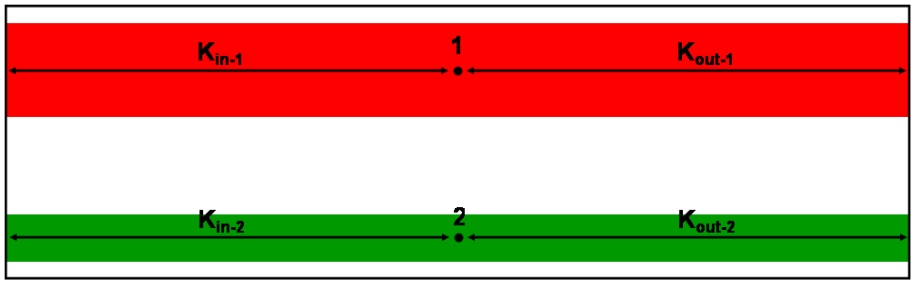

Figure 6.2: The sample is partitioned into individual pores. As these pores are not connected and have a homogeneous aperture (i.e. no bottlenecks are present), the two channels completely make up two separate pores, regardless the value of α. The network is constructed by placing a node in the centre of these pores and connecting the node to the inlet and outlet.

The conductivities of the links are computed by a direct numerical simulation:

K_{in-1} = 33185 voxel³
K_{out-1} = 33185 voxel³
K_{in-2} = 4144 voxel³
K_{out-2} = 4144 voxel³

Analytically solving the conductivities of these links using Poiseuille's law for parallel plates (equation (5.17)) gives 33333 and 4167 voxel³ respectively. This differs from the conductivities computed by the direct numerical simulation by less than 1%. The difference results from the discretization of the links (**error 5: discretization error**).

In the network approach, the following matrix equation is then constructed:

$$\begin{pmatrix} 33185+33185 & 0 \\ 0 & 4144+4144 \end{pmatrix} \cdot \begin{pmatrix} p_1 \\ p_2 \end{pmatrix} = \begin{pmatrix} 33185 \cdot (p_{in} - p_{out}) \\ 4144 \cdot (p_{in} - p_{out}) \end{pmatrix}$$

Assuming an inlet pressure of 10 bar and an outlet pressure of 0 bar, p_1 and p_2 are 5 bar. The water flux [*voxel³/s*] flowing through the sample is then:

$$\mathbf{q} = \sum_j \mathbf{q}_{ij} = \sum_j \frac{K_{ij}}{\mu}(p_i - p_j) = \frac{33185+4144}{0.001002} \cdot 5 = 186 \cdot 10^6$$

From this flux and the pressure difference imposed on the sample, the conductivity [*voxel³*] of the whole sample is determined:

$$k = \frac{\mu \cdot \mathbf{q}}{\Delta p} = \frac{0.001002 \cdot 186 \cdot 10^6}{10} = 18665$$

This result almost completely matches the analytically obtained conductivity. The small difference can be explained by the error that is made when a mesh is constructed for the computation of the local conductivities of the links (**error 5: discretization error**). However, this first test sample can hardly be called challenging. In the following case the sample is slightly adjusted.

6.1.2 Case 2

Both channels of the previous sample are connected near their centres by a third channel. The channel is 110 voxels long, 40 voxels wide and also 200 voxels deep. Where this channel connects to the other channels, it narrows from 40 voxels to 20 voxels over a length of 5 voxels. This is illustrated in figure 6.3. The narrowing is necessary to make the channel be considered as an individual pore in the partitioning of the pore space.

Figure 6.3: Geometry of the second artificial sample. (a) The sample is similar to the previous sample except for a connecting channel between the two rectangular channels. (b) The connecting channel is 200 voxels deep. It is 110 voxels long and 40 voxels wide except at the connection with the other channels. There the channel narrows to 20 voxels over a length of 5 voxels.

As both channels have uniform shapes in the longitudinal direction, the pressure loss over the channel is linear. Therefore the pressure in both channels at the connecting channel is the same and there is no resulting flow between the upper and the lower channel. Consequently, this sample has the same conductivity as the sample in case 1.

But in the pore network approach the sample does behave differently from the previous sample. The partition of the sample depends on the value of α. Figure 6.4 shows the three possible partitions. The first partition (figure 6.4a) is obtained when α is higher than 80%. The second partition (figure 6.4b) results from an α between 40% and 80% and the last partition (figure 6.4c) applies for an α lower than or equal to 40%.

The conductivity of the first and the last partition are equal to conductivity computed for case 1. But the conductivity of the pore network from the second partition is different. The conductivities of the links between the nodes are again computed by the direct numerical simulation. The results from these computations are:

$K_{in\text{-}1}$ = 33185 voxel³
$K_{out\text{-}1}$ = 33185 voxel³
$K_{1\text{-}2}$ = 11412 voxel³
$K_{in\text{-}2}$ = 3454 voxel³
$K_{out\text{-}2}$ = 3454 voxel³

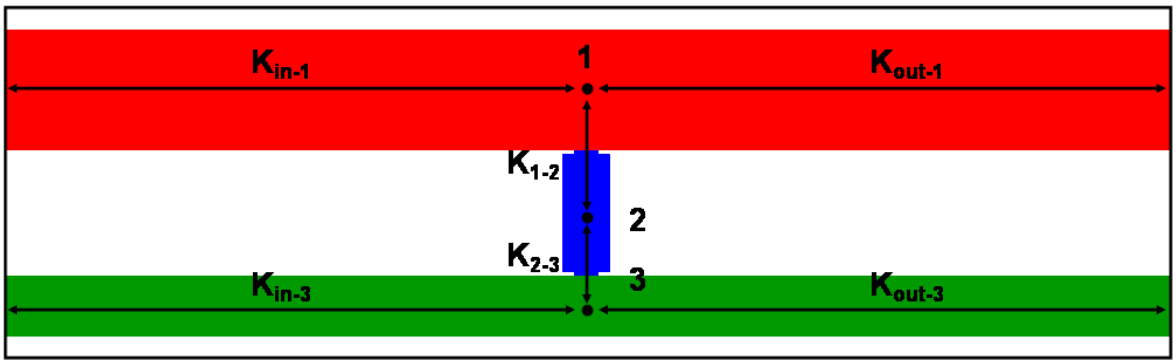

(a)

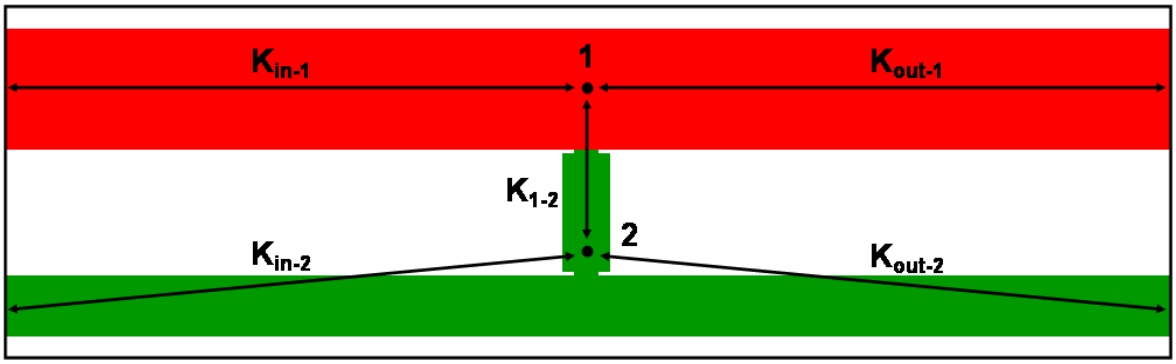

(b)

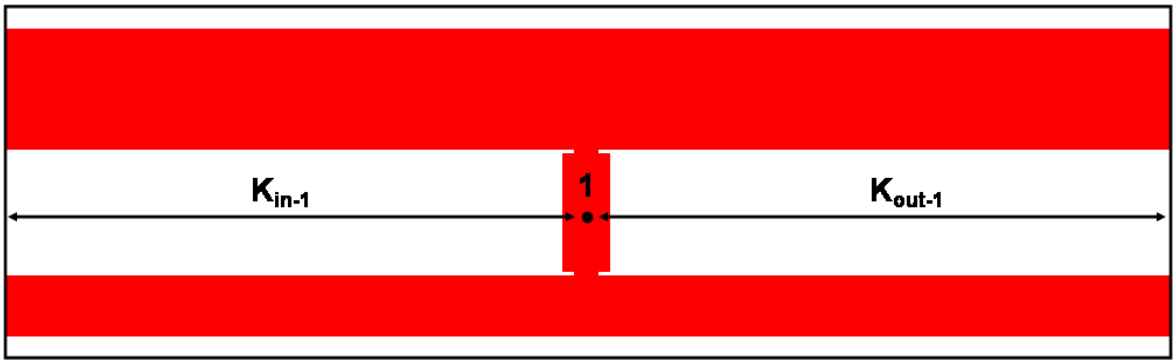

(c)

Figure 6.4: Partition of the pore space of the test sample depends on the merge parameter α used. (a) When α is higher than 80%, the three different channels are recognized as different pores. (b) When α is lower than 80% the lower channel and the connecting channel are merged into one pore. (c) For an α lower than 40%, the complete pore space is considered to be one single pore.

Because of the symmetry p_1 and p_2 are both equal to 5 bar when the inlet pressure is set on 10 bar and an outlet pressure on 0 bar. The water flux flowing through the sample is:

$$\mathbf{q} = \frac{33185 + 3454}{0.001002} \cdot 5 = 183 \cdot 10^6$$

The conductivity of the whole sample is then:

$$k = \frac{\mu \cdot \mathbf{q}}{\Delta p} = \frac{0.001002 \cdot 183 \cdot 10^6}{10} = 18320$$

This is smaller than the analytically computed conductivity and the conductivity obtained from the pore network approach on the other two partitions. The error arises because the fluid in the network is forced to flow from node to node (**error 4: network topography error**). This can complicate the fluid flow in the network compared to the flow in the real sample and thus a lower conductivity is obtained. The network geometry depends on the value of α. Different values for α therefore results in different conductivities. In the sample considered here, a high value for α (>80%) and a low value (<40%) give more or less correct results. For an α between 40% and 80% a network is created which results in a conductivity that differs from the analytically correct value. There is thus not a straight correlation between the value of α and the accuracy of the computed permeability.

Figure 6.5 is a simulation of the flow velocity as it appears in the pore network for case 1 and case 2. It is a composite image that incorporates the fluid flow computed for the different links. The flow in these links results from a body force applied on the fluid. The body force is parallel to the link between the nodes. The flow in the lower channel is clearly hindered in the second partition of case 2 because the flow has to make a detour to the node 2. This illustrates the error that is made by forcing the fluid to flow from node to node in the network (see also figure 5.12).

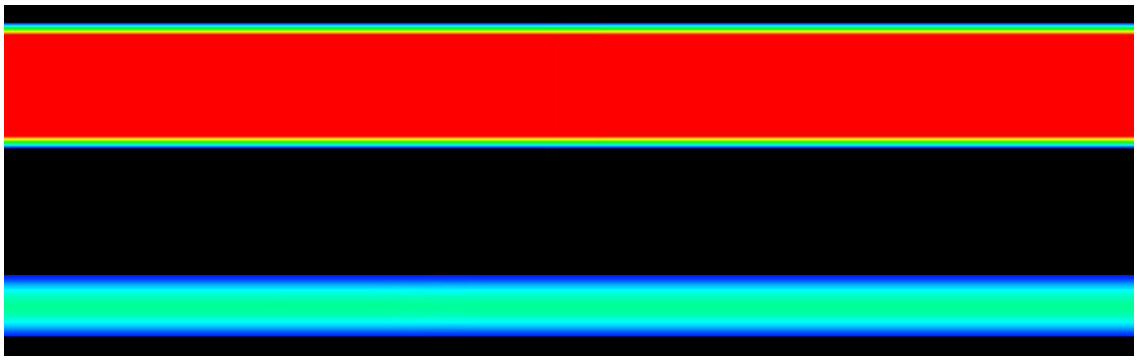

(a)

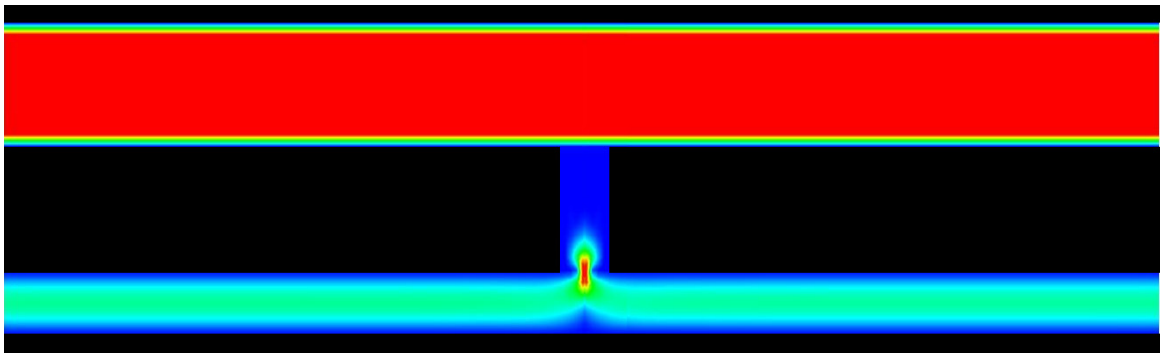

(b)

Figure 6.5: Fluid velocity simulation (blue: low velocity; red: high velocity) in the pore network for case 1 (a) and case 2 (b). The simulation is a composite image incorporating the fluid flows computed for the different links in the network. The fluid velocities in these computations are determined by direct numerical simulation.

6.1.3 Case 3

Finally a rectangular channel (40x10 voxels) that makes two corners of 90° is considered. The geometry of the sample is given in figure 6.6. The inflow is perpendicular to the inlet. Again, this is a purely artificial situation. It is used to demonstrate the error made because a body force parallel to the link between two nodes is imposed on the fluid (**error 6: boundary condition error**) (see also figure 5.19).

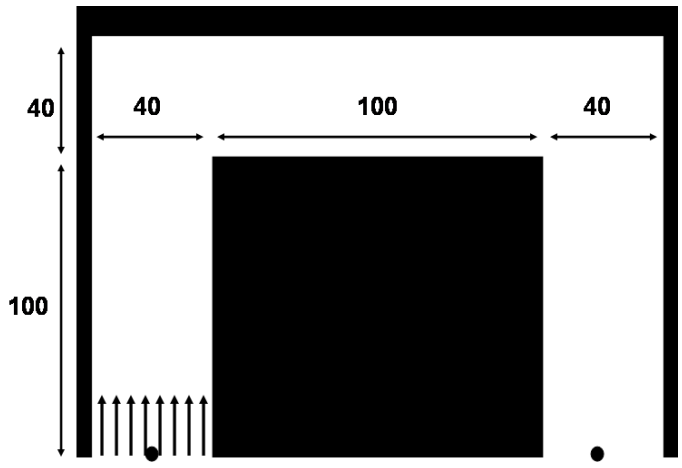

Figure 6.6: Rectangular channel (40x10 voxels in cross-section) that takes two 90° corners.

The conductivity of this channel is computed by considering the channel as a serial connection of three channel, each 100 voxels long and 40x10 voxels in cross-section. The conductivity of a channel with a length of 100 voxels and a rectangular cross-section of 40x10 voxels is 33 voxel³ (cf. equation (5.17)). When the effect of the corners is neglected, the conductivity of the complete channel is 11 voxel³. This is an overestimation of the conductivity as the effect of the corners is not taken into account.

To compute the conductivity of the link by the direct numerical simulation, a regular grid is constructed and a body force parallel to the link between the nodes is imposed. This means that also the inflow of the fluid is parallel to the link, as is illustrated in figure 6.7. This situation differs from the situation described above (figure 6.6) as a different boundary condition is imposed. Applying the direct numerical simulation results in a conductivity of 37 voxel³.

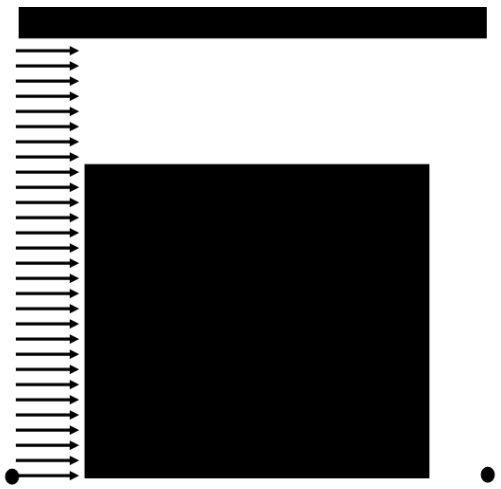

Figure 6.7: In the network approach the fluid flow between two nodes is parallel to the link between the nodes because a bode force is imposed which is also parallel to this link.

The conductivity is overestimated by the pore network approach. This is because boundary conditions do not result in a realistic simulation of the fluid flow between the nodes. This can in some cases, as in the case shown here, result in an overestimation of the conductivity of the link.

Figure 6.8 shows the fluid velocities in the channel for the two boundary conditions. Clearly, the fluid velocity in the channel is higher when the inflow is considered to be parallel to the link between the nodes.

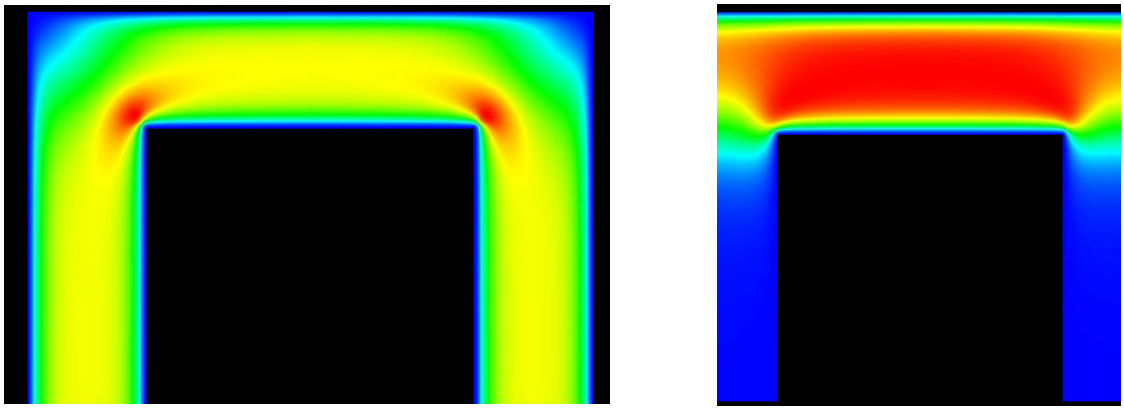

(a) (b)

Figure 6.8: Fluid velocity (blue: low velocity; red: high velocity) in the sample when the inflow is perpendicular to the inlet (a) and when the inflow is parallel to the link between the nodes (b). The latter situation is the case when the conductivity of the link is computed in the pore network approach.

A validation on larger and more realistic samples remains necessary. In the next sections the pore network approach is compared to a direct numerical simulation and laboratory experiments.

6.2 Comparison to direct numerical simulation

The pore network approach is developed to save computational power compared to the direct numerical simulation. The latter is however a relatively accurate method. Therefore a direct numerical simulation is used to compute the permeability of some samples for validation purposes. As the direct numerical simulation requires a lot of computation time and memory, the size of the samples is limited to 400x400x100 voxels. Hereto the scanned and thresholded samples described in chapter 4 are cut in slices of 100 voxels in height. Figure 6.9 illustrates this. As the CT image of the pavestone samples are 900 voxels high and the limestone samples 700 voxels high, 32 samples of 400x400x100 voxels are obtained.

The computed permeabilities for both methods are given in figure 6.10. The permeabilities obtained by the pore network approach are obtained using an α of 100%.

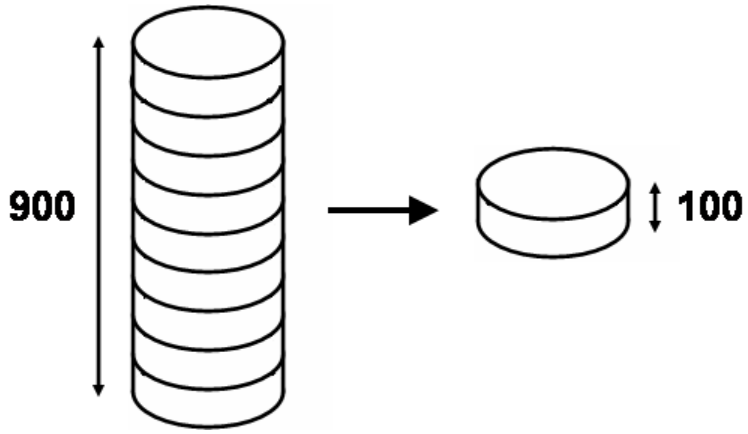

Figure 6.9: The samples are too large to compute their permeability by the direct numerical simulation. Therefore the samples are cut in slices of 400x400x100. The permeabilities of these slices are then determined by both methods.

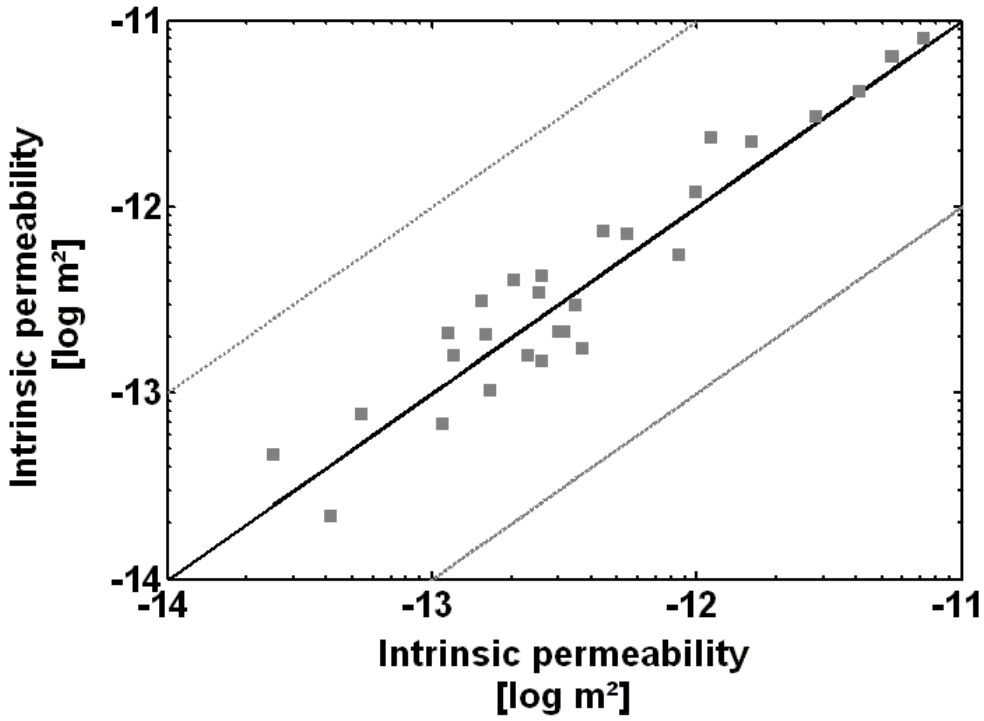

Figure 6.10: Intrinsic permeabilities below computed by the direct numerical simulation over the permeabilities obtained by the pore network approach using an α of 100%. The black line indicates the result of the direct numerical simulation. The grey lines mark a difference of one order of magnitude from the direct numerical simulation result.

The permeabilities computed by the pore network approach and the direct numerical simulation are in the same order of magnitude. In the 8th slice of the pavestone B sample a zero permeability was obtained as there was no connection between the inlet and the outlet. This confirms the zero permeability measured on the pavestone B sample (cf. table 2.1). The difference between both methods is larger for the slices with a lower permeability. This can be explained by the small sizes of the samples (being only 100 voxels high). Errors have a relatively higher impact than when they occur in larger samples.

The pore network approach was also applied on these samples using different values for the merge parameter α, i.e. for an α of 75%, 50% and 25%. The results for 16 samples are shown in figure 6.11. The trend noticed in the other 16 samples was exactly the same, but these are not plotted to avoid an overload of information on the plots.

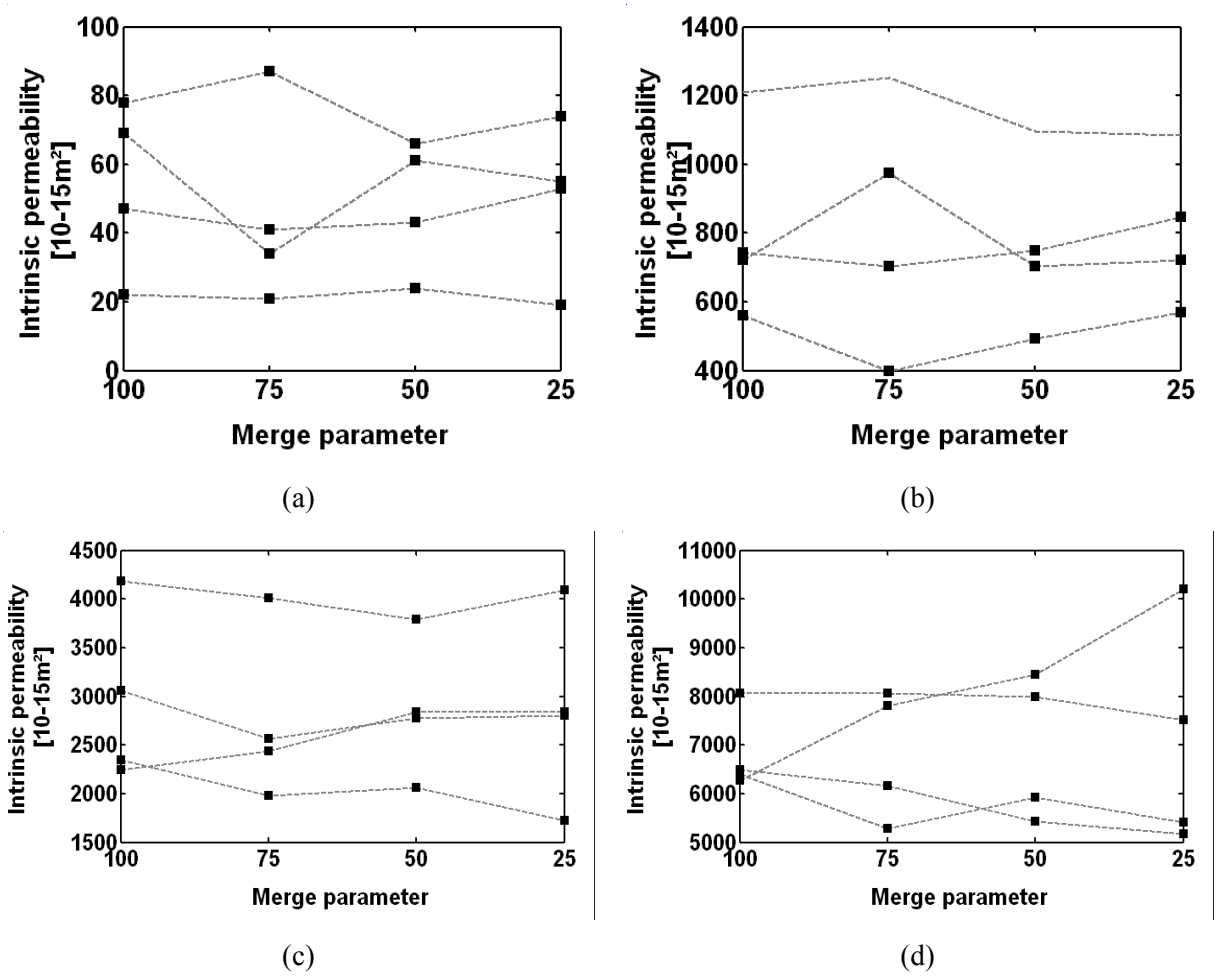

Figure 6.11: Intrinsic permeabilities obtained by the pore network approach using an α of 100%, 75%, 50% and 25%. There is no correlation between the merge parameter α and the intrinsic permeability.

No uniform trend in the computed intrinsic permeability can be seen when increasing or decreasing α. For some samples a lower α results in a lower permeability, for others the opposite is true. This is also noticed in the previous section. The flow of the fluid in the network can be complicated or facilitated by merging pores. This is illustrated in figure 6.12. These Miró-like drawings are only generic. Some details might therefore not be correct. The nodes might for example not have been placed perfectly at the geometrical centre of the pores.

When the blue and yellow pores in figure 6.12a are merged, the partition shown in figure 6.12b is obtained. As a fluid can more directly go from the green pore to the red pore (or in the opposite direction) in the latter figure, the conductivity increases as the blue and yellow pore are merged. For figures 6.12c and 6.12d the opposite applies. Therefore it is not possible to predict whether the permeability will increase or decrease when α is changed.

Performing permeability computations using different values for α is however useful to assess its impact and to assess the sensitivity of the obtained permeabilities to this parameter.

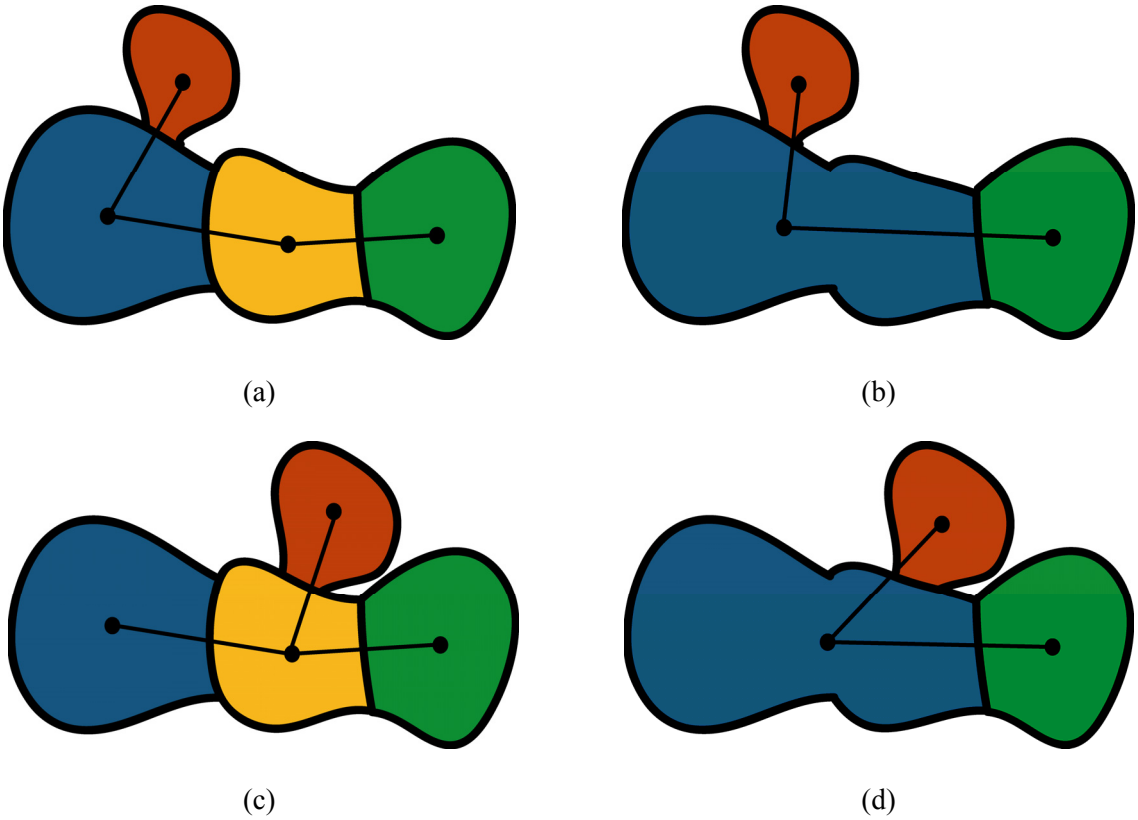

Figure 6.12: Merging two pores can result in an increased or a decreased conductivity. This is because the fluid is supposed to flow between the nodes of the different pores. Merging the yellow and blue pores in figure (a) results in figure (b). The fluid in (b) can more directly travel between the green and red pore and thus the computed permeability increases. The opposite is true for the situation shown figures (c) and (d).

The pore network methodology was around 12 times faster than a direct numerical simulation[20]. Beside the computation time, the memory needed for a direct simulation is much larger than for the pore network method. The latter is therefore able to handle samples that are too large for a direct simulation.

6.3 Comparison to laboratory measurements

A mercury intrusion experiment was performed by CoreLab on the Altamura limestones. This experiment is also simulated by the pore network model. Also the laboratory permeabilities are compared to the permeabilities obtained from the pore network approach.

6.3.1 Mercury intrusion experiments

Mercury intrusion experiments enable getting an insight in the pore size distribution of the pore space. The pore network can simulate these experiments as the pores are separated from each other at the bottlenecks between them. Comparing the results from a mercury intrusion experiment to the

[20] The computations were performed on the AMD Opteron Cluster of the K.U.Leuven. It consists of 164 dual Opteron250 servers, with 2GB RAM, 123 4-way Opteron servers with 4GB RAM, several nodes with 16GB RAM, and two 8-way nodes. In total, 256 nodes are interconnected with a fast Infiniband network.

simulation of this experiment by the model can therefore provide insight in the quality of the pore partition.

By plotting the intruded mercury volume over the applied pressure, a continuous curve is obtained in a mercury intrusion experiment. Due to the limited resolution of the pore space image, the throat apertures have discrete values. A mercury intrusion simulation therefore appears as dots on a pressure-volume plot.

In the simulation the interface between two pores is assumed to be circular. The radius is computed by equation (5.40). This is of course a simplification. Moreover, the limited resolution of the images also affects the simulated mercury intrusion. The pore sizes are continuous values, but because of the discrete sizes of the voxels, these continuous values are grouped into classes of discrete values. In that way the sizes of some pores are overestimated while the sizes of other pores are underestimated.

The results of the experiments and simulations on the limestone samples are shown in figure 6.13.

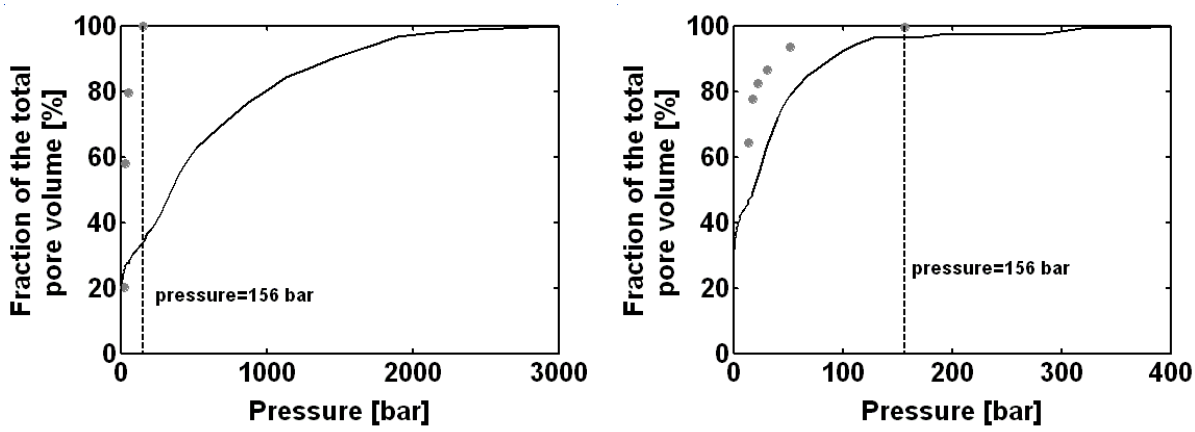

Figure 6.13: Mercury intrusion experiments (black full line) and simulations (grey dots) on the Altamura limestone samples. A pressure of 156 bar (dashed vertical line) corresponds to the pressure required to intrude a pore with a voxel size of 95 µm which is the image resolution.

The simulation of the mercury intrusion differs completely from the experimental mercury intrusion for the sample plotted in figure 6.13a. At a pressure of 156 bar, corresponding to the voxel size of 95 µm, only 34,5% of the total volume is filled with mercury. It is important to bear in mind, when interpreting these data, that smaller pores can prevent the intrusion of larger pores which results in an underestimation of the intruded volume (cf. section 5.4.2). Therefore one cannot conclude that 65,5% of the pore volume has dimensions below 95 µm. But it is an indication that a large fraction of the pore volume might fall below the image resolution (**error 1: resolution error**).

As explained in section 4.1.2, the procedure to select a threshold value by matching the porosity of the thresholded image to the porosity of the sample measured in the laboratory will cause an error when a large fraction of the pores fall below the resolution. These pores are not included in the porosity of the thresholded image and as a result the pores that are larger than the resolution and hence can be detected in the thresholded image, have to compensate for the pores than cannot be detected. The larger pores are thus overestimated (**error 2: threshold value error**). This can explain the result for the mercury intrusion shown in figure 6.13a. As the larger pores are overestimated, the mercury can intrude these pores at a lower pressure which can be seen in figure 6.13a.

The same can be seen, although less pronounced, for the limestone sample B shown in figure 6.13b. At a pressure of 156 bar 96,5% of the pore volume is intruded by mercury. This implies that at least

96,5% of the pore volume is above the resolution and can be detected from the CT images. The simulated mercury intrusion values more or less follow the same trend as the experimental values, but are slightly higher.

6.3.2 Permeability measurements

The permeabilities of the samples were measured in the laboratory and computed from the CT images using the pore network approach. The CT images of the pavestone samples contained 400x400x900 voxels. The limestone samples are 400x400x700 voxels large. Table 6.1 gives the results for both methods. The relative error of the pore network results compared to the laboratory results are given in table 6.2.

	Intrinsic permeability by CoreLab [log m²]	**Intrinsic permeability by the pore network model [log m²]**			
		α=100%	**α=75%**	**α=50%**	**α=25%**
pavestone A	-10.50	-10.83	-11.02	-11.05	-11.04
pavestone B	-	-	-	-	-
limestone A	-14.00	-14.68	-14.74	-14.80	-14.74
limestone B	-10.64	-11.29	-11.31	-11.35	-11.33

Table 6.1: Permeabilities of the pavestone and limestone samples measured in the laboratory and computed by the pore network methodology using different values for the merge parameter α.

	Intrinsic permeability by CoreLab [log m²]	**Relative error compared to the intrinsic permeability measured in the laboratory [%]**			
		α=100%	**α=75%**	**α=50%**	**α=25%**
pavestone A	-10.50	-3.16	-4.99	-5.26	-5.10
pavestone B	-	-	-	-	-
limestone A	-14.00	-4.84	-5.32	-5.68	-5.32
limestone B	-10.64	-6.11	-6.32	-6.67	-6.45

Table 6.2: Relative error on the intrinsic permeabilities of the pavestone and limestone samples compared to the intrinsic permeability measured in the laboratory using different values for the merge parameter α.

No data are included for pavestone B as this sample was impermeable. This results was also found by the pore network approach. The laboratory experiments and the pore network model computations result in permeabilities of the same order of magnitude. The permeabilities are underestimated in the

pore network approach by approximately 5%. Again, there appears to be no straightforward correlation between the computed permeability and the merge parameter α.

It is difficult to indicate the importance of the different errors in these results as in some cases the errors compensate for each other. The limestone A contains a large pore fraction that falls below the image resolution. This causes two errors: a resolution error (**error 1**) and a threshold value error (**error 2**). The resolution error results in an underestimation of the permeability as a fraction of the pore space is not detected as such. This leads to a loss in connectivity which affects the permeability computation. By the later selection of the threshold value the size of the larger pores are overestimated which evidently leads to an overestimation of the permeability. Which error is responsible for which deviation from the laboratory result and to what extent, is not possible to tell. Also because other errors are made by applying the developed pore network model.

6.4 Impact of the threshold value and resolution

The complete methodology to compute the permeability from CT images does not only consists of the pore network computation, but also involves the acquisition of the CT images and the subsequent thresholding. Errors induced in the acquisition and in the thresholding evidently affect the finally computed permeability. The resolution achieved in the CT image is a crucial parameter as this determines the minimal size of the pores that can be detected. The impact of the resolution and the sensitivity of the permeability to the threshold value are evaluated in this section.

6.4.1 Sensitivity of the permeability to the threshold value

By applying one global threshold value on the CT image of the different samples, an error is made (**error 3: segmentation error**). It is not possible to quantify the impact of this error on the computed permeability. Yet, as for the porosity (cf. section 4.2.1), the sensitivity of the permeability to the threshold value can be assessed.

The pavestone A and limestone A sample are thresholded using different threshold values and subsequently the permeability of these thresholded images is computed using the pore network approach. Figure 6.14 contains the obtained permeabilities together with the porosities for these threshold values determined in section 4.2.1.

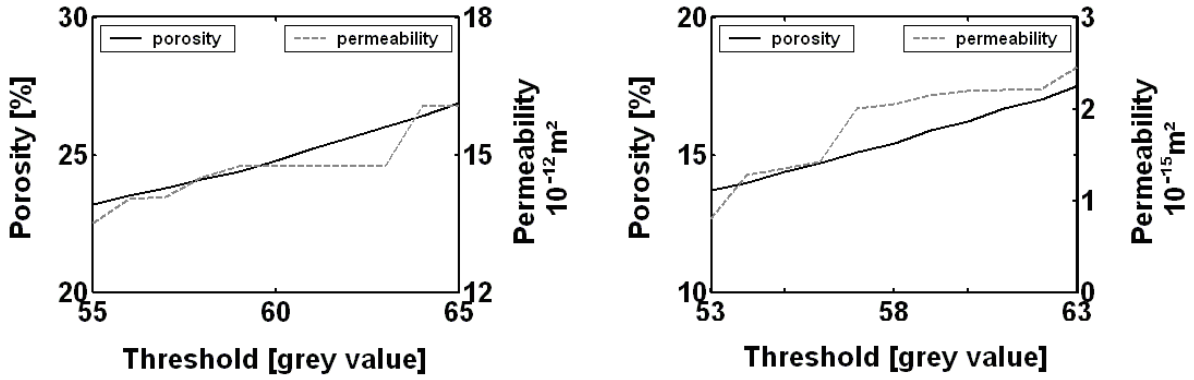

Figure 6.14: Sensitivity of the permeability and porosity of the pavestone A sample (a) and limestone A sample (b) to the threshold value.

A change of 5 units in the threshold value with respect to the determined threshold value (cf. section 4.2.1) results in an absolute change in permeability of approximately 8% for the pavestone.

Increasing the threshold value for the limestone sample by 5 units results in a permeability increase of 20%. The permeability decreases by 60% when the threshold value is decreased 5 units.

A change in threshold value is directly reflected in a change in porosity. The permeability however does not necessarily change with the threshold value. In that case the pore volume that is gained or lost, has not affected the permeability. The gained or lost pore volume might for instance be non-effective porosity. In other cases the permeability significantly changes for a changed threshold value. This can be due to new connections that are created or by connections that are lost due to a different threshold value.

6.4.2 Impact of the resolution

To examine the impact of the resolution on the permeability computations, the resolution of the acquired CT images of the pavestone A and limestone A sample is artificially decreased by merging several voxels in the CT image. The resolution is for instance decreased by a factor 2 by merging 2x2x2 voxels into one voxel. The attenuation coefficient of this voxel is the average of the 8 voxels that are grouped into one. Again, the threshold value was determined by matching the porosity of the thresholded image to the laboratory porosity. Subsequently the permeability of the new images is computed using an α of 100%. The results are summarized in table 6.3.

pavestone A		**limestone A**	
voxel size [µm]	**permeability [10^{-15} m²]**	**voxel size [µm]**	**permeability [10^{-15} m²]**
100	14745	100	2,0
200	8696	200	0,4
300	6315	300	0,2
400	1507	400	0,0
500	413	500	0,0

Table 6.3: Permeability of the pavestone A and limestone A sample for different spatial resolutions. An α of 100% is used in the permeability computations.

The permeability significantly decreases when images with a lower spatial resolution are used. When the resolution of the limestone sample is decreased by a factor 4 or more, the computed permeability becomes zero. For the pavestone sample the permeability decreases by a factor 36 when the resolution is decreased by a factor 5. This demonstrates the large impact the resolution has on the permeability computations.

6.5 Validation of the simplification to cylindrical links in the link conductivity computation

In chapter 5 it was described how the local conductivities of the links in the network are computed using a direct numerical simulation. Most pore network approaches determine the local conductivities by simplifying the links to uniform channels with regular cross-sectional shapes (*Kovscek et al., 1993; Blunt, 1997a; Blunt, 1998; Fenwick and Blunt, 1998; Dillard and Blunt, 2000*; *Hui and Blunt, 2000, Vandersteen et al., 2003*). Delerue considered the links to be cylindrical (*Delerue, 2001*). This simplification was considered to be too radical and hence the resulting computed permeability likely to be inaccurate. This justified the choice for the application of a direct numerical simulation that requires more computation time. The assumption that the simplification of the links to cylinders leads to inaccurate permeability computations is validated in this section.

This is done using the pore network construction developed in this work (cf. section 5.1). But instead of using the direct numerical simulation to compute the local conductivities of the links, these are now considered as a serial connection of two cylinders. The length of the cylinders is the distance from the centre of the pore to the centre of the interface between the pores. The radius is slightly more difficult to obtain. Delerue created a pore network by inflating balls and used the radii of these balls for the cylinder radii (figure 5.15). Here three different approaches to determine the cylinder radius are followed. The first uses the maximum aperture of the pore which will result in an overestimation of the conductivity. The second uses the aperture of the throat between the two neighbouring pores which will result in an underestimated conductivity. A last approach uses cylinders having a volume equal to the half of the pore volume. The radius of these cylinders is then computed as follows:

$$\frac{V_{pore}}{2} = \pi r_{cilinder}^2 \cdot L_{cilinder} \Rightarrow r_{cilinder} = \sqrt{\frac{V_{pore}}{2\pi \cdot L_{cilinder}}} \tag{6.1}$$

Figure 6.15 contains the computed permeabilities for the 32 samples used in section 6.2. The network was constructed using an α of 100%.

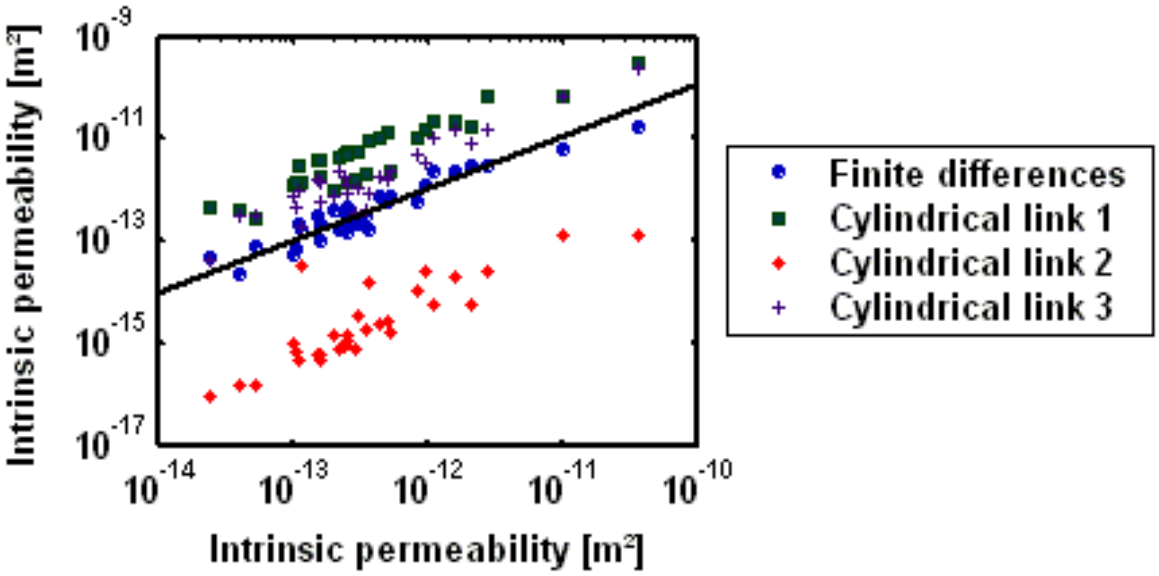

Figure 6.15: Intrinsic permeabilities computed by the direct numerical simulation over the permeability obtained by the pore network approach using a simplification to cylindrical links and a direct numerical simulation for the computation of the local conductivities. The cylinder radius used is respectively the maximum aperture of the pore (cylindrical link 1), the aperture of the throat (cylindrical link 2) and a radius obtained from formula (6.1) (cylindrical link 3). The black line indicates the result of the direct numerical simulation.

A large difference appears between the different calculations where the links are simplified to cylinders. When the maximum aperture in the pore is used for the radius of this cylinder, the conductivity is largely overestimated (factor 15). When the aperture of the throat between the pores is used as the radius, a large underestimation (factor 61) is obtained. Using formula (6.1) gives the best results, but still the permeabilities are overestimated by a factor 5. The results from the approach using a direct numerical simulation to compute the local conductivities of the links, are closest to the results obtained by the full direct numerical simulation. The use of direct numerical simulations to compute the link conductivities instead of simplifying these links to cylinders thus results in more accurate permeability computations.

6.6 Simulation of the impact of erosion and cementation on the permeability

A simplified model of erosion and cementation is included in the network model. The voxels at the interfaces are altered from the one form into the other to imitate erosion or cementation processes. This was explained in section 5.4.1 and illustrated in figure 5.24.

Different stages of erosion are first applied on the four samples. The computed permeabilities are given in table 6.4. The erosion thickness indicates how many voxels are removed from the interface between the matrix and the pore space.

erosion thickness [voxel]	permeability [10^{-15} m²]			
	pavestone A	pavestone B	limestone A	limestone B
0	31478	0	10	23047
1	52346	8402	4518	50565
2	63867	16374	7912	64000
3	68724	23894	9512	72577

Table 6.4: Permeability of pavestone A and limestone A for different stages of erosion. An α of 100% is used in the permeability computations.

Evidently, the permeabilities of all samples increase when erosion takes place. The impermeable pavestone B sample becomes permeable for an erosion thickness of 1.

Subsequently cementation is simulated. Table 6.5 contains the resulting permeabilities.

cementation thickness [voxel]	permeability [10^{-15} m²]			
	pavestone A	pavestone B	limestone A	limestone B
0	31478	0	10	23047
1	18780	0	3	6551
2	3065	0	0	131
3	74	0	0	0

Table 6.5: Permeability of pavestone A and limestone A for different stages of cementation. An α of 100% is used in the permeability computations.

When cementation is simulated, the permeabilities of the samples decrease and eventually they all become zero.

As demonstrated, the pore network approach can be used to assess the impact of erosion and cementation on the permeability. Finer erosion and cementation models exist (*Russ, 2002; The MathWorks, Inc., 2007*) and other models simulate reactive transport in which, beside changes in solid and pore geometry, also advection, diffusion, reactions between multiple aqueous species and reactions between the aqueous solution and minerals are taken into account (*Kang et al., 2006; Li et al., 2006; Tartakovsky et al., 2007*).

6.7 Conclusions

The pore network approach to compute the permeability of samples based on their X-ray computed tomography images is validated in this chapter. The approach is first applied on some generic samples for which the conductivity could be computed analytically. This revealed some shortcomings of the

pore network approach. In the approach, the fluid is forced to flow between the nodes of the network. This flow path can significantly differ from the real fluid path when the nodes in the network are not placed along the real flow path (**error 4: network topography error**). This can make fluid flow through the network more complicated than the fluid flow in the real sample and thus a lower permeability is obtained. Predicting the impact of the merge parameter on this error is not possible as merging pores can as well complicate as facilitate the fluid flow.

Furthermore, errors occur in the computation of the local conductivities of the links. A discretization error is made by the generation of the grid because the cells at the edges of the grid does not always coincide perfectly with the voxels of the pore space image (**error 5: discretization error**). This error can however be kept small as the number of cells in the grid can be increased without largely affecting the computation time and memory required. Another error in the computation of the local conductivities of the links is made because a body force parallel to the link between two nodes is imposed on the fluid (**error 6: boundary condition error**). In that way boundary conditions are applied in the conductivity computation that do not correctly simulate the fluid flow.

When comparing the permeability computed by the direct numerical simulation and by the pore network approach, the results from both approaches matched well. The results were in the same order of magnitude and the same trends in permeability between the samples could be observed. However no clear correlation exists between the merge parameter α and the permeability. This makes it impossible to predict whether the permeability will increase or decrease when α is changed. Beside a good match between the permeabilities obtained from both approaches, the pore network methodology also appeared to be around 12 times faster than the direct numerical simulation. Both computations were performed on the AMD Opteron Cluster of the K.U.Leuven. Moreover, the pore network approach was also able to handle samples that are much larger than the ones that can be treated by the direct numerical simulation.

Mercury intrusion experiments and simulations were performed for the limestone samples. This revealed that a large fraction of the pore space of the limestone A sample falls below the image resolution (**error 1: resolution error**). This in turn results in an error made by the methodology to determine the threshold value (**error 2: threshold value error**). The same applies for the limestone B sample, but the fraction of the pore space below the image resolution is rather small for this sample. Hence, the errors induced can expected to be smaller.

The complete methodology, including the acquisition of CT images and thresholding, was validated by a comparison to laboratory experiments for the four test samples. The computed permeabilities and the experimentally obtained permeabilities are in the same order of magnitude. The pavestone B sample turned out the be impermeable from the laboratory measurements. This was also discovered by the pore network approach.

Beside the errors listed in this chapter, an error is made by threshold method, namely the use of one global threshold value (**error 3: segmentation error**). This error was evaluated more in detail in chapter 4. In this chapter the sensitivity of the permeability to the threshold value was assessed. It appeared that the threshold value has a larger impact on the permeability than on the porosity. This is logical as only a small increase or decrease in porosity can have large implications for the connectivity of the pore space and hence for the permeability.

The validation addressed all the errors that arise in the developed methodology. Yet, it is not possible to quantify their impact on the resulting error.

7. Conclusions and perspectives

7.1 Conclusions

The purpose of this work is to use X-ray computed tomography to compute the permeability of porous samples. This is done by first obtaining an image of the pore space from a CT image of the sample and then modelling the fluid flow through this pore space. The advantage of such an approach, compared to the classical methods as laboratory measurements and geophysical loggings, is that a model allows changing several parameters. The impact of, for instance, processes like erosion or cementation on the permeability of the sample can be assessed by simulating these processes on the image of the pore space. This can be useful information in the characterization of a reservoir rock. Also because CT is more and more used in the characterization of reservoirs.

By the development of a methodology computing the permeability of a porous sample based on a CT image of the sample, this works aims to provide a useful tool that can aid and support such characterization campaigns. In these campaigns CT can be used to get 3D information on the porosity and mineralogy of samples (*Remeysen, 2007*). Once the pore space of these samples is obtained, the methodology developed can, relatively quickly, be assessed the permeability of the sample in addition. And in case the pore space of the sample is cemented, the cementation material can be removed from the CT image by thresholding and the permeability can be computed in the assumption that the pore space was not cemented.

However, the developed methodology does not offer (and also does not intend to) an approach for a complete characterization of the permeability of a reservoir. Such a characterization requires a multi-scale approach. This work is only occupied by the question how the permeability of a sample can be derived from a CT image of that sample.

The methodology starts by acquiring a CT image of the sample. Subsequently an image of the pore space is extracted from the CT image by a threshold procedure. After the image of the pore space is obtained, the permeability of this pore space is computed by the use of a pore network. Such a pore network is a simplified representation of the pore structure. This is necessary as the images acquired by the X-ray CT scanner are too large for a direct numerical simulation of the fluid flow through the sample. The developed methodology is applied on two pavestones and two Altamura limestones.

The samples are scanned using an AEA Tomohawk μCT scanner. The sources used in μCT scanners are smaller than in classical CT scanners and thus a higher resolution can be achieved. The limited spatial resolution of the imaging system poses a serious limitation on the applicability of the presented methodology. Pores having dimensions that fall below the image resolution can evidently not be detected in the CT images. Consequently these pores are not taken into account in the subsequent permeability computation. This causes an error which can become very significant when a lot of connectivity in the pore structure is lost (**error 1: resolution error**). Computing the permeability as is done in this work is thus only possible when the resolution is lower than the size of the pores making up the pore space.

This already illustrates the importance of the acquisition of CT images of a sufficiently high quality. This quality depends on a lot of factors that are strongly interrelated. By trial-and-error experiments it is possible to look for parameters resulting in an image of a satisfying quality. But such an approach demands a lot of time and is often not possible. Therefore a simulator for the used CT scanners was developed.

The simulator is based on the 2D simulator developed by De Man at UZ Gasthuisberg in 2001 (*De Man, 2001*). Also a 3D simulator was developed. Filtration of the spectrum, noise, scatter and the EEGE effect are included in the simulations. The noise is implemented by using a pragmatic model.

The model takes into account the most important features affecting the noise such as the number of integration frames and the use of filters. Scatter is also implemented using a very simple model. More accurate scatter models can be implemented, but they require a lot of computation time.

The simulator is adjusted to the Skyscan 1072 Desktop μCT scanner and the AEA Tomohawk μCT scanner of the Department of Metallurgy and Materials Engineering (MTM) of the K.U.Leuven. For both scanners a spectral reconstruction of the radiation produced by their X-ray sources was performed (*Aiello et al, 2004; Stumbo et al, 2004*).

The simulator has the advantage that every parameter or phenomenon in the scanning process can be changed. A lot of simulations can be done in a relatively short time. This makes the simulator a suitable tool to perform trial-and-error experiments. Moreover, the simulator does not require real objects and the objects simulated are perfectly known. This can be convenient in calibration procedures and to compare the reconstructed to the original image. The use of the simulator in image optimization is demonstrated by a small case. But maybe more important than image optimization is the applicability of the simulator in assessing the impact of several parameters and phenomena on the image quality. The simulator allows the user to examine the limitations of the imaging technique and the processes affecting the image quality and eventually to look for solutions. This is demonstrated by measuring the gold content in rock samples using X-ray computed tomography.

After the four samples are scanned, an image of their pore space is obtained by thresholding. A global threshold value is defined and all pixels with a grey value below this threshold value are considered to be pore pixels. The threshold value is selected by matching the porosity of the thresholded images to porosities measured in the laboratory.

Two types of errors arise when applying this threshold method. The first is caused by the selection procedure of the threshold value. Pores smaller than the image resolution are not detected in the CT images and do not contribute to the porosity of the thresholded image. As a result the larger pores in the thresholded image are overestimated as they have to compensate for the non-detected pores (**error 2: threshold value error**).

The second types of errors are related to the use of one global threshold value (**error 3: segmentation error**). The limited resolution of the imaging technique causes a blurring of the edges and pores having different sizes require different threshold values. And due to beam hardening the reconstructed attenuation does not only depend on the material contained in a pixel, but also on the position of that pixel in the object. Pores at the edge therefore might by thresholded differently than pores at the centre of the sample. Also the EEGE effect and image noise causes errors in the reconstruction of the attenuation coefficient and might hinder a correct thresholding.

The impact of these factors is assessed using the 3D simulator. The simulator makes it possible to examine noise, beam hardening, the EEGE effect and the limited resolution separately. Moreover, the object used in the simulations is exactly known. This facilitates a comparison between the thresholded image and the original image. The thresholding was mainly affected by the limited resolution which has a bigger impact for the limestones. This is explained by the larger fraction in small pores in the limestones. A decrease in resolution mainly affects the detection of the small pores and the estimation of their size.

Once images of the pore structure are obtained, the permeability of the samples is computed. It is assumed that the sample is completely saturated by the fluid for which the permeability is computed. This implies that only one-phase flow is considered and that no relative permeabilities are determined. Direct numerical simulations exist to compute the permeability using the Navier-Stokes equations. These methods however require a lot of computational power which becomes immense for large datasets. The datasets used in this work, i.e. the images obtained by computed tomography, generally contain 1000x1000x1000 voxels. To be able to handle these datasets, a pore network approach is used.

A pore network is a simplified representation of the pore space in which the individual pores are replaced by nodes that are connected by hydraulic links.

The partitioning of the pore space into individual pores brings up the question how a pore can be defined. Different approaches using different definitions for a pore were developed. Delerue first performed a skeletonization algorithm on the pore space and rebuilt the pore space from the skeleton (*Delerue, 2001*). The skeletonization algorithm is beside computationally very expensive, not very robust. A small adaptation to the pore space sometimes gives rise to a completely different partition. A new approach is therefore developed. It is based on the rather intuitive definition that pores are separated from each other at the bottlenecks in the pore space. This turned out to be a fast and robust algorithm dividing the pore space into individual pores.

The algorithm uses a merge parameter α, ranging from 0% to 100%. This parameter is used to decide whether or not a narrowing between two pores is considered to be a throat separating the two pores. In case the narrowing is relatively wide compared to the width of the pores, the pores are considered to be one pore containing a narrowing. In the other case the pores are separated. Different values for α result in different partitions. An α of 100% results in a partition with a maximal number of pores having a maximal connectivity. Using an α equal to zero makes every connected pore to be merged into one pore. This leads to a very rough partition in which the connectivity of the pores is zero.

Once the pore space is partitioned into individual pores, the pores are replaced by nodes and the nodes of neighbouring pores are connected by links. The fluid is now assumed to flow from node to node in the network. This flow path in the network differs from the path the fluid follows through the real sample when the nodes are not placed on this real flow path (**error 4: network topography error**). In case the nodes are not on this path, the flow in the network is complicated compared to the real flow path and the conductivity to flow from one pore to the other is underestimated.

After the construction of the pore network, the local conductivities of the links are computed. Again, a new approach is used. Most authors determine these local conductivities by simplifying the links to standard geometrical shapes (*Kovscek et al, 1993; Blunt, 1997a; Blunt, 1998; Fenwick and Blunt, 1998; Dillard and Blunt, 2000; Hui and Blunt, 2000*). This however is a very strong assumption. The local conductivities in this work are computed by a direct numerical simulation solving the Stokes equations. The Stokes equation can be used for non-compressible, Newtonian fluids and for a steady state, laminar flow. A direct numerical simulation offers an accurate method to model the fluid flow. But instead of applying a direct numerical simulation on the sample as a whole the sample is divided into a large number of smaller samples by the network model. In that way, the accuracy of a direct numerical simulation is combined with the advantage of the network model towards computational power.

The application of the direct numerical simulation requires the generation of a grid and the definition of the boundary conditions. A regular grid is constructed as this allowed using the freely available Stokes solver developed by Verleye *et al.* (2007 & 2008). The cells in the grid are parallel to the link connecting the two nodes. As the cells at the edges of the grid do not always coincide perfectly with the voxels of the pore space image, a discretization error is made (**error 5: discretization error**).

The boundary condition imposed is a body force parallel to the link between the two nodes. This leads in some cases not to a realistic simulation of the fluid flow between the two nodes (**error 6: boundary condition error**).

When the local conductivities in the network are known, the flow through the network can be computed. First a mass conservation equation is constructed for every node. From the obtained system of equations the local pressures in and subsequently the flux through the network are determined. In addition a simple cementation and erosion model is implemented. In that way the impact of cementation and erosion on the permeability can be assessed. Also a mercury intrusion experiment can be simulated by the network model. During the partitioning of the pore space the aperture of the

bottlenecks in the pore space is computed. Thus the pressure to intrude mercury from one pore into another pore can be determined and the intrusion of mercury can be simulated.

The model is validated by several experiments and the errors made in the methodology are demonstrated and further evaluated. A comparison between the permeability of relatively small samples obtained by a direct numerical simulation and the pore network approach however revealed that the results from the both approaches were in the same order of magnitude.

The model developed is more or less generally applicable. A lot of pore network models use standard geometrical shapes to compute the conductivity of the links in the network. Often the used standard shape is chosen in function of the shape of the pores. By using a direct numerical simulation to determine these local conductivities no assumption on the shape of the pores is necessary. The partition procedure can however still be optimized, certainly for channel-shaped pores. This is further discussed in the next section where recommendations for further research are formulated.

The complete methodology to go from a CT image to a value for the permeability of the sample was considered. As stated already, the quality of the CT images and the thresholding procedure are crucial for accurate permeability computations. By using a simulator for the CT scanning process, the quality of the CT images and the subsequent thresholding was evaluated. It was also demonstrated how the impact of the threshold algorithm and the spatial resolution can be examined. By doing so the user can not only perform permeability computations, but he also gets an idea of the quality of these computations.

This is very important as the limited spatial resolution of the imaging system poses a serious limitation on the applicability of the presented methodology. Computing the permeability as is done in this work is only possible when the resolution is lower than the size of the pores making up the pore space. The resolution limitations are a bigger issue in permeability computations than when the porosity or composition of samples is measured. When trying to determine the permeability based on CT images, an evaluation of the pore sizes in relation to the resolution is therefore absolutely necessary.

7.2 Recommendations and perspectives

As stated in the introduction, the aim of this work is the development of a methodology to compute the permeability of a sample based on a CT image of the sample. The snake bites its tail in the conclusions where the developed methodology is summarized and evaluated. This evaluation sums the shortcomings of the methodology and the errors introduced in the complete process going from the CT image to the finally obtained value for the permeability. Some shortcomings are inherent to the technique of X-ray CT and the nature of a modelling approach which is a simplification of reality. Other shortcomings leave room for improvement. This section discusses the perspectives in the research domain where this work is situated. Moreover it gives recommendations how these shortcomings can be handled and how the methodology can be improved.

The perspectives and recommendations are structured according to the errors that are made when applying the developed methodology. Some errors can only be minimised, other might be solved by using a different approach.

- **Error 1: resolution error**

  The technique of X-ray computed tomography will certainly further improve. This will lead to an improved resolution, but also to a better image quality in general. More accurate detectors, better reconstruction and post-processing algorithms can minimize several artifacts such as beam hardening. Concerning the resolution, there is always a counterplay between the sample size and the resolution. A high resolution can be achieved using nano-scanners, but this is at the expense of

sample size. The relation between resolution, a representative sample size and the size of the pores will always remain an issue in permeability computations. Future research in this domain should therefore always take into account a thorough evaluation of the applicability of the developed methodology for the samples that are considered.

Examining the relation between the pore size distribution and the permeability can seriously help in such evaluations. It allows assessing the impact of the pore size on the permeability. In that way the minimal pore size that should be detected, and hence the minimal resolution, to get accurate permeability computations, can be defined.

A simulation of the scanning process can also help. Further improvements on the developed simulator can be obtained by implementing a more accurate noise and scatter model. When using CT images for the purpose of this work, noise and scatter did however not pose serious problems. The noise is limited by using a lot of integration frames and the amount of scatter can assumed to be low. The contrast is mainly affected by the X-ray spectrum which is often not known. It is recommended to try to measure the X-ray spectrum of the scanner for which a simulator is used.

The simulator is most useful in the assessment of the impact of several parameters and to examine the applicability of the CT technique. As is demonstrated in this work, the limitations of the technique for a given purpose can be determined by a simulator. Also the applied threshold algorithm can be properly evaluated by the simulator. Future work on X-ray computed tomography can benefit from such a simulation approach. Image optimization can also be performed, but the limitations one is confronted with, are often inherent to the technique or to the scanner that is used. Again, a simulator can help in outlining these limitations, but enhancing the image quality is only possible to a limited extent.

- **Error 2 and 3: threshold value error and segmentation error**

  A global threshold value is used to distinguish pore from matrix pixels. The porosity is used to select the threshold value as the porosity of the thresholded image is matched to the laboratory porosity. Both the application of the global threshold value as its selection pose problems. As it was not the purpose of this work to develop a technique to segment a CT image into a binary image of the pore space, this relatively simple threshold technique was applied.

  Yet, other segmentation techniques can be used to perform a more correct segmentation. Selecting or advising one method is not possible as no method with globally relevance and applicability exists. The recommended segmentation method and its optimal segmentation parameters depend on the material used, the application and the quality of the images. Hence, every application requires an evaluation of the appropriate segmentation technique.

- **Error 4: network topography error**

  This error arises when the position of the node in the network results in a more complicated fluid flow between the nodes than the real flow path in the sample. The error is thus caused by the algorithm converting the pore space into a pore network. There is undoubtly room for improvement to this algorithm and other partition techniques can be applied. The conversion of the pore space into a pore network could be improved by using a different approach to place the node. The choice of the position of the node could for example take into account the position of the throats with neighbouring pores. Another possibility to improve the partitioning is to avoid the merging of pores which result in links making up a small angle (figure 5.19).

  A solution for the merge parameter α might also be advisable as it introduces a user dependence. The consequent use of a merge parameter α of 100% can solve this issue. On the other hand, it is the author's opinion that in some cases the flexibility to use a different merge parameter is

convenient. For some samples an α of 100%, partitioning the pore space at every narrowing, can lead to an unnecessarily detailed partition.

The pores in the samples used in this research are more or less spherical and they do not have a direction in which the pores are substantially longer than in the other directions. When the pores are more tunnel-shaped, a different partitioning algorithm might be more appropriate. This algorithm can for instance make sure that every node can be seen by his neighbouring nodes. Two nodes "see each other" when the line between the two nodes lies completely in the two pores considered. When this is not the case, a node is added to the partition so that the "seeing" criterion is fulfilled. This is illustrated in figure 7.1.

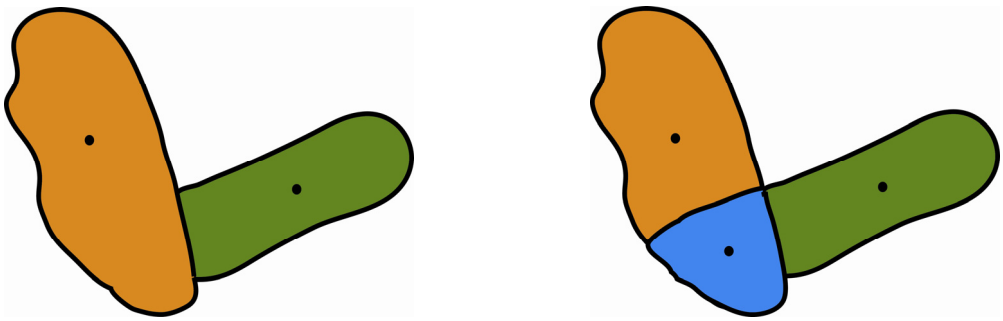

(a) (b)

Figure 7.1: When the pore space consists of tunnel-shaped pores, a different and more appropriate partitioning algorithm can be preferred. The partition obtained by the partitioning algorithm developed in this work (a) can further be partitioned by demanding that every node can be "seen" by his neighbouring nodes (b).

- **Error 5 and 6: discretization error and boundary condition error**

The boundary condition used in the direct numerical simulation of the fluid flow in the links of the network is a body force parallel to the link between the two nodes. In some cases this does not accurately simulate the real fluid flow between the two nodes. Boundary conditions taking into account the topography of the two pores of the link can result in a significant improvement of the methodology.

The direct numerical simulation used here requires a regular mesh. As the body force is imposed parallel to the link, the mesh also has to be constructed parallel to this link. The discretization error arises because the cells at the edges of the grid do not always coincide perfectly with the voxels of the pore space image. This can also be solved by using different boundary conditions that do not require that the orientation of the cells in the mesh differs from the orientation of the voxels in the CT image. In that case the cells in the grid coincide perfectly with the edges in the voxel based image. Still, a dicretization error is made because the CT image contains discrete voxels. But this in turn becomes more an issue of the limited resolution of the imaging technique and at least no further discretization error is made in the construction of the grid. However, the discretization error made in the construction of the grid does not pore serious problems as the grid can be constructed at a high resolution without increasing the computation time significantly.

References

Aiello, S., Bottigli, U., Fauci, F., Golosio, B., Lo Presti, D., Masala, G.L., Oliva, P., Raso, G., Stumbo, S. and Tangaro, S., 2004. FLUXEN portable equipment for direct X-ray spectra measurements. Nuclear Instruments and Methods in Physics Research, 518, pp. 389–390.

Akin, S. and Kovscek, A.R., 2003. Computed tomography in petroleum engineering research Geological Society, London, Special Publications, 215, pp. 23-38.

Alvarez, R.E. and Macovski, A., 1976. Energy selective reonstructions in X-ray computerized tomography. Physics in Medicine and Biology, 21, pp. 733-744.

Anderson, S.H. and Hopmans, J.W., 1994. Tomography of soilwater-root processes. Proceedings of a symposium of the soil science society of America in Minneapolis, Minnesota, 4 Nov., 1992. SSSA Special Publication, 36, pp. 148. American Society of Agronomy, Inc., Soil Science Society of America, Inc., Madison, Wisconsin, USA.

Arns, C. H., Bauget, F., Limaye, A., Sakellariou, A., Senden, T. J., Sheppard, A. P., Sok, R. M., Pinczewski, W. V., Bakke, S., Berge, L. I., Øren, P. E. and Knackstedt, M. A., 2005. Pore-scale characterization of carbonates using X-ray microtomography. SPE Journal, 10, pp. 475-484.

Asker, M. and Derin, D., 1981. A recursive algorithm for the Bayes solution of the smoothing problem. IEEE Trans. Automat. Contr. AC26, pp. 558-561.

Ashbridge, D.A., Thorne, M.S., Rivers, M.L., Muccino, J.C. and O'Day, P.A., 2003. Image optimization and analysis of synchrotron X-ray computed microtomography (CT) data. Computers & Geosciences, 29, pp. 823-836.

ASTM, E1695-95, 1981. Standard Test Method for Measurement of Computed Tomography (CT) System Performance. American Society for Testing and Materials, 1816 Race ST., Philadelphia, Pa 19103.

Bastiaens, W., 2000. Constructie van een µCT-simulator voor geologische doeleinden. Master's thesis, Katholieke Universiteit Leuven, Belgium.

Bentz, D.P., 1997. Three-Dimensional Computer Simulation of Portland Cement Hydration and Microstructure Development. Journal of the American Ceramic Society, 80(1), pp. 3-21.

Berland, L.L., 1987. Practical CT: Technology and Techniques. Raven Press, New York, US, 271 p.

Bernard, D. and Chirazi, A., 2006. Numerically enhanced microtomographic imaging method using a novel ring artefact filter. In: Desrues, J., Viggiani, G. and Besuelle, P. (eds). Advances in X-Ray Tomography for Geomaterials, pp. 119-124. Hermes Science Publishing Ltd., London, UK.

Beucher, S., 1991. The watershed transform applied to image segmentation. Proceedings of the Pfefferkorn Conference on Signal and Image Processing in Microscopy and Microanalysis, pp. 299-314.

Beucher, S. and Meyer, F., 1992. The morphological approach of segmentation: the watershed transformation. In: Dougherty, E. (ed). Mathematical Morphology in Image Processing, chapter 12, pp. 433-481, Marcel Dekker, New York.

Bjørndal, L., Carlsen, O., Thuesen, G., Darvann, T., Kreiborg, S. ,1999. External and internal macromorphology in 3D-reconstructed maxillary molars using computerized X-ray microtomography. International Endodontic Journal, 32, pp. 3-9.

Blumenfeld, S.M. and Glover, G., 1981. Spatial resolution in computed tomography. In: Newton, T.H. and Potts, D.G. (eds). Radiology of the Skull and Brain: Technical Aspects of Computed Tomography, 5, pp. 3918-3940. C.V. Mosby Company, St.-Louis, US.

Blunt, M. and King, P., 1991. Relative Permeabilities from 2-Dimensional and 3-Dimensional Pore-Scale Network Modeling, Transport in Porous Media, 6, pp. 407-433.

Blunt, M.J., 1997a. Effects of heterogeneity and wetting on relative permeability using pore level modeling. SPE Journal, 2, pp. 70-87.

Blunt, M.J., 1998. Physically-based network modeling of multiphase flow in intermediate-wet porous media, Journal of Petroleum Science and Engineering, 20, pp. 117-125.

Brooks, R.A. and DiChiro, G., 1976a. Principles of computer assisted tomography (CAT) in radiographic and radioisotopic imaging. Physics in Medicine and Biology, 21, pp. 689-732.

Brooks, R.A. and DiChiro, G., 1976b. Beam hardening in X-ray reconstructive tomography. Physics in Medicine and Biology, 21, pp. 390-398.

Brown, G.O., Hsieh, H.T. and Lucero, D.A., 2000. Evaluation of laboratory dolomite core sample size using representative elementary volume concepts. Water Resources Research, 36, pp. 1199-1207.

Bryant, S., and Blunt, M., 1992. Prediction of Relative Permeability in Simple Porous-Media. Physical Review A, 46, pp. 2004-2011.

Bryant, S.L., King, P.R. and Mellor, D.W., 1993a. Network Model Evaluation of Permeability and Spatial Correlation in a Real Random Sphere Packing. Transport in Porous Media, 11, pp. 53-70.

Bryant, S.L., Mellor, D.W. and Cade, C.A., 1993b. Physically Representative Network Models of Transport in Porous-Media. AIChE Journal, 39, pp. 387-396.

Cardinal, H.N. and Fenster, A., 1990. An accurate method for direct dual-energy calibration and decomposition. Medical Physics, 17, pp. 327-341.

Carlson, W.D., Rowe, T., Ketcham, R.A. and Colbert, M.W., 2003. Applications of high-resolution X-ray computed tomography in petrology, meteoritics and palaeontology Geological Society, London, Special Publications, 215, pp. 7-22.

Carmeliet, J., Delerue, J.F., Vandersteen, K. and Roels, S., 2004. Three-dimensional liquid transport in concrete cracks, International journal for numerical and analytical methods in geomechanics, 28, pp. 671-687.

Carmeliet, J., Descamps, F. and Houvenaghel, G., 1999. A Multiscale Network Model for Simulating Moisture Transfer Properties of Porous Media. Transport in Porous Media, 35(1), pp. 67-88.

Chan, H.P. and Doi, K., 1985. Physical characteristics of scattered radiation in diagnostic radiology: Monte carlo simulation studies. Medical Physics, 12(2), pp. 152–165.

Chatzis, I. and Dullien, F.A.L., 1977. Modelling pore structures by 2-D and 3-D networks with application to sandstones. Journal of Canadian Petroleum Technology, 16, pp. 97-108.

Cheng, C.-W., Taylor, K.W. and Holloway, A.F., 1995. The spectrum and angular distribution of X-rays scattered from a water phantom. Medical Physics, 22(8), pp. 1235-1245.

Chien, Y.P. and Fu, K.S., 1974. Preprocessing and feature extraction of picture patterns. TR-EE 74-20, Purdue University, West-Lafayette, Indiana.

Cnudde, V. and Jacobs, P., 2004. Monitoring of weathering and conservation of building materials through non-destructive X-ray computed microtomography. Environmental Geology, 46, pp. 477-485.

Cho, S., Haralick, R. and Yi, S., 1989. Improvement of Kittler and Illingworth's minimum error thresholding. Pattern Recognition, 22(5), pp. 609–617.

Cho, Z.E., Jones, J.P. and Singh, M., 1993. Foundations of Medical Imaging, John Wiley & Sons.

Constantinides, G.N. and Payatakes, A.C., 1989. A three dimensional network model for consolidated porous media. Basic studies, Chemical Engineering Communications, 81, pp. 55-81.

Cormack, A.M., 1981. Early tomography and related topics. In: Herman, G.T. and Natterer, F. (eds). Mathematical aspects of computerized tomography. Springer-Verlag, Berlin, pp. 1-6.

Cox, I.J., Rehg, J.M. and Hingorani, S., 1993. A bayesian multiple hypothesis approach to edge grouping and contour segmentation. International Journal of Computer Vision, 11, pp. 5–24.

Cressie, N.A.C., 1993. Statistics for Spatial Data. Revised Edition. John Wiley and Sons, New York, US, 900 p.

Curry, T.S., Dowdey, J.E. and Murry, R.C., 1990. Christensen's Physics of Diagnostic Radiology. Lea and Febiger, London, UK, 522 p.

Davis, L.S., 1975. A survey of edge detection techniques. Computer Graphics Image Processes, 4, pp. 248-270.

Degryse, P., Van Geet, M., Waelkens, M., Swennen, R., Wevers, M., Viaene, W., 2001. Microfocus computer tomography as a means of assessing first damage in modern restoration mortars. International Journal for Restoration of Buildings and Monuments, 7(1), pp. 47 -61

Delerue, J.-F., 2001. Segmentation 3D, application à l'extraction de réseaux de pores et à la caractérisation hydrodynamique des sols. Thèse de doctorat, Paris XI Orsay.

Delerue, J.-F., Lomov, S.V., Parnas, R.S, Verpoest, I. and Wevers, M., 2003. Pore network modelling of permeability for textile reinforcements. Polymer Composites, 24(3), pp. 344-357.

Derin, H. Elliott, H., Cristi, R. and German, D., 1984. Bayes smoothing algorithms for segmentation of binary images modeled by Markov random fields, IEEE Transactions on Pattern Analysis and Machine Intelligence, 6, 707-720.

Derin, H. and Elliott, H., 1987. Modelling and segmentation of noisy and textured images using Gibbs Random Fields. IEEE Transactions on Pattern Analysis and Machine Intelligence, 9(1), pp. 39-55.

Desplentere, F., Lomov, S.V., Woerdeman, D.L., Verpoest, I., Wevers, M. and Bogdanovich, A., 2005. Micro-CT characterization of variability in 3D textile architecture. Composites Science and Technology, 65(13), pp. 1920 -1930.

De Graef, B., Cnudde, V., Dick, J., De Belie, N., Jacobs, P. and Verstraete, W., 2005. A sensitivity study for the visualisation of bacterial weathering of concrete and stone with computerised X-ray microtomography (CT). Science of the Total Environment, 341(1-3), pp. 173-183.

De Man, B., Nuyts, J., Dupont, P., Marchal, G. and Suetens, P., 1999. Metal streak artifacts in X-ray computed tomography: a simulation study. IEEE Transactions on Nuclear Science (46), pp. 691-696.

De Man, B., 2001. Iterative Reconstruction for Reduction of Metal Streak Artifacts in Computed Tomography. PhD-dissertation, Katholieke Universiteit Leuven, Belgium, 150 p.

Dillard, L.A. and Blunt, M.J., 2000. Development of a pore network simulation model to study nonaqueous phase liquid dissolution, Water Resources Research, 36, pp. 439-454.

Ding, M., Odgaard, A. and Hvid, I., 1999. Accuracy of cancellous bone volume fraction measured by micro-CT scanning. Journal of Biomechanics, 32, pp. 323-326.

Dixit, A.B., McDougall, S.R. and Sorbie, K.S., 1998. Analysis of relative permeability hysteresis trends in mixed-wet porous media using network models, proceedings of the 11th Symposium on Improved Oil Recovery, Society of Petroleum Engineers, Tulsa.

Du, X. and Ostoja-Starzewski, M., 2006. On the size representative volume element for Darcy law in random media. Proceedings of the Royal Society, London A, 462, pp. 2949-2963.

Duerinckx, A.J. and Macovski, A., 1979. Nonlinear polychromatic and noise artifacts in X-ray computed tomography images. Journal of Computer Assisted Tomography, 3(4), pp. 519-526.

Dullien, F.A.L., 1992. Porous media: Fluid transport and pore structure. Academic Press, 574 p.

Fagerlund, G., 1973. Determination of pore size distribution by suction porosimetry. Materials and Structures, 6(33), pp. 191-201.

Farber, L., Tardos, G. and Michaels, J. N., 2003. Use of X-ray tomography to study the porosity and morphology of granules. Powder Technology, 132, pp. 57-63.

Fatt, I., 1956a. The network model of porous media I. Capillary pressure characteristics, Trans AIME (207), pp. 144-159.

Fatt, I., 1956b. The network model of porous media II. Dynamic properties of a single size tube network, Trans AIME (207), pp. 160-163.

Fatt, I., 1956c. The network model of porous media III. Dynamic properties of networks with tube radius distribution, Trans AIME (207), pp. 164-181.

Franke, L., Pinsler, F., Hauenschild, C. and Gross-Fengels, W., 1995. X-ray diagnosis applied to study salt migration in impregnated structural elements. Surface treatment of building materials with water repellent agents, 1st international symposium, Delft, the Netherlands, pp. 13.1-13.10.

Fenwick, D.H. and Blunt, M.J., 1998. Network modeling of three-phase flow in porous media, SPE Journal, 3, pp. 86-97.

Freundlich, D. and Zaklad, H, 1981. Scintillation crystal-photomultiplier tube detectors. In: Newton, T.H., Potts, D.G. (eds). Radiology of the Skull and Brain: Technical Aspects of Computed Tomography, 5, pp. 4104-4111. C.V. Mosby Company, St. Louis.

Gambotto, J.P., 1993. A new approach to combining region growing and edge detection. Pattern Recognition Letters, 14, pp. 869–875.

Ganne, P., Vervoort, A. and Wevers, M., 2007. Quantification of pre-peak brittle damage: Correlation between acoustic emission and observed micro-fracturing. International Journal of Rock Mechanics and Mining Sciences, 44(5), pp. 720 -729.

Garboczi, E.J. and Bentz, D.P., 1996. Modelling of the Microstructure and Transport Properties of Concrete. Construction and Building Materials, 10(5), pp. 293-300.

Geman, S. and Geman, D., 1984. Stochastic relaxation, Gibbs distribution and the Bayesian restoration of images, IEEE Transactions on Pattern Analysis and Machine Intelligence, 6, pp. 721-741.

Glasbey, C.A., 1993. An analysis of histogram-based thresholding algorithms. CVGIP: Graphical Models and Image Processes, 55(6), pp. 532–537.

Glover, G.H., 1982. Compton scatter effects in CT reconstructions. Medical Physics, 9, pp. 860-867.

Gnos, E., Hofmann, B. Franchi, I.A. Al-Kathiri, A. Hauser, M. and Moser, L., 2002. Sayh al Uhaymir 094: A new martian meteorite from the Oman desert. Meteoritics and Planetary Science, 37, pp. 835-854.

Goh, K.L., Liew, S.C. and Hasegawa, B.H., 1997. Energy-dependent systematic errors in dual-energy X-ray CT. IEEE Transactions on Nuclear Science, 44, pp. 212-217.

Griebel, M., Dornseifer, T. and Neunhoeffer, T., 1998. Numerical Simulation in Fluid Dynamics, a Practical Introduction. SIAM, Philadelphia.

Guan, H. and Gordon, R., 1996 Computed tomography using Algebraic Reconstruction Techniques (ARTs) with different projection access schemes: a comparison study under practical situations. Physics in Medicine and Biology, 41, pp. 1727–1743.

Hsieh, J., 1998. Adaptive streak artifact reduction in computed tomography resulting from excessive X-ray photon noise. Medical Physics, 25(11), pp. 2139–2147.

Gupta, L. and Sortrakul, T., 1998. A gaussian-mixture based image segmentation algorithm. Pattern Recognition, 31(3), pp. 315–325.

Hallai, C. and Kulcar, P., 1992. Non-destructive testing. Proceedings of the 13th World conference on non-destructive testing, Sao Paulo, Brazil. Elsevier, Amsterdam.

Hangartner, T.N., 1987. Correction of scatter in computed tomography images of bone. Medical Physics, 14(3), pp. 335–340.

Haque, P., 1981. Scintillation crystal-photodiode array detectors. In: Newton, T.H., Potts, D.G. (eds). Radiology of the Skull and Brain: Technical Aspects of Computed Tomography, 5, pp. 4127-4132. C.V. Mosby Company, St. Louis.

Haque, P., Stanley, J.H., 1981. Basic principles of computed tomography detectors. In: Newton, T.H., Potts, D.G. (eds). Radiology of the Skull and Brain: Technical Aspects of Computed Tomography, 5, pp. 4097-4103. C.V. Mosby Company, St. Louis.

Hammersberg, P. and Mångård, M., 1997. Correction for beam hardening artefacts in computerised tomography. In: Hammersberg, P. (eds). Techniques for the Optimal Performance of High Resolution

Computerised Tomography, PhD-dissertation, pp. 149-173. Linköpings Universitet, Linköping, Sweden.

Hammersberg, P., Stenström, M., Hedtjärn, H. and Mångård, M., 1998. Measurements of absolute energy spectra for an industrial micro focal X-ray source under working conditions using a Compton scattering spectrometer. Journal of X-ray Science and Technology, 8, pp. 5-18.

Hara, T., Tanck, E., Homminga, J. and Huiskes, R., 2002. The influence of microcomputed tomography threshold variations on the assessment of structural and mechanical trabecular bone properties. Bone, 31, pp. 107-109.

Herman, G.T., 1979. Correction for beam hardening in computed tomography. Physics in Medicine and biology, 24, pp. 81-106.

Herman, G.T., 1980. Fundamentals of Medical Imaging. Academic Press.

Herman, G.T., Lakshminarayanan, A.V. and Naparstek, A., 1976. Convolution reconstruction techniques for divergent beams. Computers in Biology and Medicine, 6, pp. 259–271.

Herman, G.T. and Lent, A., 1976. Iterative reconstruction algorithms. Computers in Biology and Medicine, 6, pp. 273-294.

Hui, M.-H. and Blunt, M.J., 2000. Effects of wettability on three-phase flow in porous media, Journal of Physical Chemistry B, 104, pp. 3833-3845.

Ikeda, S., Nakano, T. and Nakashima, Y., 2000. Three dimensional study on the interconnection and shape of crystals in a graphic granite by X-ray CT and image analysis. Mineralogical Magazine, 64, pp. 945-959.

Jacobs, P. and Cnudde, V., 2005.Can X-ray computed tomography contribute to cultural heritage and stone conservation through the non-destructive monitoring of deterioration and restoration processes? In: Van Grieken and Janssens (eds.). Cultural Heritage Conservation and Environmental Impact assessment by Non-Destructive Testing and Micro-Analysis. Taylor and Fracis Group, London, pp.117-126.

Jansen, S., Pletsers, A., Steppe, K., Cnudde, V., Masschaele, B., Choat, B., Sano, Y., Pesacreta, T. and Connell, S., 2007. Three-dimensional imaging of wood anatomical characters using X–ray computed microtomography (microCT) and atomic force microscopy (AFM). In: Botany and Plant Biology, Chicago, Illinois, July 7-11 2007, p. 154.

Jansen, S., Pletsers, A., Steppe, K., Cnudde, V., Masschaele, B., Choat, B., Sano, Y., Pesacreta, T. and Connell, S., 2007. Three-dimensional analysis of wood structure: X–ray computed microtomography (microCT) of vessel networks and atomic force microscopy (AFM) of pit membranes. In: IAWA Pan American Regional Group meeting, San Luis Potosi, San Luis Potosi, Mexico, July 16-20 2007, p. 37.

Jenkins, R., 1989. X-ray detectors. In: Bish, D.L. and Post, J.E. (eds). Modern Powder Diffraction, Reviews in Mineralogy, 20, pp. 31-36. The Mineralogical Society of America, Washington DC.

Jennings, R.J., 1988. A method for comparing beam-hardening filter materials for diagnostic radiology. Medical Physics, 15, pp. 588-599.

Jerauld, G.R., Hatfield, J.C., Scriven, L.E. and Davis, H.T., 1984a. Percolation and Conduction on Voronoi and Triangular Networks – a 2nd Case-Study in Topological Disorder, Journal of Physics C: Solid State Physics, 17, pp. 1519-1529.

Jerauld, G.R., Hatfield, J.C., Scriven, L.E. and Davis, H.T., 1984b. Percolation and Conduction on the 3D Voronoi and Regular Networks – a 2nd Case-Study in Topological Disorder, Journal of Physics C: Solid State Physics, 17, pp. 3429-3439.

Jerauld, G.R. and Salter, S.J., 1990. Effect of pore-structure on hysteresis in relative permeability and capillary pressure: Pore-level modeling. Transport in Porous Media, 5, pp. 103-151.

Johns, H.E. and Cunningham, J.R., 1971. The Physics of Radiology. Charles C. Thomas.

Johns, P.C. and Yaffe, M.J., 1985. Theoretical optimization of dual-energy X-ray imaging with application to mammography. Medical Physics, 12, pp. 289-296.

Johns, R.A., Stuede, J.S., Castanier, L.M. and Roberts, P.V., 1993. Non-destructive measurements of fracture aperture in crystalline rock cores using X-ray computed tomography. Journal of Geophysical Research, 98, pp. 1889-1900.

Joseph, P.M., 1981. Artifacts in computed tomography. In: Newton, T.H. and Potts, D.G. (eds). Radiology of the Skull and Brain: Technical Aspects of Computed Tomography, 5, pp. 3956-3992. C.V. Mosby Company, St.-Louis, US.

Kak, A. C. and Slaney, M., 1988. Principles of Computerized Tomographic Imaging. IEEE Press, New York, US, 329 p.

Kang, Q., Lichtner, P.C. and Zhang, D., 2006. Lattice Boltzmann pore-scale model for multicomponent reactive transport in porous media. Journal of Geophysical Research, 111, pp. .

Keller, J., Qiu, H. and Tahani, H., 1986. The fuzzy integral in image segmentation. Proceedings NAFIPS-86, New Orleans, Louisiana, pp. 324-338.

Keller, J.M. and Carpenter, C.L., 1990. Image segmentation in the presence of uncertainty. International Journal of Intelligent Systems, 5, pp. 193–208.

Kelly, M., 1971. Edge detection by computer using planning. Machine Intelligence, 6, pp. 397-409, Edinburgh University Press, Edinburgh.

Kerckhofs, G. , Schrooten, J., Van Cleynenbreugel, T., Lomov, S.V. and Wevers, M., 2008. Validation of X-ray microfocus computed tomography as an imaging tool for porous structures. Review of Scientific Instrument , 79, pp. 1-9.

Ketcham, R.A. and Carlson, W.D., 2001. Acquisition, optimization and interpretation of X-ray computed tomographic imagery: applications to the geosciences. Computers & Geosciences, 27, pp. 381-400.

Ketcham, R.A., 2005. Three-dimensional grain fabric measurements using high-resolution X-ray computed tomography. Journal of Structural Geology, 27, pp. 1217-1228.

Ketcham, R.A., 2006. Accurate three-dimensional measurements of features in geological materials from X-ray computed tomography data. In: Desrues, J., Viggiani, G. and Bésuelle, P. (eds). Advances in X-Ray Tomography for Geomaterials, pp. 143-148. Hermes Science Publishing Ltd., London, UK.

Kittler, J. and Illingwood, J., 1986. Minimum error thresholding. Pattern Recognition, 19(1), pp. 41-47.

Klinkenberg, L.J., 1941. The permeability of Porous media to liquids and gases. American Petroleum Institute, Drilling and Productions Practices, pp. 200–213.

Koplik, J., 1982. Creeping flow in two-dimensional networks. Journal of fluid mechanics, 119, pp. 219-247.

Koplik, J. and Lasseter, T.J., 1985. Two-phase flow in random network models of porous media, Society of Petroleum Engineers Journal, 25, pp. 89-100.

Kovscek, A.R., Wong, H. and Radke, C.J., 1993. A Pore-Level Scenario for the Development of Mixed Wettability in Oil-Reservoirs, AIChE Journal, 39, pp. 1072-1085.

Lee, T.C., Kashyap, R.L. and Chu, C.N., 1994. Building Skeleton Models Via 3-D Medial Surface Axis Thinning Algorithms, Cvgip-Graphical Models and Image Processing, 56, pp. 462-478.

Leliveld, C.J., 1996. A Fast Monte Carlo Simulator for Scattering in X-ray Computerized Tomography. PhD thesis, Technische Universiteit Delft.

Lewitt, R.M., 1983. Reconstruction algorithms: Transform methods. Proceedings of the IEEE, 71(3), pp. 390–408.

Li, L., Peters, C.A. and Celia, M.A., 2006. Upscaling geochemical reaction rates using pore-scale network modeling. Advances in Water Resources, 29, pp. 1351-1370.

Lin, C. and Cohen, M.H., 1982. Quantitative methods for microgeometric modelling. Journal of Applied Physics, 53, pp. 4152-4165.

Lindquist, W.B., Lee, S.M., Coker, D.A., Jones, K.W. and Spanne, P., 1996. Medial axis analysis of void structure in three-dimensional tomographic images of porous media. Journal of Geophysical Research-Solid Earth, 101, pp. 8297-8310.

Lindquist, W.B. and Venkatarangan, A., 1999. Investigating 3D geometry of porous media from high resolution images, Physics and Chemistry of the Earth, Part A: Solid Earth and Geodesy, 24, pp. 593-599.

Lindquist, W.B., Venkatarangan, A., Dunsmuir, J. and Wong, T., 2000. Pore and throat size distributions measured from synchrotron X-ray tomographic images of Fontainebleau sandstones. Journal of Geophysical Research-Solid Earth, 105(B9), pp. 509-527.

Mees, F., Swennen, R.,Van Geet, M. and Jacobs, P., 2003. Applications of X-ray Computed Tomography in the Geosciences. The Geological Society London, Special Publication 215.

Moga, A.N. and Gabbouj, M., 1998. Parallel maker-based image segmentation with watershed transformation. Journal of Parallel and Distributed Computing, 51, pp. 27-45.

Moström, U. and Ytterbergh, C., 1986. Artifacts in computed tomography of the posterior fossa: a comparative phantom study. Journal of Computer Assisted Tomography, 10, pp. 560-566.

Muller, R., Van Campenhout, H., Van Damme, B., Van Der Perre, G., DeQueker, J., Hildebrandt, T. and Ruegsegger, P., 1998. Morphometric analysis of human bone biopsies: A quantitative structural comparison of histological sections and microcomputed tomography. Bone, 23, pp. 59-66.

Murthy, C.A. and Pal, S.K., 1990. Fuzzy thresholding: mathematical framework, bound functions and weighted moving average technique. Patter Regonition Letters, 11, pp. 197-206.

Nakagawa, Y. and Rosenfeld, A., 1979. Some experiments on variable thresholding. Pattern Recognition, 11(3), pp. 191–204.

Nickoloff, E.L. and Riley, R., 1985. A Simplified Approach for Modulation Transfer Function Determinations in Computed Tomography. Medical Physics , 12(4), pp. 437-442.

Obrist, A.F., Flisch, A. and Hofmann, J., 2004. Point cloud reconstruction with sub-pixel accuracy by slice-adaptive thresholding of X-ray computed tomography images. NDT&E International, 37, pp. 373-380.

Ohnesorge, B., Flohr, T. and Klingenbeck-Regn, K., 1999. Efficient object scatter correction algorithm for third and fourth generation CT scanners. European Radiology, 9, pp. 563–569.

Ohtani, T., Nakano, T., Nakashima, Y. and Muraoka, H., 2001. Three dimensional shape analysis of miarolitic cavities and enclaves in the kakkonda granite by X-ray computed tomography. Journal of Structural Geology, 23, pp. 1741-1751.

Oppenheim. B.E., 1977. Reconstruction tomography from incomplete projections. In Ter-Pogossian, M.M., Phelps, M.E., Brownell, G.L., Cox, J.R., Davis, D.O. and Evens, R.G. (eds). Reconstruction Tomography in Diagnostic Radiology and Nuclear Medicine, University Park Press, pp. 155–183.

Otsu, N.A., 1979. Threshold selection methods from gray-level histogram. IEEE Transactions on Systems Man and Cybernetics, 9(1), pp. 63–66.

Pal, N.R. and Bhandari, D., 1992. On object-background classification. International Journal of System Science, 23(11), pp. 1903-1920.

Pal, N.R. and Pal, S.K., 1991. Image model, Poisson distribution and object extraction. International Journal of Pattern Recognition and Artificial Intelligence, 5, pp. 459-483.

Pal, N.R. and Pal, S.K., 1993. A review on image segmentation techniques. Pattern Recognition, 26(9), pp. 1277-1294.

Pang, S. C. and Genna, S., 1976. Corrections for X-ray polychromaticity effects on three-dimensional reconstruction. IEEE Transactions on Nuclear Science, 23, pp. 623-626.

Parnas, R.S., Wevers, M. and Verpoest, I., 2003. Using textile topography to analyze X-ray CT data of composite microstructure. Polymer Composites, 24(2), pp. 212 -220.

Penumadu, D. and Dean, J., 2000. Compressiblity effect in evaluating the pore-size distribution of kaolin clay using mercury intrusion porosimetry. Canadian Geotechnical Journal, 37, pp. 393-405.

Peschmann, K.R., 1981. Xenon gas ionization detectors. In: Newton, T.H., Potts, D.G. (eds), Radiology of the Skull and Brain: Technical Aspects of Computed Tomography, 5, pp. 4112-4126. C.V. Mosby Company, St. Louis.

Photometrics Ltd., 1990. Charge-coupled devices for quantitative electronic imaging. Photometrics Ltd., Tuscon, Arizona. 36 p.

Pullan, B.R., Ritchings, R.T. and Isherwood, I., 1981. Accuracy and meaning of computed tomography attenuation values. In: Newton, T. H. and Potts, D. G. (eds). Radiology of the Skull and Brain: Technical Aspects of Computed Tomography, vol. 5, pp. 3904-3917. C.V. Mosby Company, St.-Louis, US.

Randmer, J.A., Koller, T.J. and Holland, W.P., 1981. X-ray sources and controls. In: Newton, T.H. and Potts, D.G. (eds). Radiology of the Skull and Brain: Technical Aspects of Computed Tomography, 5, pp. 4058-4095. C.V. Mosby Company, St. Louis.

Remeysen, K. and Swennen, R., 2006. Combination of dual energy microfocus computed tomography and petrography for objective 3D reservoir characterization. In: Desrues, J., Viggiani, G. and Bésuelle, P. (eds). Advances in X-Ray Tomography for Geomaterials, pp. 155-160. Hermes Science Publishing Ltd., London, UK.

Remeysen, K., 2007. Combination of Medical Computed Tomography, Microfocus Computed Tomography and Petrography in Reservoir Characterization. PhD-dissertation, Katholieke Universiteit Leuven, Belgium.

Robertson, D.D. and Huang, H.K., 1986. Quantitative bone measurements using X-ray computed tomography with second-order correction. Medical Physics, 13, pp. 474-479.

Roels, S., Vandersteen, K. and Carmeliet, J., 2003. Measuring and simulating moisture uptake in a fractured porous medium. Advances in Water Resources, 26(3), pp. 237-246.

Roels, S., Carmeliet, J., Hens, H., Adan, O., Brocken, H., Cerny, R., Pavlik, Z., Ellis, A.T., Hall, C., Kumaran, K., Pel, L. and Plagge, R.A., 2004. Comparison of Different Techniques to Quantify Moisture Content Profiles in Porous Building Materials. Journal of Thermal Envelope and Building Science, 7(4), pp. 261-276.

Roels, S. and Carmeliet, J. Analysis of moisture flow in porous materials using microfocus X-ray radiography. International Journal of Heat and Mass Transfer 2006, 49(25-26), pp. 4762-4772.

Rogers, S.W. 1999. Allosaurus, crocodiles, and birds: evolutionary clues from spiral computed tomography of an endocast. Anatomical Record, 257, pp. 162–173.

Rosenfeld, A. and Kak, A.C., 1982. Digital Picture Processing, Academic press, New York.

Rowe, T., Ketcham, R.A. Denison, C. Colbert, M. Xu, X. and Currie, P.J., 2001. Forensic palaeontology: The Archaeoraptor forgery. Nature, 410, pp. 539-540.

Ruiz de Argandoña, V.G, Rodriguez-Rey, A., Celorio, C., Calleja, L. and Suárez del Rio, L.M., 2003. Characterization by X-ray computed tomography of water absorption in a limestone used as building stone in the Oviedo Cathedral (Spain). Geological Society, London, Special Publications, 215, pp. 127-134.

Russ, J.C., 2002. The Image Processing Handbook. Fourth Edition. CRC Press, Boca Raton, US, 732 p.

Saad, Y. and Schultz, M.H., 1986. GMRES: A generalized minimal residual algorithm for solving nonsymmetric linear systems. SIAM Journal on Scientific and Statistical Computing, pp. 856–869.

Saraf, D.N., 1981. Methods of In-Situ saturation determination during core tests involving multiphase flow. Petroleum Recovery Institute, Report 1981-6.

Sellers, E., Vervoort, A. and Van Cleynenbreugel, J., 2003. Three-dimensional visualization of fractures in rock test samples, simulating deep level mining excavations, using X-ray computed tomography. Geological Society, London, Special Publications, 215, pp. 69-80.
Shepp, L.A. and Logan, B.F., 1974. The Fourier reconstruction of a head section. IEEE Transactions on Nuclear Science, 21, pp. 21–43.

Simons, F. J., Verhelst, F. and Swennen, R., 1997. Quantitative characterization of coal by means of microfocal X-ray computed microtomography (cmt) and color image analysis (cia). International Journal of Coal Geology, 34, pp. 69-88.

Skyscan, 1997. Instruction manual for the Skyscan 1072: Desktop X-ray Microscope-microtomograph, Aartselaar, 43 p.

Spiess, R., Peruzzo, L. Prior, D.J. and Wheeler, J., 2001. Development of garnet porphyroblasts by multiple nucleation, coalescence and boundary misorientation-driven rotations. Journal of Metamorphic Geology, 19, pp. 269–290.

Stonestrom, J.P., Alvarez, R.E. and Macovski, A., 1981. A framework for spectral artifact corrections in X-ray CT. IEEE Transactions on Biomedical Engineering, 28, pp. 128-141.

Stoppie, N., Wevers, M., Naert, I., 2007. Feasibility of detecting trabecular bone around percutaneous titanium implants in rabbits by in vivo microfocus computed tomography. Journal of Microscopy, Oxford, 228(1), pp. 55 -61.

Stoppie, N., Van der Waerden, J.P., Jansen, J.A., Duyck, J., Wevers, M., Naert, I., 2005. Validation of microfocus computed tomography in the evaluation of bone implant specimens. Clinical Implant Dentistry and Related Research , 7(2), pp. 87 -94.

Stumbo, S., Bottigli, U., Golosio, B. and Oliva, P., 2004. Direct analysis of molybdenum target generated X-ray spectra with a portable device. Medical Physics, 31(10), pp. 2763-2770.

Suetens, P., De Man, B., D'hooge, J., Maes, F., Michiels, J., Nuyts, J., Van Cleynenbreugel, J. and Vande Velde, K., 2002. Fundamentals of medical imaging, Cambridge University Press.

Tanaka, H., 2003. Pore size distribution and hydraulic conductivity characteristics of marine clay. 2nd International Symposium on Contaminated Sediments.

Takinawa, W., Shimamoto, T., 2006. Klinkenberg effect for gas permeability and its comparison to water permeability for porous sedimentary rocks. Hydrology and Earth System Sciences Discussions, 3, pp. 1315-1338.

Tartakovsky, A.M., Meakin, P., Scheibe, T.D. and Wood, B.D., 2007. A smoothed particle hydrodynamics model for reactive transport and mineral precipitation in porous and fractured porous media. Advances in Water Resources, 29(9), pp. 1351-1370

Taylor, L.A., Keller, R.A., Snyder, G.A., Wang, W.Y., Carlson, W.D., Hauri, E.H., McCandless, T. Kim, K.R. Sobolev, N.V. and Bezborodov, S.M., 2000. Diamonds and their mineral inclusions, and what they tell us: A detailed 'pullapart' of a diamondiferous eclogite. International Geology Review, 42, pp. 959–983.

Ter-Pogossian, M.M., Phelps, M.E., Brownell, G.L., Cox, J.R., Davis, D.O. and Evens, R.G., 1977. Reconstruction Tomography in Diagnostic Radiology and Nuclear Medicine. University Park Press, Baltimore.

The MathWorks, Inc., 2007. Image Processing Toolbox Users Guide. Available online, www.mathworks.com, 1156 p.

Thovert, J.F., Yousefian, F., Spanne, P., Jacquin, C.G. and Adler, P.M., 2001. Grain reconstruction of porous media: Application to a low-porosity Fontainebleau sandstone. Physical Review E (63).

Tivey, M.K., 1998. Documenting textures and mineral abundances in minicores from the TAG active hydrothermal mound using X-ray computed tomography. In: Herzig, P.M., Humphris, S.E., Miller, D.J. and Zierenberg, R.A. (eds) Proceedings of the Ocean Drilling Pogram, Scientific Results. 158, pp. 201-210.

Trivedi, M. and Bezdek, J.C., 1986. Low-level segmentation of aerial images with fuzzy clustering. IEEE Transactions on Systems Man and Cybernetics, 16(4), pp. 589–598.

Tsuchiyama, A., Uesugi, K., Nakano, T. and Ikeda, S., 2005. Qualitative evaluation of attenuation contrast of X-ray computed tomography images using monochromatized beams. American Mineralogist, 90, pp. 132-142.

Valvatne, P.H. and Blunt, M.J., 2004. Predictive pore-scale modeling of two-phase flow in mixed-wet media. Water Resources Research, 40.

Valvatne, P, 2004. Predictive pore-scale modelling of multiphase flow. PhD-dissertation, Imperial College London.

VandenBygaart, A.J. and Protz, R., 1999. The representative elementary area (REA) in studies of quantitative soil micromorphology. Geoderma, 89, pp. 333-346.

Vandersteen, K., Busselen, B., Van Den Abeele, K.E.A. and Carmeliet, J., 2003. Quantitative characterisation of fracture apertures using microfocus computed tomography. In: Mees, F., Swennen, R., Van Geet, M. and Jacobs, P. (eds). Applications of X-ray Computed Tomography in the Geosciences, pp. 61-80. The Geological Society London, Special Publication 215.

Vandersteen, K., Carmeliet, J. and Feyen, J., 2003. A network approach to derive unsaturated hydraulic properties of a rough-walled fracture. Transport in Porous Media 50(3), pp. 197-221.

Van Geet, M., Swennen, R. and Wevers, M., 2000. Quantitative analysis of reservoir rocks by microfocus X-ray computerised tomography. Sedimentary Geology, 132, pp. 25-36.

Van Geet, M., 2001. Optimisation of microfocus X-ray computed tomography for geological research with special emphasis on coal components (macerals) and fractures (cleats) characterisation. PhD-dissertation, Katholieke Universiteit Leuven, Belgium.

Van Geet, M., Swennen, R. and David, P., 2001. Quantitative coal characterisation by means of microfocus X-ray computer tomography, colour image analysis and back scatter scanning electron microscopy. International Journal of Coal Geology, 46, pp. 11-25.

Van Geet, M., Swennen, R. and Wevers, M., 2001. Towards 3-D petrography: application of microfocus computer tomography in geological science. Computers and Geosciences, 27(9), pp. 1091-1099.

Van Marcke, P. and Swennen, R., 2006. Optimising X-ray computer tomography images with a CT-simulator: The development and use of a CT-simulator. In: Desrues, J., Viggiani, G. and Bésuelle, P. (eds). Advances in X-Ray Tomography for Geomaterials, pp. 161-166. Hermes Science Publishing Ltd., London, UK.

Verhelst, F., Swennen, R., Vervoort, A., Marchal, G. and Dusar, M., 1997. X-ray computerised tomography study of heterogenities in Westphalian A and B coal strata (Peer coalbed methane project, Campine Basin, NE-Belgium). ZentralBlatt fur Geologie und Palaeontologie, 1(11/12), pp. 1119-1124.
Verleye, B., Klitz, M., Croce, R., Roose, D., Lomov, S. and Verpoest, I., 2007. Computation of permeability of textile with experimental validation for monofilament and non crimp fabrics. In: Zeng, X. and Li, Y. and Ruan, D. and Koehl, L. (eds.). Computational Textiles, Studies in Computational Intelligence, 55, pp. 93-110. Springer.

Verleye, B., 2008. Computation of the permeability of multi-scale porous media with application to technical textiles. PhD-dissertation, Katholieke Universiteit Leuven, Belgium.

Villafana, T., 1975. The role of sampling apertures in computerized tomography (abstract). Medical Physics, 2, pp. 167.

Vinegar, H.J. and Wellington, S.L., 1987. Tomographic imaging of three-phase flow experiments. Review of Scientific Instruments, 58, pp. 96-107.

Vogel, H.J., 1997. Morphological determination of pore connectivity as a function of pore size using serial sections. European Journal of Soil Science, 48, pp. 365-377.

Vogel, H.J., 2000. A numerical experiment on pore size, pore connectivity, water retention, permeability, and solute transport using network models. European Journal of Soil Science, 51, pp. 99-105.

Vogel, H.J. and Roth, K., 2001. Quantitative morphology and network representation of soil pore structure. Advances in Water Resources, 24, pp. 233-242.

Vogel, H.J., Cousin, I. and Roth, K., 2002. Quantification of soil structure and gas diffusion as a function of scale. European Journal of Soil Science, 53, pp. 465-473.

Vogel, J.R. and Brown, G.O., 2003. Geostatistics and the representative elementary volume of gamma ray tomography attenuation in rock cores. In: Mees, F., Swennen, R., Van Geet, M. and Jacobs, P. (Eds.). Applications of X-ray Computed Tomography in the Geosciences, Special Publications 215, pp. 81-93. Geological Society, London, UK.

Wang, G., Snyder, D.L., O'Sullivan, J.L. and Vannier, M.W., 1996. Iterative deblurring for CT metal artifact reduction. IEEE Transactions on Medical Imaging, 15(5), pp. 657–664.

Wellington, S.L. and Vinegar, H.J., 1987. Tomographic imaging of three-phase flow experiments. Journal of Petroleum Technology, 58, pp. 885-898.

Wevers, M., de Meester, P., Swennen, R., 2001. Microfocus X-ray computer tomography in materials research. Insight, 43(10), pp. 658 -663.

Whitaker, S., 1969. Fluid motion in porous media. Industrial and engineering chemistry, 61(12), pp. 32-46.

Wise, W.R., 1992. A new insight on pore structure and permeability. Water Resources Research, 28, pp. 189-198.

Yester, M.W. and Barnes, G.T., 1977. Geometrical limitations of computed tomography (CT) scanner resolution. Proceedings SPIE, 127, pp. 296–303.

Zatz, L. M. and Alvarez, R. E., 1977. An inaccuracy in computed tomography: the energy dependence of CT values. Radiology, 124, pp. 91-97.

Zhou, Y.T., Venkateswar, V. and Chellappa, R., 1989. Edge detection and linear feature extraction using 2-D random field model. IEEE Transactions on Pattern Analysis and Machine Intelligence, 11, pp. 84–95.

A. Mathematical derivations in the noise model

In this appendix the formulas used to simulate the autocorrelation in the noise as described in section 3.1.9, are derived. All derivations deal with the calculation of the standard deviation of a series. The standard deviation of a series does not change by adding or subtracting a constant to or from this series. Therefore all derivations can be performed assuming that the mean value of the series is zero.

- A series of z points and a standard deviation s_0 is extended to $n \cdot z$ points by adding new points between the existing points. The value of these new points is determined by interpolating between the values of the old points. The standard deviation s_n of the new series is then:

$$
\begin{aligned}
s_n^2 &= \frac{\sum_{i=1}^{z} x_{n(i-1)+1}^2 + \sum_{i=1}^{z} x_{n(i-1)+2}^2 + \cdots + \sum_{i=1}^{z} x_{ni}^2}{nz} \\
&= \frac{\sum_{i=1}^{z} x_{n(i-1)+1}^2}{nz} + \frac{\sum_{i=1}^{z} \sum_{j=1}^{n-1} \left[\frac{(n-j)x_{n(i-1)} + jx_{ni}}{n} \right]^2}{nz} \\
&= \frac{s_0^2}{n} + \sum_{i=1}^{z} \frac{\sum_{j=1}^{n-1} \left[(n-j)^2 x_{n(i-1)}^2 + j^2 x_{ni}^2 + 2j(n-j) x_{n(i-1)} x_{ni} \right]}{n^3 z} \\
&= \frac{s_0^2}{n} + \sum_{j=1}^{n-1} \frac{(n-j)^2 \cdot \frac{\sum_{i=1}^{z} x_{n(i-1)}^2}{z} + j^2 \cdot \frac{\sum_{i=1}^{z} x_{ni}^2}{z} + 2j(n-j) \cdot \overbrace{\frac{\sum_{i=1}^{z} x_{n(i-1)} x_{ni}}{z}}^{\overset{(*)}{=0}}}{n^3} \\
&= \frac{s_0^2}{n} + s_0^2 \cdot \sum_{j=1}^{n-1} \frac{(n-j)^2 + j^2}{n^3} \\
&\overset{(**)}{=} \frac{s_0^2}{n} + s_0^2 \cdot \frac{2 \cdot \sum_{j=1}^{n} (j-1)^2}{n^3} \\
&= \frac{n^2 + 2 \cdot \sum_{i=1}^{n} (i-1)^2}{n^3} \cdot s_0^2
\end{aligned}
\tag{A.1}
$$

This is the equation (3.14):

$$
s_n = \sqrt{\frac{n^2 + 2 \cdot \sum_{i=1}^{n} (i-1)^2}{n^3}} \cdot s_0 \tag{3.14}
$$

(*) $$mean(x \cdot y) = mean(x) \cdot mean(y) \tag{A.2}$$

(**)
$$
\begin{aligned}
\sum_{j=1}^{n-1} \left[(n-j)^2 + j^2 \right] &= \sum_{j=1}^{n-1} (n-j)^2 + \sum_{j=1}^{n-1} j^2 \\
&= \sum_{j=n-1}^{1} j^2 + \sum_{j=1}^{n-1} j^2
\end{aligned}
$$

$$= 2 \cdot \sum_{j=1}^{n-1} j^2$$
$$= 2 \cdot \sum_{j=2}^{n} (j-1)^2$$
$$= 2 \cdot \sum_{j=1}^{n} (j-1)^2 \qquad \text{(A.3)}$$

- The standard deviation of the first derivative of this new series is:

$$s'^2_n = \frac{\sum_{i=1}^{z-1}(x_{ni+1} - x_{ni})^2 + \sum_{i=1}^{z-1}(x_{ni} - x_{ni-1})^2 + \cdots + \sum_{i=1}^{z-1}(x_{n(i-1)+2} - x_{n(i-1)+1})^2}{nz}$$
$$\overset{(*)}{=} \sum_{i=1}^{z-1} \frac{\sum_{i=1}^{z-1}(x_{ni+1} - x_{n(i-1)+1})^2}{n^2}$$
$$= \frac{s'^2_0}{n^2}$$
$$\overset{(**)}{=} \frac{2}{n^2} \cdot s_0^2$$
$$\overset{(3.14)}{=} \frac{2}{n^2} \cdot \frac{n^3}{n^2 + 2 \cdot \sum_{i=1}^{n}(i-1)^2} \cdot s_n^2$$
$$= \frac{2 \cdot n}{n^2 + 2 \cdot \sum_{i=1}^{n}(i-1)^2} \cdot s_n^2 \qquad \text{(A.4)}$$

Thus equation (3.15) is obtained:

$$s'_n = \sqrt{\frac{2 \cdot n}{n^2 + 2 \cdot \sum_{i=1}^{n}(i-1)^2}} \cdot s_n \qquad \text{(3.15)}$$

(*)
$$\frac{\sum_{i=1}^{z-1}(x_{ni+1} - x_{ni})^2 + \sum_{i=1}^{z-1}(x_{ni} - x_{ni-1})^2 + \cdots + \sum_{i=1}^{z-1}(x_{n(i-1)+2} - x_{n(i-1)+1})^2}{nz}$$
$$= n \cdot \sum_{i=1}^{z-1}\left[\frac{x_{ni+1} - x_{n(i-1)+1}}{n}\right]^2$$
$$= \frac{\sum_{i=1}^{z-1}\left[x_{ni+1} - x_{n(i-1)+1}\right]^2}{n} \qquad \text{(A.5)}$$

(**)
$$s'^2_0 = \frac{\sum_{i=1}^{z-1}(x_{i+1} - x_i)^2}{z}$$

$$
\begin{aligned}
&= \frac{\sum_{i=1}^{z-1} x_{i+1}^2}{z} + \frac{\sum_{i=1}^{z-1} x_i^2}{z} + 2 \cdot \frac{\overbrace{\sum_{i=1}^{z} x_{i+1} x_i}^{(D.2)\ = 0}}{z} \\
&= s_0^2 + s_0^2 \\
&= 2 \cdot s_0^2
\end{aligned}
\tag{A.6}
$$

B. Simulator parameters for the Tomohawk

Just as for the Skyscan 1072 Desktop µCT scanner, some parameters of the AEA Tomohawk need to be determined to be able to simulate its scanning process. The radiographs generated by the Skyscan are tiff-files and information can be obtained directly from these images. The Tomohawk does not generate tiff-files, but rad-files. These files need further post-processing. This hinders the experiments that were performed for the Skyscan. Moreover, compared to the Skyscan, less information is available for the Tomohawk. There are for example no detailed specifications on the fluorescent screen used in the Tomohawk. Therefore not all properties of the AEA Tomohawk could be determined.

An eventual non-linearity, the level of noise and the impact of the fluorescent screen are not measured. This should not pose serious limitations to the use of the simulator for the Tomohawk. The detector is assumed to be linear. The characteristics of the fluorescent screen in the Skyscan are used to simulate the behaviour of the screen in the Tomohawk. And the noise level can still be changed by the k_{noise} parameter in the noise model (3.13).

More essential are the spectra and the geometrical parameters. The spectra were measured for the three sources (tungsten, copper and molybdenum) of the Tomohawk (cf. appendix C). The geometrical parameters are obtained from the specifications of the Tomohawk. These parameters are:

- distance between source and detector: 1500 mm
- secondary magnification: 1
- fanangle: 6,8°
- focal spot size: 5-200 µm
- apparent detector element size: 175,1 x 175,1 µm²

C. X-ray spectra measurements

The spectra of the Skyscan 1072 Desktop µCT scanner and the AEA Tomohawk µCT scanner were measured. This was done by an apparatus which is, together with dedicated software, able to perform a spectral reconstruction of the radiation produced by the X-ray tubes (*Aiello et al., 2004; Stumbo et al., 2004*). The apparatus could only measure the spectra for a tube voltage up to 50 kV. In the Tomohawk scanner a tungsten, a copper or a molybdenum source can be used. The spectra were measured for all these sources. Here, only the tungsten source is considered as the Tomohawk scans performed in this work all used the tungsten source. The measured 50 kV spectrum of the tungsten source in the Tomohawk is shown in figure C.1.

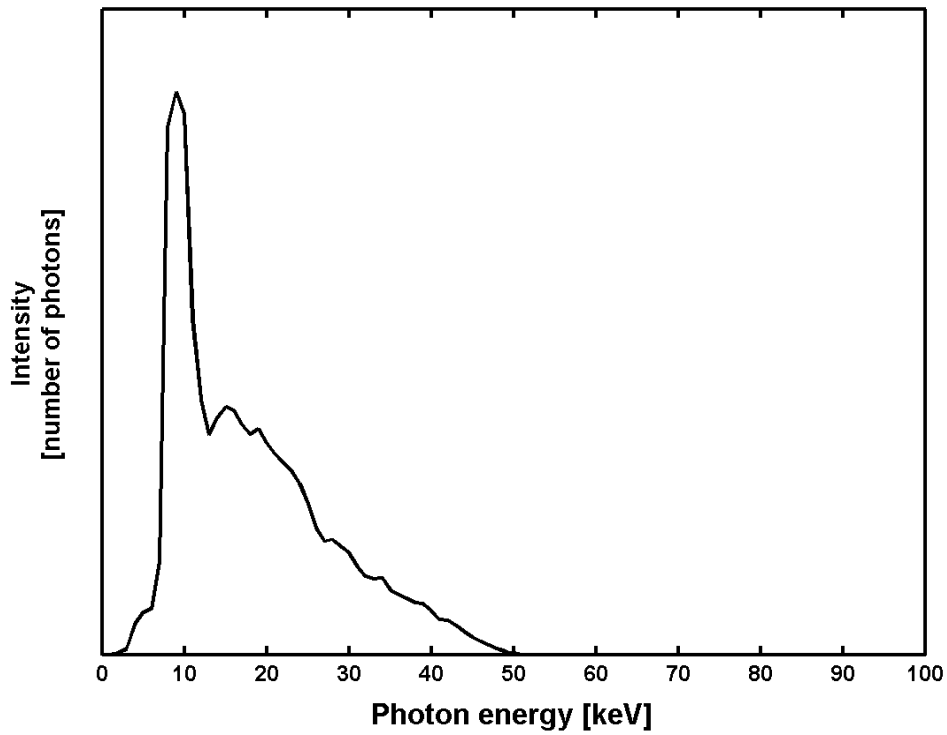

Figure C.1: Measured 50 kV spectrum of the tungsten source in the AEA Tomohawk µCT scanner.

The spectra for higher tube voltages are computed by extrapolating the measured spectra at lower tube voltages. This is done using the spectra for higher tube voltages determined by Hammersberg (*Hammersberg, 1998*). This is done by fitting the peaks in both spectra and adding the tail of the Hammersberg spectrum to the measured 50 kV spectrum. This 100 kV spectrum is given in figure C.2. As the lower energies are the most important energies in X-ray computed tomography, the fitted spectra are supposed to be sufficiently accurate to generate realistic simulations.

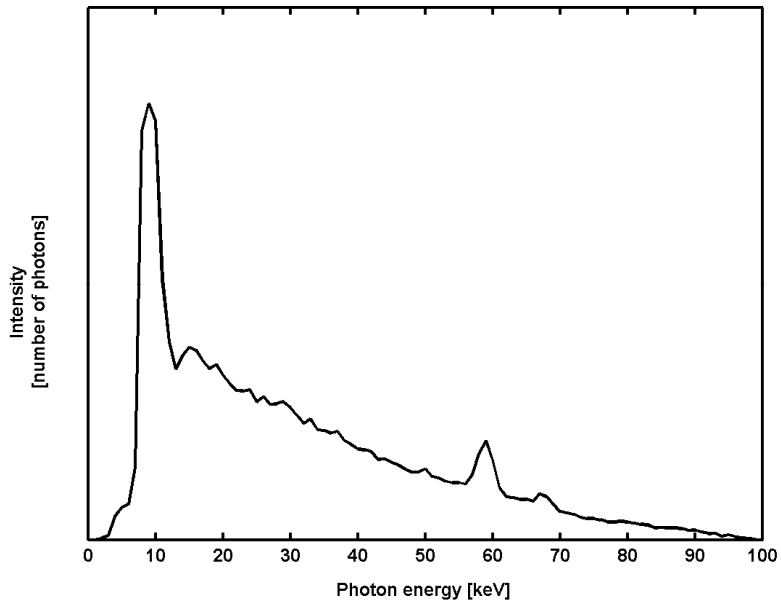

Figure C.2: 100 kV spectrum of the tungsten source in the Tomohawk. The spectrum is obtained from the measured 50 kV spectrum and the 100 kV spectrum determined by Hammersberg (*Hammersberg, 1998*).

Finally a correction is applied on the measured and fitted spectra of the Tomohawk. In front of the detector of the Tomohawk is an 0,8 mm thick aluminium plate that filters the X-ray spectrum. The same filtration is applied on the spectra of the Tomohawk. This is done using Beer's law (cf. equation (3.9)). Figure C.3 shows the effect of the filtration on the 100 kV spectrum of the tungsten source in the Tomohawk.

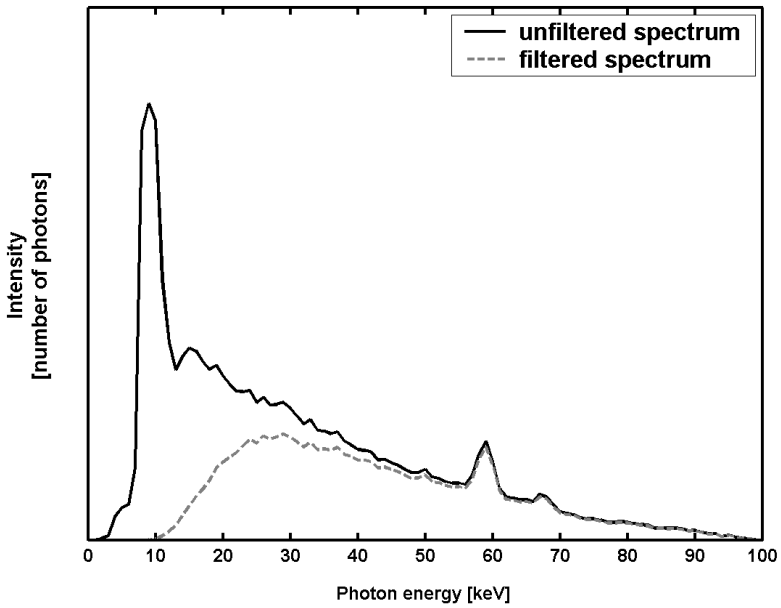

Figure C.3: Filtered 100 kV spectrum of the tungsten source in the Tomohawk. The spectrum is filtered by a 0,8 mm thick aluminium filter to take into account the effect of the aluminium plate in front of the detector.

D. Assessment of the applicability of X-ray computed tomography in measuring the gold content of rock samples

In chapters 3 and 4 it is demonstrated how the CT simulator can be used to look for optimal acquisition parameters or to investigate the impact of these parameters on the resulting CT images. But the simulator is also a useful tool when examining new applications of X-ray computed tomography. Limitations and drawbacks of the technique can early be identified and possible solutions can be tested in advance. In that way time can be saved and eventually it can lead to the conclusion that X-ray computed tomography is not suitable for the given application.

This is demonstrated here by using the simulator to assess the applicability of X-ray CT in measuring the gold content of rock samples. Several techniques exist to measure the gold content in rock samples like fire assaying or geochemical analyses. But these techniques are difficult to perform and CT measurements are often performed faster and more easily. Moreover, gold is a very attenuating material and can thus easily be detected in CT images. Therefore X-ray computed tomography might be a useful technique to obtain a quick indication of the gold content and to link the gold content to other rock characteristics such as sedimentary features. However, the high attenuation of gold will result in a large amount of scatter which deteriorates the images. Also the presence of pyrite, which has a high attenuation coefficient, can complicate the measurements.

The simulator is used to assess the suitability of X-ray CT for this application. More specifically, it is examined if it is possible to derive the dimensions of gold particles in a rock sample from CT images. Using simulations has the advantage that all parameters and phenomena involved in the scanning process can be controlled separately. Moreover, a lot of measurements can be performed in a relatively short time and the input material in the simulator is exactly known. This is not always so when real samples are used.

D.1 Methodology

As gold has a very high attenuation coefficient, the contrast between gold and the surrounding material is in most cases high. This makes it easy to isolate the gold by thresholding. However, errors arise due the finite resolution of CT images (cf. section 4.2.2). The limited resolution causes a blurring of the image and can mathematically be expressed by a point-spread function (PSF). The PSF of a CT imaging system can be approximated by a Gaussian function (*Nickoloff and Riley, 1985*). Figure D.1 illustrates the effect of a Gaussian PSF on square objects of various sizes.

Because of the blurring of the object edges different threshold values result in different estimated dimensions of the object. Moreover, when the object is smaller than the PSF, its peak attenuation is lowered. A threshold value that correctly determines the dimensions of an object bigger than the PSF, underestimates the size of an object smaller than the PSF. Another problem when thresholding the gold particles is beam hardening. Because of the high attenuation of gold severe beam hardening takes place in these particles. As a result the reconstructed attenuation coefficient of gold particles differs significantly with varying size and shape of the particle. This is illustrated in figure D.2. As a consequence, applying one general threshold value again leads to wrong estimations. Using a percentage of the peak attenuation value in a particle as a threshold value might be a solution. In figure D.2 50% of this peak value is used a threshold value.

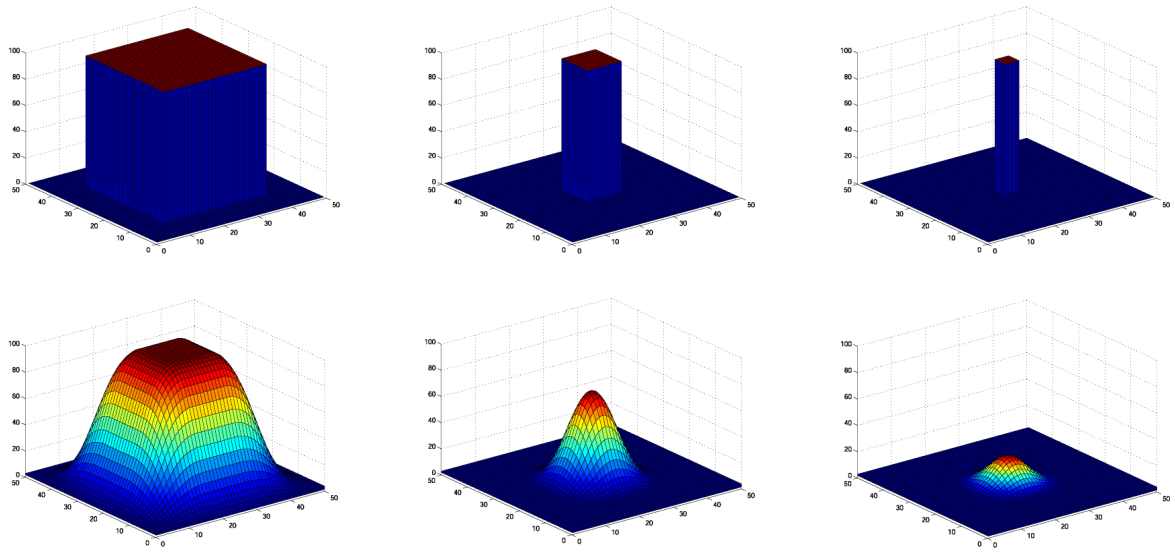

Figure D.1: Effect of a Gaussian PSF on square objects of various sizes. The upper row represents the attenuation coefficient of the object and its surrounding material. The lower row shows the effect of the PSF on the reconstructed attenuation coefficient. When the size of the box is smaller than the PSF, the PSF does not only result in a blurring of the edges, but also in a lower peak attenuation.

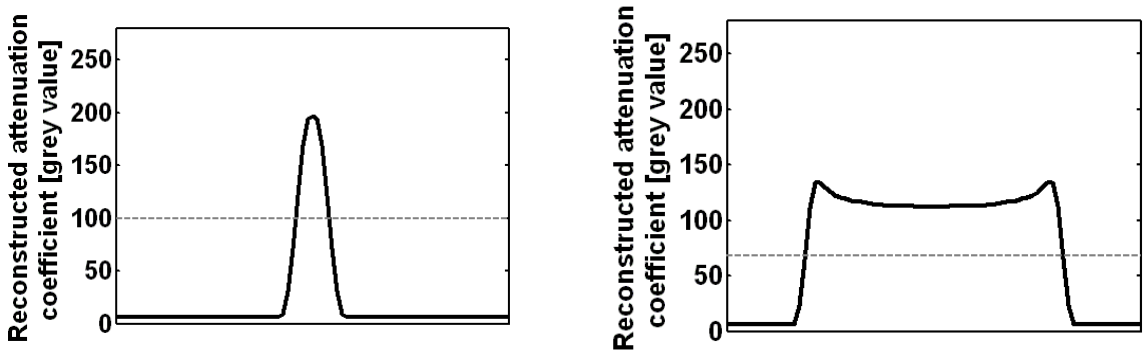

Figure D.2: The reconstructed attenuation coefficient in two spherical gold particles with a radius of (a) 8 and (b) 50 voxels (full line). Because of beam hardening the attenuation in the particle is not constant (cupping) and the reconstructed attenuation coefficient is different for the two particles. To correctly determine the dimensions of both particles different threshold values are needed. The use of a relative threshold value is suggested: 50% of the peak attenuation coefficient in the considered particle (dashed line).

Another approach is not to look for the edges of the gold particle to determine its size. As the PSF only spreads out the attenuation signal, but does not change the total attenuation, the amount of gold can also be determined by calculating the increase in attenuation coefficient that is caused by the gold particles (*Ketcham, 2006*). This is expressed by the following formula where all the attenuation coefficients above the attenuation of the surrounding material are summed:

$$d = v \cdot \sum_{i=1}^{N} \frac{\mu_i}{\mu_{gold}} \tag{D.1}$$

In this equation d is the volume of the gold particle, v is the volume of one voxel, N is the total number of voxels and μ_i and μ_{gold} are respectively the reconstructed attenuation coefficient of voxel i and the reconstructed attenuation coefficient of gold.

But again, due to beam hardening the reconstructed attenuation coefficient of gold depends on the size and shape of the gold particle. Formula (D.1) thus requires a different value for μ_{gold} for every particle with a different size and shape. Determining which μ_{gold} must be used for a particle of which the size and shape are still unknown, is of course not possible. The global use of the reconstructed attenuation value μ_{gold} of a particle with a specific size leads to an underestimation for bigger particles. These particles have undergone more beam hardening and therefore the reconstructed attenuation value μ_{gold} in these particles is smaller. As the value for μ_{gold} is overestimated for these particles, their dimensions are underestimated by formula (D.1). In the same way, the dimensions of smaller particles are overestimated.

D.2 Evaluation of the proposed methodologies

The simulator is used to compare both approaches, i.e. applying a (relative) threshold value and using formula (D.1) to compute the increase in attenuation. 3D simulations of spherical gold particles of different sizes in a quartz matrix are performed. The half of the peak difference between the attenuation value of gold and quartz is used as threshold value. The width of the PSF amounts approximately 8 voxels. The peak difference in attenuation value between gold and quartz for a particle of 8 voxels in diameter voxels is used as μ_{gold} in formula (D.1). Table D.1 summarizes the results for both approaches.

radius [voxels]	volume [voxels³]	thresholding		formula (D.1)	
		volume [voxels³]	relative error [%]	volume [voxels³]	relative error [%]
1	4	20	-377	7	-71
2	34	74	-121	47	-40
3	113	195	-72	141	-25
4	268	340	-27	322	-20
5	524	424	19	576	-10
6	905	606	33	959	-6
7	1437	977	32	1480	-3
8	2145	1587	26	2166	-1
9	3054	2290	25	3054	0
10	4189	3896	7	4021	4
15	14137	13854	2	12299	13
20	33510	34516	-3	27814	17
25	65450	64141	2	49087	25
50	523599	528835	-1	324631	38
100	4188790	4188790	0	2345723	44

Table D.1: Estimated dimensions of 3D spherical gold particles by using a relative threshold value and using formula (D.1).

It appears from table D.1 that a relative threshold value of 50% of the maximum difference in attenuation between gold and quartz for a given particle gives good results for particles bigger than the

PSF. For particles smaller than or in the same order as the PSF a large error is made. The results of the other approach confirm the above mentioned problem. Using the μ_{gold} of a spherical particle with a diameter of 8 voxels gives good results for particles that are slightly bigger or smaller. But a serious error is made for particles that are significantly bigger or smaller than the spherical particle with a diameter of 8 voxels.

Based on these simulations, some first conclusions can already be drawn. The first approach suffers from the limited resolution which is more important for smaller particles. By applying one relative or absolute threshold value it is not possible to accurately determine the size of particles below the resolution or in the same order as the resolution of the imaging system.

The second approach is seriously hindered by beam hardening. Using a synchrotron scanner can be a solution. Table D.2 contains the volumes obtained by formula (D.1) using monochromatic simulations. These estimations are quite accurate. Synchrotron scanners are however more expensive and the sample sizes that can be used are small.

radius [voxels]	**volume [voxels³]**	**formula (D.1)**	
		volume [voxels³]	**relative error [%]**
1	4	4	-7
2	34	32	-5
3	113	110	-3
4	268	263	-2
5	524	514	-2
6	905	896	-1
7	1437	1423	-1
8	2145	2166	1
9	3054	3085	1
10	4189	4231	1
15	14137	14420	2
20	33510	34180	2
25	65450	67414	3
50	523599	534071	2
100	4188790	4356342	4

Table D.2: Estimated dimensions of 3D spherical gold particles by using formula (D.1) based on monochromatic simulations.

To completely describe the eventual applicability of X-ray computed tomography in estimating the gold content of rock samples, a lot of other issues like the impact of the surrounding material, the EEGE effect, effects related to the third dimension, etc. have to be addressed. This can again be performed using the simulator, but is beyond the scope of this appendix which purpose is to demonstrate the usefulness of the simulator in assessing the applicability of X-ray computed tomography for certain applications.

Dankwoord

Het is bijzonder plezant om eindelijk aan dit stukje thesis toe te komen. Vooral omdat dit het laatste is natuurlijk, maar ook omdat het de gelegenheid biedt om de mensen te bedanken zonder wie dit doctoraat er niet was gekomen. En dat zijn in de eerste plaats mijn promotoren professor Rudy Swennen en professor Jan Carmeliet. Beiden stuurden me bij telkens wanneer dat nodig was, maar gaven me de vrijheid om zelf mijn onderzoek in te vullen. Ik ben hen bijzonder dankbaar dat ze me daar de kans en de tijd voor hebben gegeven. En ik heb het dan niet alleen over de periode van mijn doctoraat, maar ook bij het uitwerken van mijn IWT-aanvraag. Zonder hen had ik dit doctoraat niet eens kunnen beginnen.

Het aandeel van Bart Verleye in de start van mijn doctoraat is onbestaande. Maar zijn aandeel in het beëindigen ervan kan moeilijk overschat worden. Zijn werk vormde het laatste stukje in deze puzzel en ik kijk met veel voldoening terug op onze samenwerking. Ik kon altijd vragen om bepaalde berekeningen nog maar eens opnieuw uit te voeren. En dan nog eens. En nog één keer om zeker te zijn. Dat was voor Bart nooit een probleem en ik ben hem daarvoor heel veel dank verschuldigd.

Greet Kerckhofs verdient het zeker ook om een bloemetje toegeworpen te krijgen voor alle hulp bij alles wat met CT scanning te maken had. Ook bedankt zijn professor Johan Nuyts, professor Martine Wevers, professor Stepan Lomov, Bruno De Man, Maarten Van Geet en Katleen Remeysen. Zij hebben elk op hun domein hun deskundig licht laten schijnen over dit werk. Herman Nijs, Dirk Steeno en Katrien Smeets mag ik ook niet vergeten. Omwille van hun technische en administratieve hulp, maar ook omdat ze zulke sympathieke collega's waren.

Sympathiek zijn ook mijn collega’s van het SCK. Zij hebben me de mogelijkheid gegeven om een fantastische job te combineren met het afwerken van mijn doctoraat. In het bijzonder wil ik daarvoor Marc Buyens, Wim Bastiaens en Geert Volckaert bedanken.

Wie ik eigenlijk niet zou mogen bedanken, is Pieter Bertier. Had ik telkens “ja” gezegd wanneer hij me vroeg om mee op stap te gaan, dan was dit doctoraat nooit afgeraakt. Maar toch ook een beetje bedankt, Pieter. Ik heb veel aan onze gesprekken tijdens tal van pauzes gehad. Ook Kaat, Roel en Els wil ik graag vermelden omdat ze er werkelijk altijd voor me zijn. Maar ik wil al mijn vrienden bedanken, want ik prijs me bijzonder gelukkig dat ik er zulke goede heb. Dat geldt ook voor mijn ouders. Ik kan hen niet bedanken voor dit of voor dat, want dat zou afbreuk doen aan de steun en warmte die ze me in alles geven.

En tenslotte wil ik Sarah bedanken. Sarah, bedankt voor alle liefde en steun die je me hebt gegeven tijdens de voorbije jaren.

ISBN 978-90-8649-203-9
D/2008/10.705/50